
An interacting Fermi-Fermi mixture at the crossover of a narrow Feshbach resonance

Louis Costa



München 2011

An interacting Fermi-Fermi mixture at the crossover of a narrow Feshbach resonance

Louis Costa

Dissertation
an der Fakultät für Physik
der Ludwig-Maximilians-Universität
München

vorgelegt von
Louis Costa
aus München

München, März 2011

Erstgutachter: Prof. Dr. Theodor W. Hänsch

Zweitgutachter: Prof. Dr. Ulrich Schollwöck

Tag der mündlichen Prüfung: 8. Juni 2011

Abstract

This work describes experiments with quantum-degenerate atomic mixtures at ultracold temperatures, where quantum statistics determine macroscopic system properties. The first heteronuclear molecules at ultracold temperatures are formed in a quantum degenerate two-species Fermi-Fermi mixture on the repulsive side of a narrow s -wave Feshbach resonance. Elastic collisions in this mixture are investigated with the method of cross-dimensional relaxation. Long-lived two-body bound states on the atomic side of the resonance are detected due to a many-body effect at the crossover of the narrow Feshbach resonance. In addition, atom scattering with fermionic ^{40}K on a light field grating in the Bragg and Kapitza-Dirac regimes is realized for the first time.

The versatile experimental platform, where the investigations are done, offers the possibility to perform studies on mixtures involving the bosonic species ^{87}Rb and the two fermionic species ^6Li and ^{40}K . Within this work, mainly interactions between the two fermionic species are considered. A quantum-degenerate mixture of ^6Li and ^{40}K can be used to create heteronuclear bosonic molecules close to an interspecies s -wave Feshbach resonance. By an adiabatic magnetic field sweep, up to 4×10^4 molecules are produced with conversion efficiencies close to 50%. A direct and sensitive molecule detection method is developed to probe molecule properties. The lifetime of the molecules in an atom-molecule mixture exhibits a strong magnetic field dependence. Close to resonance, lifetimes of more than 100 ms are observed what offers excellent starting conditions for further investigation and manipulation of the molecular cloud.

The interspecies Feshbach resonance, which serves for the production of molecules, is further characterized. The method of cross-dimensional relaxation is applied for the first time to a Fermi-Fermi mixture. For this method, a non-equilibrium state is created, which rethermalizes by pure interspecies collisions due to the fermionic nature of the two species. The lighter atomic species, ^6Li , relaxes faster in the mixture than the heavier one, ^{40}K . This is verified by an analytical model, Monte-Carlo simulations, and measurements. With this technique, elastic scattering cross sections are measured over a wide range of magnetic field strengths across the Feshbach resonance. The position ($B_0 = 154.71(5)$ G) and the magnetic field width of the Feshbach resonance ($\Delta = 1.02(7)$ G) are determined. By comparison of the several measurements, long-lived bound states exist on the atomic side of the resonance due to a many-body effect in the crossover regime of the resonance.

In addition, atomic scattering with ultracold ^{40}K on a light field crystal is studied for the first time. The light grating is generated by two counter-propagating laser beams. Suitable pulse parameters for the realization of atom scattering in the Bragg and Kapitza-Dirac regime are found. The momentum spread of the cloud determines the efficiency of the scattering process, which is increased by lowering the temperature of the system.

Zusammenfassung

Diese Arbeit beschreibt Experimente mit quantenentarteten atomaren Mischungen bei ultrakalten Temperaturen, bei denen die Quantenstatistik der Atome relevant wird. Auf der molekularen Seite einer schmalen s -Wellen Feshbach Resonanz werden aus einer Mischung mit zwei fermionischen Spezies zum ersten Mal heteronukleare Moleküle bei ultrakalten Temperaturen gebunden. Mit der Methode der cross-dimensionalen Relaxation werden zudem in der gleichen Mischung elastische Kollisionen nahe der Resonanz untersucht. Langlebige gebundene Zustände auf der atomaren Seite der Feshbach Resonanz werden detektiert, die auf Grund einer Eigenschaft des Vielteilchensystems an der schmalen Feshbach Resonanz existieren. Darüber hinaus wird die Streuung von fermionischem ^{40}K an einem Lichtgitter im Bragg- und Kapitza-Dirac Regime zum ersten Mal untersucht.

Die vielseitig einsetzbare Apparatur, mit der die Experimente durchgeführt worden sind, eröffnet die Möglichkeit Untersuchungen an Mischungen, die das bosonische ^{87}Rb und die beiden fermionischen Teilchensorten ^6Li und ^{40}K beinhalten, durchzuführen. Im Rahmen der vorliegenden Arbeit wurde hauptsächlich die Wechselwirkung zwischen den beiden fermionischen Teilchensorten studiert. Eine quantenentartete Mischung aus ^6Li und ^{40}K kann verwendet werden, um heteronukleare bosonische Moleküle nahe einer interspezies s -Wellen Feshbach Resonanz zu bilden. Mit Hilfe einer adiabatischen Magnetfeldrampe werden bis zu 4×10^4 Moleküle produziert mit Konversionseffizienzen von bis zu 50 %. Eine direkte Detektionsmethode für die Moleküle wird entwickelt, um deren Eigenschaften zu untersuchen. Die Lebensdauer der Moleküle in einem Atom-Molekülgemisch zeigt eine starke Magnetfeldabhängigkeit. Nahe der Resonanz, werden Lebensdauern von mehr als 100 ms beobachtet, die eine exzellente Ausgangslage für weitere Untersuchungen und Manipulationen der molekularen Wolke bieten.

Die interspezies Feshbach Resonanz, die zur Molekülproduktion dient, wird weiter charakterisiert. Die Methode der cross-dimensionalen Relaxation wird zum ersten Mal auf eine Fermi-Fermi Mischung angewendet. Für diese Methode wird ein Nichtgleichgewichtszustand präpariert, der durch reine interspezies Kollisionen rethermalisiert. Die Teilchensorte mit der kleineren Masse, ^6Li , relaxiert schneller in der Mischung als die größere Masse, ^{40}K . Dies wird durch ein analytisches Modell, Monte-Carlo Simulationen und Messungen bestätigt. Mit dieser Methode werden außerdem elastische Streuquerschnitte über einem weiten Magnetfeldbereich nahe der Resonanz gemessen. Position ($B_0 = 154.71(5) \text{ G}$) und Magnetfeldbreite der Resonanz ($\Delta = 1.02(7) \text{ G}$) werden bestimmt. Durch Vergleich der verschiedenen Messungen werden langlebige gebundene Zustände auf der atomaren Seite der Resonanz gefunden, die auf Grund von Eigenschaften des Vielkörpersystems existieren.

Außerdem wird atomare Streuung von ultrakaltem ^{40}K an einem Lichtkristall zum ersten Mal untersucht. Das Lichtgitter wird durch zwei entgegengesetzt verlaufende Laserstrahlen gebildet. Geeignete Pulsparameter für atomare Streuung im Bragg und Kapitza-Dirac Regime werden optimiert. Die Impulsbreite der atomaren Wolke bestimmt die Effizienz des Streuprozesses, die durch Verringern der Temperatur des Systems erhöht werden kann.

Contents

1	Introduction	1
1.1	Quantum degenerate Fermi gases	1
1.2	Many-body physics and the BEC-BCS crossover	2
1.3	Atom scattering from light gratings	4
1.4	Outline of this thesis	5
2	Theory	9
2.1	Ultracold quantum gases	9
2.1.1	Quantum statistics	9
2.1.2	Fermionic quantum gases	11
2.2	Ultracold collisions	13
2.2.1	Two-body Hamiltonian	13
2.2.2	Differential and total elastic scattering cross section	14
2.2.3	s -wave regime, low energy limit	15
2.3	Feshbach resonances	16
2.3.1	Magnetic field induced Feshbach resonances	17
2.3.2	Feshbach resonances in the ${}^6\text{Li}$ - ${}^{40}\text{K}$ mixture	20
2.3.3	Classification of broad and narrow Feshbach resonances	22
2.3.4	Many-body regimes in the zero temperature limit	24
2.3.5	Few-body problem close to a narrow Feshbach resonance	29
2.4	Cross-species thermalization in atomic gases	29
2.4.1	Boltzmann equation	29
2.4.2	Cross-dimensional thermal relaxation	32
3	Experimental apparatus	43
3.1	Experimental concept and overview	43
3.2	From a MOT to quantum degeneracy	45
3.3	Benchmark tests of an experimental cycle	46
3.4	Potassium laser system	47
3.4.1	Overview	48
3.4.2	Bragg beam setup	48
3.5	Optical dipole trap	49
3.5.1	Principle	49

CONTENTS

3.5.2	Technical realization	51
3.5.3	Alignment of beams	52
3.5.4	Characterization of trap	53
3.6	Feshbach magnetic fields	54
3.6.1	Feshbach coils and current control	54
3.6.2	Stability and ambient magnetic fields	56
3.6.3	Magnetic field calibration	57
3.7	Detection of atoms at high magnetic field	58
3.7.1	Absorption imaging	58
3.7.2	Stern-Gerlach setup	60
4	Diffraction of fermions from light gratings	61
4.1	Diffraction of atoms from a standing wave	61
4.1.1	Atom-light interaction	61
4.1.2	Principle of Bragg scattering	63
4.1.3	Principle of Kapitza-Dirac scattering	65
4.2	Experimental results	66
4.2.1	Influence of finite temperature of atomic cloud	66
4.2.2	Bragg scattering	67
4.2.3	Kapitza-Dirac scattering	71
4.2.4	Discussion and conclusions	72
5	Ultracold Fermi-Fermi molecules at a narrow Feshbach resonance	75
5.1	Experimental sequence	76
5.1.1	Loading of the optical dipole trap	76
5.1.2	State preparation	77
5.2	Feshbach loss spectroscopy	78
5.3	Heteronuclear Fermi-Fermi molecules	80
5.3.1	Adiabatic conversion of atoms to molecules	80
5.3.2	Reconversion to atoms from dissociated molecules	81
5.3.3	Direct detection of molecules	82
5.3.4	Molecule lifetime in an atom-molecule ensemble	84
6	<i>s</i>-wave interaction in a two-species Fermi-Fermi mixture	87
6.1	Experimental sequence	87
6.2	Cross-dimensional thermal relaxation	89
6.3	Elastic scattering cross sections	90
6.4	Position and width of Feshbach resonance	92
6.5	Two-body bound states at the crossover of a narrow Feshbach resonance	93
7	Conclusions and Outlook	97
A	Level schemes	101
B	Center of mass and relative coordinates	103

C Initial parameters and constraints for cross-dimensional relaxation	105
C.1 Validity of kinetic model	105
C.2 Initial conditions for cross-dimensional relaxation	106
C.2.1 Dependence on particle number and initial anisotropy	106
C.2.2 Initial imbalance of mean energies per particle	109
C.3 Energy dependence of scattering cross section	112
D Optical transition strength for high magnetic field	115
D.1 Representation of the hyperfine structure and Zeeman operator	115
D.2 Optical transition strength	117
Danksagung	138

CONTENTS

Chapter 1

Introduction

The area of ultracold atomic gases is today one of the fastest evolving fields in physics. The foundation of this fast progress was laid by the development of laser cooling and trapping of atoms, which was honored with the Nobel prize in 1997 (S. Chu, C. Cohen-Tannoudji, W.D. Phillips). The understanding of trapping and cooling of neutral atoms was the prerequisite for the first observation of Bose-Einstein condensation (BEC) in a dilute atomic vapor gas (Anderson *et al.*, 1995; Bradley *et al.*, 1995; Davis *et al.*, 1995) in 1995. This outstanding experimental achievement took place seventy years after its prediction by (Einstein, 1924; Bose, 1924) in 1924, and was awarded the Nobel prize in 2001 (E.A. Cornell, W. Ketterle, C.E. Wieman). By extending the developed experimental techniques for laser cooling and controllability of atoms, several other experimental milestones were achieved in the subsequent decade.

1.1 Quantum degenerate Fermi gases

Shortly after the first observation of BEC, a lot of effort is made to cool also fermionic atomic species into the quantum-degenerate regime. This is accomplished in a gas of fermionic ^{40}K atoms (DeMarco and Jin, 1999) in 1999 for the first time, only four years after the first observation of a BEC. In the zero temperature limit, spin-polarized fermionic atoms occupy in a trap all quantum mechanical states up to the Fermi energy only once, since the Pauli exclusion principle holds. The Fermi energy is related to the number of atoms confined in the trap. Achieving quantum degeneracy in fermionic gases is technically more challenging compared to the bosonic case, since the Pauli principle at low temperatures suppresses the rate of s -wave collisions and evaporation in a one-component fermionic cloud of atoms becomes inefficient. The successful realization of quantum degeneracy in 1999 uses the strategy of evaporative cooling of a spin mixture of atoms in a magnetic trap. Other methods of achieving a degenerate Fermi gas are pursued by (Schreck *et al.*, 2001; Truscott *et al.*, 2001) by sympathetic cooling of fermionic ^6Li with the bosonic isotope ^7Li , and by (Granade *et al.*, 2002) using all-optical techniques. The technique of sympathetic cooling of fermions with bosons is realized in many other mixtures such as ^6Li - ^{23}Na (Hadzibabic *et al.*, 2002), ^{40}K - ^{87}Rb (Roati *et al.*, 2002), ^6Li -

1.2 Many-body physics and the BEC-BCS crossover

^{87}Rb (Silber *et al.*, 2005), $^3\text{He}^* - ^4\text{He}^*$ (McNamara *et al.*, 2006), $^{171}\text{Yb} - ^{174}\text{Yb}$ (Fukuhara *et al.*, 2007), $^{87}\text{Sr} - ^{84}\text{Sr}$ (Tey *et al.*, 2010), and $^6\text{Li} - ^{174}\text{Yb}$ (Okano *et al.*, 2010). In the present experiment of this thesis work, sympathetic cooling of a mixture with two different fermionic species $^6\text{Li} - ^{40}\text{K}$ is realized by a large bath of bosonic ^{87}Rb atoms.

The first experimental investigations with Fermi gases involve measurements of the mean energy per particle and momentum distributions (DeMarco and Jin, 1999), the study of Fermi pressure (Truscott *et al.*, 2001), and the investigation of Pauli blocking of collisions (DeMarco *et al.*, 2001). The great potential of Fermi gases manifests itself in the exploration of so-called Feshbach resonances. Such scattering resonances allow to control the strength of two-body interactions by applying an external magnetic field and even the sign of the scattering length a of the atoms can be varied. For s -wave Feshbach resonances in spin mixtures of Fermi gases, the rate of three-body losses is suppressed for increasing scattering length due to the Pauli exclusion principle (Petrov *et al.*, 2004a). Therefore, strongly correlated states can be realized in these atomic systems by the exploitation of Feshbach resonances. This stands in contrast to the case of bosons, where strong interactions induced by Feshbach resonances lead always to strong losses and prevent the study of strongly interacting systems (Courteille *et al.*, 1998; Inouye *et al.*, 1998; Cornish *et al.*, 2000). Strongly correlated bosonic systems can be investigated in lower dimensions with the techniques of optical lattices (Greiner *et al.*, 2002; Paredes *et al.*, 2004; Kinoshita *et al.*, 2004). In 2002, intraspecies s -wave Feshbach resonances involving two different hyperfine states are observed in ^6Li (O'Hara *et al.*, 2002a; Dieckmann *et al.*, 2002; Jochim *et al.*, 2002) and in ^{40}K (Loftus *et al.*, 2002). This achievement of interaction control in Fermi gases opens the way to explore strongly correlated systems at the unitary regime and many-body physical phenomena at the BEC-BCS crossover of a Feshbach resonance. This will be described in the next section.

1.2 Many-body physics and the BEC-BCS crossover

Dilute atomic gases are believed to be an ideal candidate to model solid-state systems because of their purity and high controllability. For reviews on solid-state models based on ultracold atoms see e.g. (Lewenstein *et al.*, 2007; Bloch *et al.*, 2008). The first work in this context involves the study of the superfluid to Mott-insulator transition of cold atoms in an optical lattice (Jaksch *et al.*, 1998; Greiner *et al.*, 2002). The accuracy of experimental control expresses itself on the one hand by the ability to load bosons into optical lattices and on the other hand by the interaction control of fermions by means of Feshbach resonances. Although the particle density in atomic gases is typically 10^8 times lower as in solids, interactions and correlations become relevant at ultracold temperatures. Feshbach resonances allow to enter the strongly interacting regime in ultracold Fermi gases (Bourdell *et al.*, 2003). Stable molecular states with a long lifetime are formed by a pair of fermions in highly excited rovibrational states on the repulsive side of the Feshbach resonance with $a > 0$ (Cubizolles *et al.*, 2003; Strecker *et al.*, 2003). The long lifetimes can exceed the thermalization time what allows to evaporate the molecules directly to form a molecular BEC (Greiner *et al.*, 2003; Jochim *et al.*, 2003a; Zwierlein

et al., 2003).

If heteronuclear mixtures of alkali-metal atoms are prepared at interspecies Feshbach resonances, a more exotic quantum many-body behavior is expected (Micheli *et al.*, 2006; Lewenstein *et al.*, 2007). In a Bose-Fermi mixture of ^{87}Rb and ^{40}K atoms, fermionic molecules are formed on the repulsive side of an interspecies Feshbach resonance in a three-dimensional optical lattice (Ospelkaus *et al.*, 2006) and in an optical dipole trap by association with a radiofrequency field (Zirbel *et al.*, 2008; Klempt *et al.*, 2008). In Bose-Bose systems, bosonic molecules are produced in a ^{85}Rb - ^{87}Rb (Papp and Wieman, 2006) and in a ^{87}Rb - ^{41}K mixture (Weber *et al.*, 2008). Mixtures of different fermionic species with unequal masses could provide novel quantum phases (Petrov *et al.*, 2007). Within the present thesis work, the first creation of longlived heteronuclear bosonic molecules from a quantum-degenerate ^6Li - ^{40}K mixture is realized (Voigt *et al.*, 2009).

On the attractive side ($a < 0$) of the Feshbach resonance a Bardeen-Cooper-Schrieffer (BCS) type state with correlation in momentum space is expected, and the Fermi gas becomes superfluid. On the BCS side, pairing is a many-body effect, whereas individual non-condensed molecules on the repulsive side of the resonance can be described on the two-body level. The critical temperature T_C for the transition to superfluidity on the BCS side is on the order of the Fermi temperature T_F , and condensation of fermion pairs on the BCS side of the resonance has been observed (Regal *et al.*, 2004a; Zwierlein *et al.*, 2004). Because of the tunability of the scattering length, the crossover from weakly bound molecules with pairing in real space to pairing in momentum space due to many-body effects can be characterized (Bartenstein *et al.*, 2004; Bourdel *et al.*, 2004). The correlation in momentum space is directly detected with shot-noise spectroscopy in (Greiner *et al.*, 2005). Superfluidity on the BCS side of the resonance is probed with radiofrequency spectroscopy by observing the pairing gap (Chin *et al.*, 2004) or more directly by exciting a vortice lattice across the BEC-BCS crossover (Zwierlein *et al.*, 2005) in a strongly interacting Fermi gas.

More recently, the work involving fermionic gases concentrates on systems with imbalanced particle number in the spin states. Several exotic pairing mechanisms with different Fermi surfaces are expected, which may serve as a model system for the simulation of cold dense matter in neutron stars (Casalbuoni and Nardulli, 2004). First experiments within the field of polarized Fermi gases involve the observation of phase separation (Partridge *et al.*, 2006) and fermionic superfluidity under an imbalanced spin population (Zwierlein *et al.*, 2006). Later, the superfluid phase diagram by variation of the spin imbalance is mapped out (Schunck *et al.*, 2007; Shin *et al.*, 2008), collective oscillations (Nascimbéne *et al.*, 2009) are studied, and spin-imbalance in an one-dimensional optical lattice (Liao *et al.*, 2010) is investigated. In the present experiment, the unequal masses of ^6Li and ^{40}K lead to a mismatch in the Fermi energies even at equal particle number, and the mass ratio needs to be considered as a new parameter in the many-body phase diagram (Baranov *et al.*, 2008; Gubbels *et al.*, 2009; Gezerlis *et al.*, 2009). In multi-species Fermi mixtures, a close analogy to color superconductivity in quantum chromodynamics is expected (Bowers and Rajagopal, 2002; Liu and Wilczek, 2003; Rapp *et al.*, 2007).

The Fermi-Fermi mixture of ^6Li and ^{40}K studied within the present work offers several advantages. Each of the species has been extensively studied in the quantum de-

1.3 Atom scattering from light gratings

generate regime as outlined above. In contrast to these investigations, with the ${}^6\text{Li}$ - ${}^{40}\text{K}$ Fermi-Fermi mixture the first observation of a Bose-Einstein condensate of heteronuclear molecules and the study of the BEC-BCS crossover under the influence of a mass imbalance are within reach. Additionally, not only the Fermi-Fermi mixture ${}^6\text{Li}$ - ${}^{40}\text{K}$, but even the Bose-Fermi mixture ${}^{87}\text{Rb}$ - ${}^6\text{Li}$ with a large mass ratio has not been investigated by the time when the present experiment was built up. With the present ${}^{87}\text{Rb}$ - ${}^6\text{Li}$ - ${}^{40}\text{K}$ mixture, several interspecies Feshbach resonances or eventually triple species trimer resonances can be expected.

1.3 Atom scattering from light gratings

One of the main goals in atom optics is to coherently manipulate atomic waves. Not only internal quantum states of atoms can be controlled by laser light, but also external degree of freedoms such as the momentum state of the atoms. Quantized momentum can be transferred coherently from light to atoms by photon absorption and emission processes. This is observed in (Moskowitz *et al.*, 1983) for the first time with an atomic beam. Within the framework of this thesis, two coherent regimes for momentum transfer are relevant, which can be distinguished by the duration of atom-light interaction: Bragg and Kapitza-Dirac regime.

Bragg diffraction was first investigated by W.H. Bragg in 1912 by scattering processes of X-rays in solid crystals. Because of the particle-wave duality, atoms, i.e. matter waves, can be scattered from a light crystal in close analogy to the original experiment of W.H. Bragg. In atomic systems, Bragg scattering is observed in (Martin *et al.*, 1988) for the first time. Bragg diffraction is often used as a spectroscopic tool as e.g. applied for the study of the momentum distribution (Ovchinnikov *et al.*, 1999) and mean-field energy of a BEC (Stenger *et al.*, 1999). The goal of these early investigations in a BEC with Bragg spectroscopy involved mainly the characterization of the coherence properties of a BEC as a macroscopic wavefunction (see also below). Bragg spectroscopy can also be used to study strongly correlated atomic systems since this technique provides access to the structure factor and molecular signatures become available (Combescot *et al.*, 2006). Bragg spectroscopy is applied to a strongly interacting BEC close to a Feshbach resonance in (Papp *et al.*, 2008), to a BEC in an optical lattice in (Ernst *et al.*, 2010), and to strongly correlated bosons in an optical lattice in (Clément *et al.*, 2009). The technique has also been employed to Fermi gases. A strongly interacting Fermi gas at the BEC-BCS crossover of the very broad Feshbach resonance at 834 G in ${}^6\text{Li}$ is studied with Bragg spectroscopy (Veeravalli *et al.*, 2008). By determining the static structure factor of a strongly interacting fermionic ${}^6\text{Li}$ gas, universal behavior of pair correlations (Kuhnle *et al.*, 2010; Zou *et al.*, 2010) is studied. The critical temperature and condensate fraction of a fermion pair condensate is investigated in (Inada *et al.*, 2008). In relation to fermionic quantum gases, many other proposals can be found in the literature such as Bragg scattering of Cooper pairs (Challis *et al.*, 2007), a probe for Fermi superfluidity (Büchler *et al.*, 2004; Guo *et al.*, 2010) and the BCS pairing gap (Bruun and Baym, 2006).

The second regime for atomic scattering, which is relevant for the present thesis work, is first described by P.L. Kapitza and P.A.M. Dirac in 1933 in the context of diffraction of a collimated electron beam by a standing light wave through stimulated Compton scattering. In atomic systems, Kapitza-Dirac scattering is first proposed by (Altshuler *et al.*, 1966) and experimentally realized by (Gould *et al.*, 1986). For instance, Kapitza-Dirac scattering can be used to probe superfluidity of fermions in an optical lattice (Chin *et al.*, 2006).

Beside their application as a spectroscopic method, sequences of Bragg and Kapitza-Dirac pulses can also be used to realize an atom interferometer. Pioneering atom interferometry experiments are (Keith *et al.*, 1991) with sodium atoms and (Carnal and Mlynek, 1991) with metastable helium atoms, which both use microfabricated mechanical gratings. Over the last two decades, matter waves have been extensively studied by interferometry experiments. Decoherence in interferometry experiments (Gould *et al.*, 1991; Clauser and Li, 1994; Chapman *et al.*, 1995), which-way-information of interferometer paths (Dürr *et al.*, 1998a,b), or the size of the interfering object (Arndt *et al.*, 1999) can test the transition from quantum-mechanical to classical behavior. With the help of interferometry the coherence properties of a BEC (Andrews *et al.*, 1997; Stenger *et al.*, 1999; Kozuma *et al.*, 1999) or atom lasers (Anderson and Kasevich, 1999; Bloch *et al.*, 2000) can be probed. Also atomic clocks based on precision interferometry allow to measure fundamental physical constants (for a review see e.g. Cronin *et al.*, 2009). A robust interferometry scheme for the determination of h/m and the finestructure constant α is presented in (Gupta *et al.*, 2002). In this experiment, the interferometry sequence consists of one Kapitza-Dirac and one Bragg pulse, and is applied to a BEC of sodium atoms. Mean-field effects in a BEC can influence interferometric measurements. Interactions are crucial as they introduce phase diffusion, which limits the phase accumulation times in interferometers (Grond *et al.*, 2010). On the other hand, interferometry with Fermi atoms is shown in (Roati *et al.*, 2004) by observing oscillations of a Fermi gas in an one-dimensional optical lattice. Long-lived oscillations are found due to Pauli exclusion principle what could have advantageous consequences for future applications in precision interferometry. Another experiment presents a Ramsey-interferometer with an ultracold ${}^6\text{Li}$ cloud (Deh *et al.*, 2009). Also in this study, long-lived oscillations of a Fermi gas are influenced and damped by imposing an impureness with a bosonic species due to interactions.

Within the present work, the basis for applications involving pulses both for spectroscopic and interferometric purposes is laid by the development of efficient Bragg and Kapitza-Dirac diffraction of an ultracold cloud of fermionic atoms.

1.4 Outline of this thesis

This thesis describes experiments with a strongly interacting and quantum-degenerate two-species Fermi-Fermi mixture at a narrow Feshbach resonance. For the first time, heteronuclear bosonic molecules are formed from two different fermions by an adiabatic magnetic field sweep across an interspecies Feshbach resonance. In addition, the method

1.4 Outline of this thesis

of cross-dimensional relaxation is investigated in a two-species Fermi-Fermi mixture. The mass difference plays a crucial role for the determination of system properties. The method of cross-dimensional relaxation is used to measure elastic scattering cross sections across the same interspecies Feshbach resonance, where molecules were produced previously. Position and width of the Feshbach resonance are experimentally obtained. A comparison of several measurements reveals that heteronuclear molecules with very long lifetimes are present on the atomic side of the resonance. This observation is related to a theoretically predicted many-body property of the resonantly interacting Fermi-Fermi mixture at a narrow Feshbach resonance. This establishes the first experimental observation of a many-body effect at a narrow Feshbach resonance and paves the way to study superfluidity for this case.

As a second topic, the experimental control of atomic scattering in a quantum-degenerate Fermi gas from a light grating is demonstrated. This opens up possibilities to investigate interferometry with fermions and to apply Bragg spectroscopy in the future.

The thesis is organized as follows:

- Ch. 2 gives a theoretical overview. Properties of quantum-degenerate Fermi gases, ultracold collisions, Feshbach resonances, and kinetic phenomena in ultracold quantum gases are discussed. Classical Monte-Carlo simulations are introduced and employed to model rethermalization experiments.
- Ch. 3 presents the experimental apparatus for the investigation of a quantum-degenerate Fermi-Fermi mixture. Detailed descriptions of the parts of the experiment are given, which were adjoined and altered during the course of this work. The first part of this chapter involves the illustration of the concept of the setup, the description of the experimental sequence, and the maintenance of the apparatus by comprehensive benchmark tests on the experimental cycle. The second part deals with specific parts of the setup such as the potassium laser system, which is extended during the course of this work by a Bragg beam setup and a laser system for high field detection. In addition, the optical dipole trap, which is used for the exploration of Feshbach resonances, is brought forward for discussion. Moreover, the setup and control for the creation of a Feshbach magnetic field are elucidated. The last part involves the description of the direct detection method for heteronuclear molecules comprising a strong magnetic field gradient in combination with resonant high field absorption imaging.
- Ch. 4 is a self-contained part, where atomic scattering of Fermi atoms from a standing wave is realized. First, a theoretical description is presented for atom scattering by light, where one discriminates two relevant regimes, Bragg and Kapitza-Dirac scattering, depending on the duration of the atom-light interaction. Bragg and Kapitza-Dirac scattering of ^{40}K atoms are experimentally characterized thereby demonstrating the controllability for possible prospective applications.
- Ch. 5 presents the first creation of heteronuclear bosonic molecules from a two-species Fermi-Fermi mixture. As a first point, the experimental sequence is presented. Then, a suitable interspecies Feshbach resonance is located by inelastic loss

spectroscopy. The adiabaticity of the molecule production process is investigated by varying the rate of the magnetic field ramp. Evidence for molecule production is given by reconversion of atoms from dissociated molecules. The molecules are directly detected by using a combination of a Stern-Gerlach pulse and absorption imaging at high magnetic field. With this direct detection method, the lifetime of the molecules in an atom-molecule mixture is measured and an increased lifetime of more than 100 ms is observed close to resonance. Parts of this chapter are published in (Voigt *et al.*, 2009).

- In Ch. 6, the method of cross-dimensional relaxation is applied to a two-species Fermi-Fermi mixture for the first time. First, the experimental sequence is introduced. Subsequently, cross-dimensional relaxation is investigated experimentally in a ${}^6\text{Li}$ - ${}^{40}\text{K}$ mixture, where only interspecies collisions are allowed at ultracold temperatures. The method is applied to the same interspecies Feshbach resonance, which serves already for molecule production, and elastic scattering cross sections are measured over a wide range of magnetic field strengths. The position and width of the Feshbach resonance is experimentally determined. This chapter concludes with a comparison and interpretation of the several measurements performed on the investigation of properties of the heteronuclear molecules and of the employed Feshbach resonance. Based on the consistency of the results with a previously predicted effect from a two-channel model, a significant number of molecules is present on the atomic side of the Feshbach resonance and the crossover region extends to a magnetic field range related to the sum of the Fermi energies of the constituents. The very long lifetimes of more than 100 ms are exhibited by two-body bound states, which are present on the atomic side of the resonance, and the stabilization against dissociation occurs most probably by unbound fermions in the mixture. This establishes the first observation of a many-body effect at the crossover of a narrow interspecies Feshbach resonance. Parts of this chapter are published in (Costa *et al.*, 2010).

1.4 Outline of this thesis

Chapter 2

Theory

The present work in this thesis deals with atomic ensembles, which are laser-cooled to sub- μK temperatures. At such ultracold temperatures, the quantum nature of the individual atoms becomes significant for the description of thermodynamic quantities of a gas cloud of atoms. In the experiments, information on several thermodynamic properties are extracted from density profiles of the cloud. The focus of this thesis will be mainly on mixtures of Fermi gases. Therefore, the description for quantification in the experiments is only elucidated for Fermi gases in Sec. 2.1. In Sec. 2.2, scattering of atoms at ultracold temperatures is discussed, which is necessary to understand the mechanism of Feshbach resonances as presented in the subsequent Sec. 2.3. This chapter concludes with a discussion of kinetic phenomena in ultracold quantum gases that are relevant for the present thesis. As one of the main results in this work, a nonequilibrium state of the gas clouds is used to determine properties of an interspecies Feshbach resonance in the ${}^6\text{Li}$ - ${}^{40}\text{K}$ Fermi-Fermi mixture.

2.1 Ultracold quantum gases

During the course of this work, mixtures of atomic gases, both fermionic and bosonic species, are routinely cooled in different trap configurations to densities and temperatures, where the quantum nature of particles influences the observable thermodynamic properties considerably. For the interpretation of experiments a profound understanding is required how to assign temperature, particle number, and other measurable quantities to a trapped cloud of atoms. The quantitative analysis of density profiles is discussed in the following section. Other descriptions can also be found in various work (Ketterle *et al.*, 1999; Pethick and Smith, 2002; Ketterle and Zwierlein, 2008).

2.1.1 Quantum statistics

An ideal quantum gas is characterized by the property that interparticle interactions are negligible due to very low densities in the trap. Hence, a single particle confined in an external harmonic potential $V(\mathbf{r}) = m/2 (\omega_x^2 x^2 + \omega_y^2 y^2 + \omega_z^2 z^2)$ with angular trapping

2.1 Ultracold quantum gases

frequencies $\omega_i = 2\pi\nu_i$ ($i = x, y, z$) is described by the Hamiltonian

$$H(\mathbf{r}, \mathbf{p}) = \frac{1}{2m} (p_x^2 + p_y^2 + p_z^2) + \frac{m}{2} (\omega_x^2 x^2 + \omega_y^2 y^2 + \omega_z^2 z^2). \quad (2.1)$$

Here, the geometric mean trapping frequency is given by $\bar{\omega} = (\omega_x \omega_y \omega_z)^{1/3}$. In the semiclassical approximation the thermal energy $k_B T$ is much larger than the quantum mechanical level spacings $\hbar\omega_i$. The occupation of a phase space cell (\mathbf{r}, \mathbf{p}) is given by

$$f(\mathbf{r}, \mathbf{p}) = \frac{1}{e^{\frac{1}{k_B T} \left(\frac{\mathbf{p}^2}{2m} + V(\mathbf{r}) - \mu \right)} \pm 1}. \quad (2.2)$$

The upper sign (+) is valid for fermions (Fermi-Dirac statistics), whereas the lower sign (−) holds for bosons (Bose-Einstein statistics). The chemical potential μ is determined from the particle number normalization condition $N = \int f(\mathbf{r}, \mathbf{p}) / h^3 d\mathbf{p} d\mathbf{r}$, where N is the total atom number. By defining the fugacity $\tilde{z} = \exp(\mu / (k_B T))$, the spatial intratrap density distribution of the atoms in the excited states is determined to be

$$n_{\text{ex}}(\mathbf{r}) = \int \frac{d\mathbf{p}}{h^3} f(\mathbf{r}, \mathbf{p}) = \mp \frac{1}{\lambda_{\text{dB}}^3} \cdot g_{3/2} \left(\mp \tilde{z} e^{-\frac{V(\mathbf{r})}{k_B T}} \right), \quad (2.3)$$

and for the momentum distribution one obtains by assuming the harmonic potential $V(\mathbf{r})$ from Eq. (2.1)

$$n_{\text{ex}}(\mathbf{p}) = \int \frac{d\mathbf{r}}{h^3} f(\mathbf{r}, \mathbf{p}) = \mp \frac{1}{m^3 \bar{\omega}^3 \lambda_{\text{dB}}^3} \cdot g_{3/2} \left(\mp \tilde{z} e^{-\frac{1}{k_B T} \frac{\mathbf{p}^2}{2m}} \right). \quad (2.4)$$

In the last expression the de Broglie wavelength

$$\lambda_{\text{dB}} = h / \sqrt{2\pi m k_B T} \quad (2.5)$$

and the polylogarithm function $g_\alpha(s)$ are introduced. Note that $n_{\text{ex}}(\mathbf{p})$ is isotropic, whereas $n_{\text{ex}}(\mathbf{r})$ depends on the trap potential. The polylogarithm function can be expressed as a series expansion

$$g_\alpha(s) = \sum_{k=1}^{\infty} \frac{s^k}{k^\alpha}. \quad (2.6)$$

This expression is valid for all complex numbers α and s where $|s| \leq 1$. The integral representation of the polylogarithm function is invoked in Eqs. (2.3) and (2.4)

$$\int_0^\infty \frac{t^\alpha}{s^{-1} e^t \pm 1} dt = \mp \Gamma(\alpha + 1) g_{\alpha+1}(\mp s), \quad (2.7)$$

where $\Gamma(x)$ is the Gamma function. A useful relation for integrating density distributions in order to obtain column and line densities is

$$\int_{-\infty}^{\infty} dx g_\alpha(z e^{-x^2}) = \sqrt{\pi} g_{\alpha+1/2}(z). \quad (2.8)$$

In the semiclassical approximation the total atom number is on the order of the number of atoms in the excited states $N \approx N_{\text{ex}}$. The latter is given by

$$N_{\text{ex}} = \int d\mathbf{r} n_{\text{ex}}(\mathbf{r}) = \mp \left(\frac{k_B T}{\hbar \bar{\omega}} \right)^3 g_3(\mp \tilde{z}). \quad (2.9)$$

For the derivation of macroscopic thermodynamic quantities, it is convenient to define a continuous density of states $g(\epsilon)$

$$g(\epsilon) = \frac{1}{h} \int d\mathbf{r} d\mathbf{p} \delta(\epsilon - H(\mathbf{r}, \mathbf{p})). \quad (2.10)$$

This yields for the harmonic trap from Eq. (2.1) (Bagnato *et al.*, 1987; Pethick and Smith, 2002)

$$g(\epsilon) = \frac{\epsilon^2}{2(\hbar \bar{\omega})^3}. \quad (2.11)$$

With the integral representation of the polylogarithm function, the total energy in the atomic gas can be derived

$$U(T) = \int_0^\infty \epsilon f(\epsilon) g(\epsilon) d\epsilon. \quad (2.12)$$

For the harmonic case, this yields

$$U(T) = -3k_B T \left(\frac{k_B T}{\hbar \bar{\omega}} \right)^3 g_4(\mp \tilde{z}). \quad (2.13)$$

2.1.2 Fermionic quantum gases

All relations presented so far are valid both for Bose-Einstein as well as Fermi-Dirac statistics. In the following, only the case of Fermi-Dirac statistics is considered, since Fermi gases are predominantly investigated within this work.

2.1.2.1 Fermi gas in a harmonic trap

An ensemble of N particles with Fermi statistics at temperature T is described by the Fermi-Dirac distribution

$$f_{\text{FD}}(\epsilon) = \frac{1}{1 + e^{\frac{\epsilon - \mu}{k_B T}}}, \quad (2.14)$$

where the chemical potential μ is determined from the condition of particle number normalization. According to Pauli exclusion principle, in a system of identical fermions, particles can occupy a single quantum mechanical state only once. A system of fermions at zero temperature $T = 0$ confined in a trap is characterized by the Fermi energy E_F , which is defined as the energy of the highest occupied state in the trap. The associated Fermi temperature is expressed by $T_F \equiv E_F/k_B$. For increasing degeneracy parameter T/T_F , the occupation probability is gradually smeared out over a region on the order

2.1 Ultracold quantum gases

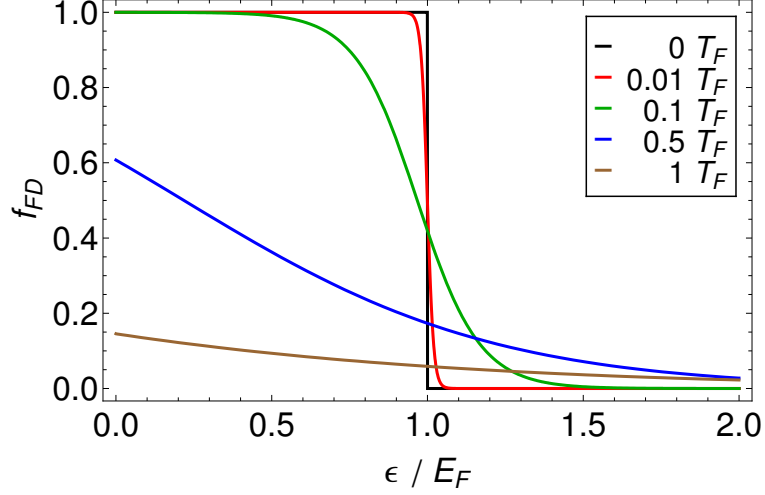


Figure 2.1: The occupation probability for Fermi-Dirac statistics as a function of the single particle energy is shown for the temperatures $T = 0$, $T = 0.01 T_F$, $T = 0.1 T_F$, $T = 0.5 T_F$ and $T = T_F$ and fixed particle number.

of $E_F \cdot T/T_F$ as presented in Fig. 2.1. For zero temperature, the distribution function f_{FD} is one for energies $\epsilon < \mu (T \rightarrow 0) \equiv E_F$, and zero for energies larger than the Fermi energy, see Fig. 2.1.

In order to determine E_F , the density of states $g(\epsilon)$ needs to be considered. By integrating the density of states over all possible energy states at zero temperature, the particle number is obtained

$$N = \int_0^{\infty} f_{\text{FD}}(\epsilon) g(\epsilon) d\epsilon = \int_0^{E_F} g(\epsilon) d\epsilon, \quad (2.15)$$

where every level up to E_F is fully occupied. After integration of the expression given in Eq. (2.11), the Fermi energy of a harmonically confined gas can be obtained

$$E_F = \hbar \bar{\omega} (6 N)^{1/3}. \quad (2.16)$$

In combination with Eq. (2.9), an implicit equation for the fugacity \tilde{z} can be derived. The fugacity depends only on the degeneracy parameter T/T_F of the Fermi gas according to

$$\frac{T}{T_F} = \left(\frac{-1}{6 g_3(-\tilde{z})} \right)^{1/3}. \quad (2.17)$$

The fugacity is strongly dependent on T/T_F for small values and approaches zero for large T/T_F in the classical limit. The mean energy per particle $E = U/N$ for a Fermi gas of atoms confined in a harmonic potential is according to Eqs. (2.9) and (2.13)

$$E = 3 k_B T \frac{g_4(-\tilde{z})}{g_3(-\tilde{z})}. \quad (2.18)$$

In the classical limit, i.e. $\tilde{z} \ll 1$, this reduces to $E = 3k_B T$. For $T \rightarrow 0$, the mean energy per particle E becomes $3/4 E_F$. The fractional energy $E/(3k_B T)$ diverges in the limit of zero temperature. The reason for this behavior is Pauli blocking since at $T = 0$ the atoms are prohibited to fall collectively to the ground state of the harmonic potential.

2.1.2.2 Density distributions and free expansion

The density distribution of an ideal gas of fermions in an arbitrary potential $V(\mathbf{r})$ at finite temperature is given in Eq. (2.3). In the limit of $T = 0$, the phase space density is h^{-3} for $\mathbf{p}^2/2m + V(\mathbf{r}) \leq E_F$ and zero otherwise. The integration of the phase space density over momentum yields the following intratrap distribution of a Fermi gas at zero temperature

$$n(\mathbf{r}, T = 0) = \frac{(2m)^{3/2}}{6\pi^2 \hbar^3} (E_F - V(\mathbf{r}))^{3/2} \quad (2.19)$$

for positions \mathbf{r} where $E_F > V(\mathbf{r})$ and is zero in the other case. The density distribution of fermions expanding freely from a harmonic trap for an arbitrary time-of-flight t is described by

$$\begin{aligned} n(\mathbf{r}, t) &= \int \tilde{\rho}(\mathbf{r}_0, \mathbf{p}) \delta^3\left(\mathbf{r} - \mathbf{r}_0 - \frac{\mathbf{p}t}{m}\right) d\mathbf{r}_0 d\mathbf{p} \\ &= -\frac{\prod_i \eta_i(t)}{\lambda_{\text{dB}}^3} g_{3/2}\left(-\tilde{z} e^{-\frac{m}{2k_B T} \sum_i [\omega_i r_i \eta_i(t)]^2}\right), \end{aligned} \quad (2.20)$$

which is simply a rescaling of the coordinates by the factors $\eta_i(t) = [1 + \omega_i^2 t^2]^{-1/2}$ and r_i denote the spatial coordinates x, y, z .

2.2 Ultracold collisions

Ultracold collisions play a central role in experiments with ultracold gases. For example evaporative cooling relies on collisional rethermalization, and repulsive and attractive collisional interactions near Feshbach resonances give rise to many-body physical phenomena at ultracold temperatures. In the following Sec. 2.2.1 the Hamiltonian of two interacting particles is considered. The problem can be reexpressed by a scattering process in the center-of-mass frame on a central potential. In Sec. 2.2.2 the elastic scattering cross section is introduced, which incorporates all details of the scattering problem. The quantum nature of the atoms becomes again relevant for scattering at ultracold temperatures as outlined in Sec. 2.2.3.

2.2.1 Two-body Hamiltonian

The system of two interacting particles 1 and 2 can be described by the following Hamiltonian expressed in center of mass and relative coordinates, cf. App. B,

$$H = H_{\text{hf}} + H_Z + H_{\text{rel}}, \quad (2.21)$$

2.2 Ultracold collisions

where the first two terms describe the hyperfine and Zeeman energy of each of the two particles and H_{rel} represents the interaction energy of the relative motion of the particles given by

$$H_{\text{rel}} = \frac{\mathbf{p}_{\text{rel}}^2}{2m_r} + V_{\text{sc}}(\mathbf{r}). \quad (2.22)$$

The energy of the relative motion comprises a kinetic energy term $\mathbf{p}_{\text{rel}}^2/2m_r$, where $m_r = m_1 m_2 / (m_1 + m_2)$ is the reduced mass of the two particles, and an effective scattering potential between the atoms $V_{\text{sc}}(\mathbf{r})$. The relative momentum is given by $\mathbf{p}_{\text{rel}} = m_r (\mathbf{v}_1 - \mathbf{v}_2) = m_r \mathbf{v}_{\text{rel}} = \hbar \mathbf{k}$.

The part H_{hf} of the hyperfine interaction for the two individual particles 1 and 2, see also App. D.1, can be written as

$$H_{\text{hf}} = hA_{\text{hf},1} \mathbf{I}_1 \cdot \mathbf{J}_1 + hA_{\text{hf},2} \mathbf{I}_2 \cdot \mathbf{J}_2. \quad (2.23)$$

The hyperfine Hamiltonian H_{hf} describes the coupling between the electronic spin \mathbf{J} and the nuclear spin \mathbf{I} , and $A_{\text{hf},i}$ are the hyperfine coupling constants in Hertz. This coupling gives rise to the total spin operator $\mathbf{F} = \mathbf{I} + \mathbf{J}$ with the quantum numbers F and m_F . The states $|F, m_F\rangle$ are eigenfunctions of H_{hf} . The Zeeman term H_Z can be expressed as

$$H_Z = \mu_B (g_S \mathbf{S} + g_{I,1} \mathbf{I}_1 + g_{I,2} \mathbf{I}_2) \cdot \mathbf{B} \quad (2.24)$$

This expression for H_Z is non-zero, if an external magnetic field \mathbf{B} is present. The internal spin configuration of the electrons $\mathbf{S} = \mathbf{J}_1 + \mathbf{J}_2$ and of the nuclei \mathbf{I}_i couple then to \mathbf{B} . The quantities g_S and $g_{I,i}$ are the Landé g -factors of the electron configuration and the nuclei, respectively, and μ_B is the Bohr magneton.

The solutions with $E < 0$ of the eigenvalue problem defined by the Hamiltonian in Eq. (2.21) and the corresponding eigenfunctions lead to vibrational bound levels of the scattering potential, see Sec. 2.3. The problem for eigenvalues $E > 0$ of the Hamiltonian given in Eq. (2.21), will be treated in the next section.

2.2.2 Differential and total elastic scattering cross section

The energy of the relative motion of the two particles is described by H_{rel} in the center of mass frame as given in Eq. (2.22). For the solution of the problem, an incident plane wave $\Psi_{\text{in}}(\mathbf{r}) = e^{i\mathbf{k}\cdot\mathbf{r}}$ is assumed. For large distances from the scattering center $r \rightarrow \infty$, the solution for the wavefunction contains two parts. One term represents the unscattered part of the wavefunction and the second term is the scattered contribution, which describes a spherical wave

$$\lim_{r \rightarrow \infty} \Psi_{\mathbf{k}}(\mathbf{r}) \propto e^{i\mathbf{k}\cdot\mathbf{r}} + f(k, \theta, \phi) \frac{e^{ikr}}{r}, \quad (2.25)$$

with the spherical coordinates (r, θ, ϕ) . Here, the quantity $f(k, \theta, \phi)$ represents the probability amplitude for scattering of the reduced mass m_r with wavenumber k into the direction (θ, ϕ) . The differential scattering cross section is given by

$$\frac{d\sigma(k, \theta, \phi)}{d\Omega} = |f(k, \theta, \phi)|^2, \quad (2.26)$$

where $d\Omega = \sin(\theta) d\theta d\phi$ denotes the differential solid angle. Carrying out the integration over the solid angle yields the total elastic scattering cross section $\sigma(k)$.

It can be shown that the effective scattering potential $V_{\text{sc}}(\mathbf{r})$ only depends on the internuclear distance r and on the total electron spin S configuration of the colliding atoms

$$V_{\text{sc}}(\mathbf{r}) = V_{\text{sc}}(r) = \sum_S |S\rangle V_S(r) \langle S|. \quad (2.27)$$

$|S\rangle\langle S|$ is the projection operator and $V_S(r)$ is the interaction potential for total electron spin quantum number S . For spin-1/2 atoms, i.e. alkali atoms, the total electron spin is either a singlet ($S = 0$) or triplet ($S = 1$) state. As a consequence of the central symmetry, the solution of the scattering problem can be expanded in spherical harmonics $Y_{l,m_l}(\theta, \phi)$

$$\Psi_{\mathbf{k}}(\mathbf{r}) = \sum_{l,m_l} \frac{u_{k,l,m_l}(r)}{r} Y_{l,m_l}(\theta, \phi) \quad (2.28)$$

where l denotes the angular momentum and m_l its projection onto the z -axis. If the z -axis is chosen to be collinear with \mathbf{k} , only the terms with $m_l = 0$ contribute. The time independent Schrödinger equation can be written as

$$\left[-\frac{\hbar^2}{2m_r} \frac{d^2}{dr^2} + \frac{\hbar^2 l(l+1)}{2m_r r^2} + V_{\text{sc}}(r) \right] u_{k,l}(r) = E u_{k,l}(r). \quad (2.29)$$

Here, the contributions with $l = 0, 1, 2, \dots$ are called s -, p -, d -, ... waves.

The scattering process involves solutions with $E > 0$. In the asymptotic limit $r \rightarrow \infty$ and for a short-range potential, the radial wave function satisfies

$$u_{k,l}(r) \propto \left((-1)^{l+1} e^{-ikr} + e^{2i\delta_l} e^{ikr} \right), \quad (2.30)$$

where the phase shifts δ_l are introduced. The effective scattering potential induces a phase shift δ_l between the incoming and outgoing partial waves. The angular momentum l is a conserved quantity for elastic scattering at a central potential. For a central scattering potential $V_{\text{sc}}(r)$ the total cross section can be expressed as a sum over all partial waves according to

$$\sigma(k) = \sum_{l=0}^{\infty} \sigma_l(k) = \sum_{l=0}^{\infty} \frac{4\pi}{k^2} (2l+1) \sin^2(\delta_l). \quad (2.31)$$

In the case of particles in identical quantum states, the symmetry of the two-particle wavefunction influences the value of the total cross section. For bosons, the wavefunction is symmetric under the exchange of two particles, what leads to the fact that only even partial waves contribute to the scattering process. For fermions, on the other hand, the wavefunction is antisymmetric and only odd partial waves need to be considered.

2.2.3 s -wave regime, low energy limit

In the case of ultracold collisions, where only partial s -waves contribute to the scattering process and $k \rightarrow 0$, the relative kinetic energy of the scattering process $E = \hbar^2 k^2 / (2m_r)$

2.3 Feshbach resonances

is small. In this limit the total scattering cross section is

$$\lim_{k \rightarrow 0} \sigma(k) = \begin{cases} 8\pi a^2 & \text{for bosons} \\ 0 & \text{for fermions} \\ 4\pi a^2 & \text{for distinguishable particles,} \end{cases} \quad (2.32)$$

where the s -wave scattering length is defined as

$$a = - \lim_{k \rightarrow 0} \frac{\tan(\delta_0(k))}{k}. \quad (2.33)$$

The scattering length a is in principle not limited and can take values from $-\infty$ to $+\infty$. At low temperatures, where s -wave scattering is only possible, fermions do not interact due to the Pauli exclusion principle. The energy dependence of the phase shift can be determined within an expansion of the scattering potential $V_{sc}(r)$. In the limit of small wavenumber compared to the inverse of the range of the interatomic potential r_0 , the phase shift can be described implicitly as

$$k \cot \delta_0 = -\frac{1}{a} + r_{\text{eff}} \frac{k^2}{2}, \quad (2.34)$$

where r_{eff} is an effective range of the scattering potential. In the case of a van der Waals potential $V_{sc}(r) = -C_6/r^6$ and for a broad Feshbach resonance, the effective range r_{eff} is on the order of the characteristic van der Waals length $r_{0,\text{vdW}}$, which is given by (Köhler *et al.*, 2006)

$$r_{0,\text{vdW}} = \frac{1}{2} \left(\frac{2m_r C_6}{\hbar^2} \right)^{1/4}. \quad (2.35)$$

With the expression given in Eq. (2.34), the scattering amplitude can be rewritten as (Landau and Lifshitz, 1991)

$$f(k) = \frac{1}{-\frac{1}{a} + \frac{1}{2} r_{\text{eff}} k^2 - ik}. \quad (2.36)$$

If $k|a| \gg 1$ and $|r_{\text{eff}}| \ll 1/k$ the total cross section is $\sigma = 4\pi/k^2$ and depends only on momentum. This regime is called the unitarity limit. For small k , the scattering amplitude $f(k) = -\frac{1}{ik}$ diverges and a Feshbach resonance occurs, whose properties are discussed in more detail in the next section for the case of a magnetic field induced resonance.

2.3 Feshbach resonances

The problem of Feshbach resonances, i.e. a bound state coupled to the continuum, was investigated in the 1930s for the first time (Rice, 1933; Fano, 1935). Fano discusses in this early work the asymmetric line shapes, *Fano profiles*, occurring in such coupling phenomena as a result of quantum interference. A concise theory is independently carried out in the respective contexts of nuclear physics (Feshbach, 1958, 1962) and atomic

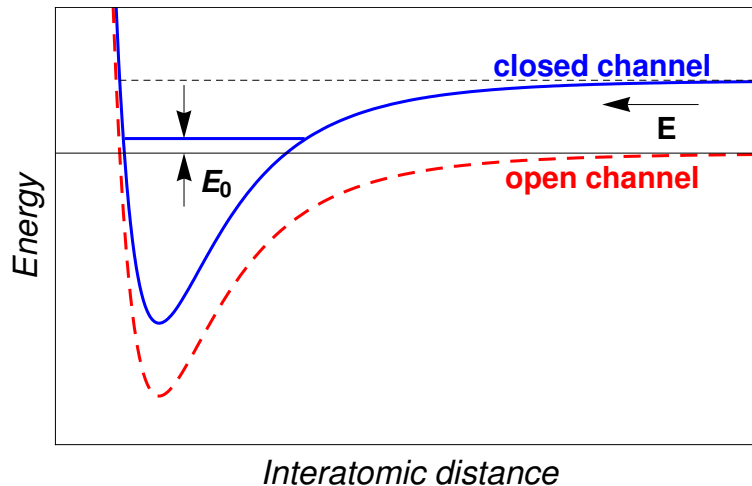


Figure 2.2: Illustration of the two-channel model for coupling of a bound state to the continuum.

physics (Fano, 1961). Magnetically induced resonances have been studied in several ultracold atomic systems over the last decade (Inouye *et al.*, 1998; Courteille *et al.*, 1998; Vuletić *et al.*, 1999; Dieckmann *et al.*, 2002; Jochim *et al.*, 2002; Loftus *et al.*, 2002; Marte *et al.*, 2002; O’Hara *et al.*, 2002a; Regal *et al.*, 2003b,c; Simoni *et al.*, 2003; Inouye *et al.*, 2004; Werner *et al.*, 2005). But it is also possible to induce resonances by optical means (Fedichev *et al.*, 1996; Fatemi *et al.*, 2000; Theis *et al.*, 2004; Enomoto *et al.*, 2008), and even to control and manipulate a magnetic Feshbach resonance with laser light (Bauer *et al.*, 2009) or radiofrequency radiation (Hanna *et al.*, 2010; Kaufman *et al.*, 2010). In the present work magnetically tunable Feshbach resonances are investigated in a ${}^6\text{Li}$ - ${}^{40}\text{K}$ mixture. Some review articles on Feshbach resonances can be found in (Timmermans *et al.*, 1999; Köhler *et al.*, 2006; Chin *et al.*, 2010).

2.3.1 Magnetic field induced Feshbach resonances

As seen in the previous section, the properties of the scattering potential is solely determined by the s -wave scattering length a for $k \rightarrow 0$. The value of a can be resonantly enhanced when coupling to a two-body bound state, a so-called closed channel, is possible. This can be achieved by tuning an external magnetic field, since, according to Eq. (2.27), the interaction energy depends on the total spin configuration of the two particles. Varying the magnetic field will shift the bound states of the potential with respect to the zero-field position. As a result, the energy level of a bound state can cross the scattering energy of the two colliding atoms, which are occupying the so-called open channel in the center-of-mass frame. At this crossover, the scattering length diverges and a Feshbach resonance occurs. This simplified picture of a Feshbach resonance is called two-channel approach and considers two molecular potentials $V_{\text{cc}}(B, r)$ and $V_{\text{bg}}(r)$ for the closed and open channel, respectively. The molecular potentials are schematically

2.3 Feshbach resonances

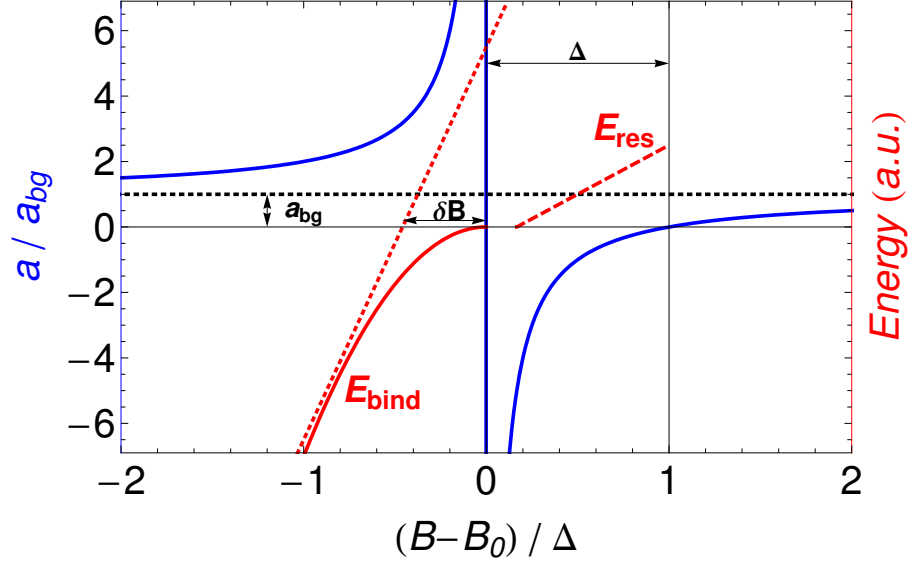


Figure 2.3: Scattering length and the binding energy of molecules in the vicinity of a Feshbach resonance.

illustrated in Fig. 2.2. For large interatomic distances the background potential $V_{\text{bg}}(r)$ for the open channel vanishes consistent with a van der Waals potential. In general, the magnetic moments of the bound state μ_{mol} and of the asymptotically unbound pair of atoms μ_{atoms} are different. By defining $\mu_{\text{res}} = |\mu_{\text{atoms}} - \mu_{\text{mol}}| > 0$, the energy difference between the two channels is given to first order by (Moerdijk *et al.*, 1995)

$$E_0 = \mu_{\text{res}}(B - B_{\text{res}}), \quad (2.37)$$

where B_{res} is the threshold crossing of the bare, uncoupled state. In the zero momentum limit the scattering length takes the simple form (Moerdijk *et al.*, 1995)

$$a(B) = a_{\text{bg}} \left(1 - \frac{\Delta}{B - B_0} \right), \quad (2.38)$$

where a_{bg} is the background scattering length of the potential $V_{\text{bg}}(r)$ and B_0 the position of the resonance. Δ is the width of the resonance and corresponds to the difference between the magnetic field positions of the divergence and the zero-crossing of the scattering length. A magnetic field induced Feshbach resonance is fully characterized by B_0 , a_{bg} , μ_{res} and Δ . According to the expression in Eq. (2.38), close to the Feshbach resonance, the scattering length is efficiently tunable by the magnetic field (cf. Fig. 2.3 in blue). The energy of the weakly bound molecular state is also shown in Fig. 2.3. The energy approaches threshold at $E = 0$ from scattering length values which are large and positive. Away from resonance, the energy varies linearly with B according to Eq. (2.37). Near

resonance the binding energy of the molecule varies with the scattering length according to

$$E_{\text{bind,univ}} = -\frac{\hbar^2}{2m_r a^2} < 0. \quad (2.39)$$

The energy $E_{\text{bind,univ}}$ depends quadratically on the magnetic field detuning ($B - B_0$) (cf. Fig. 2.3 in red). This behavior is characteristic for the universal regime of two-body interactions and the scattering cross section takes the universal form

$$\sigma(k) = 4\pi \frac{a^2}{1 + k^2 a^2}. \quad (2.40)$$

The position of the divergence of the scattering length B_0 is shifted with respect to B_{res} due to interchannel coupling, and, assuming a van der Waals potential, this shift δB can be expressed by (Köhler *et al.*, 2006)

$$\delta B = B_0 - B_{\text{res}} = \Delta \cdot \frac{a_{\text{bg}}}{\bar{a}} \frac{\left(1 - \frac{a_{\text{bg}}}{\bar{a}}\right)}{1 + \left(1 - \frac{a_{\text{bg}}}{\bar{a}}\right)^2}, \quad (2.41)$$

where the mean scattering length \bar{a} is defined as (Gribakin *et al.*, 1993; Chin *et al.*, 2010)

$$\bar{a} = \frac{4\pi}{\Gamma(1/4)^2} r_{0,\text{vdW}}. \quad (2.42)$$

The van der Waals length $r_{0,\text{vdW}}$ is given in Eq. (2.35).

With $E = \hbar^2 k^2 / (2m_r)$ and for a two-channel model, which will be presented in more detail in Sec. 2.3.3, the scattering amplitude from Eq. (2.36) can be equivalently rewritten (Sheehy and Radzihovsky, 2006; Gurarie and Radzihovsky, 2007)

$$f(E) = -\frac{\hbar}{\sqrt{2m_r}} \cdot \frac{\Gamma_0^{1/2}}{E - E_0 + i\Gamma_0^{1/2} E^{1/2}}, \quad (2.43)$$

where

$$E_0 = \frac{\hbar^2}{am_r r_{\text{eff}}}, \quad \Gamma_0 = \frac{2\hbar^2}{m_r r_{\text{eff}}^2}. \quad (2.44)$$

Γ_0 is the energy scale of the Feshbach resonance coupling strength, and E_0 is the detuning from resonance¹, cf. Eq. (2.37). The value of the effective range of the scattering potential close to resonance can be approximated by (Petrov, 2004b)

$$r_{\text{eff}} = -\frac{\hbar^2}{|m_r \cdot a_{\text{bg}} \cdot \Delta \cdot \mu_{\text{res}}|} < 0. \quad (2.45)$$

For the classification of Feshbach resonances, the relevant energy scales are Γ_0 and the Fermi energy. The many-body properties of a finite density s -wave resonant Fermi gas is characterized by an average atom spacing $n^{-1/3} \propto 1/k_F$, the scattering length a and the effective range r_{eff} . This will be discussed in more detail in Sec. 2.3.3.

¹Some authors use different definitions for Γ_0 , E_0 and r_{eff} . Here the notation of (Gurarie and Radzihovsky, 2007) is chosen.

2.3 Feshbach resonances

2.3.2 Feshbach resonances in the ${}^6\text{Li}$ - ${}^{40}\text{K}$ mixture

The collisional properties of Feshbach molecules crucially depend on the quantum statistical properties of the constituents. In spin mixtures of fermionic atoms exceptionally longlived molecules are formed by exploiting broad Feshbach resonances.

The scattering properties of an ultracold heteronuclear ${}^6\text{Li}$ - ${}^{40}\text{K}$ mixture is investigated in (Wille *et al.*, 2008). With the help of atom loss spectroscopy thirteen interspecies Feshbach resonances are located. Those resonance positions represent valuable information since with different theoretical models the ground-state scattering properties of ${}^6\text{Li}$ - ${}^{40}\text{K}$ can be fully characterized. With the help of coupled channels calculations and an asymptotic bound state model (ABM) nine s - (depicted in Tab. 2.1) and four p -wave Feshbach resonances are assigned. By using model potentials and optimized fits to the

M_F	$m_{F,\text{Li}}, m_{F,\text{K}}$	Experiment	ABM extended		CC	
		B_0 (G)	B_0 (G)	Δ (G)	B_0 (G)	Δ (G)
-5	$-1/2, -9/2$	215.6	216.2	0.16	215.6	0.25
-4	$+1/2, -9/2$	157.6	157.6	0.08	158.2	0.15
-4	$+1/2, -9/2$	168.2 168.217(10)	168.5	0.08	168.2	0.10
-3	$+1/2, -7/2$	149.2	149.1	0.12	150.2	0.28
-3	$+1/2, -7/2$	159.5	159.7	0.31	159.6	0.45
-3	$+1/2, -7/2$	165.9	165.9	0.0002	165.9	0.001
-2	$+1/2, -5/2$	141.7	141.4	0.12	143.0	0.36
-2	$+1/2, -5/2$	154.9 154.71(5) 154.707(5)	154.8	0.50	155.1	0.81
-2	$+1/2, -5/2$	162.7	162.6	0.07	162.9	0.60
+5	$+1/2, +9/2$	114.47(5)	115.9	0.91	114.78	1.82

Table 2.1: Magnetic field positions of all experimentally observed s -wave interspecies Feshbach resonances between ${}^6\text{Li}$ and ${}^{40}\text{K}$ (Wille *et al.*, 2008; Voigt *et al.*, 2009; Spiegelhalder *et al.*, 2010; Tiecke *et al.*, 2010a,b; Costa *et al.*, 2010; Naik *et al.*, 2011). The positions are assigned with the asymptotic bound state model (ABM) and coupled-channels calculations (CC).

measured resonance positions crucial scattering parameters can be extracted. Threshold energies of the last bound state of the $S = 0$ and $S = 1$ potential are determined to be $E_{S=0}/h = 716(15)$ MHz and $E_{S=1}/h = 425(5)$ MHz (Wille *et al.*, 2008), respectively, for $l = 0$. This corresponds to a singlet scattering length of $a_s = 52.1(3) a_0$ and a triplet scattering length of $a_t = 63.5(1) a_0$. These parameters are important input quantities for the simple ABM. In an extension of the ABM (Tiecke *et al.*, 2010a,b) a calculation of the magnetic field width Δ of Feshbach resonances is presented. As examples for the ABM, the bound state (black) and threshold energies (red) are presented in Fig. 2.4 for s -wave channels and for the total projection quantum numbers $M_F = -2$ and $M_F = +5$. At

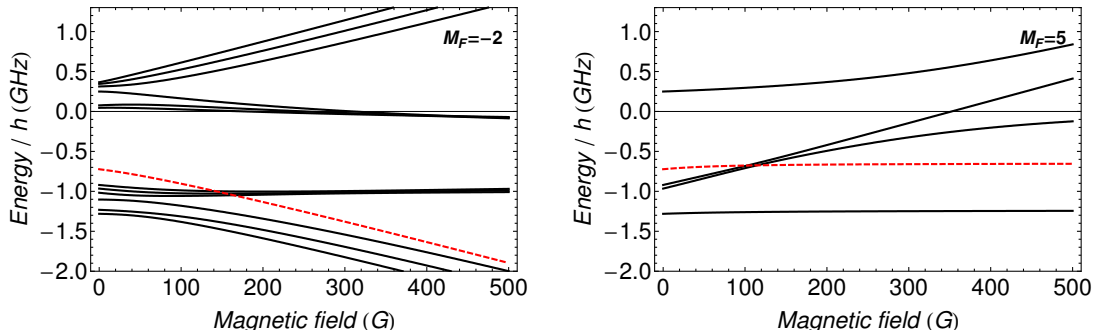


Figure 2.4: Bound state and threshold energy for s -wave scattering channels. The calculation is based on the asymptotic bound state model (Wille *et al.*, 2008). At crossing points of the bound state energy (solid) and the threshold energy (dashed), the open-channel can couple to the closed channel, and a Feshbach resonance occurs. Two cases are considered for the projection quantum numbers $M_F = -2$ (left) and $M_F = 5$ (right). The Feshbach resonance existing near 155 G with $M_F = -2$ is studied in detail within the present work.

magnetic field strengths where the threshold energy crosses the energy of a bound state a resonance occurs. In the present work within this thesis, mainly the Feshbach resonance occurring close to $B_0 = 155$ G with the projection quantum number $M_F = -2$ and magnetic field width $\Delta = 0.81$ G is investigated. This resonance involves the hyperfine states of ${}^6\text{Li}|1/2, 1/2\rangle$ and ${}^{40}\text{K}|9/2, -5/2\rangle$. The hyperfine state for ${}^{40}\text{K}$ possesses a lower optical transition strength at high magnetic field as compared to the maximally stretched state $|9/2, -9/2\rangle$, cf. App. D. The magnetic moment of the bound state is close to zero what allows to apply a molecule sensitive detection method as will be presented in Sec. 5.3.3. The Feshbach resonance with $M_F = +5$ at $B_0 = 114.78$ G with a width of $\Delta = 1.82$ G (Tiecke *et al.*, 2010a,b) is broader and involves hyperfine states which can be imaged efficiently at high magnetic fields. But the bound state for this resonance has a finite magnetic moment. Inelastic collisional losses at this specific resonance are expected to be considerably larger as compared to the Feshbach resonance located at 155 G. The rate is a factor of 3.7 higher (Naik *et al.*, 2011).

Later, the assignment of the several interspecies Feshbach resonances is supported by high-resolution Fourier transform spectroscopy and by calculations using Born-Oppenheimer potentials for the electronic ground states (Tiemann *et al.*, 2009). All known Feshbach resonances in ${}^6\text{Li}$ - ${}^{40}\text{K}$ mixtures are expected to be narrow and closed-channel dominated. The distinction between closed- and open-channel dominated resonances will be presented in more detail in the following Sec. 2.3.3. Open-channel dominated resonances would be of great interest for the study of universal many-body properties at the BEC-BCS crossover. But the relatively low background scattering length of $a_{\text{bg}} \approx 63.5 a_0$ (Wille *et al.*, 2008) suggests their existence to be unlikely (Chin *et al.*, 2010). Many other resonances are found in (Tiecke, 2009) for magnetic fields < 3 kG, but the widths

2.3 Feshbach resonances

are not considerably larger (< 2 G). From the experimental point of view, the exploration of narrow Feshbach resonances require an excellent magnetic field control. As discussed in the next section the underlying physics of narrow and broad Feshbach resonances are quite distinct and offer different regimes for investigating strongly interacting Fermi mixtures.

2.3.3 Classification of broad and narrow Feshbach resonances

In this section we consider the homonuclear case, where two fermionic atoms with different spin states interact. In the vicinity of a Feshbach resonance, the many-body system composed of atoms and molecules, which interact resonantly by a Feshbach coupling parameter g_s in the s -wave channel, can be described by the two-channel Hamiltonian (Timmermans *et al.*, 1999; Gurarie and Radzihovsky, 2007)

$$\begin{aligned}
 H_{2\text{-ch}} = & \sum_{\mathbf{k},\sigma} \frac{k^2}{2m} a_{\mathbf{k},\sigma}^\dagger a_{\mathbf{k},\sigma} + \sum_{\mathbf{p}} \left(\epsilon_0 + \frac{p^2}{4m} \right) b_{\mathbf{p}}^\dagger b_{\mathbf{p}} \\
 & + \sum_{\mathbf{k},\mathbf{p}} \frac{g_s}{\sqrt{V}} \left(b_{\mathbf{p}} a_{\mathbf{k}+\frac{\mathbf{p}}{2},\uparrow}^\dagger a_{-\mathbf{k}+\frac{\mathbf{p}}{2},\downarrow}^\dagger + b_{\mathbf{p}}^\dagger a_{-\mathbf{k}+\frac{\mathbf{p}}{2},\downarrow} a_{\mathbf{k}+\frac{\mathbf{p}}{2},\uparrow} \right).
 \end{aligned} \tag{2.46}$$

Here $a_{\mathbf{k},\sigma}$ ($a_{\mathbf{k},\sigma}^\dagger$) is a fermionic annihilation (creation) operator of an atom with spin σ and momentum \mathbf{k} , and $b_{\mathbf{p}}$ ($b_{\mathbf{p}}^\dagger$) annihilates (creates) a boson of mass $2m$ and momentum \mathbf{p} . The first term in the Hamiltonian describes propagating fermions in the open channel which interact by the background potential $V_{\text{bg}}(r)$. The second term represents propagating bosons in the closed channel of the potential $V_{\text{cc}}(B, r)$. The energy ϵ_0 is the bare molecular rest energy and can be tuned with the magnetic field. The third term is the coupling term where two fermionic atoms are annihilated and create a boson in the closed channel (or vice-versa) by conserving energy and momentum. In the s -wave two-channel model, the atom-molecule interaction is controlled by g_s . For $g_s \rightarrow 0$, the b -particle is pointlike and the size of the molecule is given by the length scale of the interatomic potential. For $g_s \neq 0$, the physical molecule is a linear combination of b -particles and a surrounding cloud of a -particles whose size diverges as $a \rightarrow \infty$. With the spatial extent given by the scattering length a , the molecules can overlap at finite atom density. The Zeeman energy splitting between the open and closed channel (Gurarie and Radzihovsky, 2007)

$$E_0 = \epsilon_0 - \frac{g_s^2 m \Lambda}{2\pi^2 \hbar^2} \tag{2.47}$$

can be tuned with the magnetic field and can be approximated within first order by the expression presented in Eq. (2.37). Λ is a cut-off length scale of the long-range interatomic potential. The first term in Eq. (2.47) is the energy of the closed channel and the second term arises from the atom-molecule interaction.

From the two-channel model a parameter γ_s can be defined that is related to the square-root of the ratio between the Feshbach resonance width Γ_0 , cf. Eq. (2.44), and

the Fermi energy (Sheehy and Radzihovsky, 2006; Gurarie and Radzihovsky, 2007)

$$\gamma_s \equiv \frac{g_s^2 g(E_F)}{E_F} = \frac{g_s^2 (2m)^{3/2}}{4\pi^2 \hbar^3 \sqrt{E_F}} = \frac{\sqrt{8}}{\pi} \sqrt{\frac{\Gamma_0}{E_F}} = \frac{8}{\pi} \frac{1}{k_F |r_{\text{eff}}|}, \quad (2.48)$$

where $g(E) = \frac{(2m)^{3/2}}{4\pi^2 \hbar^3} \sqrt{E}$ is the three-dimensional density of states for a one-component Fermi gas. This parameter γ_s allows to classify resonances in "broad" ($\gamma_s \gg 1$) and "narrow" ($\gamma_s \ll 1$) finite density Feshbach-resonant behaviors. The parameter $\gamma_s \propto g_s^2$ determines a perturbative expansion in the Feshbach resonant interaction of any physical quantity of the many-body system. The expansion is performed about an exactly solvable zero-coupling limit $g_s = 0$. γ_s is independent on a and the detuning E_0 , and serves as a suitable expansion parameter as it remains small throughout the entire BEC-BCS crossover. The two-channel model predictions for a narrow Feshbach resonance, i.e. $\gamma_s \ll 1$, are quantitatively accurate throughout the BEC-BCS crossover (Gurarie and Radzihovsky, 2007). In contrast, for the broad resonance $\gamma_s \gg 1$, the two-channel model is not quantitatively solvable. Here, the gas parameter $n^{1/3}|a(B)|$ is the only dimensionless parameter and can be used for a perturbative analysis away from a broad resonance.

For narrow Feshbach resonances, the coupling energy Γ_0 is comparable or smaller than the Fermi energy E_F . An equivalent criterion, as given in Eq. (2.48), is that for increasing scattering length $a(B)$ the spatial extent of the physical molecule reaches first the mean atom separation $n^{-1/3}$. In the case of narrow resonances the molecular state affects the many-body physics of the system. This is contrary to the case of broad resonances, where many-body physical phenomena are negligibly influenced by the closed channel (Partridge *et al.*, 2005), and where for increasing $a(B)$ the molecular spatial extent reaches first the effective range $|r_{\text{eff}}|$ for this situation.

System	$m_{F,1}, m_{F,2}$	B_0 (G)	Δ (G)	a_{bg} (a_0)	μ_{res} (μ_B)	$ r_{\text{eff}} $ (a_0)	Γ_0/k_B (μK)
${}^6\text{Li}-{}^{40}\text{K}$	+1/2, -5/2	155.1	0.81	63	1.7	5.7×10^3	2.0
	+1/2, -9/2	168.2	0.10	63	1.8	4.4×10^4	0.035
	+1/2, +9/2	114.78	1.82	63	1.6	2.7×10^3	9.1
${}^{40}\text{K}-{}^{40}\text{K}$	-9/2, -7/2	202.10(7)	7.8(6)	174	1.7	56	5.5×10^3
${}^6\text{Li}-{}^6\text{Li}$	+1/2, -1/2	834.15	300	1405	2.0	0.10	1.1×10^{10}
	+1/2, -1/2	543.26	0.10	61.6	2.1	6.6×10^4	0.026

Table 2.2: Comparison of different s -wave Feshbach resonances in homonuclear and heteronuclear Fermi mixtures (Wille *et al.*, 2008; Tiecke *et al.*, 2010a). The intraspecies ${}^{40}\text{K}$ resonance is investigated in (Regal, 2005), and the reference values for ${}^6\text{Li}$ given in the table are from (Bartenstein *et al.*, 2005; Chin, 2008).

In Tab. 2.2 some experimentally investigated Feshbach resonances in Fermi systems are presented. Taking into account typical Fermi energies on the order of $\approx k_B 1 \mu\text{K}$,

2.3 Feshbach resonances

the two intraspecies Feshbach resonances in ${}^6\text{Li}$ (834 G) and ${}^{40}\text{K}$ (202 G) are broad resonances. In these systems a molecular BEC is realized for the first time (Greiner *et al.*, 2003; Jochim *et al.*, 2003a; Zwierlein *et al.*, 2003). Beside the very broad resonance in ${}^6\text{Li}$, there exists also a very narrow Feshbach resonance (543 G), which is experimentally first investigated in (Dieckmann *et al.*, 2002; Bourdel *et al.*, 2003; Strecker *et al.*, 2003). The coupling energies of the ${}^6\text{Li}$ - ${}^{40}\text{K}$ interspecies Feshbach resonances are on the order of typical Fermi energies and can be considered as narrow and closed-channel dominated (Wille *et al.*, 2008). It is mentioned here that, by decreasing the trapping frequencies, the Fermi energy can be lowered such that Feshbach resonances can be classified as broad in spite of current experimental conditions make them appear as narrow. However, from the experimental perspective, trap configurations with frequencies on the order of a few Hertz are unstable and the confined atoms in the trap are more prone to heating due to mechanical vibrations. Most studies so far focused on the characterization of the strongly interacting regime at the BEC-BCS crossover of broad Feshbach resonances, where the influence of the closed channel can be neglected.

2.3.4 Many-body regimes in the zero temperature limit

In the following, a summary is given of the differing many-body properties in the regime of a broad and a narrow Feshbach resonance (Ohashi and Griffin, 2002, 2005; Bruun, 2004; Jensen *et al.*, 2006; Romans and Stoof, 2006; Haussmann *et al.*, 2007; Gurarie and Radzihovsky, 2007; Ketterle and Zwierlein, 2008).

2.3.4.1 Broad Feshbach resonances

The central parameter for broad Feshbach resonances is $n^{1/3}|a(B)| \propto k_F|a(B)|$. In case that $a > 0$ and $n^{1/3}|a(B)| \ll 1$ is satisfied, the fermions form pairs (molecules) which condense into a BEC. For the homonuclear case and in the regime where $a \gg |r_{\text{eff}}|$, although $a \ll n^{-1/3}$, the scattering length of dimer-dimer collisions is related to the atomic scattering length $a_{dd} \approx 0.6 a$ (Petrov *et al.*, 2005a), and the condensate becomes a weakly interacting Bose gas. For increasing a , the molecular lifetime in the atom-molecule mixture is about ≈ 100 ms for ${}^{40}\text{K}_2$ molecules (Regal *et al.*, 2004b) and several seconds for ${}^6\text{Li}_2$ molecules (Cubizolles *et al.*, 2003; Jochim *et al.*, 2003b). The mechanism for the increased lifetimes relies on the suppression of the collisional relaxation of the weakly bound dimers to deep bound states due to Pauli exclusion principle (Petrov *et al.*, 2004a). For broad Feshbach resonances, the spatial extent of the dimers is on the order of $\approx a$. On the other hand, the size of deep bound states is on the order of $r_{0,\text{vdW}} \ll a$. Therefore, the relaxation requires the presence of at least three fermions at distances $\approx r_{0,\text{vdW}}$ from each other. For such a relaxation process, two fermions are necessarily identical. The characteristic momentum spread of the atoms is $k \approx 1/a$. Because of Pauli blocking the relaxation probability is therefore suppressed by a certain power of $(k r_{0,\text{vdW}}) \approx (r_{0,\text{vdW}}/a)$. The exact relaxation rate in the s -wave channel is

derived in (Petrov *et al.*, 2004a)

$$\alpha_s \propto \frac{\hbar r_{0,\text{vdW}}}{m} \left(\frac{r_{0,\text{vdW}}}{a} \right)^s, \quad (2.49)$$

where, assuming equal masses, the exponent is $s \approx 2.55$ for dimer-dimer relaxation, and $s \approx 3.33$ for the relaxation in atom-dimer collisions. For different masses involved in the collision processes, the exponent s depends on the mass ratio and is given in (Petrov *et al.*, 2005b). For the mass ratio of ${}^6\text{Li}$ - ${}^{40}\text{K}$, the exponents are $s \approx 1.40$ for dimer-dimer relaxation, and $s \approx 5.04$ for atom-dimer relaxation.

As the interactions become stronger close to resonance and $n^{1/3}|a(B)| > 1$ the system is mostly described by numerical methods, especially for the case of finite temperature, see for a review e.g. (Giorgini *et al.*, 2008). In this BEC-BCS crossover regime, the Fermi sea becomes superfluid and the closed-channel fraction vanishes. In particular, the unitary regime where $n^{1/3}|a| \rightarrow \infty$ is intriguing since the superfluid becomes universal (Stewart *et al.*, 2006; Hu *et al.*, 2007; Nascimbène *et al.*, 2010). This means that the system properties only depend on the density and not on the details of the Feshbach resonance. In (Partridge *et al.*, 2005) the closed-channel fraction for the very broad resonance in ${}^6\text{Li}$ at 834 G is measured by an optical probe which projects atom pair correlations onto vibrationally excited molecular states. In the BEC-BCS crossover the measured closed-channel fraction is nonvanishing, but very small consistent with the contention of universality for broad resonances. In (Werner *et al.*, 2009) it is shown that the observed nonvanishing closed-channel fraction in the crossover regime of a broad resonance can not be reproduced with a single-channel model, but rather with a two-channel model.

For attractive interactions $a < 0$ and $n^{1/3}|a(B)| \ll 1$, where no bound state is supported, it is energetically more favorable for the fermions to condense into Cooper pairs and to form a many-body BCS superconductor which can be accurately described by mean-field BCS theory. The transition temperature T_C for this state is on the order of the Fermi temperature T_F , $T_C \approx 0.28 T_F e^{\pi/(2k_F a)}$ (Gor'kov and Melik-Barkhudarov, 1962; Giorgini *et al.*, 2008).

2.3.4.2 Narrow Feshbach resonances

In the following, the zero-temperature and the zero-coupling limits (infinitely narrow resonance) are considered to describe the fundamental differences between a broad and a narrow Feshbach resonance. As given in (Gurarie and Radzihovsky, 2007), the molecular boson density with detuning $E - E_0$ for a two-component Fermi gas with total density n in the BEC-BCS crossover is described within the zero-coupling approximation $\gamma_s \rightarrow 0$

$$n_b = \begin{cases} 0, & \text{for } E - E_0 > 2E_F \\ \frac{n}{2} \left(1 - \left(\frac{E - E_0}{2E_F} \right)^{3/2} \right), & \text{for } 0 \leq E - E_0 \leq 2E_F \\ \frac{n}{2}, & \text{for } E - E_0 < 0. \end{cases} \quad (2.50)$$

This expression is plotted in Fig. 2.5 (in red). The situation for the BEC-BCS crossover

2.3 Feshbach resonances

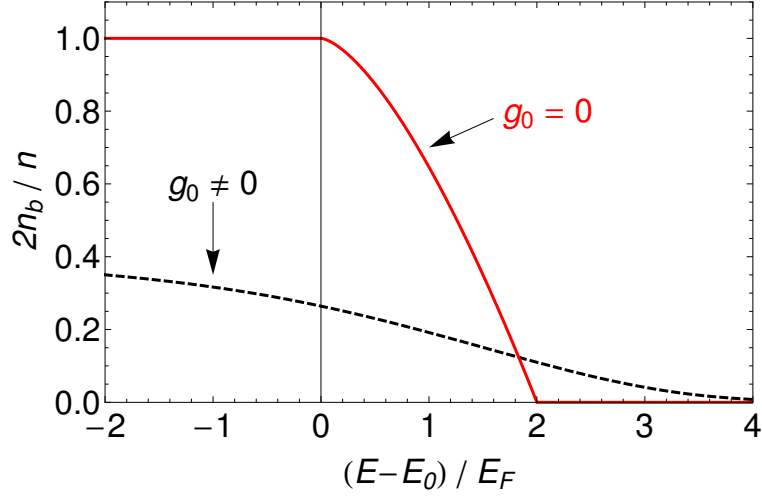


Figure 2.5: The molecular boson density normalized by the density of a two-component Fermi gas in dependence of the detuning in the vicinity of a Feshbach resonance. The zero-coupling limit (red) and the case of finite coupling γ_s (black dashed) is shown (Gurarie and Radzihovsky, 2007).

in the case of an infinitely narrow Feshbach resonance with $g_s \rightarrow 0$ is illustrated in Fig. 2.6 and discussed in the following. For an infinitely narrow Feshbach resonance, the detuning E_0 corresponds to the bare energy of the closed channel (boson), see Eq. (2.47). For detunings of $E - E_0 < 0$ all fermions are tightly bound to molecules and a pure molecular BEC is present. For values $0 < E - E_0 < 2E_F$, it is energetically favorable that a BEC coexists with a BCS-type superfluid. In this region, which extends to the atomic side to values related to the Fermi energy, bosons deplete the Fermi sea. The closed-channel fraction in the BEC-BCS crossover of a narrow Feshbach resonance is large and can not be neglected. The crossover regime from a pure molecular BEC to a BCS superfluid shows some characteristics. First, the bosons are stabilized by Pauli blocking as the lower lying momentum states are occupied in the Fermi sea. Second, as pointed out in (Bruun, 2004; Ketterle and Zwierlein, 2008), the observation of a universal many-body regime on the atomic side of a narrow Feshbach resonance turns out to be difficult. The universality marks the regime where thermodynamic quantities are solely characterized by the temperature and chemical potential of the Fermi gas and not by details of the resonance. The presence of bosons in the BEC-BCS crossover hinders the establishment of a many-body universal regime. For a narrow Feshbach resonance the interactions are weak and the region, where bosons are still present, must be overcome with detunings $E - E_0 > 2E_F$. On the other hand, for broad resonances there is a large parameter space for $E - E_0 > 0$ where the thermodynamics of the gas is universal with nearly vanishing closed-channel fraction.

For finite coupling $\gamma_s > 0$, the chemical potential μ is no longer locked to the detuning $E - E_0$. This leads to two equations, a particle number and a BEC-BCS gap equation

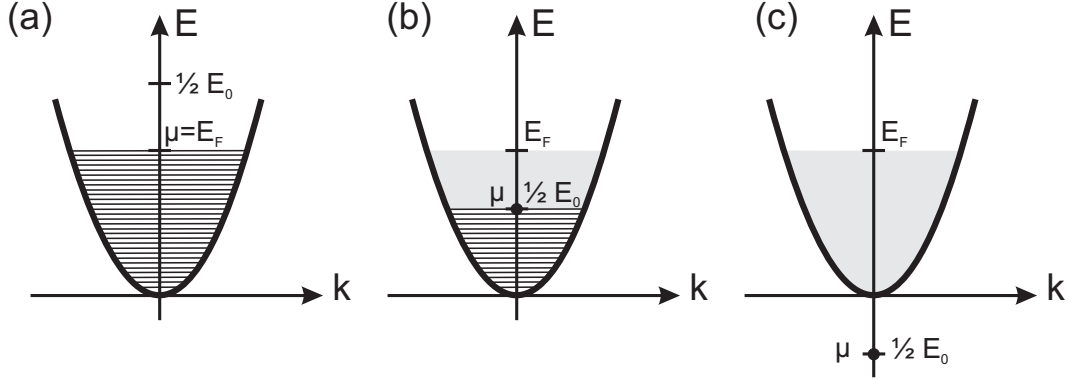


Figure 2.6: Crossover for narrow Feshbach resonance at zero temperature (from Gurarie and Radzihovsky, 2007). Fig. (a) illustrates the Fermi sea for magnetic field detunings $E_0 > 2E_F$, where no bosons are present. Fig. (b) presents the crossover region $0 < E_0 < 2E_F$ of a Fermi sea coexisting with a BEC of molecules. For $E_0 < 0$ a pure molecular BEC exists, Fig. (c).

(cf. Gurarie and Radzihovsky, 2007), which can be solved self-consistently. Qualitatively, the BEC-BCS crossover region extends to larger values and the maximum boson density decreases for a finite coupling (see Fig. 2.5 in black dashed).

Physical molecules can not exist for $a < 0$. As discussed in detail in (Gurarie and Radzihovsky, 2007), the bosons with $a < 0$ correspond to resonances which are long lived quasistationary states that eventually decay into the continuum. The resonant state is characterized by a peak at energy E_{res} and a width Γ_{res} for detunings $E_0 > 1/2\Gamma_0$, respectively $|a(B)| < |r_{\text{eff}}(B)|$, see also (Landau and Lifshitz, 1991),

$$\begin{aligned}
 E_{\text{res}} &= E_0 - \frac{1}{2}\Gamma_0 = \frac{\hbar^2}{m_r(r_{\text{eff}}(B))^2} \left(\frac{|r_{\text{eff}}(B)|}{|a|} - 1 \right) \\
 \Gamma_{\text{res}} &= \Gamma_0 \sqrt{\frac{4E_0}{\Gamma_0} - 1} = \frac{\hbar^2}{m_r(r_{\text{eff}}(B))^2} \sqrt{\frac{2|r_{\text{eff}}(B)|}{|a|} - 1}.
 \end{aligned} \tag{2.51}$$

The energy E_{res} is qualitatively depicted in Fig. 2.3. In the case of broad s -wave Feshbach resonances, the states can be only bound states, but not quasistationary.¹ The binding energy of the molecules for $a > 0$ can be formulated for a finite effective range in the narrow resonance limit as (Sheehy and Radzihovsky, 2006; Levinsen and Petrov, 2011)

$$E_{\text{bind}} = -\frac{\hbar^2}{m_r(r_{\text{eff}}(B))^2} \left(1 - \sqrt{1 + 2\frac{|r_{\text{eff}}(B)|}{a}} + \frac{|r_{\text{eff}}(B)|}{a} \right). \tag{2.52}$$

The expression from Eq. (2.39) can be recovered in the limit of small detunings $|r_{\text{eff}}(B)| \ll a$ from resonance. An expression for the magnetic field dependence of the effective range

¹In theory, there are also virtual bound states for $a < 0$, but they are not physical solutions of the Schrödinger equation.

2.3 Feshbach resonances

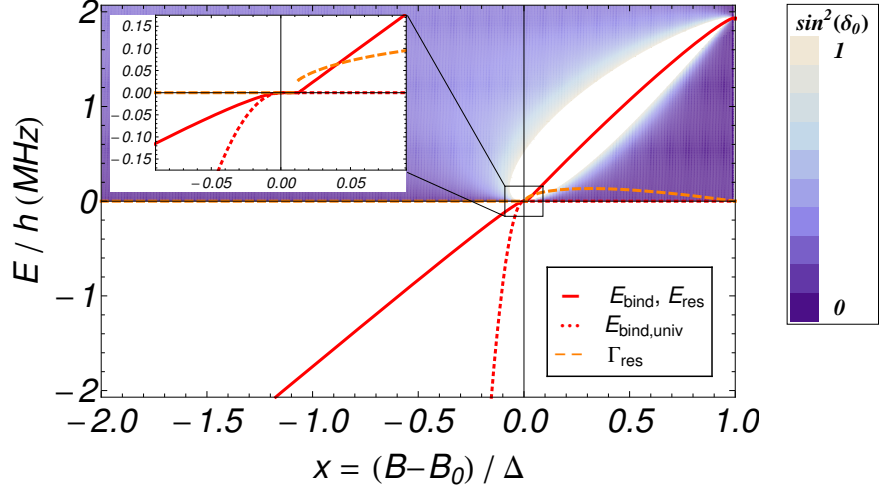


Figure 2.7: Near-threshold bound and scattering states at a narrow interspecies ${}^6\text{Li}$ - ${}^{40}\text{K}$ Feshbach resonance near 155 G. The parameters given in Tab. 2.2 for this resonance are invoked. The inset presents the behavior in an expanded view close to resonance. In the case of ${}^6\text{Li}$ - ${}^{40}\text{K}$, there is a resonant energy state above threshold E_{res} , which possesses over a small range of magnetic fields a larger width (dashed) as compared to its energy (solid) $\Gamma_{\text{res}} > E_{\text{res}}$. The phase shift $\sin^2(\delta_0)$ (cf. Eq. (2.34)) of this scattering state in the ${}^6\text{Li}$ - ${}^{40}\text{K}$ mixture above threshold is shown in the upper panel by the density plot. Below threshold the molecule energy is presented with solid lines (universal limit Eq. (2.39) with dotted lines).

for detunings $x \equiv (B - B_0) / \Delta < 1$ can be derived by assuring the asymptotic behavior for large negative detunings of Eq. (2.52) and by considering a small coupling such that

$$\lim_{x \rightarrow -\infty} E_{\text{bind}} \approx \mu_{\text{res}} (B - B_0) = \mu_{\text{res}} \Delta \cdot x. \quad (2.53)$$

Assuming the scattering length $a(B)$ from Eq. (2.38) and considering a constant differential magnetic moment μ_{res} , the magnetic field dependence of $r_{\text{eff}}(B)$ is found to be

$$r_{\text{eff}}(B) = r_{\text{eff}} \left(-\frac{1}{x-1} - \sqrt{\frac{2a_{\text{bg}}}{r_{\text{eff}}(x-1)}} \right) \quad \text{for } x < 1, \quad (2.54)$$

where r_{eff} is given in Eq. (2.45). For $x \rightarrow 1$, this expression diverges at the zero-crossing of the scattering length. At this detuning the effective range expansion Eq. (2.34) is poorly defined (Zinner, 2010). By invoking the correct magnetic field dependence of $r_{\text{eff}}(B)$ and $a(B)$, the near-threshold bound and scattering states for the narrow Feshbach resonance in the ${}^6\text{Li}$ - ${}^{40}\text{K}$ mixture near 155 G can be calculated and are presented in Fig. 2.7. For positive detunings from resonance, resonant states, as given by Eq. (2.51), are present in the ${}^6\text{Li}$ - ${}^{40}\text{K}$ mixture. There is a range of magnetic fields above threshold where the width (orange dashed) is larger than the energy of the resonant state $\Gamma_{\text{res}} > E_{\text{res}}$. The decay

rate of the resonances is given by $\Gamma_{\text{res}}/\hbar$, and a maximum rate of ≈ 840 kHz occurs at a detuning $x \approx 0.3$. For positive scattering lengths, the binding energy of the molecules is plotted with solid lines (see Eq. (2.52)), and the prediction for the universal limit is shown with dotted lines as expressed by Eq. (2.39). For the case of the ${}^6\text{Li}$ - ${}^{40}\text{K}$ Feshbach resonance, only a very narrow magnetic field range below threshold of a few mG satisfies the universal limit Eq. (2.39) according to this model.

2.3.5 Few-body problem close to a narrow Feshbach resonance

The finite value of the effective range r_{eff} as given in Eq. (2.45) influences scattering and molecule properties in the few-body problem at short distances close to a narrow Feshbach resonance (cf. also App. C.3). In (Levinsen and Petrov, 2011) some important scattering properties for the ${}^6\text{Li}$ - ${}^{40}\text{K}$ mixture are calculated for the case of a narrow Feshbach resonance. The atom-dimer relaxation in the s -wave channel as presented in Eq. (2.49) needs to be altered due to the finite value of the length parameter $r^* \equiv -r_{\text{eff}}/2$ (Levinsen *et al.*, 2009). In the limit $r_{0,\text{vdW}} \ll r^* \ll a$ the atom-dimer relaxation in the s -wave channel can be written as

$$\alpha_{\text{s,narrow}} \propto \frac{\hbar r_{0,\text{vdW}}}{m_{\text{Li}}} \left(\frac{r^*}{a} \right)^s, \quad (2.55)$$

where the exponent is $s \approx 5.04$ for the heteronuclear case of ${}^6\text{Li}$ - ${}^{40}\text{K}$. For all known interspecies Feshbach resonances in the ${}^6\text{Li}$ - ${}^{40}\text{K}$ mixture (cf. Tab. 2.1) the condition $r_{0,\text{vdW}} \ll r^*$ is satisfied. In the special case of the resonance close to 155 G, which will be studied mainly within the present work, the length parameter r^* is $r^* \approx 160$ nm $\approx 3000 a_0$ and the van der Waals range is $r_{0,\text{vdW}} \approx 2.2$ nm, cf. Eqs. (2.35) and (2.45). The dependence of the dimer-dimer relaxation rate on the detuning r^*/a is also considered in this cited work (Levinsen and Petrov, 2011). For small detunings from resonance the dimer-dimer scattering length is related to the atomic scattering length $a_{dd} = 0.89 a$ for the heteronuclear case of the ${}^6\text{Li}$ - ${}^{40}\text{K}$ mixture.

2.4 Cross-species thermalization in atomic gases

Within this work, information about collisional relaxation time scales in a Fermi-Fermi mixture is experimentally extracted by using the technique of cross-dimensional relaxation. This method involves a non-equilibrium state which relaxes to thermal equilibrium by elastic collisions. In Sec. 2.4.1, the concept of the Boltzmann equation is introduced, see also (Reif, 1987; Walraven, 2010). This theory allows to determine and to describe time scales for relaxation processes from non-equilibrium states. A kinetic model based on this Boltzmann equation and tests with Monte-Carlo simulations, which will be introduced in Sec. 2.4.2, allow for the interpretation of experimental findings.

2.4.1 Boltzmann equation

A dilute cloud of atoms is described by a distribution function $f(\mathbf{r}, \mathbf{p}, t)$. This quantity describes the phase space occupation at the point (\mathbf{r}, \mathbf{p}) at time t . In contrast to Sec.

2.4 Cross-species thermalization in atomic gases

2.1.1, we consider here the time-dependence of an occupation probability. The temporal evolution of this function is predictable in the absence of collisions. That means after a small time t' , the same amount of atoms will be found at a slightly displaced and distorted phase volume element $d\mathbf{r}'d\mathbf{p}'$ near the point $(\mathbf{r}', \mathbf{p}')$

$$f(\mathbf{r}', \mathbf{p}', t')d\mathbf{r}'d\mathbf{p}' = f(\mathbf{r}, \mathbf{p}, t)d\mathbf{r}d\mathbf{p}. \quad (2.56)$$

From this follows that the phase space density along the trajectory of the atoms is conserved

$$\left(\dot{\mathbf{r}} \cdot \frac{\partial}{\partial \mathbf{r}} + \dot{\mathbf{p}} \cdot \frac{\partial}{\partial \mathbf{p}} + \frac{\partial}{\partial t} \right) f(\mathbf{r}, \mathbf{p}, t) = 0, \quad (2.57)$$

in accordance with Liouville's theorem. In the presence of collisions the Boltzmann equation describes the evolution of $f(\mathbf{r}, \mathbf{p}, t)$ in phase space. In a two-component gas of distinguishable atoms, collisions influence the propagation of $f(\mathbf{r}, \mathbf{p}, t)$ in phase space. In equivalence to Eq. (2.56), a collision term takes this into account

$$f(\mathbf{r}', \mathbf{p}', t')d\mathbf{r}'d\mathbf{p}' = f(\mathbf{r}, \mathbf{p}, t)d\mathbf{r}d\mathbf{p} + \Gamma_c(\mathbf{r}, \mathbf{p}, t)d\mathbf{r}d\mathbf{p}dt, \quad (2.58)$$

where $\Gamma_c(\mathbf{r}, \mathbf{p}, t)$ is the rate at which $f(\mathbf{r}, \mathbf{p}, t)$ increases or decreases at the point (\mathbf{r}, \mathbf{p}) and time t . In the limit of small temporal steps in phase space this can be rewritten as

$$\left(\dot{\mathbf{r}} \cdot \frac{\partial}{\partial \mathbf{r}} + \dot{\mathbf{p}} \cdot \frac{\partial}{\partial \mathbf{p}} + \frac{\partial}{\partial t} \right) f(\mathbf{r}, \mathbf{p}, t) = \Gamma_c(\mathbf{r}, \mathbf{p}, t). \quad (2.59)$$

This expression is called Boltzmann equation. In (Walraven, 2010), the collision term $\Gamma_c(\mathbf{r}, \mathbf{p}, t)$ on the righthand side is derived for a two-component gas of atoms in the center of mass frame. The Boltzmann equation for species 1 colliding in a mixture with species 2 is given by

$$\begin{aligned} & \left(\dot{\mathbf{r}} \cdot \frac{\partial}{\partial \mathbf{r}} + \dot{\mathbf{p}}_1 \cdot \frac{\partial}{\partial \mathbf{p}_1} + \frac{\partial}{\partial t} \right) f(\mathbf{r}, \mathbf{p}_1, t) = \\ & \sum_{j=1,2} \frac{1}{(2\pi\hbar)^3} \int d\mathbf{p}_j d\Omega v_{1j} \sigma_{1j}(v_{1j}, \Omega) (f'_1 f'_j - f_1 f_j). \end{aligned} \quad (2.60)$$

The distribution functions are $f'_1 = f_1(\mathbf{r}, \mathbf{p}'_1, t)$, $f'_j = f_j(\mathbf{r}, \mathbf{p}'_j, t)$, $f_1 = f_1(\mathbf{r}, \mathbf{p}_1, t)$ and $f_j = f_j(\mathbf{r}, \mathbf{p}_j, t)$. The primed momentum states refer to values after the collision process and are given in App. B. $\sigma_{1j}(v_{1j}, \Omega)$ are the inter- or intraspecies scattering cross sections and $v_{ij} = |\mathbf{p}_i/m_i - \mathbf{p}_j/m_j|$ with $i \neq j$ are the relative velocities of the particles.

2.4.1.1 Collision rate

In the following, classical Maxwell-Boltzmann distributions in equilibrium, which are correctly normalized to the total particle number N_i , are considered

$$f_i(\mathbf{r}, \mathbf{p}_i) = n_i \lambda_{\text{dB}, m_i}^3 e^{-\frac{1}{k_B T} \left(\frac{\mathbf{p}_i^2}{2m_i} + V_i(\mathbf{r}) \right)}, \quad (2.61)$$

where atoms of type i with mass m_i are present in the external potential $V_i(\mathbf{r})$, $n_i = N_i / \int \exp(-\frac{1}{k_B T} V_i(\mathbf{r})) d\mathbf{r}$ is the central peak density, and λ_{dB, m_i} is the thermal de Broglie wavelength

$$\lambda_{\text{dB}, m_i} = \frac{h}{\sqrt{2\pi m_i k_B T}} \quad (2.62)$$

with the respective mass m_i . For pure interspecies collisions between particles of species 1 and 2, as present e.g. in a two-species Fermi-Fermi mixture, the collision rate is described with center of mass and relative coordinates (cf. App. B)

$$\begin{aligned} \Gamma_{12} = \tau_c^{-1} = \frac{\dot{N}_1}{N_1} = \frac{n_1 \lambda_{\text{dB}, m_1}^3 n_2 \lambda_{\text{dB}, m_2}^3}{N_1 (2\pi\hbar)^6} \int d\mathbf{P}_{\text{cm}} d\mathbf{p}_{\text{rel}} (p_{\text{rel}}/m_r) \sigma_{12}(p_{\text{rel}}) \times \\ \times \exp \left[-\frac{P_{\text{cm}}^2}{2Mk_B T} - \frac{p_{\text{rel}}^2}{2m_r k_B T} - \frac{V_1(\mathbf{r}) + V_2(\mathbf{r})}{k_B T} \right]. \end{aligned} \quad (2.63)$$

By defining the thermally averaged collision rate per unit density, which is also often referred to as the K_2 -coefficient (Burke, 1999)

$$K_2 = \langle v_{12} \sigma_{12}(p_{\text{rel}}) \rangle = \left(\frac{\lambda_{\text{dB}, m_r}}{2\pi\hbar} \right)^3 \int d\mathbf{p}_{\text{rel}} (p_{\text{rel}}/m_r) \sigma_{12}(p_{\text{rel}}) e^{-p_{\text{rel}}^2/(2m_r k_B T)}, \quad (2.64)$$

one obtains for the collision rate

$$\Gamma_{12} = \tau_c^{-1} = \frac{\dot{N}_1}{N_1} = n_{12} \langle v_{12} \sigma_{12}(p_{\text{rel}}) \rangle, \quad (2.65)$$

where $n_{12} = 1/N_1 \int d\mathbf{r} n_1(\mathbf{r}) n_2(\mathbf{r})$ is the density-density overlap of the two clouds normalized by the particle number of species 1. For an energy independent scattering cross section the averaging over momentum states can be simplified according to $\langle v_{12} \sigma_{12}(p_{\text{rel}}) \rangle = v_{\text{rel}} \sigma_{12}$ with $v_{\text{rel}} = \sqrt{8k_B T / (\pi m_r)}$ being the relative velocity of the atoms. For most cases in experiments with ultracold gases, the energy independent scattering cross section is a good approximation. See for some deviations and considerations concerning this rule also App. C.3.

2.4.1.2 Evaporation rate

Evaporative cooling is a very efficient technique to cool thermal atomic gases to sub μK temperatures and high phase-space density. The idea is based on selective removal of atoms with energies above the mean energy per particle of the ensemble and subsequent rethermalization of the cloud to a colder temperature due to elastic collisions. The rethermalization in a spin-polarized ensemble of bosons is possible in contrast to fermions, which do not interact among themselves at low temperatures, cf. Sec. 2.2.2. This strategy in combination with laser cooling led in 1995 to the first successful creation of a Bose-Einstein condensate (Anderson *et al.*, 1995; Bradley *et al.*, 1995; Davis *et al.*, 1995).

The kinetics of evaporation can be described by the Boltzmann equation. A truncated Maxwell-Boltzmann distribution serves as an ansatz for the energy distribution of the

2.4 Cross-species thermalization in atomic gases

evaporating atoms (Luiten *et al.*, 1996)

$$f_i(\epsilon) = n_i \lambda_{\text{dB},m_i}^3 e^{-\frac{\epsilon}{k_B T}} \Theta(\epsilon_t - \epsilon), \quad (2.66)$$

where ϵ_t defines the energy above which atoms are removed from the trap due to collisions. For a constant ϵ_t , collisions between the atoms in the trap produce energy states which lie above the truncation energy ϵ_t and the corresponding atoms are consequently lost due to plain evaporation. The temperature given in this expression is understood as a quasi-temperature T . The evaporation rate of atoms of species 1 due to collisions with atoms of species 2 can be expressed as

$$\Gamma_{\text{evap},1} = -\frac{\dot{N}_1}{N_1} = n_2 \langle v_{12} \sigma_{12}(p_{\text{rel}}) \rangle e^{-\eta} F(\eta), \quad (2.67)$$

where $\eta \equiv \epsilon_t / (k_B T)$ is the truncation parameter and $F(\eta)$ denotes a function of η . In most cases $F(\eta) \approx 1$ is a good approximation (Walraven, 1996). Considering intraspecies collisions (e.g. for bosons) in a harmonic trap what leads to evaporation, $F(\eta)$ can be expressed analytically in terms of incomplete Gamma functions $F(\eta) = \eta - 4R(3, \eta)$ (Walraven, 1996), where $R(a, \eta)$ satisfies $R(a, \eta) = P(a+1, \eta) / P(a, \eta)$ and $P(a, \eta) = [\Gamma(a)]^{-1} \int_0^\eta t^{a-1} e^{-t} dt$. For plain evaporation η increases, since the temperature of the gas is lowered what leads to an exponential suppression of the evaporation rate according to Eq. (2.67). By lowering the truncation energy ϵ_t the evaporation process can be preserved while keeping η nearly constant. Typical experimental values for η for efficient evaporation are between 7 and 9.

2.4.2 Cross-dimensional thermal relaxation

Within this thesis, values of elastic scattering cross sections in the vicinity of a Feshbach resonance are determined. The technique of cross-dimensional thermal relaxation (CDR) is employed. Sec. 2.4.2.1 presents the idea of the CDR method. In Sec. 2.4.2.2, a classical kinetic model based on the Boltzmann equation is presented. The analysis reveals that the rate of CDR in a mixture is mass dependent. The average number of collisions for rethermalization β is introduced, which incorporates this mass dependence. Finally, in Sec. 2.4.2.3, classical Monte Carlo simulations are performed over a wide range of parameters to test and verify the validity of the model. Predictions of the parameter β , which relates the collision rates, cf. Sec. 2.4.1.1, and the CDR rates, are given for a number of Fermi-Fermi mixtures.

2.4.2.1 Principle of cross-dimensional thermal relaxation

The method of CDR is based on the idea that a classical gas is prepared in an out-of-equilibrium state such that along different directions a thermal energy distribution is established, but at different individual mean energies per particle E_i . After preparation, the anisotropy of thermal energy between two axes, e.g. $\chi \equiv E_x - E_z$, relaxes to zero at a rate that is related to the frequency of elastic collisions. For the work with ultracold

atoms in this thesis only s -wave collisions need to be considered. Only the direction of the relative momentum is changed for a single elastic collision (cf. App. B). In the experiment, information about the relaxation process is obtained from time-of-flight absorption imaging of the gas clouds after release from the trap. After sufficiently long expansion time, the energy anisotropy is determined from the observed aspect ratio of the cloud size.

The method of CDR has already been applied to investigate s - and p -wave collisions between the same atomic species or in Bose-Fermi mixtures (Monroe *et al.*, 1993; Regal *et al.*, 2003b; Goldwin *et al.*, 2004). In an analysis of CDR in a single species cloud of bosonic atoms it was shown that the relaxation of the energy difference between two Cartesian directions follows an exponential decay with a $1/e$ time constant proportional to the collision rate (Roberts, 2001)

$$\Gamma_{\text{B,CDR}} = \frac{1}{\alpha} \langle n \rangle \sigma v_{\text{rel}}. \quad (2.68)$$

If energy independent s -wave collisions are assumed the mean collision rate can be rewritten as $\Gamma_{\text{coll}} = \langle nv\sigma \rangle = \langle n \rangle \sigma v_{\text{rel}}$, where $\langle n \rangle$ is the number density of the gas. The coefficient α describes the mean number of collisions per particle required for thermalization.

The model has been extended to describe the rethermalization process in a Bose-Fermi mixture with different masses. The relaxation rate per fermion can be expressed in a similar way as the single species case (Goldwin *et al.*, 2005)

$$\Gamma_{\text{FB,CDR}} = \frac{1}{\beta} n_{\text{FB}} \sigma_{\text{FB}} v_{\text{rel}}, \quad (2.69)$$

where n_{FB} is the density of the bosons averaged over the fermion distribution, σ_{FB} is the interspecies s -wave collision cross section, and v_{rel} is the relative velocity between the bosons and fermions. The coefficient β represents the mean number of collisions per fermion required to thermalize with the bosons.

The case of a spin-polarized mixture of two different types of fermions is considered in this work. In this situation, only interspecies collisions contribute to the rethermalization process. Under certain approximations as discussed below, the relaxation in the mixture is expected to follow an exponential decay with a time constant proportional to the mean time between interspecies collisions

$$\begin{aligned} \Gamma_{\text{F12,CDR}} &= \frac{1}{\beta_{12}} n_{12} \sigma_{12} v_{\text{rel}}, \\ \Gamma_{\text{F21,CDR}} &= \frac{1}{\beta_{21}} n_{21} \sigma_{12} v_{\text{rel}}, \end{aligned} \quad (2.70)$$

where the terms on the right hand side are defined in a similar way as in Eq. (2.69). For different masses $m_1 \neq m_2$ involved in the collision process, the coefficients β are unequal $\beta_{12} \neq \beta_{21}$. That means that the mean number of collisions per species 1 particle to thermalize with species 2 particles deviates from the mean number of collisions of species 2 to thermalize with species 1 even for identical particle numbers and starting conditions. Therefore, such a system is ideal to study mass-dependent collision processes. In the following, a kinetic model elucidates this effect.

2.4 Cross-species thermalization in atomic gases

2.4.2.2 Kinetic model

The analytic model outlined in this section follows a very similar approach as already presented by (Goldwin *et al.*, 2004, 2005) in the case of a Bose-Fermi mixture. In the present work the theory by (Goldwin *et al.*, 2005) is extended by two elements. First, we apply the model to a Fermi-Fermi mixture, where pure s -wave collisions drive the equilibration of the clouds. Second, CDR is studied for the case of an arbitrary symmetry of the energy anisotropy, i.e. $E_x \neq E_y \neq E_z$.

The analysis is based on the Boltzmann equation, as introduced in Sec. 2.4.1. According to this equation, the rate of change of the ensemble average of any function of the two species' positions and velocities, usually denoted as $\chi(\mathbf{r}_1, \mathbf{v}_1; \mathbf{r}_2, \mathbf{v}_2)$, is given by (Reif, 1987)

$$\langle \dot{\chi} \rangle = \sigma_{12} \langle n v_{\text{rel}} \Delta \chi \rangle. \quad (2.71)$$

An energy independent scattering cross section σ_{12} is here assumed, so that it can be separated from the ensemble average. $\Delta \chi$ is the change in χ due to a single collision. This quantity is defined as

$$\chi_1 \equiv E_{1,x} - E_{1,z}. \quad (2.72)$$

Fermions of type 1 only collide with fermions of type 2. The energy $E_{1,i}$ denotes the mean thermal energy per particle along the Cartesian direction i . One is interested in the change of χ_1 . The ensemble average in Eq. (2.71) is therefore only taken over the distribution function of the type-1 particles. The redistribution of kinetic energy between the axes x and z can be described by

$$\Delta \chi_1 = \Delta \left(E_{1,x}^{\text{kin}} - E_{1,z}^{\text{kin}} \right) = \frac{1}{2} m_1 \Delta \left(v_{1,x}^2 - v_{1,z}^2 \right). \quad (2.73)$$

Since $\Delta \chi$ has no position dependence one can write

$$\langle \dot{\chi}_1 \rangle = \frac{1}{2} m_1 n_{12} \sigma_{12} \langle v_{\text{rel}} \Delta \left(v_{1,x}^2 - v_{1,z}^2 \right) \rangle. \quad (2.74)$$

Center-of-mass and relative coordinates (cf. App. B) are well-suited to describe binary collisions between two different masses. One can write

$$\begin{aligned} v_{1,x}^2 - v_{1,z}^2 &= (V_{\text{cm},x}^2 - V_{\text{cm},z}^2) + \left(\frac{m_2}{m_1 + m_2} \right)^2 (v_{\text{rel},x}^2 - v_{\text{rel},z}^2) \\ &+ 2 \cdot \frac{m_2}{m_1 + m_2} (V_{\text{cm},x} v_{\text{rel},x} - V_{\text{cm},z} v_{\text{rel},z}). \end{aligned} \quad (2.75)$$

The effect of the collision is to only change the direction of \mathbf{v}_{rel} , the center-of-mass velocity \mathbf{V}_{cm} and the absolute value of the relative velocity $|\mathbf{v}_{\text{rel}}| = v_{\text{rel}}$ are conserved quantities. Therefore the first bracket on the righthand side of the equation vanishes. Additionally, only the terms after the collision need to be taken into consideration. The rate of change of χ_1 is then

$$\begin{aligned} \langle \dot{\chi}_1 \rangle &= -\frac{1}{2} \frac{m_1 m_2}{m_1 + m_2} n_{12} \sigma_{12} \left\langle v_{\text{rel}} \left[\frac{m_2}{m_1 + m_2} (v_{\text{rel},x}^2 - v_{\text{rel},z}^2) \right. \right. \\ &\quad \left. \left. + 2 (V_{\text{cm},x} v_{\text{rel},x} - V_{\text{cm},z} v_{\text{rel},z}) \right] \right\rangle. \end{aligned} \quad (2.76)$$

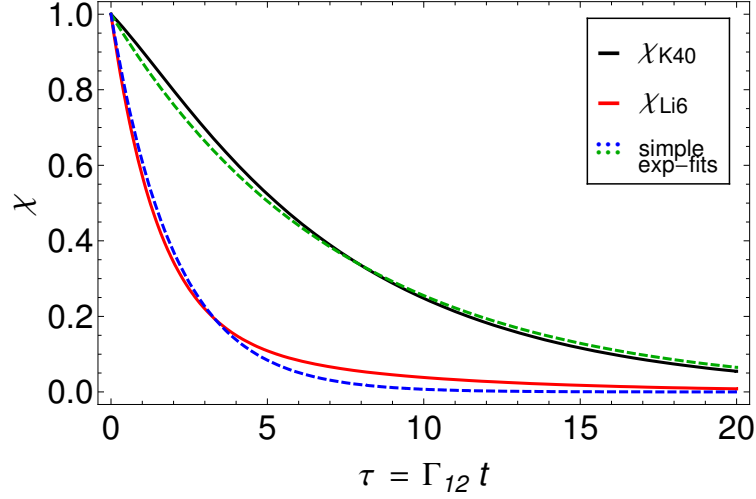


Figure 2.8: Solutions given in Eq. (2.82) and simple exponential fits to the solutions for the case of a ${}^6\text{Li}$ - ${}^{40}\text{K}$ mixture.

The resulting expression is in general not trivial to solve for arbitrary initial conditions and masses. But some approximations are applicable in the case of small deviations from thermal equilibrium and of Gaussian distribution functions. The arising ensemble averages in Eq. (2.76) can be approximated as

$$\langle v_{\text{rel}} v_{\text{rel},i}^2 \rangle \approx \frac{4}{3} \langle v_{\text{rel}} \rangle \langle v_{\text{rel},i}^2 \rangle, \quad i = x, z \quad (2.77)$$

$$\langle v_{\text{rel}} V_{\text{cm},i} v_{\text{rel},i} \rangle \approx \frac{4}{3} \langle v_{\text{rel}} \rangle \langle V_{\text{cm},i} v_{\text{rel},i} \rangle, \quad i = x, z. \quad (2.78)$$

These expressions are verified by numerical integrations with anisotropic Gaussian distribution functions and typical experimental initial conditions. The results are shown in the Suppl. C.1. Inserting the expressions yields

$$\begin{aligned} \langle \dot{\chi}_1 \rangle = & -\frac{2}{3} \Gamma_{12} \frac{m_1 m_2}{m_1 + m_2} \left\langle \frac{m_2}{m_1 + m_2} (v_{\text{rel},x}^2 - v_{\text{rel},z}^2) \right. \\ & \left. + 2 (V_{\text{cm},x} v_{\text{rel},x} - V_{\text{cm},z} v_{\text{rel},z}) \right\rangle, \end{aligned} \quad (2.79)$$

where Γ_{12} is the collision rate as defined in Eq. (2.65) in the case of an energy-independent scattering cross section. By resubstituting v_1 and v_2 , and applying $\langle v_{1i} v_{2i} \rangle = 0$, one obtains finally

$$\langle \dot{\chi}_1 \rangle = -\frac{2}{3} \Gamma_{12} \frac{m_2}{(m_1 + m_2)^2} \langle (2m_1 + m_2) \chi_1 - m_1 \chi_2 \rangle, \quad (2.80)$$

where the fact is used that the mean kinetic and potential energies in a given direction are equal. By simply swapping $1 \leftrightarrow 2$, the time dependence of χ_2 is obtained. As a

2.4 Cross-species thermalization in atomic gases

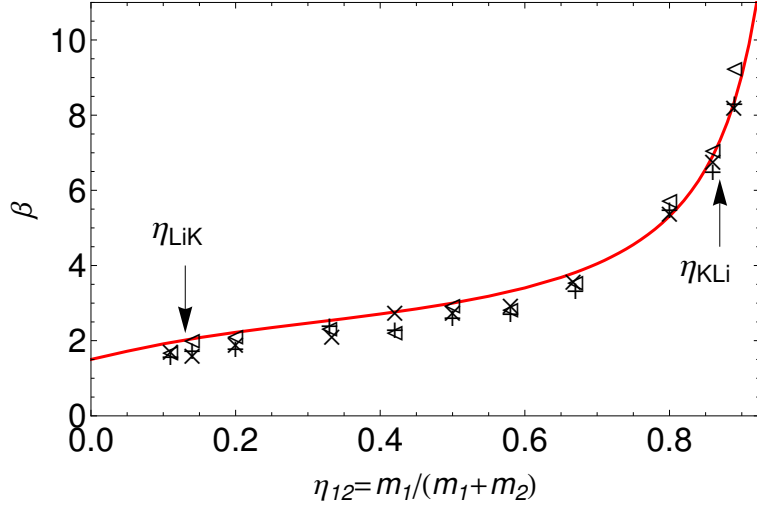


Figure 2.9: Number of collisions per fermion required for cross-dimensional thermal relaxation. Comparison of kinetic model (solid curve) and classical Monte-Carlo simulations with varying initial starting conditions (symbols): a) triangles: $N_1 = N_2$, $E_x/E_z = 1.2$, $E_y/E_z = 1.65$, b) crosses: $N_1 = N_2$, $E_x/E_z = 1.7$, $E_y/E_z = 1.4$, c) plus symbols: $N_1 = 2N_2$, $E_x/E_z = 1.6$, $E_y/E_z = 1.3$ (Hahn, 2009).

result, a system of two coupled differential equations is derived

$$\begin{aligned} \frac{d}{d\tau_1} \langle \chi_1 \rangle &= -\frac{2}{3} \frac{m_2}{(m_1 + m_2)^2} [(2m_1 + m_2) \langle \chi_1 \rangle - m_1 \langle \chi_2 \rangle] \\ \frac{d}{d\tau_2} \langle \chi_2 \rangle &= -\frac{2}{3} \frac{m_1}{(m_1 + m_2)^2} [(m_1 + 2m_2) \langle \chi_2 \rangle - m_2 \langle \chi_1 \rangle], \end{aligned} \quad (2.81)$$

where dimensionless times $\tau_1 = \Gamma_{12}t$ and $\tau_2 = \Gamma_{21}t$ are introduced. This system of coupled differential equations allows for the determination of the temporal relaxation of χ_1 and χ_2 for different initial conditions, such as different initial anisotropies $\chi_1(0)$, $\chi_2(0)$ or initial particle numbers N_1 and N_2 . For same atom numbers $N_1 = N_2$ and initial anisotropy $\chi_1(0) = \chi_2(0) = 1$, and introducing a normalized mass $\eta_1 = \frac{m_1}{m_1 + m_2}$ ($\eta_2 = \frac{m_2}{m_1 + m_2} = 1 - \eta_1$), the solution for χ_1 is

$$\chi_1(\tau_1) = \frac{(1 - \eta_1)(1 - 2\eta_1)e^{-2\tau_1/3} + \eta_1 e^{-4/3\eta_1(1-\eta_1)\tau_1}}{1 - 2\eta_1(1 - \eta_1)}. \quad (2.82)$$

The corresponding expression for χ_2 can be derived by simply swapping $1 \leftrightarrow 2$. Hence, for the general case of two-component Fermi-Fermi mixtures we find that the relaxation process is described for each individual component by a sum of two exponential decays. The respective time constants are dependent on the mass ratio of the two components. Only for identical masses a single exponential decay is recovered. For the case of a ${}^6\text{Li}$ - ${}^{40}\text{K}$ mixture and identical initial conditions $N_{\text{Li}} = N_{\text{K}}$, $\chi_{\text{Li}}(0) = \chi_{\text{K}}(0) = 1$, the solutions are plotted in Fig. 2.8.

For the purpose of simple estimations one would like to relate the time scale of the relaxation process to the mean time of collisions per atom of species 1 with species 2 by defining:

$$\Gamma_{12,\text{CDR}} \equiv \frac{1}{\beta_{12}} \Gamma_{12}. \quad (2.83)$$

Here β_{12} is a dimensionless constant, which depends on the initial conditions of CDR and masses, and describes the mean number of collisions that one particle of type 1 requires to thermalize with atoms of type 2. β is determined by fitting a simple exponential decay to Eq. (2.82) and analytically minimizing the integrated squared error

$$\text{err}^2 = \int_0^\infty d\tau \left(\chi(\tau) - e^{-\frac{\tau}{\beta}} \right)^2 \quad (2.84)$$

with respect to the parameter β . Minimizing requires $\partial/\partial\beta \text{err}^2 = 0$. This leads to

$$0 = \int_0^\infty d\tau \left(\chi(\tau) - e^{-\frac{\tau}{\beta}} \right) \tau e^{-\frac{\tau}{\beta}}. \quad (2.85)$$

Inserting $\chi(\tau)$ from Eq. (2.82) for identical initial conditions and carrying out the integration yields an implicit expression for β , which depends on the masses of the involved fermions

$$\frac{(1-2\eta)(1-\eta)}{(2\beta+3)^2} + \frac{\eta}{(4\eta(1-\eta)\beta+3)^2} = \frac{1}{36}(1-2\eta(1-\eta)). \quad (2.86)$$

This expression from the kinetic model, Eq. (2.86), and results from classical Monte-Carlo simulations (symbols, cf. Sec. 2.4.2.3) are plotted in Fig. 2.9. The simulations and the analytic model show good agreement. Performing a Taylor expansion of Eq. (2.82) for small τ gives $\beta_{\text{init}} = \frac{3}{2(1-\eta)}$. Hence the ratio of the initial slopes of thermalization curves for a mixture of fermionic atoms with masses m_1 and m_2 scales as the mass ratio $\beta_{21,\text{init}}/\beta_{12,\text{init}} = m_2/m_1$.

2.4.2.3 Monte-Carlo simulation

This section describes details of the Monte-Carlo simulations that are used to verify the validity of the analytical model presented in Sec. 2.4.2.2, and to simulate various experimental situations. A comprehensive description can also be found in (Hahn, 2009).

The simulation is initialized by preparing an ensemble consisting of N_1 type-1 and N_2 type-2 fermions in a harmonic trap with trap frequencies $(\nu_{x,1(2)}, \nu_{y,1(2)}, \nu_{z,1(2)})$ for the type-1(2) atoms. Since Gaussian distributions are considered for the position and velocity of the particles, the distributions separate for each individual spatial coordinate (x, y, z) , and position and velocity vectors are created from a random number generator for each particle and spatial direction. The classical momentum distributions are scaled such that the mean kinetic energy along different Cartesian directions are unequal leading to an energy anisotropy within the ensemble. The initial energy in a given dimension is the same for both species. The positions and velocities of each individual particle evolve on a trajectory in phase space according to Newton's laws for a small time step Δt before

2.4 Cross-species thermalization in atomic gases

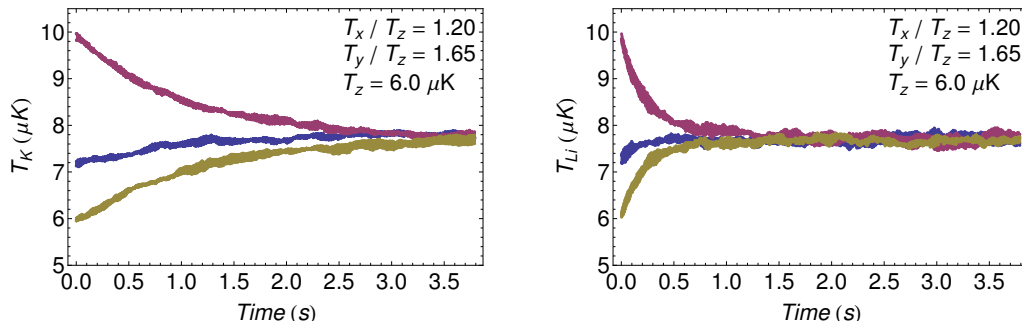


Figure 2.10: Typical relaxation curves for a ${}^6\text{Li}$ - ${}^{40}\text{K}$ mixture obtained from a classical Monte-Carlo simulation. The initial anisotropies are $T_x/T_z = 1.20$ and $T_y/T_z = 1.65$ and the same atom number for both species is chosen. The trapping frequencies (ν_x, ν_y, ν_z) are (544, 544, 769) Hz for ${}^{40}\text{K}$ (left) and (1333, 1333, 1884) Hz for ${}^6\text{Li}$ (right) and the temperature along z -direction is $T_z = 6.0 \mu\text{K}$.

a collision occurs. For a spin-polarized two-species Fermi-Fermi mixture only interspecies collisions are allowed. If two different particles k and l are found within a critical distance r_c of each other, the pair obtains the collision probability $p_{\text{coll}} = \sigma_{kl} v_{\text{rel}} \Delta t / V_c$, where σ_{kl} is the interspecies collision cross section, $v_{\text{rel}} = |\mathbf{v}_k - \mathbf{v}_l|$ is the relative collision velocity, and $V_c = 4/3\pi r_c^3$ is the critical volume for a collision process to happen. If p_{coll} is greater than a random number generated from a uniform distribution between 0 and 1, a s -wave collision takes place and the relative velocity vector is rotated into a random direction under conservation of the total energy and momentum. After all possible collision pairs have been considered, the mean energies per particle of each species in each of the three Cartesian directions $E_i = k_B T_i$ are calculated, and the next time step Δt proceeds.

The choice of parameters for a Monte-Carlo simulation is crucial. A suitable parameter space is important for plausible and reliable results from the simulation. Special attention should be addressed to the choice of the collision probability p_{coll} and the critical volume V_c . As pointed out in (Guéry *et al.*, 1999; Goldwin *et al.*, 2005) the collision probability should be kept well below 10% for accurate results. For the simulations, values in the range of 5×10^{-3} to 5×10^{-2} are used for p_{coll} . Also a poor choice of the critical volume $V_c = 4/3\pi r_c^3$ influences the reliability of results. The number of collisions per particle within a collision time $\tau_c = \Gamma_{12}^{-1}$ needs to be small for reliable results. The simulations typically use $\langle n \rangle V_c = 10^{-1}$ (Hahn, 2009), where $\langle n \rangle$ is the number density. This choice leads to ≈ 20 collisions per particle within a collision time.

A typical Monte-Carlo simulation for a thermalization process in the ${}^6\text{Li}$ - ${}^{40}\text{K}$ mixture is presented in Fig. 2.10. For identical initial conditions, the simulation reveals different time scales for the rethermalization of ${}^6\text{Li}$ and ${}^{40}\text{K}$ in the mixture consistent with the findings of the kinetic model.

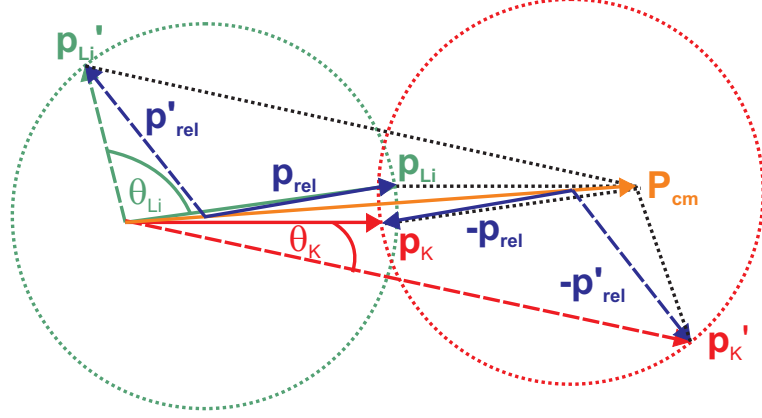


Figure 2.11: Illustration of a ${}^6\text{Li}$ - ${}^{40}\text{K}$ collision process. An example is shown where the direction of the momentum of ${}^6\text{Li}$ is rotated by $\theta_{\text{Li}} \approx 90^\circ$ and the angle of the momentum vector θ_{K} of the heavier atom ${}^{40}\text{K}$ is less changed. The vector construction follows momentum and energy conservation according to Eqs. (B.11) from App B. The unprimed (primed) quantities are associated with momenta before (after) the collision process. The center of mass momentum \mathbf{P}_{cm} and the absolute value of the relative momentum \mathbf{p}_{rel} is conserved, only the direction of \mathbf{p}_{rel} is changed. All possible final momentum states for ${}^6\text{Li}$ (${}^{40}\text{K}$) lie on the green (red) circular line.

2.4.2.4 Mass dependence of β

The Monte-Carlo simulations show that reliable results for the coefficient β can be obtained from the analytical model for mass ratios up to ≈ 7 (Hahn, 2009). This corresponds to limits of $\eta_1 = 0.875$ and $\eta_2 = 0.125$. The ${}^6\text{Li}$ - ${}^{40}\text{K}$ mixture with a mass ratio of ≈ 6.64 lies barely in this limit. This mixture is considered throughout this work and for identical initial conditions $N_{\text{Li}} = N_{\text{K}}$ and $\chi_{\text{Li}}(0) = \chi_{\text{K}}(0) = 1$ the kinetic model predicts

$$\beta_{\text{LiK}} = 2.0, \quad \beta_{\text{KLi}} = 7.3 \quad (2.87)$$

what leads to the ratio $\beta_{\text{KLi}}/\beta_{\text{LiK}} = 3.7$.

The difference in the relaxation rate follows from the mass difference and from the nature of s -wave collisions. In a single collision the direction of the relative momentum in the center of mass frame is rotated, while the absolute value of the relative momentum is conserved. In the laboratory frame this leads to a distribution of final directions after the collision covering a solid angle that is on average larger for the lighter particle than for the heavier one. Therefore, CDR of ${}^6\text{Li}$ with ${}^{40}\text{K}$ atoms is accomplished after fewer collisions than the simultaneously ongoing case of ${}^{40}\text{K}$ relaxing with ${}^6\text{Li}$. To further illustrate this, a typical collision process in the center of mass frame under the consideration of the conservation laws is presented in Fig. 2.11. All final momentum states for the two species (in green for ${}^6\text{Li}$ and red for ${}^{40}\text{K}$) lie on a circle with radius $|\mathbf{p}_{\text{rel}}|$. For this example, the angle of the momentum for ${}^6\text{Li}$ $\theta_{\text{Li}} = \angle(\mathbf{p}_{\text{Li}}, \mathbf{p}'_{\text{Li}})$ after a single collision can be rotated by even 180° , whereas the momentum of ${}^{40}\text{K}$ covers a smaller range of accessible angles

2.4 Cross-species thermalization in atomic gases

within a single collision process.

For the case of identical masses, e.g. in the situation of a spin mixture of fermions, the coefficient β is 3. With the help of Eq. (2.86) the values for β can be obtained for a wide variety of Fermi mixtures for values of η in the range 0.125-0.875.

2.4.2.5 Interpretation of experimental thermalization curves

The true solution of the temporal relaxation of χ_1 is not a simple exponential decay according to Eq. (2.82). But within typical experimental uncertainties a simple exponential decay

$$\chi_1(t) = \chi_1(0)e^{-\Gamma_{12,\text{CDR}}t} = \chi_1(0)e^{-\Gamma_{12}/\beta_{12}t} \quad (2.88)$$

describes the relaxation accurately enough, see also Fig. 2.8. In the experiment information about the relaxation process is extracted by time-of-flight absorption imaging of the gas clouds. After sufficiently long expansion time, the energy anisotropy is determined from the observed aspect ratio of the size of the cloud. A simple exponential relaxation, as derived in Eq. (2.88), leads to a ratio of exponential functions describing the relaxation of the measured aspect ratio

$$\frac{E_i(t)}{E_j(t)} = \frac{1 + \epsilon_i e^{-\Gamma_{12}/\beta_{12}t}}{1 + \epsilon_j e^{-\Gamma_{12}/\beta_{12}t}}, \quad (2.89)$$

where $\epsilon_i = 3E_i(0)/(E_x(0) + E_y(0) + E_z(0)) - 1$ and $i \neq j = x, y, z$. This expression is valid for small deviations from a cylindrically symmetric trap, i.e. for the case that along different axes in the cloud the relaxation rate Γ_{12}/β_{12} is equal. This is tested by numerical integrations over Gaussian distributions (cf. App. C).

Taking the ratio of relaxation rates obtained from least square fits of thermalization curves gives

$$\frac{\Gamma_{12,\text{CDR}}}{\Gamma_{21,\text{CDR}}} = \frac{1/\beta_{12} n_{12} v_{12} \sigma_{12}}{1/\beta_{21} n_{21} v_{21} \sigma_{21}}. \quad (2.90)$$

In the case of a Fermi-Fermi mixture this expression can be simplified since $v_{12} = v_{21}$ and $\sigma_{12} = \sigma_{21}$ holds. For the ratio of β -factors this leads to

$$\frac{\beta_{12}}{\beta_{21}} = \frac{\Gamma_{21,\text{CDR}} N_2}{\Gamma_{12,\text{CDR}} N_1}. \quad (2.91)$$

As a consequence, CDR in a Fermi-Fermi mixture allows to directly study mass-dependent effects. But the accuracy is limited to the accuracy of particle number determination, which is subject to typical measurement errors of a standard absorption imaging. In the case of a Bose-Fermi (^{87}Rb - ^{40}K) mixture as investigated in (Goldwin *et al.*, 2004, 2005), the systematic uncertainty in the particle number determination can be overcome since ^{87}Rb - ^{87}Rb and ^{87}Rb - ^{40}K collisions occur and already previously determined scattering properties of ^{87}Rb - ^{87}Rb collisions can be invoked to accurately determine the Bose-Fermi scattering parameters.

In App. C.2, the influence of initial conditions on CDR is studied on the basis of the kinetic model from Sec. 2.4.2.2 and Monte-Carlo simulations as introduced in Sec.

2.4.2.3. In the following, a summary of the results for the dependencies of particle numbers, initial anisotropies, and energy imbalance on the rethermalization rates is presented (see App. C). The analysis with the kinetic model is based on the solution of the system of coupled differential equations from Eq. (2.81) for different initial conditions, and subsequent fitting of the solutions with the expression from Eq. (2.88) in order to obtain rethermalization rates. The range of investigated initial anisotropies and particle numbers corresponds to typical experimental situations, and the parameters of a ${}^6\text{Li}$ - ${}^{40}\text{K}$ mixture are invoked. For the particle number dependence the results from the kinetic model Fig. C.4(a) and from the Monte-Carlo simulations Fig. C.2 show that the relaxation rate of ${}^6\text{Li}$ (${}^{40}\text{K}$) colliding with ${}^{40}\text{K}$ (${}^6\text{Li}$) is to a good approximation proportional to the atom number of ${}^{40}\text{K}$ (${}^6\text{Li}$), and independent on the initial particle number of ${}^6\text{Li}$ (${}^{40}\text{K}$), in accordance with Eq. (2.91). In the experiments, the clouds are usually prepared with different initial anisotropies $\chi_{\text{Li}}(0) \neq \chi_{\text{K}}(0)$. The variation of the ratio of initial anisotropies shows a strong dependence of $\Gamma_{\text{LiK,CDR}}$, in particular, as illustrated in Fig. C.4(b).

Another important systematic deviation to the CDR occurs, when an energy imbalance between the species is present in the mixture in addition to an energy anisotropy within the individual clouds. This means that the relation

$$\sum_{i=x,y,z} E_{\text{Li},i}(0) \neq \sum_{i=x,y,z} E_{\text{K},i}(0) \quad (2.92)$$

is valid and a net energy flow occurs from one species to the other. According to Fig. C.6 in Sec. C.2.2, the ratio $\beta_{\text{KLi}}/\beta_{\text{LiK}}$ shows a strong dependence if the energy imbalance between the species is changed. A pure energy imbalance equilibrating by elastic collisions in a mixture with fermionic species of different masses can be described with the present kinetic model in a similar way as outlined in Suppl. C.2.2.1. The analysis reveals a single exponential decay of the initial energy imbalance. The dependence of the number of collisions per particle on the mass ratio is presented in Fig. C.5.

According to this discussion, well-defined experimental initial parameters are crucial for studying CDR quantitatively. Experimental results will be presented in Ch. 6.

2.4 Cross-species thermalization in atomic gases

Chapter 3

Experimental apparatus

This chapter describes the experimental platform for the exploration of an interacting two-species quantum-degenerate Fermi mixture and for the investigation of properties of heteronuclear Fermi-Fermi molecules. The discussion begins by presenting the basic concept of achieving the simultaneous quantum degeneracy in a Bose-Fermi-Fermi mixture in Sec. 3.1. The experimental sequence for this undertaking is given in Sec. 3.2, and the parameter optimization of this scheme by benchmark tests is described in Sec. 3.3. In Sec. 3.4, the laser system for trapping and manipulation of the species ^{40}K is presented, which was altered during the course of this work. For the investigation of magnetic field tunable interactions the atoms are transferred into an optical dipole trap, which is brought forward for discussion in Sec. 3.5. The following Sec. 3.6 deals with the magnetic field control by an accurate and stable current feedback loop. For the studies at interspecies Feshbach resonances, the atoms are usually imaged at high magnetic field, and the corresponding technique is introduced in Sec. 3.7.

3.1 Experimental concept and overview

The principal idea of achieving quantum-degeneracy in a ^6Li - ^{40}K mixture relies on sympathetic cooling with a bosonic species, namely ^{87}Rb . The bosonic species can be cooled by forced evaporation since intraspecies collisions are present in a bosonic cloud due to quantum statistics (cf. Sec. 2.4.1.2). The sympathetic cooling scheme has the following advantages. The use of high number atom sources is circumvented, since a reduction of the atom number of the fermionic clouds, as present during a direct evaporation process, is avoided. In addition, Pauli blocking of collisions makes evaporative cooling of an ultracold Fermi mixture inefficient at the final stage.

In the following, the experimental procedure for achieving quantum degenerate atomic samples is described. The individual parts of the experimental cycle are marked with encircled numbers in the subsequent section, and the associated phase space density parameters of ^{87}Rb , namely temperature and atomic number, can be cross-referenced in Tab. 3.1.

3.1 Experimental concept and overview

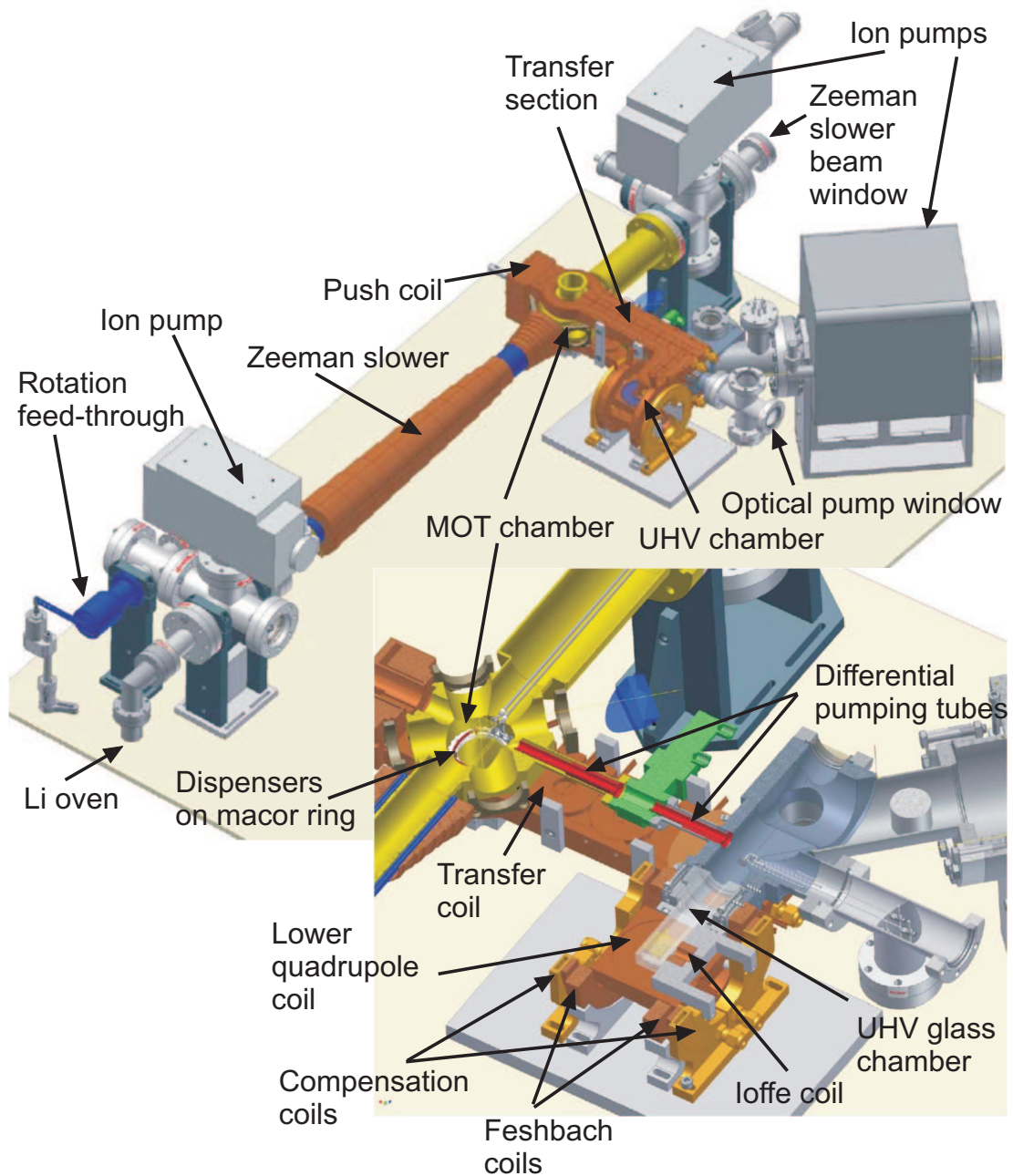


Figure 3.1: Overview of experimental apparatus for the creation of quantum-degenerate ^{87}Rb - ^6Li - ^{40}K mixtures. The three different parts of the vacuum system are presented, atomic oven for ^6Li , chamber for magneto-optical trap, and ultra high vacuum chamber with a long background gas lifetime.

3.2 From a MOT to quantum degeneracy

The atoms are loaded simultaneously into a magneto-optical trap (MOT). ${}^6\text{Li}$ is emitted from an atomic oven and loaded from a Zeeman slower, whereas ${}^{40}\text{K}$ and ${}^{87}\text{Rb}$ are captured from the background vapor pressure. A detailed description of the slower can be found in the thesis (Taglieber, 2008). For the species ${}^{40}\text{K}$ and ${}^{87}\text{Rb}$, atoms are emitted from dispensers. For the purpose of reproducibility the loading time of the MOT is chosen to be 15 s ① (in the following the individual parts of the experimental cycle are marked with encircled numbers, cf. Tab. 3.1). The phase space density of the ensemble of atoms is increased by a combined temporal dark MOT phase (dMOT) for ${}^{87}\text{Rb}$ and a compressed MOT (cMOT) phase for ${}^6\text{Li}$ ②. This strategy is crucial for the achievement of triple degeneracy in a Bose-Fermi-Fermi mixture, for details see (Taglieber, 2008). A significant density increase for ${}^6\text{Li}$ as offered by the cMOT phase is important since the scattering cross section of ${}^6\text{Li}$ colliding with ${}^{87}\text{Rb}$ is comparatively small (Silber *et al.*, 2005), and sympathetic cooling is therefore less efficient. During the first part of the cMOT/dMOT phase, the clouds are compressed by increasing the MOT magnetic field gradient to 28 G/cm within 25 ms. After the cMOT/dMOT phase, the MOT magnetic fields are turned off and a short molasses phase of 2 ms duration for ${}^{87}\text{Rb}$ only follows ③. The duration of this molasses phase is as short as possible, since the ${}^6\text{Li}$ and ${}^{40}\text{K}$ clouds expand freely during this period.

Subsequently, the mixture is optically pumped to favorable hyperfine states for magnetic trapping. Spin exchange collisions lead to losses in the magnetic trap. In fact, for the three-species mixture only one combination is stable for magnetic trapping

$${}^{87}\text{Rb} |F = 2, m_F = 2\rangle, \quad {}^{40}\text{K} |\frac{9}{2}, \frac{9}{2}\rangle, \quad {}^6\text{Li} |\frac{3}{2}, \frac{3}{2}\rangle.$$

The achievement of triple degeneracy requires very slow rates of forced evaporation of ${}^{87}\text{Rb}$ since the thermalization time of ${}^{87}\text{Rb}$ with the fermionic species is long (Taglieber, 2008). In order to reduce losses through collisions with the background gas, the clouds are transferred from the MOT chamber to an ultra high vacuum chamber (UHV), where the $1/e$ lifetime of a thermal cloud of ${}^{87}\text{Rb}$ is up to 70 s. The transfer is realized by a magnetic transport around a 90° corner into a glass cell (Greiner *et al.*, 2001). The MOT chamber is connected to the UHV chamber via two differential pumping tubes. The diameter of the differential pumping tubes is comparatively large (8 mm), as primarily the large ${}^6\text{Li}$ cloud with its low atomic mass and hot temperature requires enough space. A relatively high capture gradient of 140 G/cm is maintained in the axial, vertical direction during the whole transport sequence. In the UHV chamber the atoms are first compressed by changing the axial field gradient from 140 G/cm to 300 G/cm ④, which is created by the quadrupole coil, and then loaded from the spherical quadrupole trap into a quadrupole-Ioffe configuration trap (QUIC).

After loading the QUIC trap, a long forced evaporation period for ${}^{87}\text{Rb}$ is applied. For mixtures of ${}^{87}\text{Rb}$ and ${}^{40}\text{K}$ only, it is sufficient to use radiofrequency (RF) evaporation. This method is applied for the results presented in Ch. 4, since only a quantum degenerate ${}^{40}\text{K}$ cloud is required for this experiment. According to Eq. (2.67), hot atoms

3.3 Benchmark tests of an experimental cycle

are selectively removed from the trap by lowering the RF knife, and consequently the truncation energy. By thermalization of the ensemble, a lower temperature is achieved. This scheme is comparatively simple and fast. In a triple mixture of our species, RF evaporation would lead to strong losses of ${}^6\text{Li}$ at a lower energy. In order to selectively remove only ${}^{87}\text{Rb}$ by evaporation and to sympathetically cool the fermionic species ${}^6\text{Li}$ and ${}^{40}\text{K}$ with ${}^{87}\text{Rb}$, we apply evaporation with microwave frequencies (MW). This ensures that the relevant frequencies do neither influence ${}^{40}\text{K}$ nor ${}^6\text{Li}$ significantly, as the transition frequency (hyperfine splitting) for ${}^{87}\text{Rb}$ is ≈ 6.8 GHz, whereas for ${}^6\text{Li}$ the respective frequency is 228 MHz and for ${}^{40}\text{K}$ 1.3 GHz.

3.3 Benchmark tests of an experimental cycle

Parameter drifts or failures of devices result in vanishing or reduced atom numbers in the produced samples. In this case we identify deviations from optimal operation parameters by using a set of benchmark measurements. Some reference values are presented in Tab. 3.1. The atom number N and temperature T of ${}^{87}\text{Rb}$, which are extracted by a

Stage	TOF (ms)	$\delta\nu_{\text{det}}$ (MHz)	M	CG	N	T (μK)
after MOT loading ①	5	18	0.653	0.467	4.5×10^9	n/a
MOT with cMOT ramp ②	5	18	0.653	0.467	1.3×10^9	n/a
MOT with dMOT ②	5	18	0.653	0.467	1.6×10^9	n/a
MOT after mol. (25+1.7 ms) ③	5	18	0.653	0.467	2.1×10^9	54(10)
MOT SQMT (hold 1000 ms)	4	9	0.653	0.467	3.2×10^8	n/a
UHV SQMT (not compr.) ④	4	18	0.77	1	n/a	280(40)
UHV SQMT (compressed) ④	4	18	0.77	1	n/a	400(60)
UHV QUIC (no evaporation)	4	18	0.77	1	n/a	430(60)

Table 3.1: Typical parameters at different stages of the experimental cycle for ${}^{87}\text{Rb}$. TOF denotes the time-of-flight for imaging, $\delta\nu_{\text{det}}$ the imaging detuning from resonance, M is the camera magnification, CG the used Clebsch-Gordan coefficient in the fit routine, N the particle number, and T the temperature of the ${}^{87}\text{Rb}$ cloud. All data refer to measurements where only ${}^{87}\text{Rb}$ is loaded into the MOT, and the uncertainty in the particle number determination is assumed to be 50%. Systematic deviation, limiting the accuracy of these measurements, are not studied.

Gaussian fit to the cloud, are given for the stages directly after the MOT loading, after cMOT ramp, after dMOT phase, after the molasses phase, before the transfer in the MOT SQMT, after the transfer in the UHV chamber in the uncompressed SQMT, after compression in the SQMT, and in the QUIC trap without evaporation. The imaging light for the stages where ${}^{87}\text{Rb}$ is not spin-polarized and not optically pumped we use all available frequencies, i.e. imaging, optical pumping (OP), and OP repumping light

3. Experimental apparatus

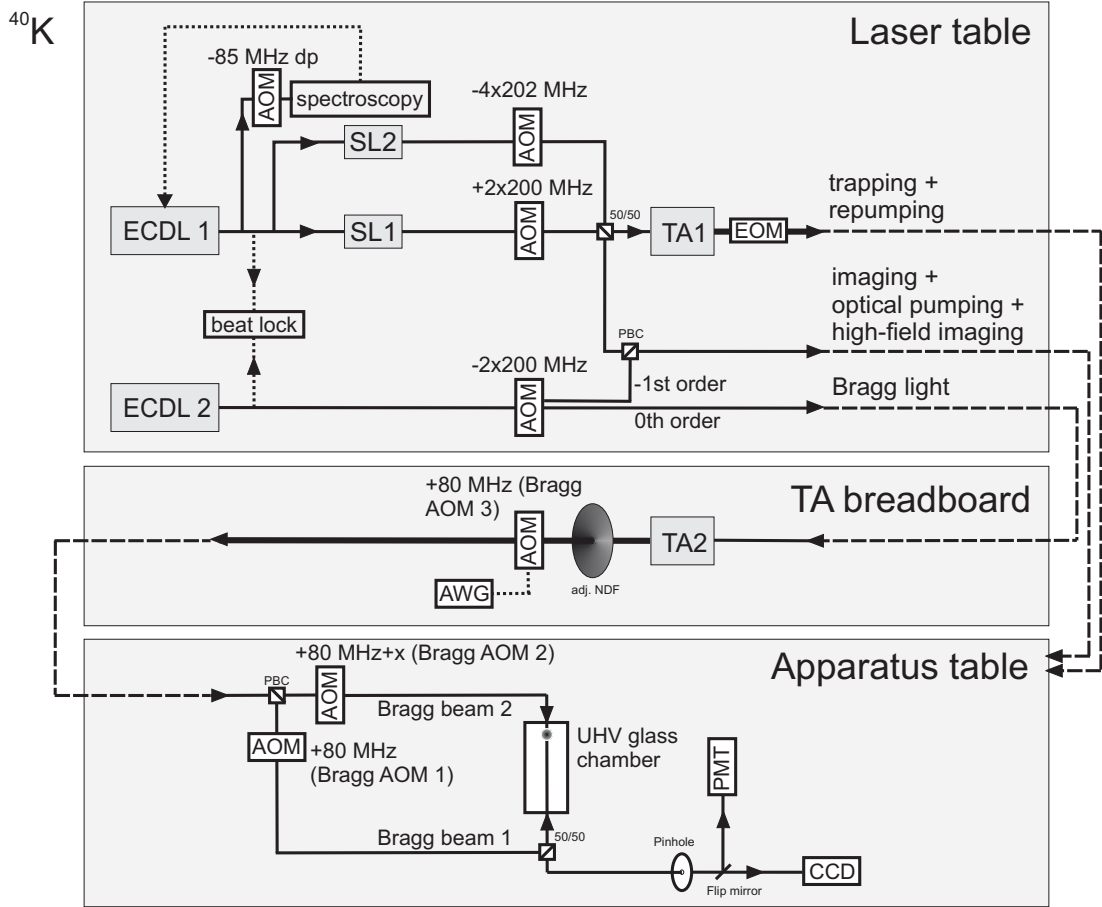


Figure 3.2: The laser beam setup for laser cooling, imaging, and fermion scattering from a light grating is presented for the atomic species ^{40}K . The dashed laser lines denote glass fiber connections between the different optical tables.

(cf. Fig. A.1). After the stage where the ^{87}Rb cloud is polarized, only the transition $F = 2 \rightarrow F' = 3$ is used for imaging. The clouds in the MOT chamber are imaged with a CCD camera (Apogee AP1E), whereas the clouds in the UHV chamber with an Andor iKon-M DU934N-BRD CCD camera, CCD1 in Fig. 3.3. The determined values for N and T are supposed to represent reproducible reference values for future measurements and benchmark tests on the setup.

3.4 Potassium laser system

For laser trapping each of the species requires near-resonant light with a specific wavelength and narrow spectral linewidth. In App. A, the level scheme for each atomic species is described which is elementary for understanding laser cooling. On total, the laser system consists of fourteen semiconductor laser diodes, three tapered amplifier sys-

3.4 Potassium laser system

tems, one fiber laser (optical dipole trap), and eight laser locks. Mainly alterations in the laser system of ^{40}K are made in comparison to previous descriptions (Henkel, 2005; Taglieber, 2008), which enabled an improved laser operation stability, high-field detection, and diffraction experiments with ^{40}K . Therefore in the following, only the laser system of ^{40}K is introduced.

3.4.1 Overview

The ^{40}K laser system is composed of two external cavity laser diodes (ECDL), two slave lasers (SL), and two tapered amplifier systems (TA). An overview of the laser setup is presented in Fig. 3.2. ECDL1 is frequency stabilized by a frequency modulation lock on the crossover signal between $|4S_{1/2}, F = 1\rangle \rightarrow |4P_{3/2}, F' = 0, 1, 2\rangle$. In order to increase magnitude and stability of the error signal, the spectroscopy cell is heated and temperature stabilized to 45.0°C . Laser light from ECDL1 seeds two slave lasers SL1 and SL2. Light from SL1 is frequency shifted by a double-pass acousto-optic modulator (AOM) configuration and serves as the trapping light for the MOT. The frequency of the light from SL2 is controlled by a four-pass AOM configuration and corresponds to the transition for repumping light of the MOT. Both the light from SL1 and SL2 are superimposed on a non-polarizing beamsplitter cube (50/50) and seeded into a TA chip (Eagleyard, EYP-TPA-0765-01500-3006-CMT03), where the two frequencies are simultaneously amplified. Typical power for trapping light is 350 mW and for repumping light up to 170 mW.

ECDL2 is used in a versatile manner. One application is the detection of ^{40}K atoms at high magnetic field strengths (cf. Sec. 3.7) and the other one is the generation of a light field for diffraction of ^{40}K atoms (cf. Ch. 4). Both operations require large frequency detunings from the atomic resonance. On the one hand, the Zeeman effect at high magnetic field strengths displaces the atomic energy states with respect to the zero field case, and the transition frequency needs to be adjusted. On the other hand, for diffraction experiments heating of atoms is considerably avoided by detuning from the atomic resonance. For these purposes, ECDL2 is stabilized to ECDL1 through an offset lock. The local oscillator signal for the offset lock is supplied by a computer controlled signal generator (Rohde & Schwarz SML02), and the bandwidth is limited by the photodetector to 1.27 GHz. Either application of ECDL2 is controlled by the light diffraction on an AOM, see Fig. 3.2. The beam of ECDL2 is frequency shifted by an AOM in double pass configuration. The Bragg diffracted beam is superimposed on a polarizing beamsplitter cube (PBC) with the usual imaging beams of ^{40}K , cf. Fig. 3.2, and is used as imaging light at high magnetic field strengths. The light propagates along the same beam path line on the apparatus table as the light used for conventional imaging.

3.4.2 Bragg beam setup

In the following, the setup for the laser beams required for experiments involving Bragg diffraction of ^{40}K atoms is described in detail, see lower part of Fig. 3.2. This extension of the beam lines were mainly carried out during the course of the work of (Mang, 2009).

For Bragg diffraction of ^{40}K , the related beams propagate a different beam path line as compared to the situation, where the light of ECDL2 is used for high field imaging. The beam of ECDL2 in this case is not Bragg diffracted in the above mentioned AOM (RF input of AOM is off) and the zeroth order is coupled into a glass fiber for spatial mode cleaning. After coupling out from the glass fiber, the light seeds a TA chip (m2k Laser, TA770), which is situated on a separate optical breadboard (TA breadboard). The power of the seeding beam is about 10 mW and is amplified in the TA chip to 110 mW. The beam waist is adjusted, and frequency shifted by a single pass through a 80 MHz AOM. This AOM is controlled by the frequency output of a direct-digital-synthesis (DDS)-board. An arbitrary waveform (AWG) can be supplied to the control input of a voltage variable attenuator (VVA). This allows to form e.g. Gaussian light pulses in time domain which are advantageous for Bragg scattering of atoms (cf. Sec. 4.2.2). The beam can be attenuated by an adjustable neutral density filter wheel (adj. NDF). Afterwards, the light is coupled into a second glass fiber. The beam is coupled out on the apparatus table of the experiment. Here the beam is separated into two components by means of polarization optics. Each part is frequency shifted by an individual AOM with a frequency of +80 MHz. The beams are then directed into the glass chamber in a counter-propagating configuration and superimposed in order to form a standing optical wave for diffraction of atoms. By tuning the relative frequency of the two individual AOMs, a lattice potential with net momentum is created at the position of the atoms. By monitoring the Bragg diffracted ^{40}K atoms, the recoil frequency of the atoms can be determined. For the purpose of detecting a matter wave of ^{40}K atoms (see Ch. 4), light is backscattered from the atoms and is supposed of being detected by a sensitive photomultiplier tube (PMT). The pinhole in front of the PMT only collects light which originates from the atom cloud position in the glass cell, and is adjusted with a CCD camera, labelled as CCD2 in Fig. 3.3 (Apogee AP1E). The beams are blue-detuned by 1.43 GHz in comparison to the MOT transition of ^{40}K . This suppresses spontaneous photon scattering, and therefore losses and heating of the atoms.

3.5 Optical dipole trap

For the investigation of interspecies Feshbach resonances the mixture is loaded into a far-off resonant optical dipole trap (ODT). As the trapping frequencies are independent on the spin, any spin state can be confined optically. This is advantageous for the study of interspecies interactions. Also for the measurements on cross-dimensional relaxation (cf. Ch. 6), cloud aspect ratios are changed by varying the optical power of the ODT in order to induce large energy anisotropies in the clouds. Especially an ODT allows a versatile application of trap configurations with different trapping frequencies. For a review article on optical traps, see (Grimm *et al.*, 2000).

3.5.1 Principle

The interaction of an atom with a classical electric field is described in many textbooks (e.g. Milonni and Eberly, 1988). The laser field $\mathbf{E} = \mathbf{E}_0 \cos(\omega_0 t)$ induces a dipole moment,

3.5 Optical dipole trap

which oscillates with the same driving frequency ω_0 as the electric field. The interaction of the induced dipole moment with the external laser field \mathbf{E} causes a dipole potential, which is proportional to the laser intensity $I(\mathbf{r})$ and depends on the frequency $\omega_0 = 2\pi c/\lambda$ of the laser field, the frequency of the atomic resonance ω , and the spontaneous decay rate Γ of the excited state. In the limit of large detunings and negligible saturation, the dipole potential $U_{\text{dip}}(\mathbf{r})$ and the scattering rate $\Gamma_{\text{sc}}(\mathbf{r})$ can be written as

$$U_{\text{dip}}(\mathbf{r}) = -\frac{3\pi c^2}{2\omega_0^3} \left(\frac{\Gamma}{\omega_0 - \omega} + \frac{\Gamma}{\omega_0 + \omega} \right) I(\mathbf{r}) \quad (3.1)$$

$$\Gamma_{\text{sc}}(\mathbf{r}) = \frac{3\pi c^2}{2\hbar\omega_0^3} \left(\frac{\omega}{\omega_0} \right)^3 \left(\frac{\Gamma}{\omega_0 - \omega} + \frac{\Gamma}{\omega_0 + \omega} \right)^2 I(\mathbf{r}). \quad (3.2)$$

Depending on the sign of the detuning $\delta = \omega - \omega_0$, the resulting potential is either attractive ($\delta < 0$) or repulsive ($\delta > 0$). In the case of $\delta < 0$ ($\delta > 0$), the potential minima are found at positions with maximum (minimum) intensity. Large detunings are favorable for the ODT as the scattering rate is inverse proportional to the square of the detuning, and heating of the atoms is reduced.

In the experiments, a crossed beam ODT is used, where two beams intersect perpendicularly in the center of the magnetic trap. The intensity is given by $I(\mathbf{r}) = I_1^k(\mathbf{r}) + I_2^l(\mathbf{r})$, where $k \neq l = x, y, z$ denotes the propagation directions of the beams. For each spatial direction there is an ODT beam available (cf. Fig. 3.3). This allows a very versatile trap configuration for the experiments. Within the harmonic approximation

$$U_{\text{dip}}(\mathbf{r}) \stackrel{!}{=} U_{\text{harm}}(\mathbf{r}) = \frac{m}{2} \cdot (\omega_x^2 x^2 + \omega_y^2 y^2 + \omega_z^2 z^2) \quad (3.3)$$

and assuming red-detuned Gaussian laser beams

$$|E(\mathbf{r})|^2 \propto I(\mathbf{r}) = \frac{2P}{\pi w_{0x}^2 w_{0y}^2 (1 + z^2/z_r^2)} \exp\left(-\frac{2}{1 + z^2/z_r^2} \left(\frac{x^2}{w_{0x}^2} + \frac{y^2}{w_{0y}^2} \right)\right) \quad (3.4)$$

$$\approx \frac{2P}{\pi w_{0x}^2 w_{0y}^2} \left(-\frac{z^2}{z_r^2} - \frac{2x^2}{w_{0x}^2} - \frac{2y^2}{w_{0y}^2} \right), \quad (3.5)$$

the atoms can be confined in the ODT center ($\mathbf{r} = 0$). Here w_{0j} denotes the minimum $1/e^2$ beam waist along the direction j , $P = \int I(\mathbf{r}) dx dy$ is the total power, and $z_r = w_{0x} w_{0y} \pi / \lambda$ is the Rayleigh range. In a classical view, the resulting trapping frequencies ω_j are the oscillation rates of the atom in the trap and can be calculated by performing a Taylor expansion of the Gaussian beam profile around the trap center to second order, cf. Eq. (3.5). Possible interference of the superimposed beams is suppressed by imposing a frequency difference between the two beams with AOMs such that the interference modulation is much faster than usual trap oscillation periods.

3. Experimental apparatus

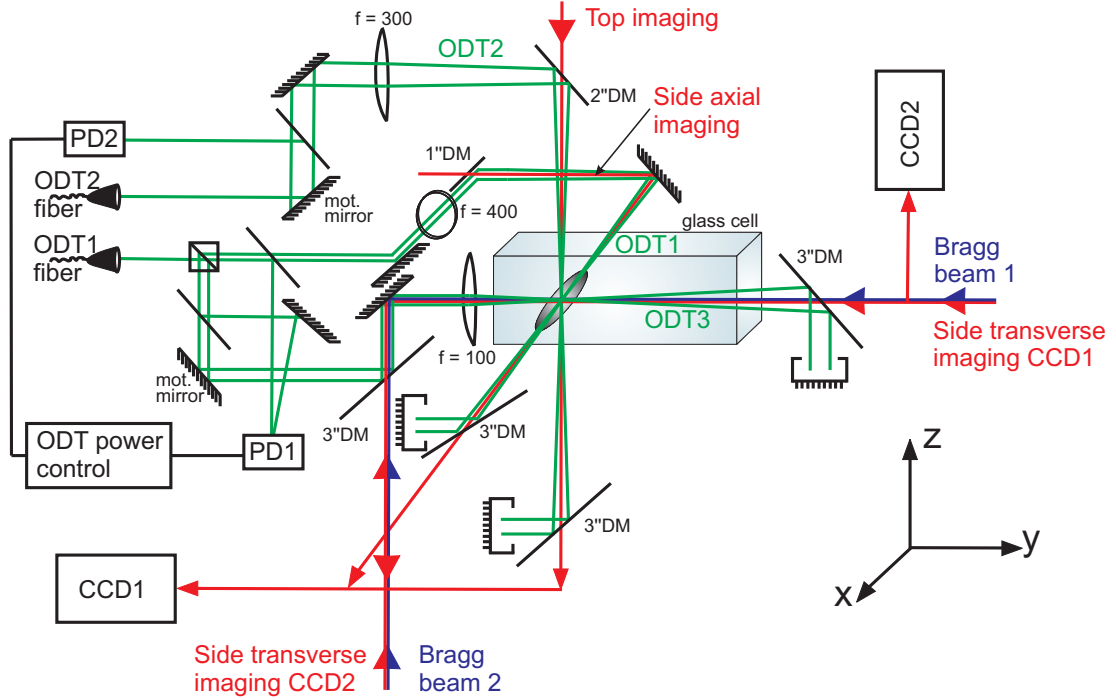


Figure 3.3: Laser beam setup in the vicinity of the glass cell. Optical dipole trap beams (ODT, in green), imaging beams (red), and Bragg beams (blue) are presented. The focal length of the trap lenses are given in mm. Imaging beams and ODT beams are overlapped with dichroic mirrors (DM) with different diameters in inch. The ODT beams are aligned with the help of motorized (mot.) mirror mounts. The ODT power is measured with photodiodes (PD) and stabilized with a feedback circuit. The ODT beams are blocked with beam dumps. The possibility of imaging from four individual directions is realized and the absorption imaging pattern of the cloud is detected with CCD cameras. The CCD cameras also allow to accurately align the Bragg beams.

3.5.2 Technical realization

A detailed description of the ODT setup is presented in (Wieser, 2006). In this chapter, we describe important issues and extensions, which are relevant during the course of this work.

The ODT is realized by two perpendicular laser beams with the two foci coinciding at the center of the magnetic trap. The first beam points along the horizontal, x direction in Fig. 3.3, whereas the second beam propagates along the vertical axis, which is denoted as z direction. This vertical-horizontal configuration is advantageous as the vertical beam (ODT2) has a minor influence on the trapping frequency along z (vertical direction). Therefore, lowering the power of the horizontal beam allows to decrease the trapping depth along z . This leads to a favorable rate of evaporative cooling since higher atomic densities can be achieved in a horizontal-vertical configuration as compared to

3.5 Optical dipole trap

a horizontal-horizontal configuration. In the setup there is the possibility to use two different horizontal beams, either along x or y (ODT1 or ODT3), see Fig. 3.3.

The laser source for the ODT is a single-mode, single-frequency ytterbium fiber laser (IPG photonics YLR-20-LP-SF) with a maximum output power of 20 W and a laser wavelength of 1064 nm. The output beam is split into two independent paths. A frequency difference of on total 220 MHz is imposed between the two beams by shifting the frequencies with independent AOMs. The two beams are coupled into optical fibers for cleaning of the spatial profile and to obtain pointing stability of the beams forming the trap. After out-coupling from the fiber, the waists, polarizations, and powers of the beams are adjusted. The powers of the beams are controlled by PI (Proportional-Integrator)-feedback loops. Part of the beam is detected with a photodiode (PD), whose output signal is compared and stabilized with a set-point electronically, and the error signal is used as a control signal for a voltage controlled oscillator (VCO) used in the AOM controller box. It is possible to run arbitrary waveforms for the power level. The details of the electronic circuit are explained in (Wieser, 2006).

For the purpose of future lattice experiments, a new electronic design for the power stabilization feedback control has been designed, but not implemented at the moment due to relocation of the entire laboratory. Fast feedback is required for lattice experiments, since small power fluctuations would destruct the potential wells of the lattice and heat the atoms. The central component of the new circuit is a fast gain controlled RF amplifier (60 dB gain voltage range) and its output is amplified and fed into the AOMs directly. In this way, the present VCO in the AOM controller box used so far would be avoided, which limits the bandwidth at the moment. Also, the influence of high power RF and MW signals, which are present during the experimental sequence, is reduced and the noise performance of the electronic circuit is improved due to the surface-mount design.

For stability reasons all optical components for the ODT are installed on a common optical breadboard, which is mounted vertically on the apparatus table. The beam height on the breadboard of only 54 mm, offers a small lever arm of mounted optical components and mechanical vibrations are therefore reduced. The interference between a beam propagating in forward direction and a retroreflected component allows to analyze the mechanical stability of the entire ODT setup with the help of a Michelson interferometer. The noise arising from mechanical vibrations is better than $\lambda/20$. This offers good starting conditions for future lattice experiments.

The ODT beams are superimposed with the imaging beams by dichroic mirrors (DM). The separation of imaging and ODT beams after propagation through the glass cell is realized again with dichroic mirrors with a three inch diameter. A large diameter of these components close to the glass cell offers a high numerical aperture necessary for high-resolution absorption imaging.

3.5.3 Alignment of beams

One of the concerns is to adiabatically transfer from the magnetic trap into the ODT without heating the atoms. Misalignment of the ODT beams is critical to heating. We follow the strategy to align the beams in such a way that the center of the cloud in the

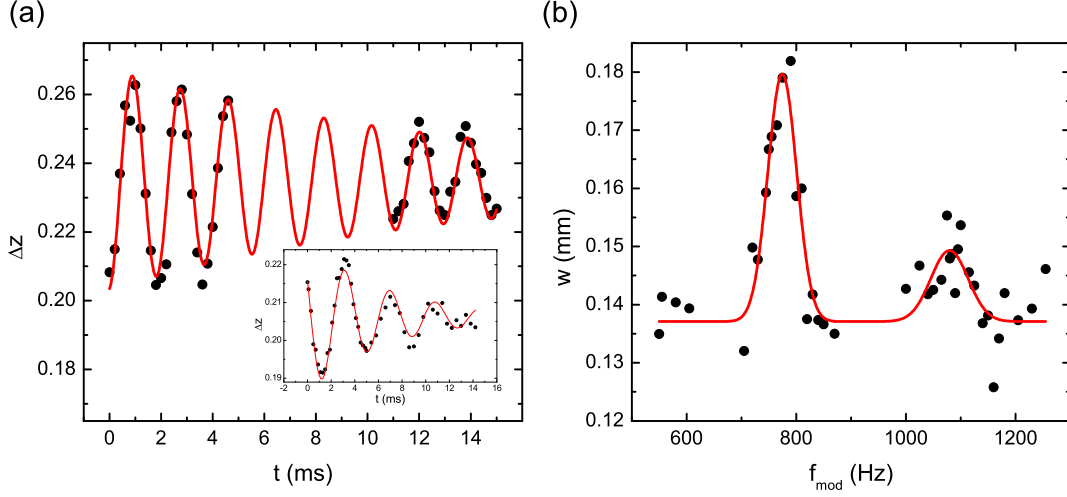


Figure 3.4: Determination of trapping frequencies. Fig. (a) shows two examples for a damped dipole oscillation of a ^{40}K cloud, which is excited by a Stern-Gerlach force in the trap. The power of the optical dipole trap for the measurement (inset) is $P_{\text{ODT1}} = 1.41$ W and $P_{\text{ODT2}} = 0.93$ W ($P_{\text{ODT1}} = 0.38$ W and $P_{\text{ODT2}} = 1.02$ W). Fig. (b) shows an example where a trapped ^{87}Rb cloud is parametrically heated when the power is modulated with twice the trapping frequency. Two maxima of the cloud waists are detected corresponding to two trapping frequencies along different directions.

magnetic trap coincides with the center of the transferred cloud in a single ODT beam. If no displacement of the cloud occurs during the transfer, undesirable heating is minimized. The vertical and horizontal ODT beams are subsequently aligned by comparing the positions of the intratrap clouds. The position of the cloud in the single beam ODT is shifted by means of motorized (mot.) mirror mounts (Newfocus, Model 8807). In the case of the vertical beam alignment, the intratrap cloud position is determined in a hybrid magnetic and optical trap (only ODT2). The purpose of the magnetic trap is to compensate the influence of gravitation on the cloud.

3.5.4 Characterization of trap

For a precise knowledge of the atom densities in the ODT, the beam waists, power, and trapping frequencies are determined. The waists are obtained by imaging the ODT beam directly with the CCD camera. At the position of the atoms in the glass cell, the ODT beams are focused to $1/e^2$ waists of $w_{\text{ODT1}} = 55 \mu\text{m}$, $w_{\text{ODT2}} = 49 \mu\text{m}$, and $w_{\text{ODT3}} = 43 \mu\text{m}$. The power of the beam at the position of the atoms in the glass cell is estimated by measuring the power directly before and after the glass cell with a power meter. For the determination of the trapping frequencies we follow different strategies. The first method is to apply a pulsed magnetic field gradient to the trapped atoms and thus displace them from the trap center. The trap frequencies are then

3.6 Feshbach magnetic fields

obtained by observing the spatial oscillations. This method is preferentially applied for the determination of the trapping frequency along the vertical (z -) direction and the oscillation in z -direction is damped according to

$$\Delta z(t) = A \cdot e^{-\gamma t} \cdot \cos(\omega_z t + \phi) + \text{const.} \quad (3.6)$$

In order to avoid that the excitation displaces the cloud too far such that the harmonic approximation would then be invalid (cf. Eq. (3.3)), the duration and amplitude of the magnetic field gradient is carefully chosen. In Fig. 3.4 (a), two examples for a damped dipole oscillation of ^{40}K are shown. The inset of Fig. 3.4 (a) shows an example with lower ODT power. For the data (inset) the trapping frequency $\nu_z = \omega_z/(2\pi) = 539(2)$ Hz ($\nu_z = 261(3)$ Hz) is obtained from a fit. Another method for measuring the trapping frequency is to parametrically heat the atoms by modulating the power of the beams, see Fig. 3.4 (b). The resonances occur at twice the trapping frequencies. Two resonances are found from the data where a thermal ^{87}Rb cloud is parametrically heated, and the corresponding trapping frequencies are $\nu_y = 541(5)$ Hz and $\nu_z = 387(2)$ Hz. In order to obtain accurately and consistently the information about the trap potential, various trapping frequencies are determined with both methods, different power levels of the ODT, and different atomic species.

3.6 Feshbach magnetic fields

A major part of this work is the investigation of interspecies Feshbach resonances in a mixture of ^6Li and ^{40}K . Those resonances are narrow and closed-channel dominated (Wille *et al.*, 2008), cf. Tab. 2.1, and therefore a precise magnetic field control is a prerequisite for the experimental studies. In the following, the setup for the Feshbach magnetic field is introduced.

3.6.1 Feshbach coils and current control

The setup for the Feshbach magnetic field is also described in detail in (Voigt, 2009). An image of the magnetic field coils and glass chamber is shown in Fig. 3.5. The Feshbach coils are designed for satisfying mechanical stability and for allowing fast field modulation. A low inductivity allows a fast modulation of the field strengths. The coils are made of a hollow copper wire with the outer dimensions of $4 \times 4 \text{ mm}^2$ and an inner diameter of 2.5 mm (Wolverine Tube Europe BV). For cooling purposes of the coils, water flows through the wire. The electrical insulation of the wire is a fiberglass covering (S & W Wire Co.). The magnetic field strength scales with current as 1.9 G/A. The coils support a maximum current of 1000 A corresponding to a maximum field of about 1800 G.

The magnetic field generated in the Feshbach coils is sensed by a current transducer (Danfysik Ultrastab 867-1000I HF). The output current of this transducer is converted to a voltage by shunt resistors and is compared to a voltage set-point from the computer control. The set-point is controlled by a high-resolution 18 bit digital-to-analog converter (DAC) (Analog Devices, AD760). The error signal between set-point and the current

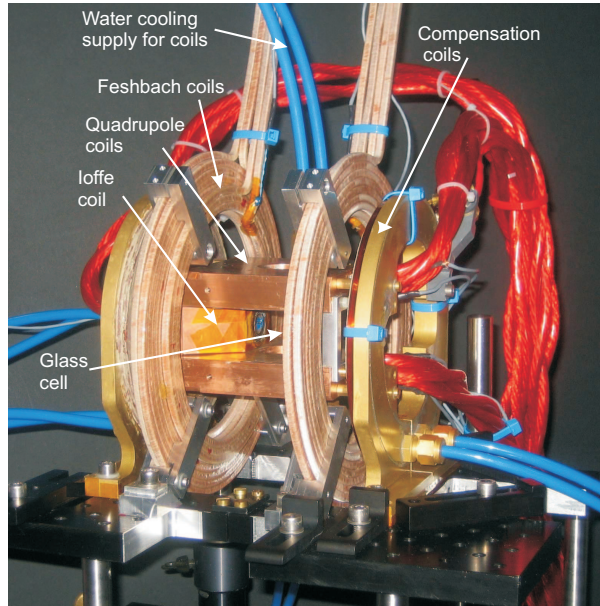


Figure 3.5: Magnetic field coils and glass chamber. Water supply tubes (blue) are connected to the coils for cooling purposes. The quadrupole-Ioffe-configuration (QUIC) trap is generated by a pair of quadrupole coils in anti-Helmholtz configuration and an Ioffe coil that produces a magnetic curvature and a finite magnetic field offset. The Feshbach coils are placed close to the glass cell.

transducer voltage drop on the shunt resistors is fed back as a control voltage to a MOSFET (IXYS, IXFN 230N10), and hence is located in the branch of a current by-pass. The MOSFET controls in a fast way the current flow through the Feshbach coils. The average value of the by-pass current is stabilized at 10 A by a PI control. The current is converted to a voltage by a $20\text{ m}\Omega$ shunt resistor and compared with a set-voltage for the high current power supply. This PI feedback acts slowly on the power supply and therefore on the current flow through the Feshbach coils. The two-fold feedback loops allow to minimize the power dissipation of the power supply without changing the control parameters.

The whole electronic circuit is temperature stabilized to better than $0.1\text{ }^\circ\text{C}$. A typical waveform of the Feshbach magnetic field strength (purple) is displayed in Fig. 3.6 with the corresponding MOSFET control voltage (green) and the $20\text{ m}\Omega$ shunt resistor voltage drop (yellow). The current flow through the Feshbach coils is measured with a high-bandwidth current clamp. One can see how the current in the by-pass drops as the current flow through the Feshbach coils is increased. The drop in the current by-pass is compensated then by the slow feedback on the power supply. Oscillations of the slow regulation (yellow) are damped and stabilized by the fast feedback in the by-pass. At the end of the waveform the current through the Feshbach coils is switched off by insulated-gate bipolar transistors (IGBT) (Semikron, SKM 800GA 126D). Two IGBT are located

3.6 Feshbach magnetic fields

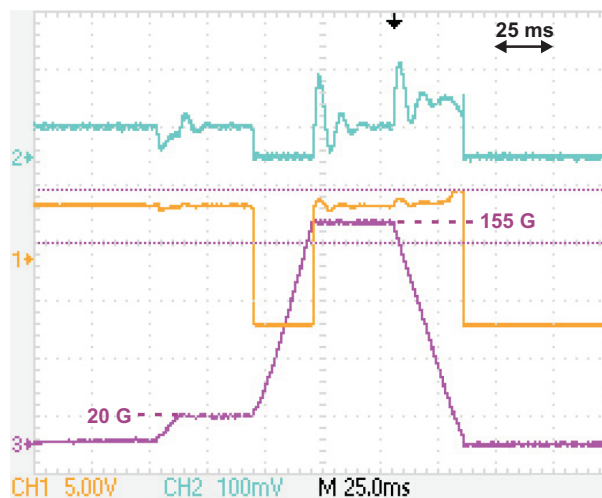


Figure 3.6: Current and voltage control are presented for an exemplary waveform of the Feshbach magnetic field strength (in purple), which is measured with a current clamp. As a reference, two approximative magnetic field values for the two plateaus are given in Gauss. In green the gate voltage of the MOSFET located in the current by-pass branch is illustrated, and in yellow the voltage drop on the $20\text{ m}\Omega$ shunt resistor is displayed.

in the circuit in parallel and switch off both the current flow through the Feshbach coils and the by-pass (IGBT all). Those IGBT together with additional high current relays separate the circuit from auxiliary fields from the QUIC trap loading procedure. Another two IGBT are in series with the Feshbach coils (IGBT coil) and affect only these coils.

3.6.2 Stability and ambient magnetic fields

The stability of the Feshbach magnetic fields and the negligible influence of ambient magnetic fields are a prerequisite for efficient molecule production at Feshbach resonances. In the case of the ${}^6\text{Li}$ - ${}^{40}\text{K}$ mixture, the Feshbach resonances are narrow and special attention needs to be addressed to this aspect. Also, unstable fields and high frequency fluctuations would broaden signals obtained from magnetic field dependent measurements. Therefore the stabilized fields and possible ambient fields are tested in various ways.

Ambient fields cause usually slow fluctuations on the order of $\leq 50\text{ Hz}$. Especially electronic devices influence the magnetic fields in the laboratory in the 50 Hz regime, which can be resolved by a three-axis magneto-resistive sensor (Honeywell, HMC 1053). When all power supplies close to the UHV chamber are switched on, the 50 Hz noise gives a peak-to-peak value of 3.3 mG , whereas for the case when the devices are turned off the noise in this band yields a peak-to-peak signal of 2.2 mG . To minimize this influence from electronic devices, the experimental cycle can be synchronized to the phase of the ambient 50 Hz signal.

Other slow fluctuations arise from the nearby passing subway with a time-scale of 20 s and amplitude of $\pm 10\text{ mG}$. Since this noise source is believed to have the largest contri-

bution, an active feedback stabilization is designed for this purpose, but not implemented at the moment.

Fast fluctuations can potentially only arise from the Feshbach current stabilization circuit itself. With a current clamp noise can be measured up to kHz frequencies. Higher frequencies are challenging to measure. We use a second current transducer (Danfysik Ultrastab 867-200I) with a specified bandwidth of up to 100 kHz in series to the Feshbach coils. The output current is converted to a voltage with a shunt resistor and monitored with a true rms multimeter (Keithley, model 2700). The analysis shows that the high frequency components of magnetic field noise are not significant.

By constantly performing measurements at some hundreds of Gauss, the environment around the glass chamber and Feshbach coils is magnetized and evolves to a steady-state and the reproducibility is therefore increased. Repeatedly performed magnetic field calibrations, as described in the following section, show that an overall magnetic field uncertainty of only 7 mG over several months can be deduced arising mainly from long-term drifts. The calibrations refer to measurements during the night, when no subways operate.

3.6.3 Magnetic field calibration

For calibration of the Feshbach magnetic field we drive a radiofrequency (RF) transition between different Zeeman states within the same hyperfine manifold. The magnetic field strength can be inferred from the magnetic field dependence of the transition frequency as described by the Breit-Rabi formula (Breit and Rabi, 1931; Eisinger *et al.*, 1952).

The calibration is performed by means of Zeeman transitions in fermionic ^{40}K , cf. App. D.1. Using fermionic atoms is beneficial, since the clock shift is absent for transitions at ultracold temperatures due to Pauli exclusion principle (Gupta *et al.*, 2003). Some preliminary measurements are done at a slightly broader Feshbach resonance at 115 G (Tiecke *et al.*, 2010a). This resonance involves the Zeeman states $|F = 9/2, m_F = 9/2\rangle$ of ^{40}K and $|1/2, 1/2\rangle$ of ^6Li which offer strong optical transition strengths for imaging at high magnetic field since both states are maximally stretched Zeeman states (Tiecke *et al.*, 2010a). For calibration, we use the Zeeman transition $|9/2, 9/2\rangle$ to $|9/2, 7/2\rangle$. The magnetic field sensitivity of this transition is 311 kHz/G at 0 G and 501 kHz/G at 115 G. Fig. 3.7 (a) presents a typical magnetic field calibration at 114.298 G. The RF pulse duration of 280 μs is optimized to satisfy a π -pulse condition.

Most measurements within this thesis are done at the Feshbach resonance close to 155 G between the Zeeman states $|9/2, -5/2\rangle$ of ^{40}K and $|1/2, 1/2\rangle$ of ^6Li . As calibration transition, we use $^{40}\text{K}|9/2, -9/2\rangle$ to $|9/2, -7/2\rangle$, which offers a magnetic field sensitivity of 181 kHz/G at 155 G. For the present π -pulse transition the duration is optimized to be 360 μs . In Fig. 3.7 (b), a sequence of magnetic field calibrations is shown for three different set points. For the calibration, the atoms in the initial Zeeman state $|9/2, -9/2\rangle$ and the transferred atoms in the state $|9/2, -7/2\rangle$ are imaged within one experimental sequence at high magnetic field. For the individual scans at different magnetic field strengths, the fit uncertainty of the obtained RF spectra is typically only ± 0.3 mG and the full width at half maximum is 8.8 mG. Since the full width at half maximum of the

3.7 Detection of atoms at high magnetic field

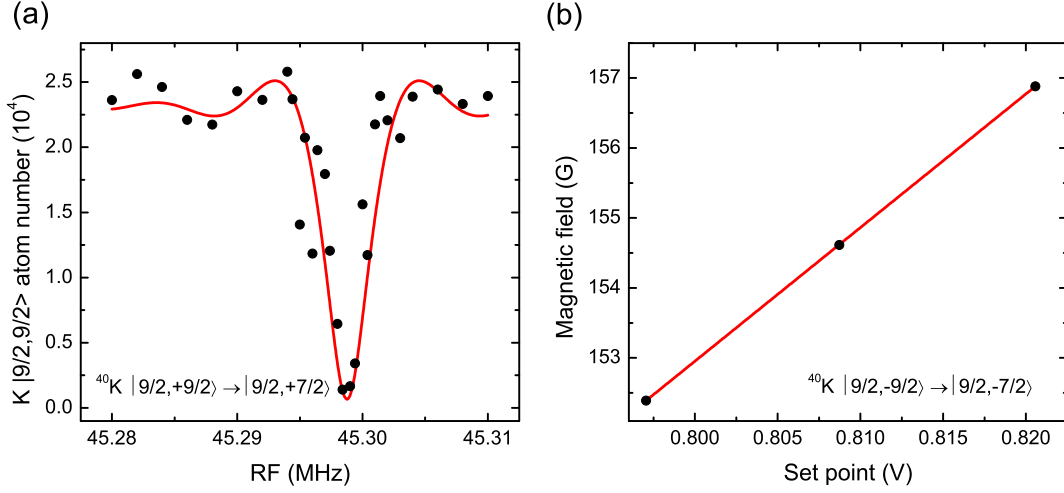


Figure 3.7: Magnetic field calibrations using radiofrequency induced energy transitions between different Zeeman states of ^{40}K at high magnetic field strengths. Fig. (a) shows the atomic number of the initial Zeeman state $^{40}\text{K} |F = 9/2, m_F = 9/2\rangle$ close to a magnetic field strength of 114 G. The atomic number decreases when the resonance condition for a transfer to $|F = 9/2, m_F = 7/2\rangle$ is satisfied. Fig. (b) presents the relation between the voltage set-point of the stabilization control and the magnetic field from a series of calibrations at different magnetic fields around 155 G.

spectrum shows consistency with the expectation from the Fourier width of the applied RF π -pulse, the calibration is not limited by magnetic field inhomogeneities or power broadening due to interaction of the atoms with the RF field. Repeatedly performed magnetic field calibrations result in an overall magnetic field uncertainty of only 7 mG, which are mainly due to long-term drifts. The magnetic field range in Fig. 3.7 (b) spans typical values occurring in the experiments. The magnetic field stabilization circuit exhibits an excellent linear behavior between set point and magnetic field strength.

3.7 Detection of atoms at high magnetic field

3.7.1 Absorption imaging

As shown in Fig. 3.3, there is the possibility to image the atomic clouds from four different directions. For avoiding stray light from the powerful ODT beam on the CCD camera, the imaging direction for experiments with the ODT is chosen to be y (side transverse imaging CCD1), since along this axis no infrared ODT beam propagates in direction to the CCD camera, which would otherwise lead to a worse imaging quality. We usually employ the ODT configuration composed of the ODT1 and ODT2 laser beams. But this choice has a drawback. Since the Feshbach field is oriented along x , and therefore it is not parallel to the propagation direction of the imaging beam, an effective transition strength

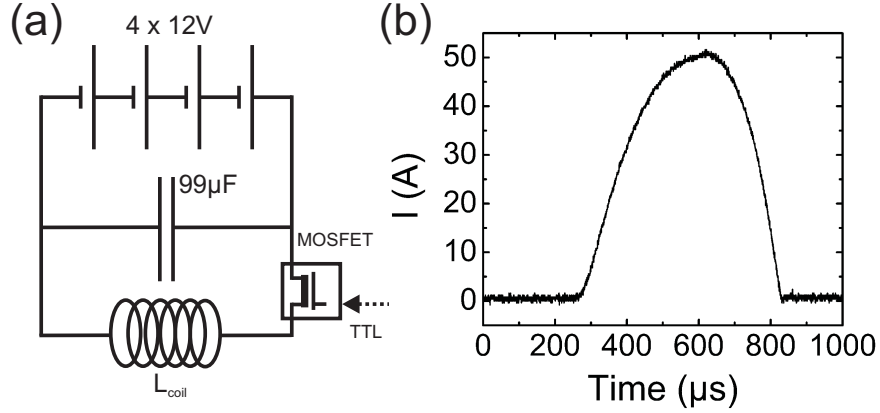


Figure 3.8: Stern-Gerlach setup. In (a) the electronic circuit for the application of short magnetic field gradient pulses is presented. Amplitude and duration of the pulse is adjusted by the number of batteries connected and the switching time of the MOSFET, respectively. As an example in (b), a magnetic field gradient pulse is shown with a duration of $570 \mu\text{s}$, which is measured with a current clamp.

needs to be taken into consideration. The polarization of the imaging light is linearly polarized along the z direction. Linear polarized light can be expressed by a summation of a right- and left-handed circular wave with equal amplitudes. Effectively, the optical power of the light field that drives the transition is reduced by a factor of four with this choice. From the discussion presented in App. D we calculate the relative transition strength. We apply high-field imaging for the detection of ^{40}K atoms in the Zeeman state $|F = 9/2, m_F = -5/2\rangle$ and of ^6Li atoms in the state $|F = 1/2, m_F = 1/2\rangle$ at 155 G. The optical transition strengths for various hyperfine states of ^{40}K and ^6Li in dependence of the magnetic field are shown in Fig. D.2. For the chosen imaging frequencies, only the optical σ^- -transitions $|m_J = -1/2, m_I = 1\rangle \rightarrow |m'_J = -3/2, m'_I = 1\rangle$ for ^6Li and $|m_J = -1/2, m_I = -2\rangle \rightarrow |m'_J = -3/2, m'_I = -2\rangle$ for ^{40}K are addressable at 155 G. The transition for ^6Li at 155 G is in good approximation a cycling transition. That means that, after photon absorption and during imaging, the excited atomic state is almost exclusively coupled to the original imaging state. Only about 4% of the atoms couple to a different state, and would be lost for further photon absorption. The situation for ^{40}K is slightly different since the imaging state is not the energetically lowest state at 155 G, the high-field limit at 155 G is not completely satisfied, and more loss channels are therefore available. About 11% of the atoms couple to different states. Experimentally the atomic number imaged at high magnetic field is a factor of 4(1) for ^{40}K and of 1.3(2) for ^6Li lower as compared to the atomic number imaged at low magnetic field. The given uncertainties rely on shot-to-shot particle number fluctuations. The strength of the above given transition for ^{40}K at 155 G is comparably strong, but the fact that the imaged atomic state does not cycle efficiently explains primarily the lower contrast of the absorption imaging signal as compared to ^6Li for same imaging polarization, see e.g. in Fig. 5.5 (a).

3.7 Detection of atoms at high magnetic field

3.7.2 Stern-Gerlach setup

As a last aspect, the setup is presented, which allows to generate strong magnetic field gradients. These are used e.g. to separate heteronuclear ${}^6\text{Li}$ - ${}^{40}\text{K}$ molecules from unbound atoms as presented in Sec. 5.3.3 or to check the state purity of atomic ensembles.

Strong gradients are created with the help of a powerful high voltage supply, see Fig. 3.8 (a). Four car batteries are connected in series which supply up to 48 V, thereby avoiding to introduce undesired ground connections to the setup. The amplitude of the Stern-Gerlach pulse can be adjusted by the number of batteries connected. The batteries charge a power capacitor with $99\ \mu\text{F}$. By switching a MOSFET the capacitor is rapidly discharged and a short current pulse through a coil occurs leading to a magnetic field gradient for the atoms. Different coils can be used such as the compensation coil or an asymmetric pair of the quadrupole coils depending on the application. In Fig. 3.8 (b) a typical magnetic field gradient pulse with approximately $570\ \mu\text{s}$ duration is presented. The pulse duration is usually adjusted with the switching time of the MOSFET.

Chapter 4

Diffraction of fermions from light gratings

In this chapter, experimental results on Bragg and Kapitza-Dirac scattering of a quantum-degenerate fermionic cloud of ^{40}K atoms are presented. After a brief introduction in Sec. 4.1.1, the two associated regimes for atom-light interaction are discussed in Sec. 4.1.2 and 4.1.3. The experimental characterization of the pulses and results are given in Sec. 4.2.2 and 4.2.3.

4.1 Diffraction of atoms from a standing wave

In the following, two formalisms for the description of atomic scattering from light gratings will be introduced. On the one hand, it can be useful to illustrate the occupied atomic momentum states in Bloch bands in reciprocal space (Bloch, 1928). On the other hand, the quantum-mechanical description of a two-level system interacting coherently with a light field (Shirley, 1965; Cohen-Tannoudji and Reynaud, 1977) allows to derive the temporal evolution of the occupation probability of the involved momentum states in the scattering process.

4.1.1 Atom-light interaction

The interaction of a two-level system with a light field can be described with an effective complex optical potential of the form (Dalibard and Cohen-Tannoudji, 1985; Oberthaler *et al.*, 1996)

$$V_{\text{opt}}(x, y) = \frac{\hbar \omega_R^2}{\delta + i\Gamma/2} \propto \frac{I(x, y)}{2\delta + i\Gamma}. \quad (4.1)$$

Within the electric dipole approximation, the single-photon Rabi frequency is defined as $\omega_R = \mu E_0/\hbar$, where E_0 is the amplitude of the electric field generated by the light and $\mu = \langle e|\mathbf{er}|g\rangle\hat{e}$ is the projection of the electric dipole matrix element connecting the ground $|g\rangle$ and excited state $|e\rangle$ along the polarization direction \hat{e} of the electric field. Γ is the atomic decay rate, and $I(x, y)$ is the light intensity. The imaginary part of the

4.1 Diffraction of atoms from a standing wave

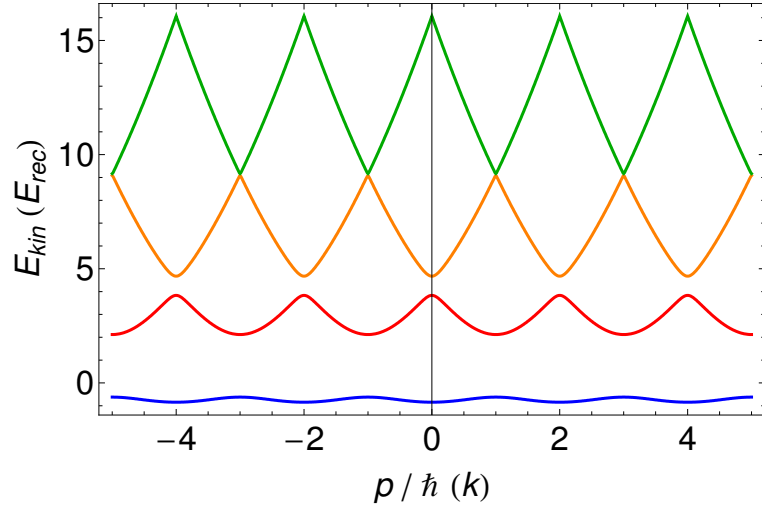


Figure 4.1: Dispersion of the atomic momentum states in the periodic potential of the light grating. The atomic parameters of ^{40}K are inserted and for the Bragg beams a waist of $w_0 = 1$ mm, a power of $P = 0.1$ mW, and a detuning from the atomic resonance of $\delta = 2\pi 1.43$ GHz is considered.

potential arises from spontaneous scattering processes, whereas the real part originates from the ac Stark shift, which is usually exploited to generate optical potentials for atoms (cf. Sec. 3.5.1). If the detuning δ of the light frequency from the atomic resonance is large ($\delta \gg \Gamma$), it is possible to generate a nearly real potential. The spatial shape of the potential is determined by the light intensity pattern $I(x, y)$. A periodic potential can be created by two interfering light beams with wavevectors \mathbf{k}_1 and \mathbf{k}_2 , which form an optical lattice with reciprocal lattice vector $\mathbf{G} = \mathbf{k}_1 - \mathbf{k}_2$.

The dispersion of the momentum states in the periodic potential of the light grating of the form

$$V(z) = V_0 \cos^2(G/2z) = \frac{V_0}{2} \cos(Gz) + \frac{V_0}{2} \quad (4.2)$$

can be derived by using Bloch's theorem (Bloch, 1928). This theorem states that the solutions for the atomic wave functions in the periodic potential can be expressed as a product of a plain wave e^{ikz} and a function with translational symmetry $u_{n,k}(z + d) = u_{n,k}(z)$. The lattice constant $d = \lambda/2$ is related to the wavelength of the light and the reciprocal lattice vector is $G = 2\pi/d = 2k$. In Fig. 4.1, the dispersion of the atomic momentum states in the periodic potential of the light grating is shown for usual parameters occurring in the experiment. As in typical experimental situations the atoms are nearly at rest, transfer of momentum from the light field to the atoms is associated here with a transfer of atomic momentum states in the lowest Bloch band to energetically higher bands by conserving energy and momentum. Two regimes for momentum transfer are considered in the following, Bragg and Kapitza-Dirac diffraction. For the description of momentum occupation probabilities in either regime, the model of dressed atomic states in the light field can be applied.

4. Diffraction of fermions from light gratings

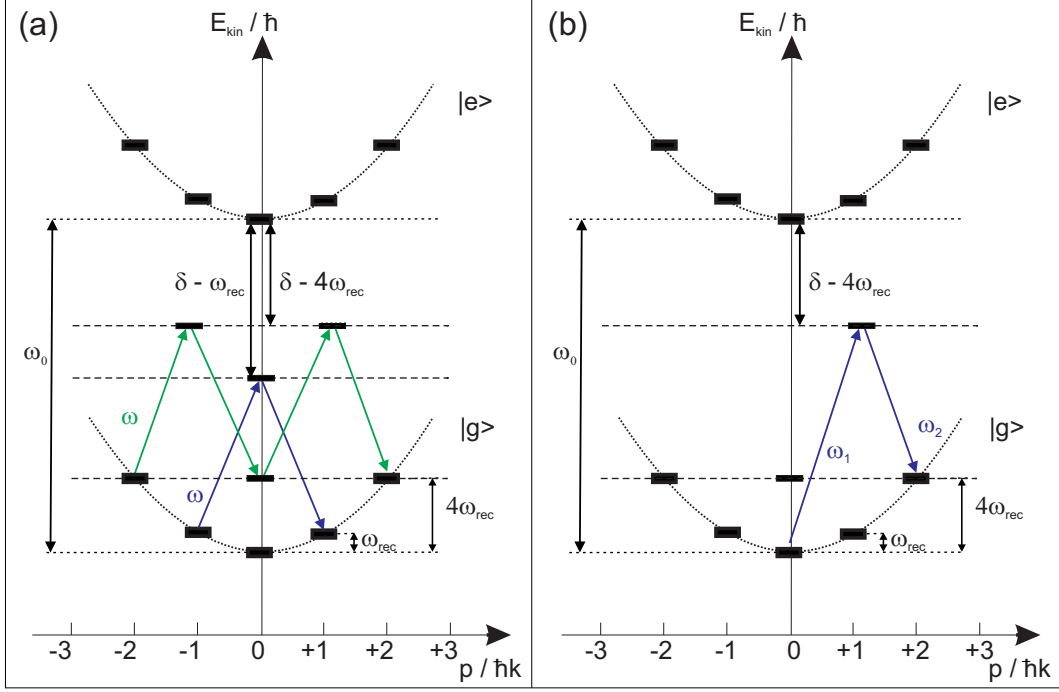


Figure 4.2: Principle of Bragg diffraction. In Fig. (a), first (blue) and second (green) order Bragg scattering of atoms with initial non-zero momentum is shown by a standing wave with zero detuning. Fig. (b) shows a first order Bragg scattering process with initial atoms at rest and laser beams detuned by $\omega_1 - \omega_2 = 4\omega_{\text{rec}}$.

4.1.2 Principle of Bragg scattering

For long interaction times, the entire propagation through the light grating needs to be considered. If the interaction time is long, but the strength of the optical potential is weak one enters the Bragg diffraction regime. The diffraction occurs only for specific Bragg angles θ_B which satisfy the Bragg condition $N_B \lambda_{\text{dB}} = \lambda \sin(\theta_B)$. The de Broglie wavelength of the atoms λ_{dB} is given in Eq. (2.5), λ is the wavelength of the light field, and N_B is an integer number which describes the order of the diffraction process. This condition is velocity selective for atoms and Bragg diffraction can be used for the characterization of velocity distributions in atomic systems. Bragg scattering is the simplest case of coherent momentum transfer from a light field to atoms. Consider a two-level atom with momentum states as a set of basis vectors in a standing wave light grating formed by two counter-propagating plane waves with equal frequency. The momentum is a good quantum number for describing the system, only if the interaction time τ between the atom and light field is significantly smaller than the mean oscillation period in the confining trap of the atoms. An atom with a mass m and momentum $N_B \hbar \mathbf{k}$ possesses the kinetic energy $E_{\text{kin}} = (N_B \hbar \mathbf{k})^2 / (2m)$. The dispersion $E_{\text{kin}}(k)$ follows a parabola, cf. Fig. 4.2. Momentum is transferred by paired stimulated absorption and emission

4.1 Diffraction of atoms from a standing wave

processes, resulting in a transfer of photons from one beam to the other. If the two beams counter-propagate, a N_B -th order Bragg process describes the transfer of N_B photons from one traveling beam to the other and alters the momentum of the atom by $2N_B\hbar k$. The atomic population is transferred only between $|g, -N_B\hbar\mathbf{k}\rangle$ and $|g, +N_B\hbar\mathbf{k}\rangle$, where $|g(e), \pm N_B\hbar\mathbf{k}\rangle$ denotes a two-level atom in its ground (excited) state with momentum $\pm N_B\hbar\mathbf{k}$ parallel to the standing wave axis, see Fig. 4.2 (a). As a consequence, for equal frequency of the laser beams, only momentum states with the same energy can couple.

We consider the case when a short pulse of the light field is applied while the atoms are not moving. In this case the Bragg angle can be varied by using a frequency detuning for the counter-propagating waves resulting in a moving optical potential. Hence the Bragg condition is represented by a resonance condition for the detuning as explained in the following. If the atoms are stationary and a moving standing wave is formed by frequency shifting the two counter-propagating beams, the momentum state $|g, 0\rangle$ of the atoms can only couple to the energetically higher non-zero momentum states $|g, 2N_B\hbar k\rangle$, see Fig. 4.2 (b). The resonance condition for this process satisfies

$$E'_{\text{kin}} - E_{\text{kin}} = \frac{\mathbf{p}'^2}{2m} - \frac{\mathbf{p}^2}{2m} = \frac{2N_B^2\hbar^2k^2}{m}, \quad (4.3)$$

where $E'_{\text{kin}} = \mathbf{p}'^2/(2m)$ ($E_{\text{kin}} = \mathbf{p}^2/(2m)$) corresponds to the kinetic energy of the atoms after (before) interacting with the light field. The frequency detuning δ_{N_B} between the two propagating beams is given by

$$\delta_{N_B} = \frac{E'_{\text{kin}} - E_{\text{kin}}}{\hbar N_B} = \frac{2N_B\hbar k^2}{m} = 4N_B\omega_{\text{rec}}, \quad (4.4)$$

where ω_{rec} denotes the recoil frequency of the absorption process of a photon and is defined by

$$E_{\text{rec}} = \hbar\omega_{\text{rec}} = \frac{\hbar^2k^2}{2m}. \quad (4.5)$$

The momentum of the atoms after the scattering process is $2N_B\hbar k$.

For moving atoms with initial momentum \mathbf{p}_i along the propagation direction of the beams, the resonance condition from Eq. (4.3) is altered by an additional term

$$E'_{\text{kin}} - E_{\text{kin}} = \frac{\mathbf{p}'^2}{2m} - \frac{\mathbf{p}^2}{2m} = \frac{2N_B^2\hbar^2k^2}{m} + \frac{2N_B\hbar\mathbf{k} \cdot \mathbf{p}_i}{m}. \quad (4.6)$$

This shows that the method of Bragg scattering can be used in a velocity selective way.

In the ideal situation, only one final momentum state can be occupied. This is ensured for long interaction times τ between the light field and the atoms. The energy uncertainty $\Delta E \approx \hbar/\tau$ is small and only one momentum state is accessible. In other words, the Fourier width of the light pulse needs to be smaller than the separation of adjacent discrete momentum states

$$\tau \gg \frac{1}{\omega_{\text{rec}}}. \quad (4.7)$$

4. Diffraction of fermions from light gratings

As shown in (Martin *et al.*, 1988; Giltner *et al.*, 1995) within a quantum-mechanical description, the time evolution for the atomic population in the momentum state $|g, +N_B \hbar \mathbf{k}\rangle$ for Bragg scattering between the states $|g, -N_B \hbar \mathbf{k}\rangle$ and $|g, +N_B \hbar \mathbf{k}\rangle$ is given by

$$P_{N_B} = \sin^2(\Phi) = \sin^2\left(\frac{\omega_R^{(2N_B)}}{2}\tau\right), \quad (4.8)$$

where Φ is the pulse area. The $2N_B$ -photon Rabi frequency for a Gaussian light pulse can be expressed by (Giltner *et al.*, 1995)

$$\omega_R^{(2N_B)} = \frac{(\omega_{R,1}\omega_{R,2})^{N_B} \sqrt{\pi/(2N_B)}}{2^{4N_B-3} [(N_B-1)!]^2 \delta^{N_B} \omega_{\text{rec}}^{N_B-1}}, \quad (4.9)$$

where $\delta = \omega - \omega_0 \gg \omega_{\text{rec}}$ describes the difference between the frequency of the light field ω and the unperturbed frequency of the atomic transition ω_0 . In the case of two counter-propagating laser beams with intensities I_1 and I_2 , the Rabi frequency for first and second order Bragg diffraction is then

$$\omega_R^{(2)} = \frac{\omega_{R,1}\omega_{R,2}}{2\delta} \sqrt{\frac{\pi}{2}}, \quad \omega_R^{(4)} = \frac{(\omega_{R,1}\omega_{R,2})^2}{32\delta^2\omega_{\text{rec}}} \sqrt{\frac{\pi}{4}}, \quad (4.10)$$

respectively, according to Eq. (4.9). The single-photon Rabi frequency of the transition with the decay rate Γ , which is driven by a light field with intensity I_i , can be calculated with (Metcalf and van der Straten, 1999)

$$\omega_{R,i} = \Gamma \sqrt{\frac{I_i}{2I_{\text{sat}}}}, \quad (4.11)$$

where $I_{\text{sat}} = \pi \hbar c \Gamma / (3\lambda^3)$ is the saturation intensity. In the case of very long interaction times τ , the spontaneous scattering rate increases and represents a limiting factor for the observation of Rabi oscillations as predicted in Eq. (4.8).

4.1.3 Principle of Kapitza-Dirac scattering

For short interaction times, the extent of the light grating has no influence on the final direction of the diffraction orders. In this case, in the so-called Kapitza-Dirac diffraction limit, it can be shown that an atomic population interacting with a short pulsed standing wave results in a symmetric distribution of atomic momentum populations into each pair of diffraction orders of opposite sign ($\pm N$, N integer number). In the case of Kapitza-Dirac scattering, many adjacent momentum states can be occupied since the Fourier width of the pulse is broader as compared to the separation of adjacent momentum states

$$\tau \ll \frac{1}{\omega_{\text{rec}}} = \frac{1}{2\pi\nu_{\text{rec}}} = 19 \mu\text{s}, \quad (4.12)$$

4.2 Experimental results

where the parameters of ^{40}K have been invoked. The occupation probability for states with momentum $2N\hbar\mathbf{k}$ in dependence of the interaction time τ for the case of Kapitza-Dirac scattering is described by (Gould *et al.*, 1986; Ovchinnikov *et al.*, 1999)

$$P_N = J_N^2(\Phi) = J_N^2\left(\frac{\omega_{R,1}\omega_{R,2}}{2\delta}\tau\right), \quad (4.13)$$

where Φ is the pulse area and $J_n(\alpha)$ are Bessel functions of first kind. Appreciable momentum transfer can be observed with large light intensities. But, as already discussed for Bragg scattering, a large number of spontaneous scattering events per atom should be avoided for efficient Kapitza-Dirac scattering as well.

4.2 Experimental results

4.2.1 Influence of finite temperature of atomic cloud

For efficient Bragg scattering of atoms, a bright source of atoms is required. This means that the momentum spread of the atoms should be small, so that the Bragg resonance condition is satisfied for the majority of atoms. The resonance condition for Bragg scattering depends on the momentum of the atom p_i as seen from Eq. (4.6). For maximum atomic population in the Bragg scattered first order, the π -phase condition $\omega_R^{(2)}\tau = \pi$ needs to be satisfied according to Eq. (4.8), where $\omega_R^{(2)}$ is the two-photon Rabi frequency and τ is the pulse duration. This π -pulse condition depends on the initial momentum p_i of the atoms, cf. also Eq. (4.6), and for a given pulse duration τ the different velocity classes in the cloud would therefore be transferred with different two-photon Rabi frequencies. For a non-zero temperature cloud the transfer efficiency of momentum decreases with increasing temperature, since the momentum distribution becomes broader and only a small part of the atoms satisfies the Bragg condition for a given detuning. As a consequence, the temperature of the cloud should be minimized for the sake of momentum transfer efficiency. For the special case of a fermionic cloud as considered within the present work, the Fermi energy E_F should be lowered to acquire a sharp momentum distribution. The majority of the atoms possesses a momentum of $p_i \approx \hbar k_F$ in the case of a fermionic cloud. The curvature of the Bloch bands of the dispersion relation $E_{\text{kin}}(k)$ determines how critical the resonance condition needs to be satisfied. The larger the curvature of the Bloch bands is, the stronger the resonance condition varies with momentum, what determines a limit for the allowed momentum spread of the atoms.

In the following, experimental results with fermionic ^{40}K released from our QUIC trap are presented. For efficient Bragg scattering, the QUIC trap frequencies are lowered as much as possible without loss of atoms. The mean trapping frequency is lowered from $\bar{\nu} = (\nu_x\nu_y\nu_z)^{1/3} = 117\text{Hz}$ to $\bar{\nu} = 83\text{Hz}$ resulting in a temperature of $T_z = 80(30)\text{nK}$ along the cloud axis, which is collinear with the Bragg beams. The ^{40}K cloud is not fully thermalized after the reduction of the trapping frequencies. Just before the ramp, remnant ^{87}Rb atoms from the RF evaporation process are removed by a resonant optical pulse, and within the detection limit of the imaging system a ^{40}K cloud with typically 5×10^4 atoms in the pure state $|F = 9/2, m_F = 9/2\rangle$ is existent in the trap with a

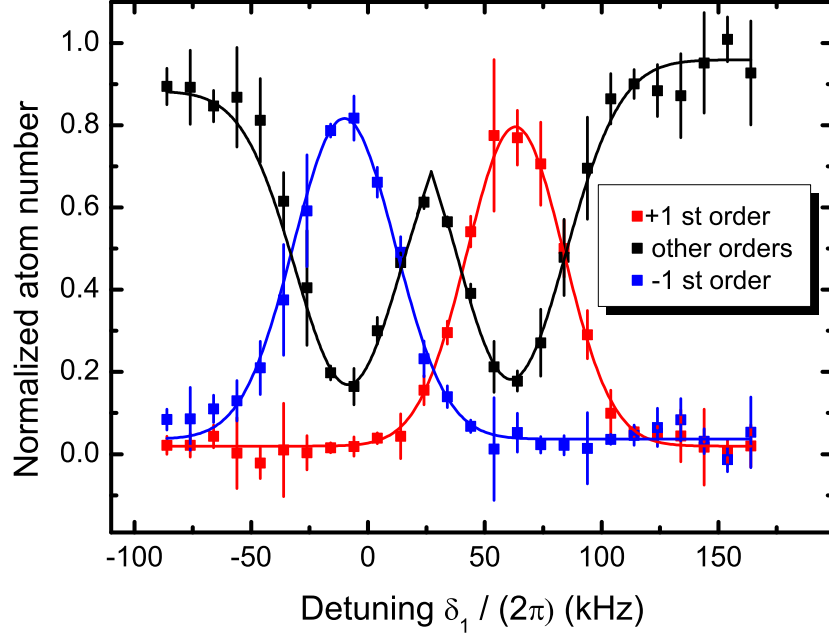


Figure 4.3: First order Bragg scattering as a function of relative detuning of laser beams. The frequency of Bragg AOM 1 is fixed at 80 MHz, while the frequency of Bragg AOM 2 is varied. For the nomenclature of the corresponding AOMs see Fig. 3.2. The graph shows the fraction of atoms scattered into the +1 st, -1 st, and remaining fraction other than the +1 st and -1 st order.

degeneracy parameter of $T/T_F \approx 0.5$. This results in the first experimental realization of highly efficient Bragg scattering with fermionic clouds.

4.2.2 Bragg scattering

In this section, the experimental results on Bragg scattering of first and second order are shown. After release of the ^{40}K cloud from the magnetic trap, the Bragg beams are applied after a time-of-flight of 6.2 ms. Due to reasons of maximum efficiency, the Bragg pulses have a Gaussian profile in time domain with a $1/e^2$ width of $10 \mu\text{s}$ in order to avoid off-resonant excitation. Absorption imaging occurs 4.0 ms after the Bragg pulses, see Fig. 4.8, such that the diffracted orders separate and the atomic number in the respective orders can be determined. The relative frequency of the two Bragg beams is varied with the help of a DDS controller for the AOM, see Fig. 3.2. Bragg AOM 1 and 3 are kept at a constant diffraction frequency of 80 MHz, whereas Bragg AOM 2 is varied with a frequency step size of 10 kHz. For first order Bragg scattering of an atomic ^{40}K cloud at rest, the detuning is expected to be $\delta_1/(2\pi) = 4 \cdot \omega_{\text{rec}}/(2\pi) = 33.9 \text{ kHz}$.

4.2 Experimental results

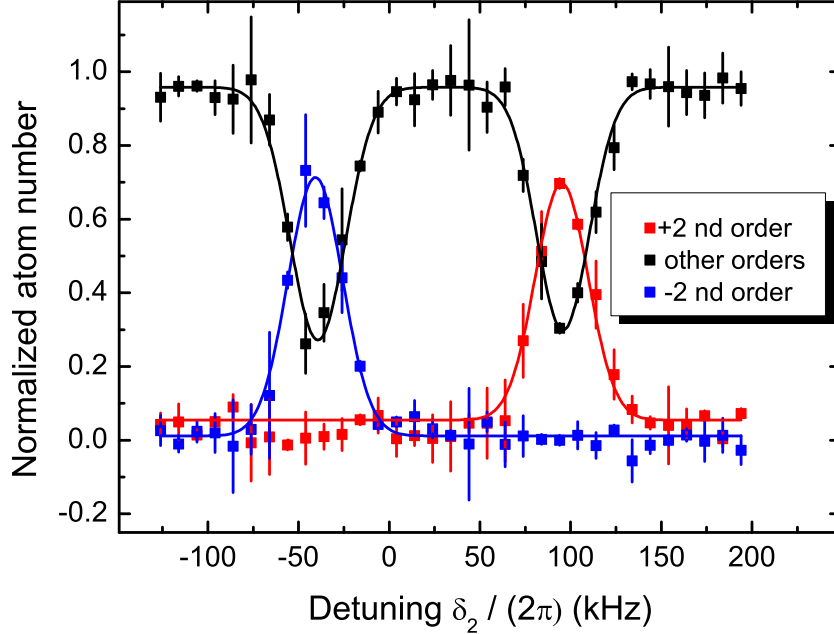


Figure 4.4: Second order Bragg scattering as a function of relative detuning of laser beams. The frequency of Bragg AOM 1 is fixed at 80 MHz, while the frequency of Bragg AOM 2 is varied. For the nomenclature of the corresponding AOMs see Fig. 3.2. The graph shows the fraction of atoms scattered into the +2 nd, -2 nd, and remaining fraction other than the +2 nd and -2 nd order.

The frequency spectra for the +1st and -1st order of Bragg scattering are shown in Fig. 4.3. The data shows normalized atomic numbers, where the individual number of atoms in the +1st, -1st order, and remaining orders other than the +1st and -1st are normalized by the sum of atom numbers occurring in all available diffraction orders. This method allows to reduce the influence of shot-to-shot atomic number fluctuations, as the measurement relies on the determination of relative atomic numbers. The optimum pulse area for maximum momentum transfer at resonance is found by varying the optical pulse power. This is realized with an additional external voltage variable attenuator (VVA) at Bragg AOM 3, see Fig. 3.2, which controls the overall power of the Gaussian light field pulse. Using simple Gaussian fits for the spectra, the difference between the maxima of +1st and -1st order is determined to be 72.2(8) kHz and deviates only by 6% from the theoretical value of $8\nu_{\text{rec}} = 67.8$ kHz. The two spectra for the +1st and -1st Bragg diffracted orders are not, as expected, centered around zero detuning, but are shifted. The reason for this shift is still under investigation. But an additional term in the potential from Eq. (4.2), which is proportional to the absolute value of the spatial coordinate $\propto z$, could lead to a tilt of the Bloch bands (Fig. 4.1) around $p = 0$, and hence

4. Diffraction of fermions from light gratings

to an asymmetry of the resonance conditions for opposite Bragg diffraction orders. This might be fulfilled e.g. with magnetic field gradients, which are present during the release from the magnetic trap. Prospective measurements in an optical dipole trap may clarify the existing situation.

If a higher detuning between the beams is applied, higher momentum states can be occupied. The result for 2nd order Bragg diffraction is shown in Fig. 4.4. The Bragg pulses are applied after a time-of-flight of 6.0 ms. The frequency difference between the maximum transfer of the momentum states $|+4\hbar k\rangle$ and $|-4\hbar k\rangle$ is 137.4(8) kHz. The value from theory $16\nu_{\text{rec}} = 135.8$ kHz only deviates by 1%. A summary of the results for 1st and 2nd order Bragg diffraction is shown in Tab. 4.1. The center frequency of the 2nd order Bragg peaks is close to the center frequency of the 1st order Bragg peaks. The $1/e^2$ widths (in units of 2π) of the Bragg peaks for the different diffraction orders are summarized in Tab. 4.1. The widths of the diffraction peaks are obtained by a convolution of several contributions. First, as already discussed above, the finite temperature of the cloud leads to a finite width of the momentum population. Different velocity classes satisfy the Bragg condition with different two-photon Rabi frequencies, what leads to a Doppler-broadening of the spectrum. A second contribution arises from the finite Fourier width of the light field, which is here about 5 kHz for the given pulse duration and the Gaussian profile (Papp, 2007). In addition, the curvatures of the Bloch bands of the involved momentum states influence the efficiency of the scattering process, and hence the width of the Bragg peaks.

Once the optimum detuning is found for efficient momentum transfer to 1st and 2nd order, the pulse area $\Phi = \omega_R^{(2N_B)}\tau$ can be varied for the investigation of Rabi oscillations between the different momentum states. From Eq. (4.8), a sinusoidal oscillation is expected by changing either the interaction time τ or $\omega_R^{(2N_B)}$. The latter can be modified in a straightforward way by varying the power of the beams, which is presented in Fig. 4.5 for an optimum detuning of first order Bragg diffraction. For this measurement, the beam power of the laser field is varied by changing the RF power for Bragg diffraction at Bragg AOM 3 with the already mentioned external VVA. One can clearly identify the expected sinusoidal dependence of the transfer efficiency on the pulse area. A fraction of 85% of the total atomic number is transferred to a different momentum state at resonance. The pulse areas for each data point are determined from measured pulse traces of a light component with a fast photodiode, and a subsequent temporal integration of the profile. For the

Diffraction order N_B	-1	+1	-2	+2
AOM frequency (MHz)	79.9907(6)	80.0629(4)	79.9590(5)	80.0965(6)
Detuning $\delta_{N_B}/(2\pi)$ (kHz)	-9.3(6)	62.9(4)	-41.0(5)	96.5(6)
Difference between peaks (kHz)	72.2(8)		137.5(8)	
Center between peaks (MHz)	80.0268(8)		80.0278(8)	
$1/e^2$ width/ 2π (kHz)	44(2)	41(1)	30(2)	29(5)

Table 4.1: Position and $1/e^2$ widths of Bragg peaks for ± 1 st and ± 2 nd order.

4.2 Experimental results

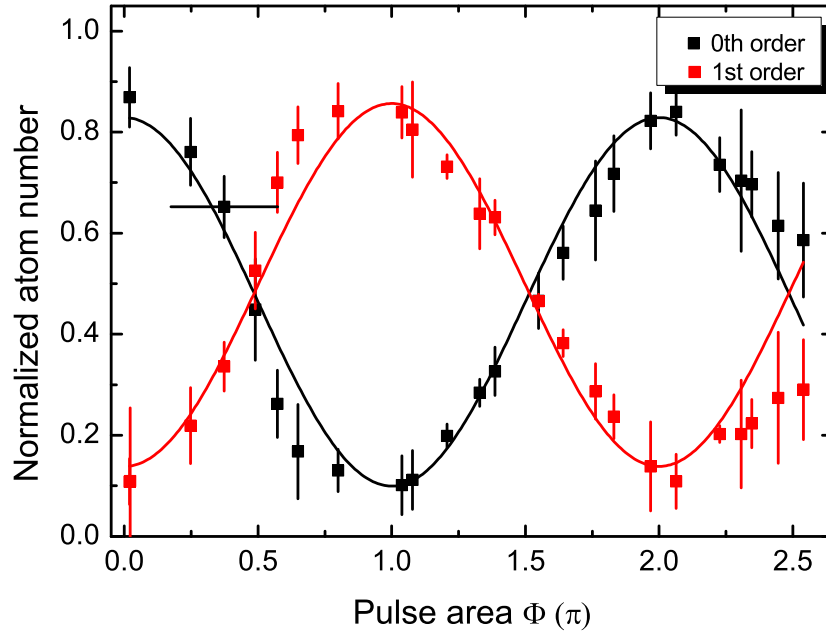


Figure 4.5: First order Bragg scattering as a function of pulse area. The duration of the Gaussian pulse with a $1/e^2$ width of $10 \mu\text{s}$ is fixed, and the power of the beams is varied.

determination of the pulse area we consider an experimental uncertainty of $\pm 0.2\pi$ arising from the nonlinearity of the external VVA, power fluctuations, and drifts. For a Gaussian profile (Martin *et al.*, 1988; Giltner *et al.*, 1995), maximum transfer is satisfied for a single-photon Rabi frequency of $\omega_R = 81 \text{ MHz}$. For the present experimental parameters, this corresponds to an optical power of $P = 243 \mu\text{W}$ with a detuning $\delta = 2\pi 1.43 \text{ GHz}$, a beam waist $w_0 = 1 \text{ mm}$, and balanced laser beam intensities $I_1 = I_2 = 2P/(\pi w_0^2)$. This value can be directly compared to the measured power in front of the glass cell, but we find a lower value. Possible deviations may arise from the fact that waists and powers of the two beams are not equal.

For second order Bragg scattering the frequency of AOM 2 is set to 80.0965 MHz . Again the population probability of the momentum state $|+4\hbar k\rangle$ follows a sinusoidal dependence on the pulse area as shown in Fig. 4.6. For higher pulse area a damped oscillation behavior is visible. This might be related to the fact that for higher optical powers the effect of spontaneous emission becomes relevant. A maximum of 80% of the total population can be transferred for 2nd order Bragg diffraction. This value is slightly smaller as compared to 1st order Bragg diffraction, since the energy difference of the involved Bloch bands for 2nd order Bragg diffraction varies with momentum stronger ($\approx 42 E_{\text{rec}}/k_{\text{rec}}$) as compared to the case of 1st order diffraction ($\approx 6 E_{\text{rec}}/k_{\text{rec}}$), cf. Fig. 4.1. The optical power for the resonance condition derived from theory and

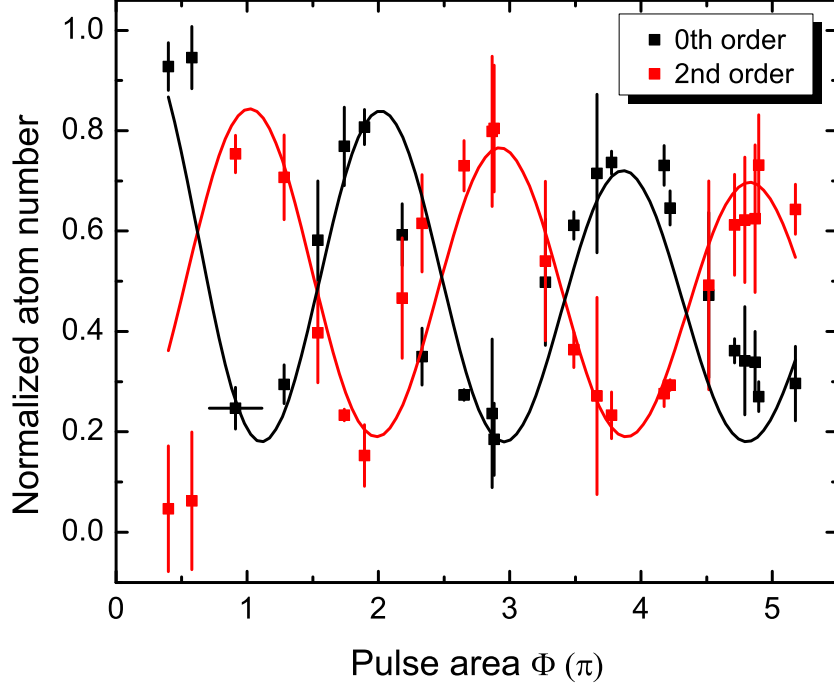


Figure 4.6: Second order Bragg scattering as a function of pulse area. The duration of the Gaussian pulse with a $1/e^2$ width of $10 \mu\text{s}$ is fixed, and the power of the beams is varied.

measurement can be compared in a similar way as shown above for 1st order diffraction. For a Gaussian 2nd order Bragg pulse the resonance condition is satisfied for a single-photon Rabi frequency of $\omega_R = 92 \text{ MHz}$. This would correspond to a power of $313 \mu\text{W}$. The measured power for the experimentally optimized π -pulse condition is deduced from a direct measurement in front of the glass cell, and is as already seen above slightly lower. For higher orders, this measurement is more prone to the above mentioned experimental uncertainties since the fourth order of the single-photon Rabi frequency enters in the resonance condition, cf. Eq. (4.10).

4.2.3 Kapitza-Dirac scattering

For Kapitza-Dirac scattering, the frequency of AOM 2 is adjusted to 80.0268 MHz and the pulse for the light grating with a square shape in time domain possesses a duration of $4 \mu\text{s}$, see condition in Eq. (4.12). The dependence of occupancy probabilities for different orders of Kapitza-Dirac scattering processes can be investigated by varying the optical power and therefore the pulse area. The results are presented in Fig. 4.7 for the 0th, +1st

4.2 Experimental results

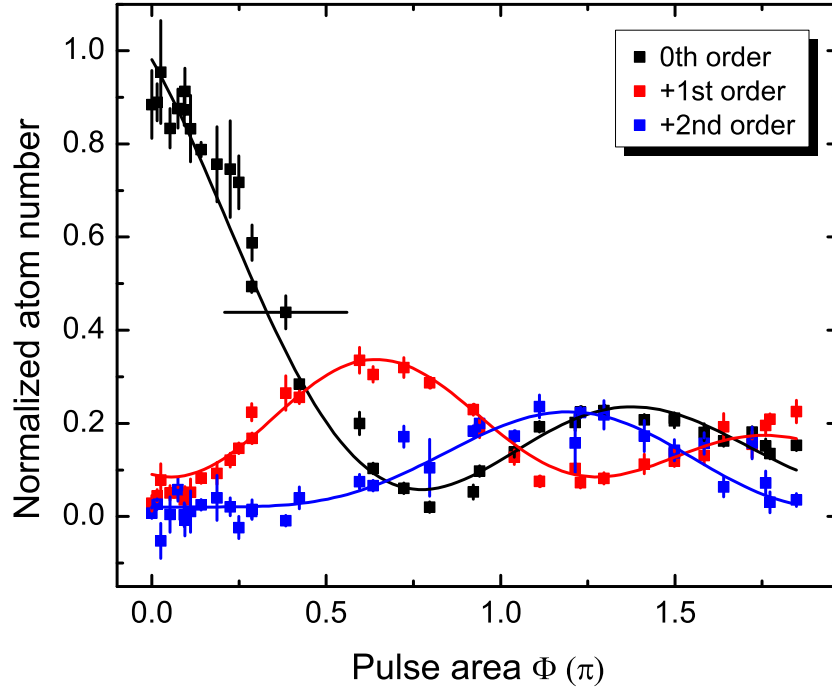


Figure 4.7: Kapitza-Dirac scattering as a function of pulse area. The pulse duration is fixed at $4 \mu\text{s}$ and the power of the beams is varied. The graph shows the fraction of atoms scattered into the +1st, +2nd order, and the unscattered fraction.

and +2nd order of Kapitza-Dirac scattering. The solid curves represent fits to squared Bessel functions of first kind J_0^2 (0th order), J_1^2 (1st order) and J_2^2 (2nd order). The fits show good agreement with the expectation from theory, cf. Eq. (4.13). For maximum transfer of the ^{40}K atoms into the momentum states $|\pm 2\hbar k\rangle$ (1st order), an expected power of $308 \mu\text{W}$ is required. The directly measured power for the maximum transfer for first order Kapitza-Dirac scattering in the experiment gives a value of $P = 230(62) \mu\text{W}$. The maximum transfer for 2nd order diffraction is expected to occur for a beam power of $511 \mu\text{W}$. For large pulse areas, the effect of spontaneous photon scattering limits the observation of Kapitza-Dirac scattering.

4.2.4 Discussion and conclusions

Fig. 4.8 illustrates absorption images of the clouds which are subject to different type of scattering processes. Fig. 4.8 (a) shows the fermionic ^{40}K cloud without pulses. In Fig. 4.8 (b) and (c) optimized Bragg pulses for first and second order are presented with a $1/e^2$ width of the Gaussian profile of $10 \mu\text{s}$. In Fig. 4.8 (d) and (e) Kapitza-

4. Diffraction of fermions from light gratings

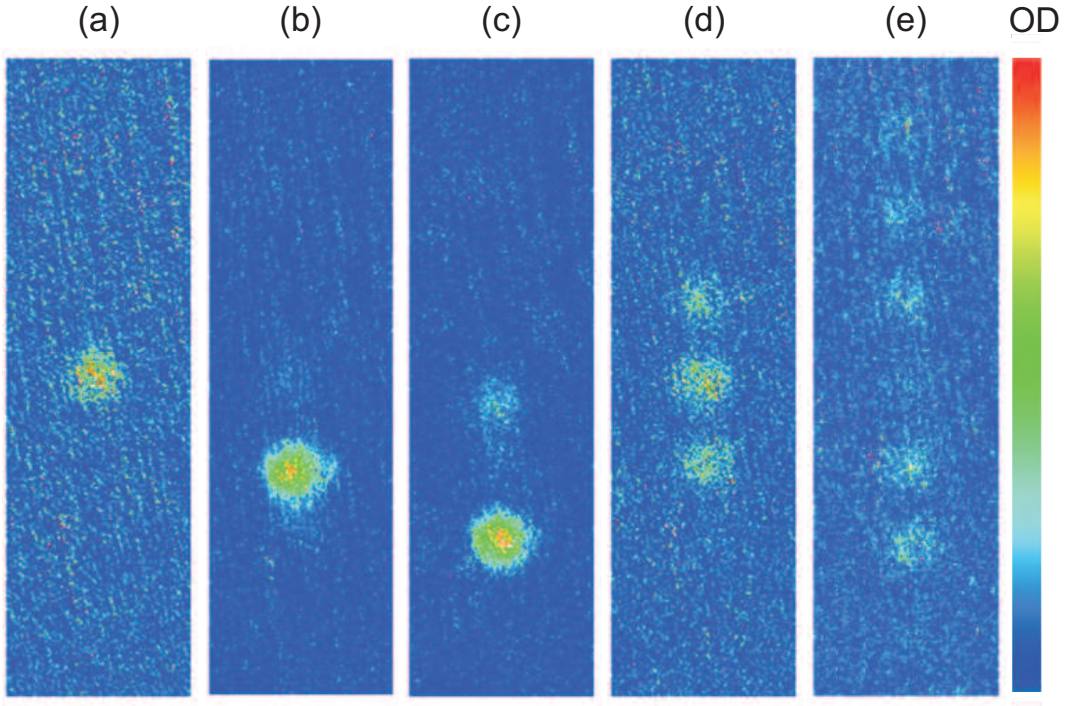


Figure 4.8: Different types of scattering processes of a fermionic ^{40}K cloud on a light grating. (a) no light pulses (b) first order Bragg scattering (c) second order Bragg scattering (d) Kapitza-Dirac scattering process with about 25% of the atoms scattered into each of the first order (± 1) (e) Kapitza-Dirac scattering up to the third order.

Dirac diffraction processes are studied. Up to the third order of Kapitza-Dirac scattering can be observed with a pulse duration of $4\mu\text{s}$. As can be seen in the illustration, the momentum transfer is efficient, and almost the entire cloud can be transferred to a different momentum state. As discussed previously, special care needs to be addressed to the fermionic nature of the atoms by preparing an atomic ensemble with a small width of the momentum distribution. This is here realized by reducing the trapping frequency of the magnetic trap. With such a bright source the majority of atoms can satisfy the resonance condition. For a BEC, as an almost ideal bright source, efficient momentum transfer was presented earlier (Ovchinnikov *et al.*, 1999). For a Fermi gas, to the best of the author's knowledge such a highly efficient momentum transfer has not been realized so far. This opens up possibilities to investigate a sequence of pulses for the creation of a matter wave interferometer or the application of Bragg spectroscopy in a Fermi mixture at a Feshbach resonance in the near future.

4.2 Experimental results

Chapter 5

Ultracold Fermi-Fermi molecules at a narrow Feshbach resonance

In this chapter, the first creation of ultracold heteronuclear bosonic molecules from a two-species Fermi-Fermi mixture of ^6Li and ^{40}K is presented. The association of the molecules is induced by an adiabatic magnetic field sweep across an interspecies s -wave Feshbach resonance close to 155 G. With this technique 4×10^4 molecules can be created with an efficiency of up to 50 % for our experimental parameters. A direct imaging method is developed which allows to probe sensitively molecule properties. For instance with this direct imaging method the molecular lifetimes in an atom-molecule mixture is investigated for various magnetic field strengths across the Feshbach resonance. For the chosen trap densities, molecular lifetimes of more than 100 ms can be observed.

The first section presents the experimental sequence for the creation of ultracold molecules. Loading of the optical dipole trap (Sec. 5.1.1) and state preparation (Sec. 5.1.2) are discussed in detail. Then, in Sec. 5.2, the Feshbach resonance is located by inelastic atom loss spectroscopy. In Sec. 5.3, heteronuclear molecules are produced and characterized by several measurements.

Parts of this chapter are published in

A.-C. Voigt, M. Taglieber, L. Costa, T. Aoki, W. Wieser, T.W. Hänsch, and K. Dieckmann, *Ultracold Heteronuclear Fermi-Fermi Molecules*, Phys. Rev. Lett. **102**, 020405 (2009).

In this publication an error is discovered, which is discussed in the errata (Voigt *et al.*, 2010E; Costa *et al.*, 2010E). A mistake in the magnetic field calibration occurred. The calibration is based on measurements of the transition frequency between different Zeeman states as presented in Sec. 3.6.3. The Zeeman transition frequency was converted into a magnetic field strength by the incorrect use of the Breit-Rabi formula (Breit and Rabi, 1931; Eisinger *et al.*, 1952). After correction, a shift of 375 mG towards lower magnetic field strengths of the correct magnetic field calibration in comparison to the old defective one is found. This correction is incorporated in all values of magnetic field strengths, which are presented in the following. The physical interpretation and conclusions based on comparison of the several measurements, which will be presented

5.1 Experimental sequence

here in Chs. 5 and 6, are not altered by this correction. We thank the Innsbruck group (Grimm and Schreck, 2010) for pointing out the discrepancy to their results (Naik *et al.*, 2011). By employing the correct conversion formulas, the magnetic field position of the Feshbach resonance near 155 G, which will be presented here in Ch. 6, is in full consistency with a later study, which uses an alternative approach (Naik *et al.*, 2011) for the measurement of the position of the same interspecies resonance under investigation.

5.1 Experimental sequence

A schematic description of the experimental sequence for the measurements presented in this chapter can be found in Fig. 5.1. The mixture is loaded from the magnetic trap into an optical dipole trap (ODT). After loading, the mixture is prepared into the relevant Zeeman states for the study of interspecies Feshbach resonances. Subsequently, magnetic field ramps are performed for the measurements. Finally, the clouds are imaged either at low or high magnetic field strengths. For the high magnetic field imaging a short magnetic field gradient is applied to the mixture, which allows for a separate detection of atoms and molecules. A more comprehensive description is given below for the individual steps of the sequence.

5.1.1 Loading of the optical dipole trap

After evaporation of ^{87}Rb for sympathetic cooling of the Fermi-Fermi mixture and before the mixture is loaded into the ODT, remnant ^{87}Rb atoms are removed by a short resonant optical pulse. Within the detection limit of our imaging system the sample is free from ^{87}Rb atoms. The power of the two beams of our crossed optical dipole trap is adiabatically increased within 149 ms with an exponential ramp. After the increase of the ODT power, the current of the QUIC trap is linearly ramped down within 100 ms. In order to define a quantization axis for the atoms, the strength of the Feshbach magnetic field is linearly increased within 100 ms from zero to 3.2 G at the same time while the QUIC current is turned off. For the measurements which will follow two different optical trap configurations are used. High trap depths are chosen with beam powers of $P_{\text{ODT1}} = 2.44 \text{ W}$ and $P_{\text{ODT2}} = 1.21 \text{ W}$. The trap frequencies are determined by the methods outlined in Sec. 3.5.4. For this configuration the trapping frequencies (ν_x, ν_y, ν_z) are

$$(1022, 1575, 1199) \text{ Hz for } ^6\text{Li} \text{ and } (595, 918, 699) \text{ Hz for } ^{40}\text{K}. \quad (5.1)$$

The second configuration possesses a lower optical power with $P_{\text{ODT1}} = 188 \text{ mW}$ and $P_{\text{ODT2}} = 96 \text{ mW}$ and trapping frequencies

$$(285, 440, 333) \text{ Hz for } ^6\text{Li} \text{ and } (168, 256, 194) \text{ Hz for } ^{40}\text{K}. \quad (5.2)$$

The uncertainty for all ν_i is about $\pm 5\%$. Depending on the trap power, atom numbers of typically $\approx 1 \times 10^5$ for each species with degeneracy parameters ranging $T/T_F \approx 0.3 - 0.5$ can be loaded from the QUIC trap to the ODT.

5. Ultracold Fermi-Fermi molecules at a narrow Feshbach resonance

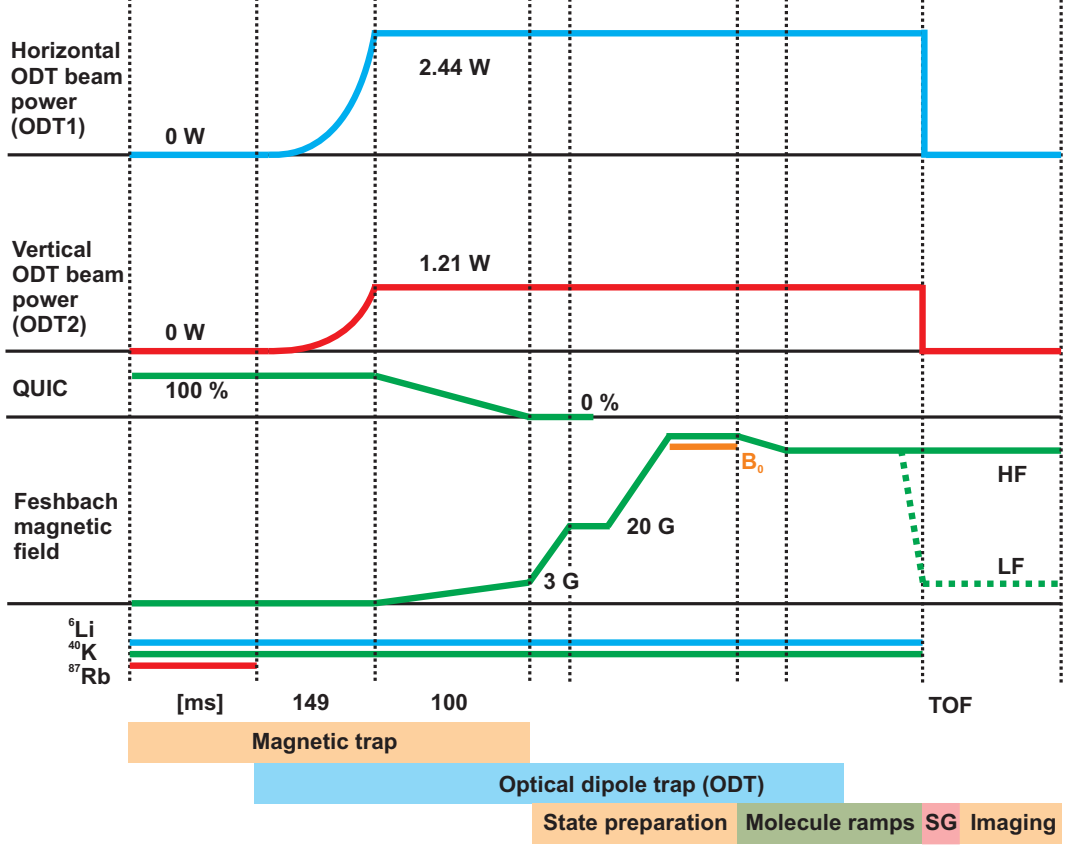


Figure 5.1: Experimental sequence for the production of heteronuclear molecules in a Fermi-Fermi mixture of ${}^6\text{Li}$ and ${}^{40}\text{K}$.

5.1.2 State preparation

After loading the mixture into the ODT, the atoms are prepared in the relevant Zeeman states for the interspecies ${}^6\text{Li}$ - ${}^{40}\text{K}$ Feshbach resonance close to 155 G. More generally, an ODT offers a variety of possible spin state configurations of ${}^6\text{Li}$ and ${}^{40}\text{K}$ to be studied. Spin state mixtures that are stable against spin-exchange collisions are

$$\begin{aligned}
 & {}^{40}\text{K}|9/2, -9/2\rangle \quad {}^6\text{Li}|1/2, m_F\rangle \\
 & {}^{40}\text{K}|9/2, -9/2\rangle \quad {}^6\text{Li}|3/2, -3/2\rangle \\
 & {}^{40}\text{K}|9/2, m_F\rangle \quad {}^6\text{Li}|1/2, 1/2\rangle.
 \end{aligned} \tag{5.3}$$

The large variety of possible configurations follows from the inverted hyperfine structure of ${}^{40}\text{K}$ and allows to study a larger set of combinations. The relevant states for ${}^6\text{Li}$ and ${}^{40}\text{K}$ are prepared with the help of adiabatic rapid passages (ARP). An electromagnetic field in the RF domain couples in this case to two levels of the atomic system, and population can be transferred if the frequency is swept across resonance. This method is robust against frequency and power fluctuations of the electromagnetic field, and against

5.2 Feshbach loss spectroscopy

external magnetic field fluctuations. The Feshbach magnetic field strength is ramped from 3.2 G to 20.3 G within 10 ms. After a short settling time for the magnetic field the Zeeman states are transferred from $|3/2, 3/2\rangle$ to $|1/2, 1/2\rangle$ for ${}^6\text{Li}$ and $|9/2, 9/2\rangle$ to $|9/2, -9/2\rangle$ for ${}^{40}\text{K}$. The external field causes a hyperfine splitting of the ground state what allows to sensitively address only one single Zeeman state. The frequency for the ${}^6\text{Li}$ Zeeman state transfer is swept from 270.016 MHz to 269.392 MHz within 735 μs . This duration allows to transfer all atoms to the desired final Zeeman state $|1/2, 1/2\rangle$ of ${}^6\text{Li}$. The comparatively large Rabi frequency of $\Omega = 2\pi \times 30(2)$ kHz based on a high power radiofrequency source admits to perform the transfer relatively fast.

After the state preparation of ${}^6\text{Li}$, the transfer frequency of ${}^{40}\text{K}$ is swept from 7.088 MHz to 5.775 MHz within 336 μs . The Rabi frequency for this transition is $\Omega = 2\pi \times 18.3(1.4)$ kHz. The duration of the sweep is long enough to transfer all ${}^{40}\text{K}$ atoms to the state $|9/2, -9/2\rangle$, and no dephasing during the transfer occurs since the duration is sufficiently smaller than the mean trapping oscillation period or the mean time between collisions. In a second ARP the ${}^{40}\text{K}$ atoms are finally transferred from the state $|9/2, -9/2\rangle$ to $|9/2, -5/2\rangle$. This second ARP is done after a magnetic field sweep from 20.3 G to 156.90 G, and at a magnetic field strength on the atomic side of the Feshbach resonance at 155 G in order to circumvent molecule formation. There is a nearby second Feshbach resonance around 163 G, which involves the same Zeeman states of ${}^6\text{Li}$ and ${}^{40}\text{K}$ (Wille *et al.*, 2008). The transfer frequency is swept from 36.9943 MHz to 39.1513 MHz in 500 μs . Depending on the specific measurement, the last state preparation for ${}^{40}\text{K}$ can be also accomplished optionally below the Feshbach resonance position on the molecular side of the resonance at 152.40 G. The frequency in this case is swept from 36.2292 MHz to 38.3241 MHz in 500 μs .

For all ARP of ${}^6\text{Li}$ and ${}^{40}\text{K}$ a sweep duration of seven times the Rabi period is chosen. Due to stability reasons, ${}^6\text{Li}$ is transferred first to the absolute ground state of the hyperfine manifold before the ARP's for ${}^{40}\text{K}$ are accomplished.

5.2 Feshbach loss spectroscopy

As depicted in Tab. 2.1, several *s*-wave interspecies Feshbach resonances are identified in (Wille *et al.*, 2008) by Feshbach loss spectroscopy of a non-degenerate ${}^6\text{Li}$ - ${}^{40}\text{K}$ mixture. In the following, the interspecies Feshbach resonance at 155 G is characterized. This specific resonance possesses a comparatively large width of 0.81 G according to coupled channels calculations (Wille *et al.*, 2008), and involves the states $|1/2, 1/2\rangle$ of ${}^6\text{Li}$ and $|9/2, -5/2\rangle$ of ${}^{40}\text{K}$. Some preparatory measurements are also done at the interspecies Feshbach resonance located at 168 G, since this resonance implies a simpler state preparation ${}^6\text{Li}|1/2, 1/2\rangle$ and ${}^{40}\text{K}|9/2, -9/2\rangle$, but the width is considerably smaller.

In this section, the lifetime of a ${}^6\text{Li}$ - ${}^{40}\text{K}$ mixture close to the interspecies Feshbach resonance at 155 G is investigated. The mixture is loaded into the ODT with trapping frequencies given in Eq. (5.1). In this trap particle numbers of $N_{\text{Li}} \approx N_{\text{K}} \approx 1 \times 10^5$ and temperatures of $T_{\text{Li}} = 0.4 T_{\text{F}}^{\text{Li}}$ and $T_{\text{K}} = 0.6 T_{\text{F}}^{\text{K}}$ (T_{F} being the Fermi temperature) correspond to peak densities of $n_{0,\text{Li}} = 1.4 \times 10^{13} \text{ cm}^{-3}$ and $n_{0,\text{K}} = 7.4 \times 10^{13} \text{ cm}^{-3}$.

5. Ultracold Fermi-Fermi molecules at a narrow Feshbach resonance

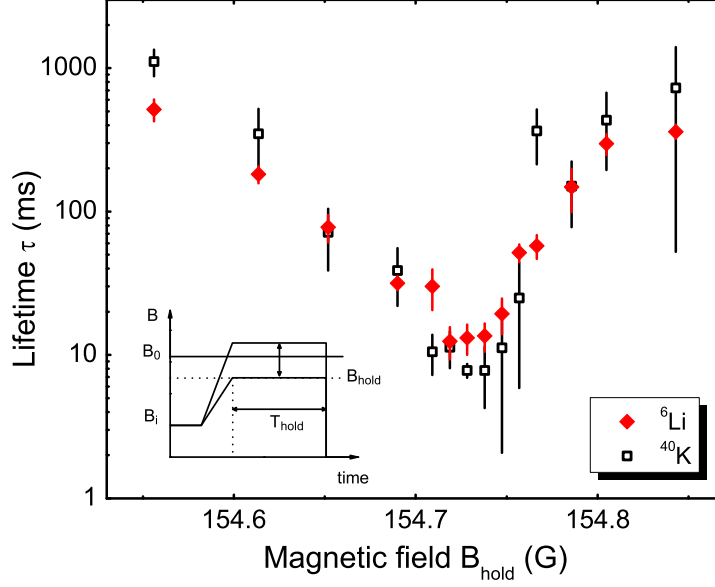


Figure 5.2: Lifetime of the ^6Li - ^{40}K mixture as a function of magnetic field in the vicinity of an interspecies Feshbach resonance. The lifetime of the mixture can be varied by two orders of magnitude. The minimum lifetime is found to be located at a magnetic field strength of $B = 154.72(5)$ G.

After preparation of the mixture in the absolute ground states, the magnetic bias field is ramped in 30 ms from 20.3 G to $B_i = 152.40$ G, i.e. to the molecular side of the Feshbach resonance. The ^{40}K atoms are then transferred to the state $|9/2, -5/2\rangle$ by an ARP. Subsequently, the magnetic field is ramped from B_i to a variable value B_{hold} within 0.5 ms where the lifetime of the mixture is investigated by holding the atoms for a variable time T_{hold} at constant magnetic field strength B_{hold} . After the holding period, the magnetic field strength is rapidly decreased with an initial slope of 820 G/ms to a bias field of 1 G. After a subsequent holding time of 5 ms, the clouds are released from the trap, and the ^6Li and ^{40}K atoms are imaged by resonant light after 1 ms and 4 ms of free expansion. The data is presented in Fig. 5.2. Each data point corresponds to a fitted time constant τ of the exponential decay of the atom numbers of ^6Li and ^{40}K at a single magnetic field strength. The lifetime of the mixture τ decreases close to the resonance position by two orders of magnitude to a minimum value of only 10 ms. The corresponding magnetic field strength of the minimum is $B = 154.72(5)$ G. This determined magnetic field position of the maximum loss will be discussed and compared to forthcoming measurements in Sec. 6.4.

The asymmetric lineshape of the losses is in qualitative agreement with predictions from three-body relaxation (D’Incao and Esry, 2006; Levinsen and Petrov, 2011). This

5.3 Heteronuclear Fermi-Fermi molecules

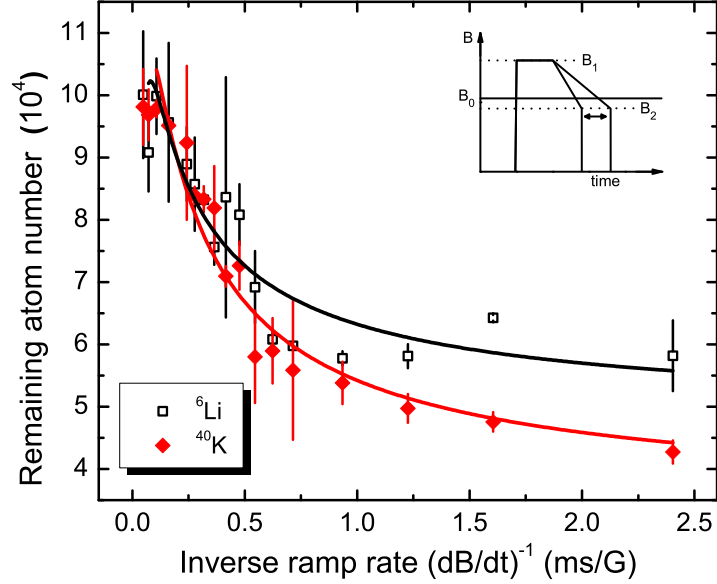


Figure 5.3: Adiabatic conversion of molecules from atoms. The fitting curve corresponds to a Landau-Zener theory for adiabatic molecule conversion at a narrow Feshbach resonance based on the two-channel model (Gurarie, 2009), cf. Sec. 2.3.3. The characteristic ramp rate is $\kappa \approx 3.5$ G/ms according to the fit.

vibrational relaxation leads to losses of atoms and molecules from the trap.

5.3 Heteronuclear Fermi-Fermi molecules

Heteronuclear molecules are formed from a quantum degenerate mixture of ${}^6\text{Li}$ and ${}^{40}\text{K}$ atoms by an adiabatic magnetic field sweep across an interspecies Feshbach resonance. In the following, the adiabaticity of molecule formation is characterized in Sec. 5.3.1, the Feshbach resonance crossover from molecules on the molecular side to unbound atoms on the atomic side is investigated in Sec. 5.3.2, and the lifetime of the molecules is studied in Sec. 5.3.4. The latter is done with a direct detection scheme for the molecules, which is brought forward for discussion in Sec. 5.3.3.

5.3.1 Adiabatic conversion of atoms to molecules

In this measurement, the inverse magnetic field ramp rate is varied to determine the time scale for adiabaticity of the molecule creation process. The magnetic field is linearly ramped from the atomic side at $B_1 = 156.44$ G to the molecular side $B_2 = 154.36$ G, while the ramp rate is varied. After the ramp, the magnetic field strength is rapidly decreased

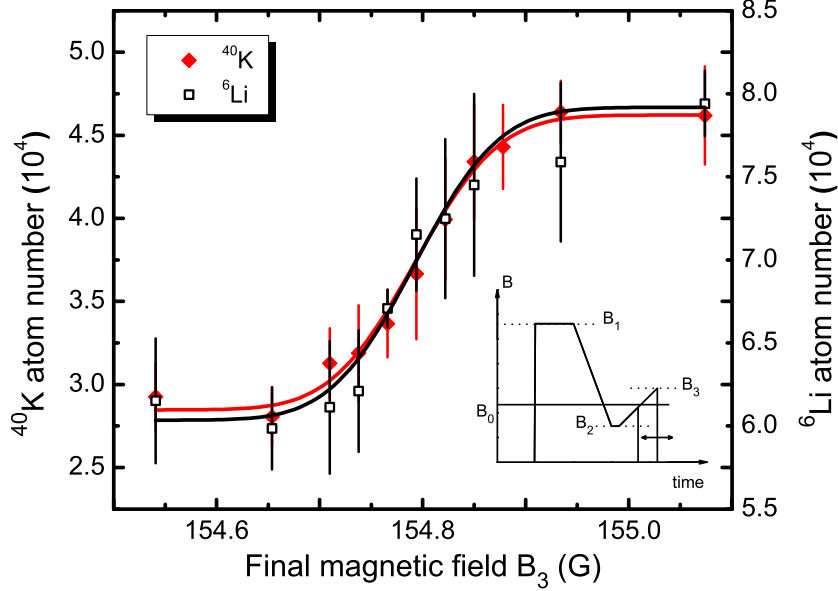


Figure 5.4: Reconversion to atoms from dissociated molecules. The center of this crossover is found with a fit to an error function at $B = 154.79(8)$ G, and the indicated uncertainty corresponds to the 10 % and 90 % levels.

for absorption imaging of the clouds, as already described for the loss measurement in Sec. 5.2. The results are presented in Fig. 5.3. The detection is only sensitive to free atoms, the missing fraction of atoms at large inverse ramp rates as observed in the measurement is attributed to the adiabatic formation of molecules. Up to 4×10^4 molecules are produced with a conversion efficiency of about 50 % according to the measurement presented in Fig. 5.3. The fitting curve is an exponential function consistent with the behavior expected from a Landau-Zener theory of the time-dependent conversion process of atoms into molecules at a narrow Feshbach resonance (Gurarie, 2009). From the fit, assuming that the Landau-Zener parameter is proportional to the inverse magnetic field ramp rate $\delta_{LZ} = \kappa (dB/dt)^{-1}$, one obtains for the characteristic parameter $\kappa \approx 3.5$ G/ms. The corresponding value derived for the broad intraspecies Feshbach resonance of ^{40}K at 202.1 G (Regal *et al.*, 2003a) is significantly smaller. This indicates that the coupling strength is indeed small and the Feshbach resonance is closed-channel dominated.

5.3.2 Reconversion to atoms from dissociated molecules

In this section it is shown that the atom number decrease from Fig. 5.3 is caused by formation of molecules. The mixture is prepared in the relevant Zeeman states at a magnetic field strength of $B_1 = 156.90$ G on the atomic side of the resonance. Molecules

5.3 Heteronuclear Fermi-Fermi molecules

are formed by an adiabatic magnetic field ramp to $B_2 = 154.54$ G on the molecular side of the resonance. The magnetic field ramp rate is constant with a value of 1 G/ms, which is smaller than the characteristic ramp rate κ obtained from the measurement in Sec. 5.3.1. After 200 μ s of holding on the molecular side, the magnetic field strength is linearly ramped to a final and variable value B_3 with the same ramp rate as the previous ramp. The atoms are imaged at low magnetic field strengths as described in the previous sections. The results are shown in Fig. 5.4. As can be seen, if B_3 is located on the molecular side of the resonance molecules are existent which can not be detected with the imaging scheme, but are noticeable by a smaller detected atom number. On the other hand, if the final magnetic field value B_3 lies on the atomic side, the molecules are adiabatically dissociated into free atoms, and a higher atom number is detected. The atom number is increased by $1.8(3) \times 10^4$, corresponding to the dissociated molecule number. Within the uncertainties the atom number increase both for ${}^6\text{Li}$ and ${}^{40}\text{K}$ are the same. This shows an excellent atom number calibration, which is independently done for both species. A crossover behavior from molecules to atoms is observed. The center of this crossover regime is determined by a fit with an error function (solid lines) and is found at $B = 154.79(8)$ G. The indicated uncertainty corresponds to the 10 % and 90 % levels. This determined position is not necessarily the Feshbach resonance position, as interpreted in a similar measurement for the broad ${}^{40}\text{K}$ intraspecies resonance in (Regal *et al.*, 2003a). This result of the localization of the crossover region across the Feshbach resonance will be discussed and compared to other measurements in Sec. 6.5.

5.3.3 Direct detection of molecules

The direct imaging method relies on the heteronuclear nature of the molecule (Ospelkaus *et al.*, 2008). For the heteronuclear case both the molecules and unbound atoms can be directly imaged with the same resonant imaging frequency of the atoms, since the transition energy of the molecules is barely shifted by the small binding energy of the Feshbach molecules. The binding energy can be varied by the magnetic field detuning, cf. Eq. (2.39). In the heteronuclear case, the weak dependence of the optical transition frequency with internuclear distance allows to detect the molecules over a wider range of magnetic field strengths. For the heteronuclear case, the van der Waals potential of the molecular ground and first optically excited state have the same dependence on the internuclear separation, namely $1/R^6$. This is a favorable property in contrast to the homonuclear case, where the resonant dipole-dipole interaction implies a $1/R^3$ dependence of the first optically excited state.

Before imaging, the unbound atoms are separated from the produced molecules by means of a magnetic field gradient, which is applied during time-of-flight. For the Feshbach resonance near 155 G with projection quantum number $M_F = -2$, which is predominantly investigated within this work, the situation for this purification step is particularly beneficial. As can be seen in Fig. 5.5(b) from the asymptotic bound state model (Wille *et al.*, 2008), cf. Sec. 2.3.2, the molecule possesses a nearly vanishing magnetic moment. In contrast, the pair of the asymptotically unbound atoms has a nonvanishing magnetic moment (in red dashed). As a consequence, the Stern-Gerlach force acts dominantly on

5. Ultracold Fermi-Fermi molecules at a narrow Feshbach resonance

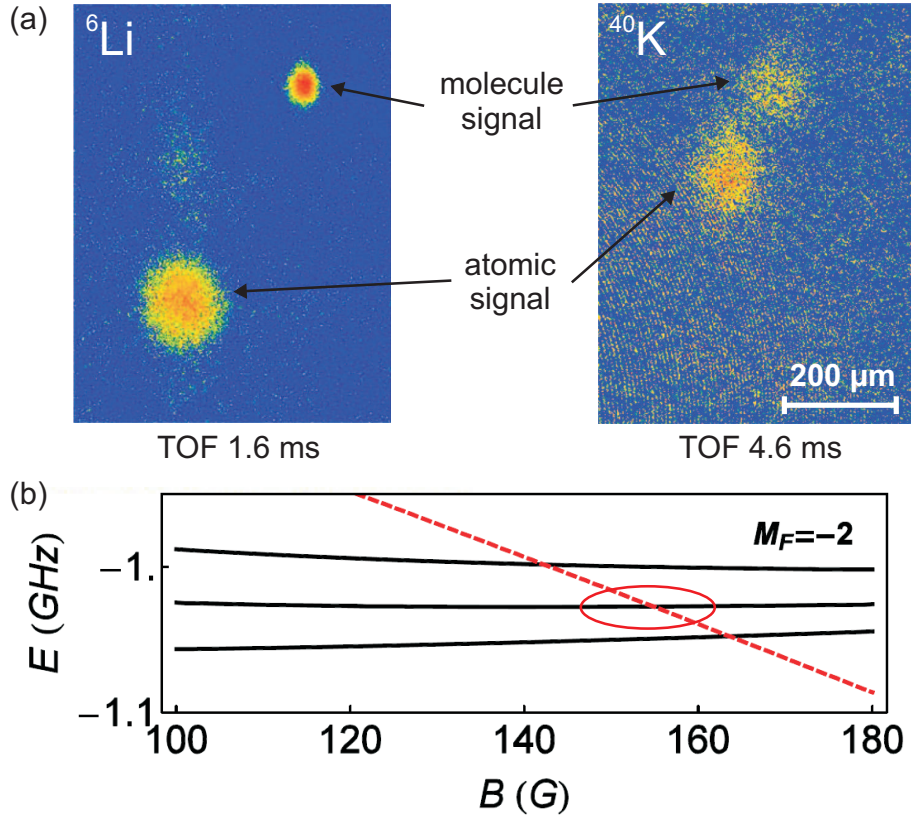


Figure 5.5: Direct detection of molecules at high magnetic field after application of a Stern-Gerlach force. In (a) an exemplary absorption image of the atomic fraction which is bound in molecules and the unbound atoms are shown. In (b), the asymptotic bound state model is applied to the s -wave interspecies ${}^6\text{Li}$ - ${}^{40}\text{K}$ Feshbach resonances, and reveals the values of the magnetic moments of the molecules and unbound atoms.

the atoms, whereas the molecules remain almost unaffected near the trap center after the magnetic field gradient is applied. Note that this behavior does not hold for any interspecies ${}^6\text{Li}$ - ${}^{40}\text{K}$ Feshbach resonance.

An example for a typical direct detection absorption image of the molecules and atoms is presented in Fig. 5.5(a). The following measurements are performed in a weaker ODT with trapping frequencies given in Eq. (5.2), and with lower temperatures. Molecules are formed at a magnetic field strength of 154.65 G. The power of the ODT beams is switched off and the clouds expand. During expansion, a magnetic field gradient of 167 G/cm and a duration of $570 \mu\text{s}$ is applied, cf. Fig. 3.8(b). After a total time of expansion of 1.6 ms for ${}^6\text{Li}$ and 4.6 ms for ${}^{40}\text{K}$ the clouds are imaged. For the mechanism of the molecule imaging, presumably the first few photons break up the molecules and the subsequent photons scatter off from the resulting unbound atoms. On the left-(right-)hand side of Fig. 5.5(a) the absorption image of ${}^6\text{Li}$ (${}^{40}\text{K}$) is shown. Because of the different masses

5.3 Heteronuclear Fermi-Fermi molecules

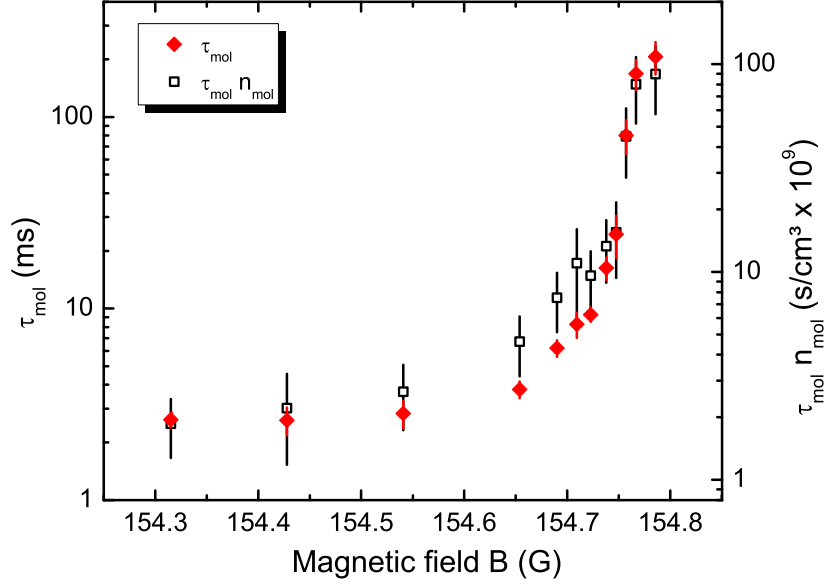


Figure 5.6: Lifetime of molecules in an atom-molecule ensemble in dependence of magnetic field in the vicinity of an interspecies Feshbach resonance. A variation of the lifetimes of the molecules in the atom-molecule mixture by almost two orders of magnitude with maximum values of more than 100 ms is observed for the investigated magnetic field range close to resonance.

of the two atomic species and molecules, the individual clouds have different expansion velocities. The contrast of the absorption signal of ${}^6\text{Li}$ and ${}^{40}\text{K}$ differ due to different optical transition strengths, cf. Sec. 3.7.1.

5.3.4 Molecule lifetime in an atom-molecule ensemble

Using the direct detection method for the molecules, a measurement of the lifetime of the molecules in an atom-molecule mixture as a function of magnetic field strength is presented in the following. For this measurement an ODT with lower trapping frequencies, as given in Eq. (5.2), is used.

Peak densities before molecule production are $n_{\text{Li}} = 2.9 \times 10^{12} \text{ cm}^{-3}$ and $n_{\text{K}} = 2.2 \times 10^{13} \text{ cm}^{-3}$ with temperatures $T_{\text{Li}} = 0.3 T_{\text{F}}^{\text{Li}}$ and $T_{\text{K}} = 0.4 T_{\text{F}}^{\text{K}}$. The mixture is prepared at a magnetic field strength of $B_1 = 156.44 \text{ G}$. The lifetime is investigated after an adiabatic sweep to a variable value B_{hold} . The atom-molecule mixture is held for a variable duration and the clouds are released from the trap and detected separately as described in the previous section. From the decaying molecule number we infer $1/e$ lifetimes. The result for the molecular lifetime in an atom-molecule mixture in dependence of the magnetic

5. Ultracold Fermi-Fermi molecules at a narrow Feshbach resonance

field strength is presented in Fig. 5.6. Lifetimes of the molecules of more than 100 ms in the atom-molecule mixture are detected close to resonance. The lifetime of the molecules is varied by almost two orders of magnitude in the vicinity of the Feshbach resonance. As will be discussed also in Sec. 6.5, the very long molecular lifetimes are measured for magnetic field strengths in the crossover regime of the Feshbach resonance, see Fig. 5.4. The numbers and hence densities of the molecules in the crossover regime are smaller towards the atomic side. Therefore, one should consider a lifetime which is weighted by the average molecule density. The product of the average molecule density and the molecule lifetime would correspond to the inverse time constant of a second order decay process. This quantity also shows a significantly increasing behavior at higher magnetic fields in the crossover regime, see Fig. 5.6. Such an increased lifetime of molecules close to the Feshbach resonance has been also observed in homonuclear fermionic spin mixtures (Cubizolles *et al.*, 2003; Jochim *et al.*, 2003b; Regal *et al.*, 2004b). The underlying mechanism for the longevity in the homonuclear case is elucidated on the basis of the Pauli exclusion principle of an open-channel dominated Feshbach resonance in fermionic systems, see Sec. 2.3.4.1, (Petrov *et al.*, 2004a). In the present situation, this explanation is not applicable since the interspecies Feshbach resonance is closed-channel dominated for the experimental trap densities.

By the time when the present measurements are performed, the exact resonance position is not known. The measurement of inelastic three-body losses in a ${}^6\text{Li}$ - ${}^{40}\text{K}$ mixture close to the Feshbach resonance as presented in Fig. 5.2 is not a necessary determination of the resonance position. For the broad intraspecies Feshbach resonance in ${}^6\text{Li}$ around 834 G, for instance, the magnetic field position of maximum three-body losses in comparison to the position of the divergence of the elastic scattering length is shifted by approximately 80 G (Dieckmann *et al.*, 2002; Bourdel *et al.*, 2003).

In the next chapter, the cross-dimensional relaxation method is applied for the first time to a Fermi-Fermi mixture to probe elastic *s*-wave scattering properties in the vicinity of the Feshbach resonance. This allows for a precise determination of the resonance position. The results of the measurements presented in this chapter will be revisited in the discussion in Sec. 6.5.

5.3 Heteronuclear Fermi-Fermi molecules

Chapter 6

s-wave interaction in a two-species Fermi-Fermi mixture

In this chapter, the method of cross-dimensional relaxation (CDR) serves as a tool to probe elastic collisions in a Fermi-Fermi mixture of ${}^6\text{Li}$ and ${}^{40}\text{K}$. In Sec. 6.1, the experimental sequence is presented for the study of CDR in the vicinity of an interspecies Feshbach resonance. In Sec. 6.2, the obtained thermalization curves allow to determine the ratio of β -factors as defined in Eq. (2.83). Under same initial conditions of ${}^6\text{Li}$ and ${}^{40}\text{K}$, a ratio of $\beta_{\text{KLi}}/\beta_{\text{LiK}} = 3.7$ is expected from the kinetic model (see Sec. 2.4.2.4). In Sec. 6.3, the method is applied to an interspecies Feshbach resonance, where elastic scattering cross sections can be deduced and a Fano-shaped profile is obtained. A precise determination of the Feshbach resonance position, as shown in Sec. 6.4, allows for a comparison to previously presented results in Ch. 5. This reveals the first observation of a many-body effect in the crossover regime of a narrow Feshbach resonance in Sec. 6.5.

Parts of this chapter are published in

L. Costa, J. Brachmann, A.-C. Voigt, C. Hahn, M. Taglieber, T.W. Hänsch, and K. Dieckmann, *s-Wave Interaction in a Two-Species Fermi-Fermi Mixture at a Narrow Feshbach Resonance*, Phys. Rev. Lett. **105**, 123201 (2010).

In this publication the same defective calibration formula was used as in (Voigt *et al.*, 2009) and the errata (Voigt *et al.*, 2010E; Costa *et al.*, 2010E) apply in a similar way as already discussed in the introduction of Ch. 5. In the following chapter, the given magnetic field values are also corrected by a shift of 375 mG towards lower magnetic fields as compared to the values given in (Costa *et al.*, 2010). The physical interpretation presented in this publication remains unaltered.

6.1 Experimental sequence

The experimental sequence for the measurements presented in this chapter is schematically illustrated in Fig. 6.1. A quantum-degenerate ${}^6\text{Li}$ - ${}^{40}\text{K}$ mixture is prepared in a cigar-shaped magnetic trap, where the lowest trapping frequency is along the x direction (Taglieber *et al.*, 2006, 2008). In order to induce an energy anisotropy, the aspect ratio of

6.1 Experimental sequence

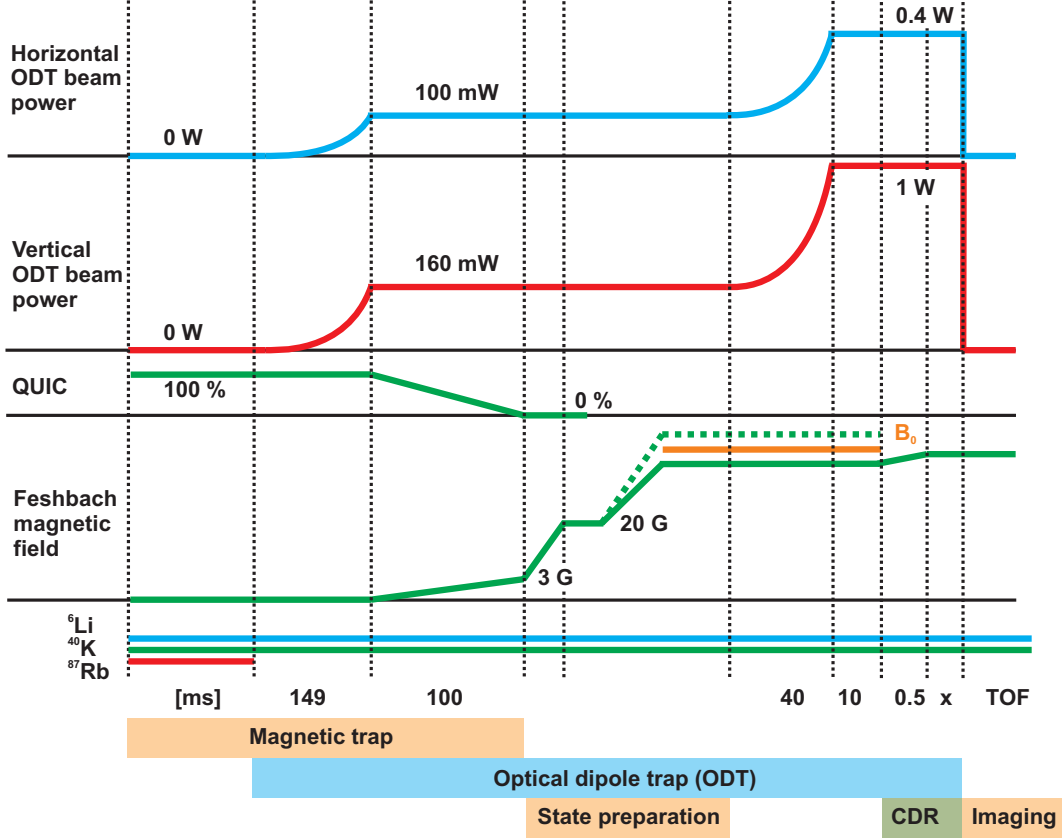


Figure 6.1: Experimental sequence for the study of cross-dimensional relaxation (CDR) in a Fermi-Fermi mixture of ${}^6\text{Li}$ and ${}^{40}\text{K}$.

the cloud is changed by transferring the atoms into a shallow crossed beam optical dipole trap. The beams are along the x and z direction and the configuration is the same as for the measurements in the previous Ch. 5. The duration of the transfer is 249 ms insuring adiabaticity with respect to the trap oscillation period, but avoiding CDR during the transfer. Because of the low densities, and hence the slow relaxation time, the energy anisotropy is preserved in the clouds during the stage where the gas is transferred to the desired Zeeman states of ${}^6\text{Li}$ $|1/2, 1/2\rangle$ and ${}^{40}\text{K}$ $|9/2, -5/2\rangle$ (cf. Ch. 5). Subsequently, the magnetic field strength is ramped close to the Feshbach resonance. In order to increase the densities and the rethermalization speed relative to the trap loss rate the ODT power is ramped up over 40 ms. This results in the trapping frequencies (ν_x, ν_y, ν_z)

$$(963, 1076, 479) \text{ Hz for } {}^6\text{Li} \text{ and } (561, 627, 279) \text{ Hz for } {}^{40}\text{K}, \quad (6.1)$$

for all $\nu_i \pm 5\%$. Hence, the aspect ratio of the trap in the observation plane (x - z) is changed. In this final trap configuration, the thermalization process of the mixture is investigated by holding the atoms for variable times t . The energy anisotropies are then inferred from the aspect ratios found in absorption imaging at high magnetic field

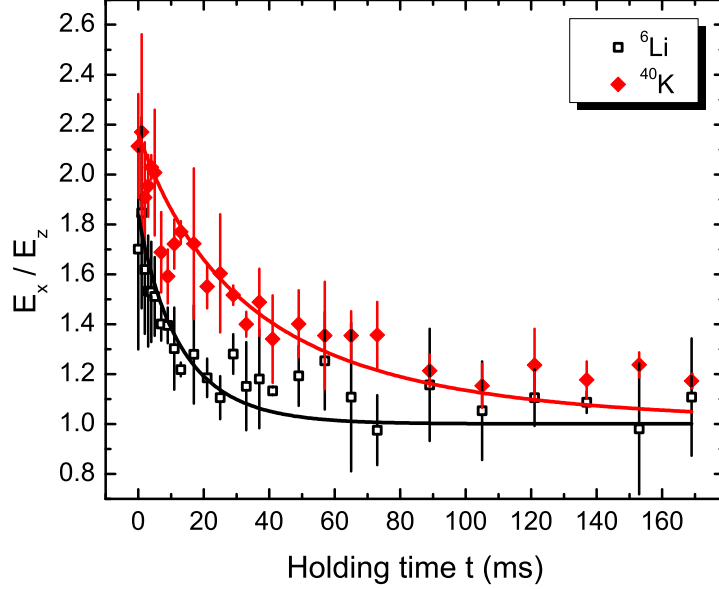


Figure 6.2: Cross-dimensional thermal relaxation of ${}^6\text{Li}$ and ${}^{40}\text{K}$ in the mixture by inter-species elastic collisions at 152.4 G. The initial conditions for ${}^6\text{Li}$ (${}^{40}\text{K}$) are $N = 3.5 \times 10^4$ (8.0×10^4), $E_x/E_z = 1.8$ (2.2) and $E_y/E_z = 1.2$ (1.8). The uncertainty in the determination of atom numbers is assumed to be 50%.

after time-of-flight of 2 ms for ${}^6\text{Li}$ and 5 ms for ${}^{40}\text{K}$. In order to obtain the size of the clouds it is sufficient to use Gaussian fits instead of Fermi-Dirac density profiles, since our Fermi-Fermi mixture is not deeply degenerate. For fully thermalized clouds in this trap, typical atom numbers of $N_{\text{Li}} \approx 5 \times 10^4$ and $N_{\text{K}} \approx 7 \times 10^4$ and temperatures of $T_{\text{Li}} = 0.5 T_{\text{F}}^{\text{Li}}$ and $T_{\text{K}} = 0.6 T_{\text{F}}^{\text{K}}$ correspond to peak densities of $n_{0,\text{Li}} = 4.0 \times 10^{12} \text{ cm}^{-3}$ and $n_{0,\text{K}} = 2.8 \times 10^{13} \text{ cm}^{-3}$. Under these conditions the error in the measured mean energy per particle obtained from the cloud size is at most 6%. Further, the description of the relaxation by the classical kinetic model is justified.

6.2 Cross-dimensional thermal relaxation

An example for a typical thermalization process in the mixture ${}^6\text{Li}$ - ${}^{40}\text{K}$ is shown in Fig. 6.2. The measurement is performed at a magnetic field value of 152.4 G on the molecular side of the Feshbach resonance, but sufficiently distant from the Feshbach resonance to avoid the formation of molecules. The CDR rates for ${}^6\text{Li}$ and ${}^{40}\text{K}$ are determined from this data by least square fits with the expression given in Eq. (2.89). The initial conditions for the mean energies are determined in a separate measurement along a different imaging direction. One obtains for the CDR rates $\Gamma_{\text{Li,K,CDR}} = 63(8) \text{ ms}^{-1}$

6.3 Elastic scattering cross sections

and $\Gamma_{\text{KLi,CDR}} = 19(2) \text{ ms}^{-1}$ as defined in Eq. (2.83). Since we only need to consider interspecies interactions for the spin-polarized fermions, the ratio of the obtained relaxation rates yields direct information about the ratios of β -factors, according to $\beta_{\text{KLi}}/\beta_{\text{LiK}} = \Gamma_{\text{LiK,CDR}} \cdot N_{\text{Li}} / (\Gamma_{\text{KLi,CDR}} \cdot N_{\text{K}}) = 1.5(1.1)$. The relaxation of ${}^6\text{Li}$ is indeed faster than the one of ${}^{40}\text{K}$. This is consistently found in similar data sets for various magnetic fields. However, the accuracy in the determination of the ratio of β -factors is limited due to systematic uncertainties in the atom number determination, which we assume to be about 50%. The measured ratio is smaller than the ratio predicted from the kinetic model. This is mainly attributed to an imbalance between the mean energies per particle averaged over all spatial directions for the two species. The ${}^6\text{Li}$ cloud possesses a higher mean energy per particle as compared to ${}^{40}\text{K}$ and the difference between the two species is up to 36%. A possible reason for this imbalance is the mismatch in the Fermi energies of the two species due to the large mass ratio. For our trap the difference of the Fermi energies of both species is about 23%. Since the influence of a mismatch in Fermi energies is not considered in our model, we perform classical Monte-Carlo simulations with a broad range of initial energy imbalance between the two species, cf. Fig. C.6. We find a strong dependence of the observed β ratio on the initial imbalance. For the initial experimental conditions of Fig. 6.2 the Monte-Carlo simulations yield 2.8 for the β ratio. For a more accurate quantitative study a precise determination of the atom numbers is required.

6.3 Elastic scattering cross sections

We use the CDR method to map elastic scattering cross sections for different magnetic field strengths B across the Feshbach resonance between ${}^6\text{Li}$ and ${}^{40}\text{K}$ at 155 G. The scattering cross section $\sigma(B)$ follows a Fano-shaped profile, cf. Eqs. (2.26) and (2.36), and is widely tunable near the Feshbach resonance as it is directly related to the scattering length, see Eq. (2.38). In Fig. 6.3, measured values of the elastic scattering cross section σ_{LiK} for different magnetic field strengths are shown. The collision rate $\Gamma_{\text{LiK,CDR}}$ is derived from thermalization curves in a same way as outlined for the measurement of Fig. 6.2, and normalized by $(\beta_{\text{LiK}}^{-1} n_{\text{LiK}} v_{\text{LiK}})$ to acquire the scattering cross section. Only the data of ${}^6\text{Li}$ is considered here, since the thermalization is faster for ${}^6\text{Li}$ than for ${}^{40}\text{K}$. This avoids long holding times close to resonance that would otherwise lead to significant molecule production. The elastic scattering cross section σ varies with B by almost three orders of magnitude in the vicinity of the resonance. Considering the uncertainty in the particle number determination we find good agreement between the values of the scattering lengths extracted from the data and predicted from theory away from resonance.

For these measurements we expect that the following deviations are not significant. First, the influence of Pauli blocking on the observed cross section is estimated to be less than 15% for the degeneracy parameters of our mixture (DeMarco *et al.*, 2001; Gehm *et al.*, 2003). Second, we exclude the influence of hydrodynamic behavior on the observed relaxation curves. Only for a magnetic field on resonance we expect that the collisions

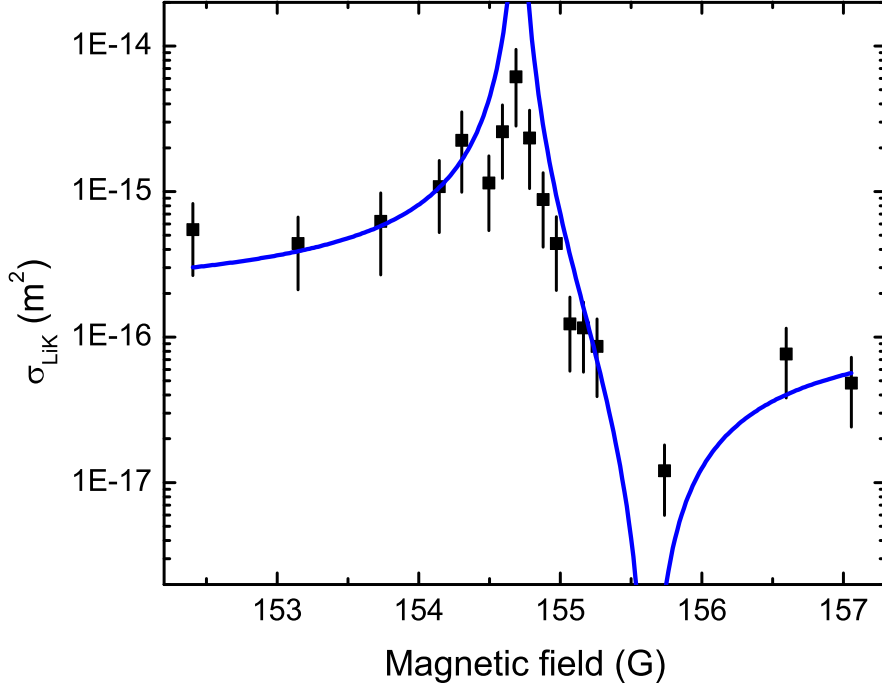


Figure 6.3: Scattering cross sections measured with cross-dimensional thermal relaxation across an interspecies Feshbach resonance between ${}^6\text{Li}$ and ${}^{40}\text{K}$. The solid line is a guide to the eye and corresponds to a theoretical Fano curve with the parameters $B_0 = 154.71$ G, $\Delta = 1.02$ G, $a_{\text{bg}} = 63.5 a_0$ (Wille *et al.*, 2008), $k = k_F$, and $\mu_{\text{res}} = 1.7 \mu_B$ as obtained from a simple asymptotic bound state model calculation (Wille *et al.*, 2008).

occur on a similar timescale as the mean trap oscillation period. Further, we observe moderate loss of ${}^6\text{Li}$ atoms due to the finite trap depth. The loss of ${}^6\text{Li}$ can be considered by a modified fit model for $\Gamma_{\text{KLi,CDR}}$. By comparison we find the correction to be less than 5%, as the time scale of the loss is much larger as compared to the relaxation. On the other hand, the relaxation rate $\Gamma_{\text{LiK,CDR}}$ of ${}^6\text{Li}$, which is the basis of the cross sections presented in Fig. 6.3, has a negligible dependence on N_{Li} , cf. Fig. C.2. From the decay rates $\Gamma_{\text{evap,Li}}$ of ${}^6\text{Li}$ due to plain evaporation $N_{\text{Li}}(t) = N_{\text{Li}}(0) \exp(-t \Gamma_{\text{evap,Li}})$, the scattering cross section can be inferred (Tiecke *et al.*, 2010a), cf. Eq. (2.67). For our measurements we find fair agreement between the absolute values of σ obtained from CDR and plain evaporation for different magnetic fields. The data of the scattering cross section is compared to a theoretical Fano curve (solid blue line in Fig. 6.3), where the separately determined values for width and position of the Feshbach resonance, which will be presented in the subsequent section, have been invoked.

6.4 Position and width of Feshbach resonance

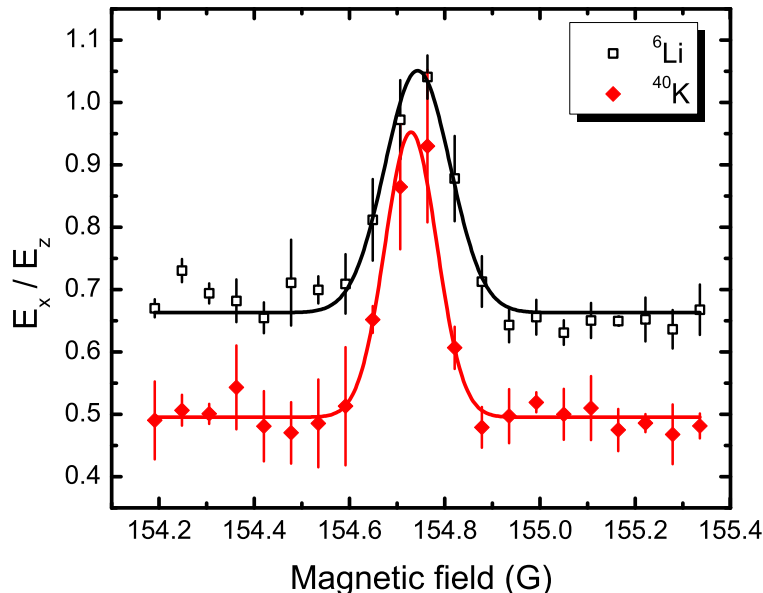


Figure 6.4: Example for a measurement of the magnetic field dependent aspect ratio after a constant holding time. The aspect ratio relaxes to one at magnetic field strengths with highest scattering cross sections. The data is fitted with a Gaussian curve and for this example the maximum of the scattering cross section occurs at $B = 154.729(5)$ G for ${}^6\text{Li}$ and $B = 154.719(3)$ G for ${}^{40}\text{K}$. The Gaussian curves have a full width at half maximum of $162(26)$ mG for ${}^6\text{Li}$ and $128(9)$ mG for ${}^{40}\text{K}$.

6.4 Position and width of Feshbach resonance

For the determination of the maximum and minimum of the scattering cross section, the mixture is prepared in a non-equilibrium state as outlined in the previous section, and the magnetic field dependent aspect ratio E_x/E_z after a constant holding time is measured. An example for such a measurement with constant holding time is shown in Fig. 6.4. For this measurement, the ${}^6\text{Li}$ and ${}^{40}\text{K}$ clouds are prepared with an aspect ratio E_x/E_z significantly smaller than one, and the aspect ratios relax to one at magnetic field strengths where the largest scattering cross sections occur. By accounting for eventual shifts of the magnetic field position of the resonance due to density effects, we perform several measurements with different trap frequencies. Taking the average of these measurements, the maximum and minimum of the scattering cross section are found at $B_{\text{max}} = 154.71(5)$ G and $B_{\text{min}} = 155.73(4)$ G, respectively. The difference of both values is a measure for the width of the resonance and yields $\Delta^* = 1.02(7)$ G. We find a slightly higher value as compared to the value $\Delta = 0.81$ G from coupled channels calculations given in (Wille *et al.*, 2008). We attribute this difference to the finite Fermi energies and temperatures of

the clouds. The position of the maximum of the elastic scattering cross section is in good agreement with the previously measured minimum of the lifetime of the ${}^6\text{Li}$ - ${}^{40}\text{K}$ mixture at 154.72(5) G, see Sec. 5.2, and hence the resonance is determined to be located at $B_0 = 154.71(5)$ G. For the temperature of the mixture, the magnetic field position of the maximum of the thermally averaged scattering cross section corresponds to the Feshbach resonance position within typical experimental uncertainties, see also App. C.3.

In (Naik *et al.*, 2011), the position and width of the same interspecies ${}^6\text{Li}$ - ${}^{40}\text{K}$ Feshbach resonance is determined with a different method based on observing the damped sloshing motion of ${}^{40}\text{K}$ due to interactions in the mixture. The obtained results $B_0 = 154.707(5)$ G, $\Delta = 0.92(5)$ G are in full consistency with the values presented here. Updated coupled channels calculations given in the same cited work yield $B_0 = 154.75$ G, $\Delta = 0.88$ G, $a_{\text{bg}} = 63.0 a_0$, and $\mu_{\text{res}} = 1.6 \mu_B$.

6.5 Two-body bound states at the crossover of a narrow Feshbach resonance

In the following section, the result for width and position of the Feshbach resonance is taken into consideration for the interpretation of the measurements described in Ch. 5.

In Fig. 6.5 the following measurements are summarized and compared with respect of their magnetic field dependence:

- density weighted lifetime of the molecules in an atom-molecule mixture (see Fig. 5.6)
- atom conversion from dissociated molecules (see Fig. 5.4)
- result for the Feshbach resonance position (see Sec. 6.4).

The comparison of the magnetic field dependent measurements is based on repeatedly performed magnetic field calibrations, which result in an overall magnetic field uncertainty of only 7 mG. In the measurements the existence of long-lived molecules at magnetic field strengths of up to 154.8 G on the atomic side of the resonance is observed. Also, the magnetic field position of the resonance is located within the uncertainty at the onset of dissociation of the molecular state and of reconversion into atoms. This property differs from similar observations in open-channel dominated resonances, where the resonance position is located in the center of the crossover (Regal *et al.*, 2003a). We now conjecture that we have demonstrated for the first time a many-body effect at the BEC-BCS crossover for a narrow Feshbach resonance, which has been theoretically predicted by (Gurarie and Radzihovsky, 2007) and outlined in Sec. 2.3.4.2. In this crossover regime, if the magnetic field is tuned above the resonance position for zero kinetic energy, the existence of molecules is energetically favorable as compared to individual atoms occupying states at the Fermi edge. For a narrow resonance this can be resolved as the coupling energy is small compared to the Fermi energy. In the limits of zero coupling and temperature, the extension of molecule existence on the atomic side occurs up to magnetic fields corresponding to the sum of the Fermi energies, here ≈ 70 mG for the trap

6.5 Two-body bound states at the crossover of a narrow Feshbach resonance

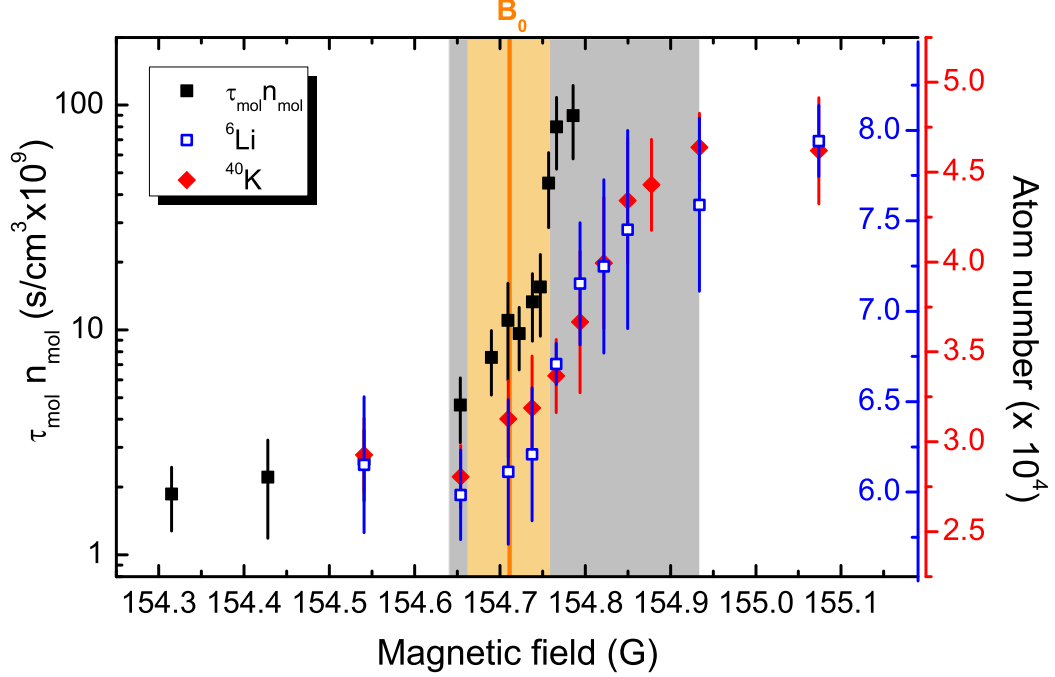


Figure 6.5: Comparison between the measurements of the magnetic field dependent density weighted lifetime of the molecules in an atom-molecule mixture (see Fig. 5.6), of the atom reconversion from dissociated molecules (see Fig. 5.4) and the result of the Feshbach resonance position. The orange shaded area is associated with the uncertainty of 50 mG for the determination of the resonance position at 154.71(5) G, the gray shaded area is a guide to the eye for describing the crossover region from bound to unbound states.

configuration given in Eq. (5.1). However, in the present case of finite coupling, because of broadening molecules are expected to be present at even higher magnetic fields.

In (Naik *et al.*, 2011), the magnetic field dependent lifetime of the molecules is calculated. The prediction is in qualitative agreement with the measurement presented here, and the sharp increased lifetime is associated with the entrance into the universal regime close to resonance as the molecular decay is suppressed by the centrifugal barrier of the scattering potential.

From a few-body description with a diagrammatic approach in (Levinsen and Petrov, 2011), it is calculated that for a detuning, where the effective range is of the order of the scattering length $-2r_{\text{eff}} \equiv r^* \approx a$, the atom-dimer relaxation rate in the s -wave channel is suppressed by three orders of magnitude for the ^6Li - ^{40}K mass ratio. This might explain the long lifetime of the molecules in the atom-molecule mixture, although the relaxation

6. *s*-wave interaction in a two-species Fermi-Fermi mixture

in the *p*-wave channel increases for $r^* \approx a$ by one order of magnitude. But similar as in (Naik *et al.*, 2011), the calculations in (Levinsen and Petrov, 2011) do not predict the existence of molecules on the atomic side of the resonance.

The unexpectedly long lifetime of the two-body bound states on the atomic side of the resonance requires further experimental investigation. The achieved experimental degeneracy parameters of the mixture do not suggest a Fermi superfluid state on the BCS side of the resonance. In the $T = 0$ limit the occupied states on the Fermi surface of the Fermi sea would suppress the dissociation of a molecular Bose-Einstein condensate by a magnetic field sweep due to Pauli blocking. For the present degeneracy parameter of the mixture, the lifetime of the molecules might still be extended and stabilized due to Pauli blocking what could be investigated by selectively removing unbound atoms in the trap. Preliminary measurements show that the two-body bound states on the atomic side of the resonance at 154.834(7) G have a small binding energy of < 1 kHz. The selective manipulation and removal of the unbound atoms must therefore be done carefully without affecting the bound states.

For the study of universal behavior throughout the entire strongly interacting regime, the Feshbach coupling energy needs to be much larger as compared to the Fermi energy $\Gamma_0 \gg E_F$. This could be achieved by lowering the particle number or trapping frequencies, while preserving submilligauss magnetic field control over an increased trapping volume. For very low density atomic samples the gravitational sag between the two fermionic species must be compensated by either an additional levitation field or by the use of the "magic" wavelength for the optical potential, where both species experience the same trapping frequency (Safronova *et al.*, 2006). This would offer a desirable density-density overlap for the study of strongly interacting Fermi gases.

6.5 Two-body bound states at the crossover of a narrow Feshbach resonance

Chapter 7

Conclusions and Outlook

Within this work the versatile experimental platform to study Bose-Fermi-Fermi mixtures has been extended by experimental techniques in order to produce bosonic heteronuclear molecules and to study many-body effects of a strongly interacting two-species Fermi-Fermi mixture at the crossover of a narrow interspecies Feshbach resonance.

The first milestone is the creation of ultracold heteronuclear bosonic molecules from a quantum-degenerate ${}^6\text{Li}$ - ${}^{40}\text{K}$ Fermi-Fermi mixture. This is accomplished by an adiabatic magnetic field sweep across a closed-channel dominated and narrow s -wave Feshbach resonance. Highest observed molecule production efficiencies are up to 50 % with a total molecule number of up to 4×10^4 . This number of produced Feshbach molecules is among the numbers reported from other experiments involving a heteronuclear mixture the highest observed one. In addition, exceptionally long molecule lifetimes of more than 100 ms in an atom-molecule ensemble have been detected. Long lifetimes were previously discovered in the pioneering experiments involving homonuclear Fermi spin mixtures. But the underlying mechanism, which leads to the observed longevity of the present system, is different due to the narrowness of the chosen interspecies Feshbach resonance in the ${}^6\text{Li}$ - ${}^{40}\text{K}$ mixture.

For obtaining a further understanding of the interacting ${}^6\text{Li}$ - ${}^{40}\text{K}$ mixture, the technique of cross-dimensional relaxation is applied to study elastic scattering properties of ${}^6\text{Li}$ and ${}^{40}\text{K}$. The method is applied for the first time to a two-species Fermi-Fermi mixture interacting via pure interspecies collisions. A kinetic model, Monte-Carlo simulations, and measurements were performed and show that the mean number of collisions required for rethermalization in the mixture are different for ${}^6\text{Li}$ and ${}^{40}\text{K}$. For pure interspecies collisions and assuming same particle number and initial energy anisotropy, the lighter particle requires on average less collisions for equilibration than the heavier one. For a quantitative analysis in the experiments identical starting conditions are challenging to obtain since the rethermalization rates exhibit a density, initial anisotropy, and temperature dependence. These dependencies are mainly investigated by Monte-Carlo simulations and by the presented kinetic model. Nonetheless the cross-dimensional relaxation method is suitable to measure relative changes of the scattering cross section in the vicinity of a Feshbach resonance. We apply the technique to the same interspecies s -wave

Feshbach resonance, where molecules are produced previously. Scattering cross sections are determined over a wide range of magnetic field strengths across the resonance, and from rethermalization measurements the position and width of the Feshbach resonance are found to be $B_0 = 154.71(5)$ G and $\Delta = 1.02(7)$ G, respectively. By comparison of the measurements, molecules are revealed on the atomic side of the resonance with very long lifetimes. This behavior is attributed to the closed-channel character of the Feshbach resonance and establishes the first observation of a many-body effect at a narrow resonance.

Most experiments so far focused predominantly on broad resonances. Although all known interspecies Feshbach resonances in the ^6Li - ^{40}K mixture are narrow and closed-channel dominated, a surprisingly long lifetime of the system is revealed and the challenges addressed for attaining the strongly interacting Fermi-Fermi mixture are worthwhile. A thorough understanding of the system's longevity and of the existence of molecules in the crossover regime is still required and both on the experimental as well as on the theoretical side efforts have to be made to investigate especially many-body effects at the crossover regime of a closed-channel dominated resonance. The closed-channel fraction in the crossover regime could be experimentally measured and quantified by an optical probe similar to (Partridge *et al.*, 2005). From the theoretical point of view, a few-body perspective can not explain the existence of molecules on the atomic side of the resonance, and only a collective property of the ensemble might account for the experimental observations. For instance, taking the limit of zero temperature, the dissociation of molecules in a pure molecular BEC by an adiabatic magnetic field sweep would be suppressed for magnetic field strengths above the resonance position and in the crossover region of a narrow Feshbach resonance. In this case the low energy and momentum states are occupied by unbound atoms in the Fermi sea, and hence the dissociation channels for the molecules would be blocked by Pauli exclusion principle. This crossover region above the resonance is predicted to be extended to magnetic field strengths related to the sum of the Fermi energies of the involved species. Due to the closed channel dominated character of the interspecies Feshbach resonances in the ^6Li - ^{40}K mixture, a quantitative analysis of the entire BEC-BCS crossover can be achieved by a two-channel approach (Gurarie and Radzihovsky, 2007). This is contrary to the case of broad resonances where different computationally intense approaches are required since the gas parameter $k_F|a|$ varies strongly throughout the crossover. The potential of narrow Feshbach resonances seems to represent an almost unexplored field and many interesting applications are thinkable. For example, the sensitivity for a measurement of the variation of fundamental constants can be enhanced close to a narrow Feshbach resonance (Chin and Flambaum, 2006). Although an excellent magnetic field control is required for narrow resonances, a magnetic field sweep for molecule production, as shown in this work experimentally (Voigt *et al.*, 2009) and discussed in theory (Gurarie, 2009), is slower compared to the broad case and hence on a much more controllable level. Therefore the study of time-dependent phenomena might be experimentally more tractable under the pre-condition of magnetic field stability.

The pioneering experiment involving a quantum-degenerate two-species Fermi-Fermi mixture of ^6Li and ^{40}K atoms offers unprecedented possibilities for further investigations.

As a next milestone, the first realization and proof of a molecular BEC of heteronuclear molecules would represent the initiation for further studies of the BEC-BCS crossover in the present system. The goal of a molecular BEC implies several aspects to be solved and a suitable strategy to be found. In principle, either a forced evaporation of the ${}^6\text{Li}$ - ${}^{40}\text{K}$ mixture away from resonance with a suitable choice of the scattering length, or a direct evaporation of the molecules close to resonance would be possible. For the former, scattering properties of the mixture have been extensively studied in this work, and with tailored optical potentials a beneficial overlap of the clouds for efficient thermalization can be achieved. Due to the mass difference, the possibility to apply component-selective methods offers a further enlargement of experimental applications (Giorgini *et al.*, 2008). By using optical lattices the effective masses of ${}^6\text{Li}$ and ${}^{40}\text{K}$ can be controlled independently. Also, species-selective optical potentials allow to exchange entropy in mixtures (LeBlanc and Thywissen, 2007; Catani *et al.*, 2009). For the direct evaporation of molecules into a BEC close to resonance, it could be advantageous to selectively remove unbound atoms in the trap. This could be achieved by transferring the atoms to different Zeeman sublevels and applying a short resonant light pulse. But for this strategy a necessary step is to clarify whether the molecules are eventually stabilized by unbound fermions. If so, a trade-off for the choice of a suitable atom-atom, atom-dimer and dimer-dimer scattering length needs to be found, cf. (Levinsen and Petrov, 2011), for undergoing the phase transition to a molecular BEC. As an excellent starting point for this endeavor, sufficiently long lifetimes, which are necessary for a direct evaporation process, have been measured in the present work for small detunings from resonance already inside the crossover regime to unbound atoms.

Within this work, a new laser beam setup for Bragg diffraction of fermionic ${}^{40}\text{K}$ atoms on a light field grating with efficiencies of more than 80 % in first order has been installed. High diffraction efficiency for fermionic atoms require very cold temperatures of the cloud, which is achieved by lowering the trapping frequencies. Two regimes of diffraction are investigated and characterized, namely the Bragg and Kapitza-Dirac regime. This allows to apply a pulse sequence to the clouds to study interferometry with a fermionic cloud of ${}^{40}\text{K}$ atoms. Other possible applications with this setup could be the investigation of heteronuclear molecules by Bragg diffraction if the binding energy is larger than the recoil energy. This technique also allows to study the crossover regime close to a Feshbach resonance as has been recently shown for the homonuclear case in bosonic ${}^{85}\text{Rb}$ (Papp *et al.*, 2008) and fermionic ${}^6\text{Li}$ (Veeravalli *et al.*, 2008; Kuhnle *et al.*, 2010).

So far, experimental efforts focused on the investigation of population imbalanced Fermi spin mixtures at the BEC-BCS crossover of a broad Feshbach resonance (Zwierlein *et al.*, 2006; Partridge *et al.*, 2006; Shin *et al.*, 2006; Schunck *et al.*, 2007; Shin *et al.*, 2008; Nascimbéne *et al.*, 2009; Liao *et al.*, 2010). The mass difference in the ${}^6\text{Li}$ - ${}^{40}\text{K}$ Fermi-Fermi mixture allows to study superfluidity for the case of unmatched Fermi surfaces although the population of the two types of fermions is balanced (Bedaque *et al.*, 2003). The phase diagram, i.e. degeneracy parameter versus population imbalance, of a strongly interacting ${}^6\text{Li}$ - ${}^{40}\text{K}$ is expected to have a larger variety of possible pairing mechanisms as compared to the homonuclear case (Petrov *et al.*, 2005b; Sheehy and Radzihovsky, 2006; Baranov *et al.*, 2008; Gubbels *et al.*, 2009). The mismatch of the Fermi surfaces gives

rise to novel quantum phases such as an interior gap superfluid (Liu and Wilczek, 2003).

Finally, an intriguing area of research involves the creation of ultracold ground-state heteronuclear molecules with long-range interaction. For this goal, the ultracold heteronuclear Feshbach molecules are an appreciable starting point for transfer to the absolute ground state by means of a stimulated Raman adiabatic passage (STIRAP) (Bergmann *et al.*, 1998). This was recently demonstrated with ^{40}K - ^{87}Rb (Ni *et al.*, 2008), $^{87}\text{Rb}_2$ (Lang *et al.*, 2008), and $^{133}\text{Cs}_2$ (Danzl *et al.*, 2008). Especially for the case of ^6Li and ^{40}K the molecules are bosons and this allows to cool further by forced evaporation and to create a polar BEC with an anisotropic long-range interaction (Santos *et al.*, 2000, 2002E). The first observation of a dipolar BEC with non-isotropic interaction is reported by (Lahaye *et al.*, 2007, 2009) with ^{52}Cr atoms, which have a permanent magnetic moment. A BEC of heteronuclear ground-state molecules would offer long lifetimes and a strong permanent dipole moment which can be controlled by an external electric field. Those ground-state molecules assembled on an optical lattice would offer a strong dipole-dipole potential which allows the molecules to interact between neighboring lattice sites with interaction energies typically in the order of several hundred nanokelvin (in units of k_B). This would represent a versatile platform to simulate many-body quantum systems and a variety of quantum phases are expected (Góral *et al.*, 2002; Micheli *et al.*, 2006; Lewenstein *et al.*, 2007) such as superfluid, supersolid, Mott insulator, checkerboard and collapse phases, and many other. The close relation to many-body systems would in addition feature an application for quantum information processing (DeMille, 2002; Jaksch and Zoller, 2005; Lewenstein *et al.*, 2007), where entanglement could be achieved between neighboring sites via controlled long-range interactions in the optical lattice. Moreover, first steps towards ultracold chemistry with heteronuclear molecules have already been achieved recently (Ni *et al.*, 2010), but several other aspects in this context can be explored (Krems, 2008; Carr *et al.*, 2009). As a last point, ultracold polar molecules serve to test the time variation of fundamental physical constants (Hudson *et al.*, 2006; Zelevinsky *et al.*, 2008; Carr *et al.*, 2009).

Appendix A

Level schemes

The atomic energy levels of ^{87}Rb , ^6Li , and ^{40}K relevant for this experiment are presented in Fig. A.1. The wavelengths are $\lambda_{\text{Rb}} = 780 \text{ nm}$, $\lambda_{\text{K}} = 767 \text{ nm}$ and $\lambda_{\text{Li}} = 671 \text{ nm}$.

In ^{87}Rb magneto-optical trapping (MOT) and cooling is done on the $|5S_{1/2}, F = 2\rangle \rightarrow |5P_{3/2}, F' = 3\rangle$ cycling transition of the D_2 -line. The same transition is used for detection. For an efficient MOT, atoms need to be repumped to the cycling transition. The repumper transition is $|5S_{1/2}, F = 1\rangle \rightarrow |5P_{3/2}, F' = 2\rangle$. Optical pumping is performed on the $|5S_{1/2}, F = 2\rangle \rightarrow |5P_{3/2}, F' = 2\rangle$ transition.

Due to a positive nuclear Landé g -factor ^{40}K possesses an inverted hyperfine structure (Eisinger *et al.*, 1952). Trapping is achieved on the $|4S_{1/2}, F = 9/2\rangle \rightarrow |4P_{3/2}, F' = 11/2\rangle$ transition of the D_2 line. For imaging in the magnetic trap the same transition is usually used. However, for measurements in the vicinity of a Feshbach resonance other relevant cycling transitions are used at high magnetic fields, cf. Sec. 3.7.1. The repumper acts on the transition $|4S_{1/2}, F = 7/2\rangle \rightarrow |4P_{3/2}, F' = 9/2\rangle$ and requires in contrast to the case of ^{87}Rb a higher intensity since the branching ratio between the excited states is smaller. The Bragg pulses for diffraction of quantum-degenerate ^{40}K atoms, cf. Ch. 4, are blue detuned by 1.43 GHz from the MOT transition.

The level structure of the excited $|2P_{3/2}\rangle$ state of ^6Li is optically not resolved since the energy separation between adjacent levels is on the order of the natural linewidth of the D_2 line. This has a consequence for the operation of the MOT. The cycling transition $|2S_{1/2}, F = 3/2\rangle \rightarrow |2P_{3/2}, F' = 5/2\rangle$ cannot be addressed individually. For a MOT, this results in an almost equal population of the two hyperfine ground states $F = 1/2$ and $F = 3/2$ and the repumper light for the transition $|2S_{1/2}, F = 1/2\rangle \rightarrow |2P_{3/2}, F' = 3/2\rangle$ requires a comparable laser intensity as for the MOT light.

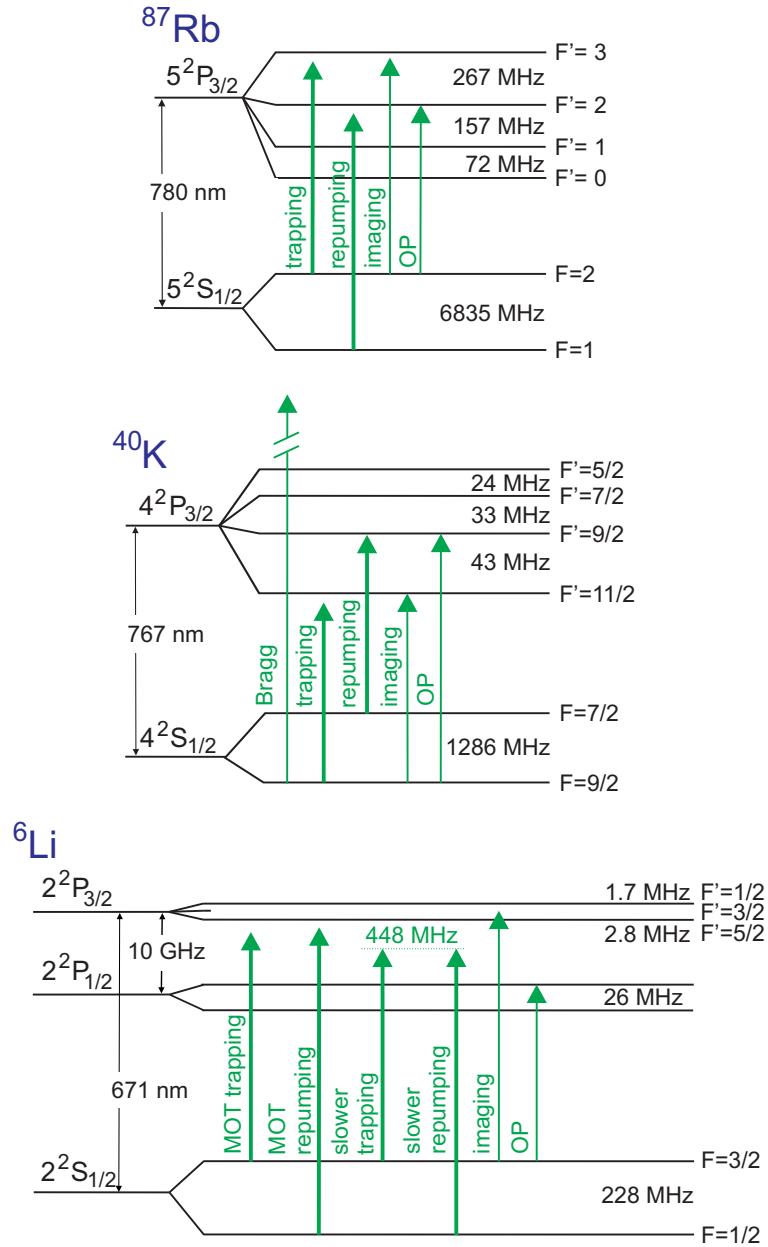


Figure A.1: Level schemes and relevant optical transitions for trapping and imaging of the atomic alkali-metal species ^{87}Rb , ^{40}K , and ^6Li .

Appendix B

Center of mass and relative coordinates

The collision process of atoms with different masses is described in the frame of center-of-mass and relative coordinates. The concept is introduced in this section following (Reif, 1987; Walraven, 2010).

The relative position between two particles 1 and 2 is given by

$$\mathbf{r} = \mathbf{r}_1 - \mathbf{r}_2. \quad (\text{B.1})$$

The relative velocity is obtained by taking the derivative with respect to time

$$\mathbf{v}_{\text{rel}} = \mathbf{v}_1 - \mathbf{v}_2 \quad (\text{B.2})$$

and the total momentum is represented by

$$\mathbf{P}_{\text{cm}} = (m_1 + m_2) \mathbf{V}_{\text{cm}} = \mathbf{p}_1 + \mathbf{p}_2 = m_1 \mathbf{v}_1 + m_2 \mathbf{v}_2. \quad (\text{B.3})$$

The position of the center of mass is found to be

$$\mathbf{R}_{\text{cm}} = \frac{m_1 \mathbf{r}_1 + m_2 \mathbf{r}_2}{m_1 + m_2}. \quad (\text{B.4})$$

With the help of Eqs. (B.2) and (B.3), the velocities of particle 1 and 2 can be written as

$$\begin{aligned} \mathbf{v}_1 &= \frac{\mathbf{P}_{\text{cm}} + m_2 \mathbf{v}_{\text{rel}}}{m_1 + m_2} \\ \mathbf{v}_2 &= \frac{\mathbf{P}_{\text{cm}} - m_1 \mathbf{v}_{\text{rel}}}{m_1 + m_2}. \end{aligned} \quad (\text{B.5})$$

The total kinetic energy of particle 1 and 2 can be separated in a contribution of the center of mass and relative motion

$$E = \frac{1}{2} m_1 \mathbf{v}_1^2 + \frac{1}{2} m_2 \mathbf{v}_2^2 = \frac{\mathbf{P}_{\text{cm}}^2}{2M} + \frac{\mathbf{P}_{\text{rel}}^2}{2m_r}, \quad (\text{B.6})$$

where $M = m_1 + m_2$, $m_r = \frac{m_1 m_2}{m_1 + m_2}$ is the reduced mass of the system, and the relative momentum \mathbf{p}_{rel} is given by

$$\mathbf{p}_{\text{rel}} = m_r \mathbf{v}_{\text{rel}} = \frac{m_r}{m_1} \mathbf{p}_1 - \frac{m_r}{m_2} \mathbf{p}_2. \quad (\text{B.7})$$

The positions \mathbf{r}_1 and \mathbf{r}_2 can be expressed by \mathbf{R}_{cm} and \mathbf{r} according to

$$\mathbf{r}_1 = \mathbf{R}_{\text{cm}} + \frac{m_2}{M} \mathbf{r}, \quad \mathbf{r}_2 = \mathbf{R}_{\text{cm}} - \frac{m_1}{M} \mathbf{r} \quad (\text{B.8})$$

and the momenta \mathbf{p}_1 and \mathbf{p}_2 are represented with center of mass and relative coordinates as

$$\mathbf{p}_1 = \frac{m_1}{M} \mathbf{P}_{\text{cm}} + \mathbf{p}_{\text{rel}}, \quad \mathbf{p}_2 = \frac{m_2}{M} \mathbf{P}_{\text{cm}} - \mathbf{p}_{\text{rel}}. \quad (\text{B.9})$$

In an elastic collision process the total momentum \mathbf{P}_{cm} and the absolute value of the relative momentum $|\mathbf{p}_{\text{rel}}|$ are conserved quantities. The collision process changes only the direction of the relative momentum \mathbf{p}_{rel} . The relative momentum changes from \mathbf{p}_{rel} to \mathbf{p}'_{rel} , with $\mathbf{q} = \mathbf{p}'_{\text{rel}} - \mathbf{p}_{\text{rel}}$. Then the individual momenta \mathbf{p}_1 and \mathbf{p}_2 are changed to \mathbf{p}'_1 and \mathbf{p}'_2

$$\begin{aligned} \mathbf{p}_1 &= \frac{m_1}{M} \mathbf{P}_{\text{cm}} + \mathbf{p}_{\text{rel}} \rightarrow \mathbf{p}'_1 = \frac{m_1}{M} \mathbf{P}_{\text{cm}} + \mathbf{p}'_{\text{rel}} \\ \mathbf{p}_2 &= \frac{m_2}{M} \mathbf{P}_{\text{cm}} - \mathbf{p}_{\text{rel}} \rightarrow \mathbf{p}'_2 = \frac{m_2}{M} \mathbf{P}_{\text{cm}} - \mathbf{p}'_{\text{rel}}. \end{aligned} \quad (\text{B.10})$$

The momentum transfer is

$$\begin{aligned} \Delta \mathbf{p}_1 &= \mathbf{p}'_1 - \mathbf{p}_1 = \mathbf{q} \\ \Delta \mathbf{p}_2 &= \mathbf{p}'_2 - \mathbf{p}_2 = -\mathbf{q} \end{aligned} \quad (\text{B.11})$$

and the energy transfer is given by

$$\begin{aligned} \Delta E_1 &= \frac{\mathbf{p}'_1{}^2}{2m_1} - \frac{\mathbf{p}_1^2}{2m_1} = \frac{\mathbf{P}_{\text{cm}} \cdot \mathbf{q}}{M} \\ \Delta E_2 &= \frac{\mathbf{p}'_2{}^2}{2m_2} - \frac{\mathbf{p}_2^2}{2m_2} = -\frac{\mathbf{P}_{\text{cm}} \cdot \mathbf{q}}{M}. \end{aligned} \quad (\text{B.12})$$

An example for a collision process in the ${}^6\text{Li}$ - ${}^{40}\text{K}$ mixture, which obeys the correct conservation laws, is illustrated in Fig. 2.11.

Appendix C

Initial parameters and constraints for cross-dimensional relaxation

C.1 Validity of kinetic model

In the derivation of cross-dimensional relaxation rates from a kinetic model in Sec. 2.4.2.2, the thermal averages $\langle v_{\text{rel}} v_{\text{rel},i}^2 \rangle$ and $\langle v_{\text{rel}} V_{\text{cm},i} v_{\text{rel},i} \rangle$ in Eqs. (2.77) and (2.78) have been approximated. In this section the validity of the approximation is tested by directly integrating thermal Gaussian distributions with different energy anisotropies for each species in momentum space. One is interested in ratios of the type

$$\frac{\langle v_{\text{rel}} v_{\text{rel},i}^2 \rangle}{\langle v_{\text{rel}} \rangle \langle v_{\text{rel},i}^2 \rangle} \quad (\text{C.1})$$

$$\frac{\langle v_{\text{rel}} V_{\text{cm},i} v_{\text{rel},i} \rangle}{\langle v_{\text{rel}} \rangle \langle V_{\text{cm},i} v_{\text{rel},i} \rangle}, \quad (\text{C.2})$$

which can be approximated by 4/3 in case that the anisotropies are not too large. The integration is performed over the distribution function $\exp(-H)$ with the Hamiltonian in center-of-mass and relative coordinates

$$\begin{aligned} H(v_{1,i}, v_{2,i}) &= \frac{1}{2} \left(\frac{m_1 v_{1,i}^2}{E_{1,i}} + \frac{m_2 v_{2,i}^2}{E_{2,i}} \right) \\ &= \left(\frac{M V_{\text{cm},i}^2}{2\varepsilon_{\text{cm},i}} + \frac{m_r v_{\text{rel},i}^2}{2\varepsilon_{\text{rel},i}} \right) - m_r \delta_i V_{\text{cm},i} v_{\text{rel},i} = H(v_{\text{rel},i}, V_{\text{cm},i}), \end{aligned} \quad (\text{C.3})$$

where $E_{\sigma,i}$ is the mean energy per particle of species σ in the direction i and

$$\begin{aligned} \varepsilon_{\text{cm},i} &\equiv \frac{(m_1 + m_2) E_{1,i} E_{2,i}}{m_2 E_{1,i} + m_1 E_{2,i}} \\ \varepsilon_{\text{rel},i} &\equiv \frac{(m_1 + m_2) E_{1,i} E_{2,i}}{m_1 E_{1,i} + m_2 E_{2,i}} \\ \delta_i &\equiv \frac{E_{1,i} - E_{2,i}}{E_{1,i} E_{2,i}}. \end{aligned} \quad (\text{C.4})$$

C.2 Initial conditions for cross-dimensional relaxation

The following averages can be derived analytically

$$\begin{aligned}\langle v_{\text{rel},i}^2 \rangle &= \frac{E_{1,i}}{m_1} + \frac{E_{2,i}}{m_2} \\ \langle V_{\text{cm},i} v_{\text{rel},i} \rangle &= \frac{E_{1,i} - E_{2,i}}{m_1 + m_2}.\end{aligned}\tag{C.5}$$

A closed analytical expression for the other averages of interest

$$\langle v_{\text{rel}} \rangle,\tag{C.6}$$

$$\langle v_{\text{rel}} v_{\text{rel},i}^2 \rangle,\tag{C.7}$$

$$\langle v_{\text{rel}} V_{\text{cm},i} v_{\text{rel},i} \rangle,\tag{C.8}$$

can only be given for a cylindrical symmetry of the initial energy anisotropy $E_x/E_z = E_y/E_z$ (Goldwin *et al.*, 2005). For the general case $E_x/E_z \neq E_y/E_z$ one carries out the integrations numerically. In Fig. C.1 the relevant ratios of thermal averages are plotted as a function of the mass ratio. The validity of the kinetic model is tested by calculating the averages with anisotropies typically occurring in the experiment. For ${}^6\text{Li}$ the largest anisotropies, which yield best signal-to-noise ratios, are $E_x/E_z = 2.8$ and $E_y/E_z = 1.9$ and for ${}^{40}\text{K}$ $E_x/E_z = 2.8$ and $E_y/E_z = 3.9$. For the ${}^6\text{Li}$ - ${}^{40}\text{K}$ mass ratio, the discrepancy of the thermal average from $4/3$ is at most 12 % according to the numerical integrations. That means that the assumptions made in Sec. 2.4.2 are legitimate within typical experimental uncertainties.

C.2 Initial conditions for cross-dimensional relaxation

In this section the validity of Eq. (2.70) is verified by performing classical Monte-Carlo simulations. Those simulations are powerful since they allow to investigate dependencies of the rethermalization rates only on the cost of computational time. In most cases, experimental parameters are difficult to be varied methodically as other system parameters are often also affected.

C.2.1 Dependence on particle number and initial anisotropy

For a classical Gaussian distribution of atoms confined in a harmonic trap, the rethermalization rate can be rewritten as

$$\begin{aligned}\Gamma_{12,\text{CDR}} &= 1/\beta_{12} n_{12} \sigma_{12} v_{\text{rel}} = \\ &= 1/\beta_{12} N_2 \left(\frac{2\pi}{k_B T} \right)^{3/2} \sigma_{12} \sqrt{\frac{8k_B T}{\pi m_r}} \prod_{i=x,y,z} \sqrt{\frac{m_1 \nu_{i,1}^2 \cdot m_2 \nu_{i,2}^2}{m_1 \nu_{i,1}^2 + m_2 \nu_{i,2}^2}} \propto \frac{N_2}{T}.\end{aligned}\tag{C.9}$$

Here the effect of the gravitational sag is omitted. The rethermalization rate $\Gamma_{12,\text{CDR}}$ is direct proportional to the atom number N_2 of species 2 and inverse proportional to the equilibrium temperature T . The quantity is expected to be independent on the

C. Initial parameters and constraints for cross-dimensional relaxation

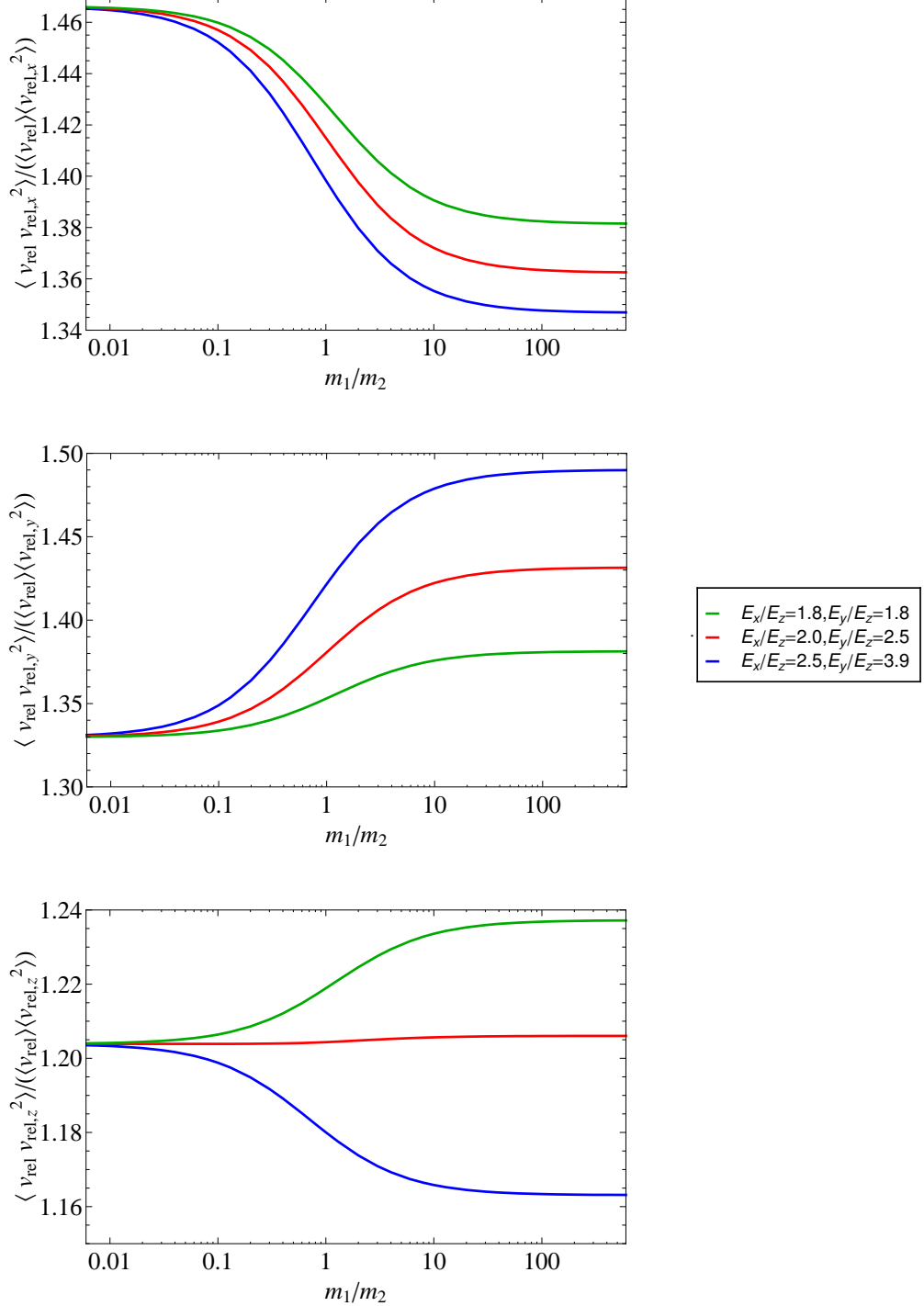


Figure C.1: Numerical integration of thermal averages over anisotropic Gaussian distribution functions. The quantities $\langle v_{\text{rel}} v_{\text{rel},i}^2 \rangle / (\langle v_{\text{rel}} \rangle \langle v_{\text{rel},i}^2 \rangle)$ ($i = x, y, z$) are plotted as a function of the mass ratio and for different energy anisotropies (Goldwin, 2005; Hahn, 2009).

C.2 Initial conditions for cross-dimensional relaxation

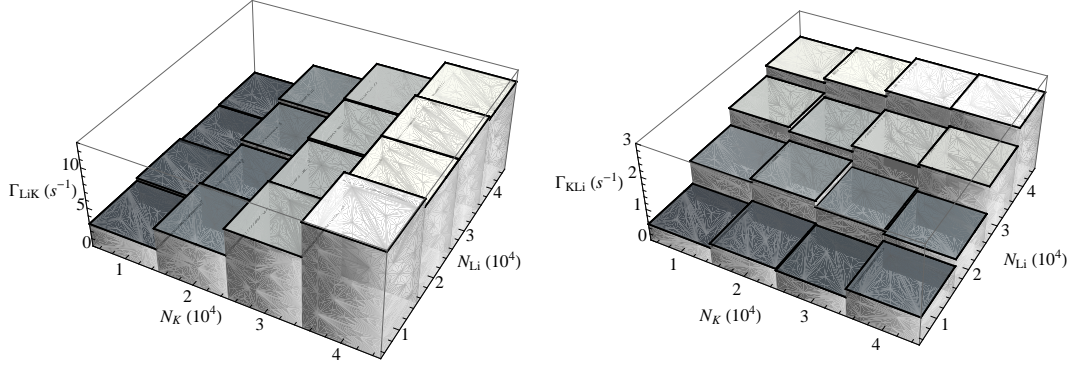


Figure C.2: Particle number dependence of the cross-dimensional rethermalization rates of ${}^6\text{Li}$ and ${}^{40}\text{K}$ in the mixture determined with Monte-Carlo simulations. The parameters for the simulations are $\bar{\nu}_{\text{Li}} = 1612 \text{ Hz}$, $\bar{\nu}_{\text{K}} = 624 \text{ Hz}$, $E_x/E_z = 1.4$, and $E_y/E_z = 1.7$.

particle number N_1 of species 1. These dependencies of the rethermalization rate can be studied with classical Monte-Carlo simulations. The results for the parameters of a ${}^6\text{Li}$ - ${}^{40}\text{K}$ mixture are presented in Fig. C.2, where the atom numbers of ${}^6\text{Li}$ and ${}^{40}\text{K}$ are varied. Fig. C.3 illustrates the behavior of the CDR rates if the temperature T is varied. The Monte-Carlo simulations are in fair agreement with the expectation from Eq. (C.9), i.e. $\Gamma_{12,\text{CDR}} \propto N_2/T$. For the presented simulations with the Monte-Carlo method the average of three relaxation rates respective to the three spatial axes is taken.

On the other hand, the kinetic model presented in Sec. 2.4.2.2 gives an intuitive interpretation of cross-dimensional relaxation. This model allows to study systematically dependencies of rethermalization rates on initial system parameters. According to the kinetic model, the relaxation process within one axis of the cloud, e.g. x - z as assumed in Eq. (2.72), is considered. The coupled differential equations given in Eq. (2.81) are solved for various initial conditions and for the ${}^6\text{Li}$ - ${}^{40}\text{K}$ mixture. The solutions are fitted with the expression from Eq. (2.88). The results are presented in Fig. C.4. Fig. C.4 (a) presents the dependence on the particle numbers. The results are consistent with a rethermalization rate $\Gamma_{12,\text{CDR}}$ being direct proportional to the atomic number N_2 of species 2, and nearly independent on the particle number of species 1, i.e. $\Gamma_{12,\text{CDR}} \propto N_2$.

In Fig. C.4 (b) the variation of the rethermalization rates with the initial energy anisotropy of the two species is studied. If the initial anisotropy for ${}^6\text{Li}$ is larger than for ${}^{40}\text{K}$ $\chi_{\text{Li}}(0) > \chi_{\text{K}}(0)$ than $\Gamma_{\text{LiK},\text{CDR}}$ is nearly independent on the ratio of the initial anisotropies. Whereas for the case where $\chi_{\text{Li}}(0) < \chi_{\text{K}}(0)$, there is a large variation of $\Gamma_{\text{LiK},\text{CDR}}$. On the other hand $\Gamma_{\text{KLi},\text{CDR}}$ is robust and nearly independent on $\chi_{\text{Li}}(0)/\chi_{\text{K}}(0)$. In the experiments, the imposed initial energy anisotropy of ${}^6\text{Li}$ is usually smaller than

C. Initial parameters and constraints for cross-dimensional relaxation

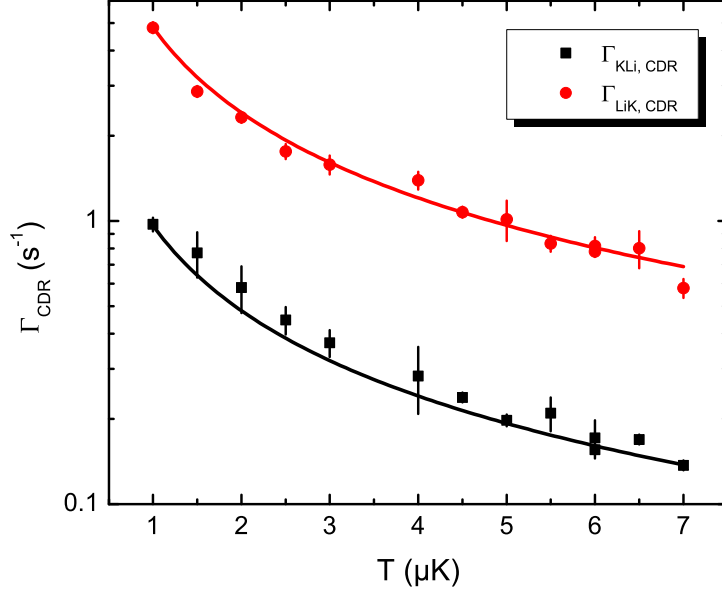


Figure C.3: Temperature dependence of the cross-dimensional rethermalization rates of ${}^6\text{Li}$ and ${}^{40}\text{K}$ in the mixture determined with Monte-Carlo simulations. The parameters for the simulations are $\bar{\nu}_{\text{Li}} = 792 \text{ Hz}$, $\bar{\nu}_{\text{K}} = 461 \text{ Hz}$, $E_x/E_z = 1.7$, and $E_y/E_z = 1.4$. The solid lines correspond to fits $\Gamma_{\text{CDR}} = A/T$, where A is a free fitting parameter.

for ${}^{40}\text{K}$, since ${}^6\text{Li}$ relaxes faster. This would lead to an expected smaller ratio $\beta_{\text{KLi}}/\beta_{\text{LiK}}$ according to the kinetic model and Fig. C.4 (b).

C.2.2 Initial imbalance of mean energies per particle

In the experiments, an imbalance of mean thermal energies between the species is detected. The temporal relaxation of such an imbalance can be derived from the kinetic model in a similar way as outlined in Sec. 2.4.2.2 for the case of CDR.

C.2.2.1 Kinetic model

The quantity of interest in this case is the difference of kinetic energies

$$\Delta K = \Delta \left(E_1^{\text{kin}} - E_2^{\text{kin}} \right) = \frac{1}{2} \Delta \left(m_1 v_1^2 - m_2 v_2^2 \right). \quad (\text{C.10})$$

A transformation into the center-of-mass frame yields

$$\frac{1}{2} m_1 v_1^2 - \frac{1}{2} m_2 v_2^2 = \frac{1}{2} \frac{m_1 m_2 (m_2 - m_1)}{(m_1 + m_2)^2} v_{\text{rel}}^2 + \frac{1}{2} (m_1 - m_2) V_{\text{cm}}^2 + 2 \frac{m_1 m_2}{m_1 + m_2} \mathbf{v}_{\text{rel}} \cdot \mathbf{V}_{\text{cm}}. \quad (\text{C.11})$$

C.2 Initial conditions for cross-dimensional relaxation

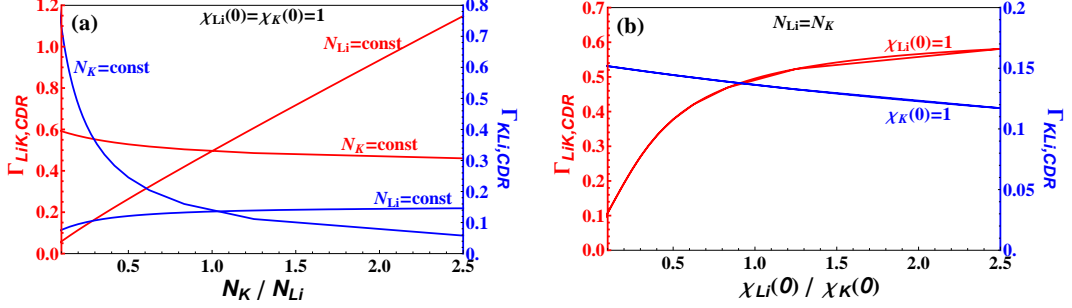


Figure C.4: Dependence of $\Gamma_{\text{LiK,CDR}}$ (in red) and $\Gamma_{\text{KLi,CDR}}$ (in blue) on initial conditions as predicted from the kinetic model for the case of a ${}^6\text{Li}$ - ${}^{40}\text{K}$ mixture. The solutions χ are fitted with exponential curves to obtain the rethermalization rates Γ_{CDR} . For Fig. (a) the particle dependence is considered. As denoted in the graph the particle number of only one species is varied while the other species' atom number is kept constant. The initial energy anisotropy of ${}^6\text{Li}$ and ${}^{40}\text{K}$ is the same, i.e. $\chi_{\text{Li}}(0) = \chi_{\text{K}}(0) = 1$. For Fig. (b) the particle numbers are the same and the ratio $\chi_{\text{Li}}(0)/\chi_{\text{K}}(0)$ is varied. Keeping the initial anisotropy of either species constant ($\chi_{\text{Li}}(0) = 1$ or $\chi_{\text{K}}(0) = 1$) while the other one is varied, leads to the same results.

The first two terms vanish since the absolute values of \mathbf{V}_{cm} and \mathbf{v}_{rel} are conserved. Using the approximations in Eqs. (2.77) and (2.78) gives

$$\langle \dot{K} \rangle = -\frac{8}{3}\Gamma_{12}\frac{m_1m_2}{m_1+m_2}\langle \mathbf{v}_{\text{rel}} \cdot \mathbf{V}_{\text{cm}} \rangle \quad (\text{C.12})$$

Resubstituting with v_1 and v_2 and reminding that the mean kinetic and potential energies are equally split up in the collisionless regime, yields the differential equation

$$\langle \dot{K} \rangle = -\frac{8}{3}\Gamma_{12}\frac{m_1m_2}{(m_1+m_2)^2}\langle K \rangle = -\frac{\Gamma_{12}}{A}\langle K \rangle \quad (\text{C.13})$$

with $A \equiv \frac{3}{8}\frac{(1+m_1/m_2)^2}{m_1/m_2} = A(m_1/m_2)$. The solution of the differential equation is a simple exponential decay

$$K(t) = K(0) \cdot e^{-\frac{\Gamma_{12}}{A} \cdot t}. \quad (\text{C.14})$$

On the basis of the same assumptions as made in Sec. 2.4.2.2, an imbalance of the single particle thermal energies between different species relaxes exponentially with a time constant that is dependent on the mass ratio. In Fig. C.5 the analytical expression for $A(m_1/m_2)$ is plotted and tested by classical Monte-Carlo simulations. For identical initial conditions, the equilibration of an imbalance is equally fast for two different species in a mixture, since $A(m_1/m_2) = A(m_2/m_1)$ is valid. A simultaneous relaxation of an energy anisotropy within the species and an energy imbalance between two species in a mixture is investigated with classical Monte-Carlo simulations (cf. Sec. 2.4.2.3) in the next section.

C. Initial parameters and constraints for cross-dimensional relaxation

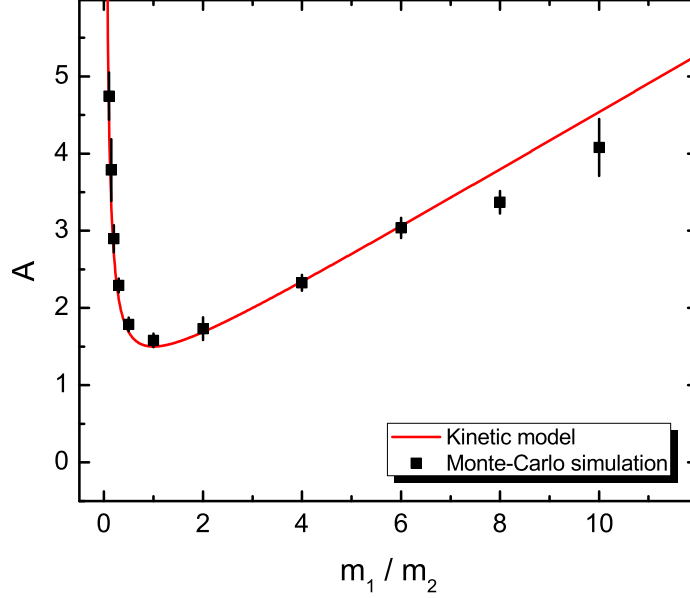


Figure C.5: Number of collisions required for the thermalization of an imbalance in the mean energy per particle in a mixture of two species with masses m_1 and m_2 . A kinetic model and classical Monte-Carlo simulations show fair correspondence for the results of the mean number of collisions per particle required for equilibration.

C.2.2.2 Cross-dimensional relaxation in the presence of imbalance of mean energies per particle between species

Fig. C.6 shows the results of classical Monte-Carlo simulations for CDR where simultaneously an energy imbalance between the species is present. The ratio $\beta_{\text{KLi}}/\beta_{\text{LiK}}$ is presented as a function of the difference in the mean energy per particle between the species. The β factors are obtained by least square fits of the rethermalization curves with the expression given in Eq. (2.89). For both species, the initial energy anisotropies are $E_x/E_z = 1.7$ and $E_y/E_z = 1.4$. The mean energy E_z along z is varied between the species what leads to an energy imbalance, and, after relaxation, to a net flow of energy from one species to the other. A strong dependence of the ratio $\beta_{\text{KLi}}/\beta_{\text{LiK}}$ is observed in dependence of the initial energy imbalance between the species. In the case of same single particle energies, the ratio is close to 3.7 as derived from the classical kinetic model, see Sec. 2.4.2.4. In the case where ${}^6\text{Li}$ possesses a higher single particle energy $\sum_{i=x,y,z} E_{i,\text{Li}}(0)$ as compared to ${}^{40}\text{K}$ $\sum_{i=x,y,z} E_{i,\text{K}}(0)$ the ratio is diminished. This can qualitatively explain the observed diminished value of the ratio $\beta_{\text{KLi}}/\beta_{\text{LiK}}$ in the experiment (cf. Sec. 6.2), as usually a higher mean energy per particle of a fully thermalized ${}^6\text{Li}$ cloud as compared to a ${}^{40}\text{K}$ cloud is detected in the harmonic trap.

C.3 Energy dependence of scattering cross section

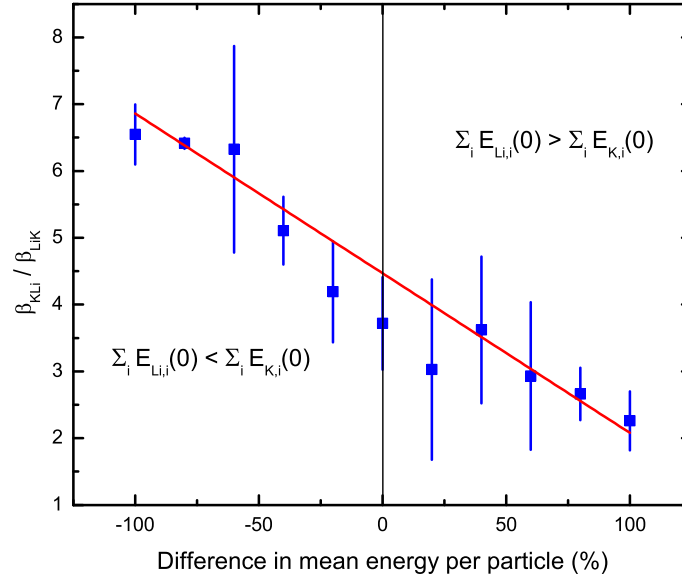


Figure C.6: Influence of an initial imbalance of the mean energy per particle between ${}^6\text{Li}$ and ${}^{40}\text{K}$ on cross-dimensional relaxation tested with classical Monte-Carlo simulations. As simulation parameters, same particle number and initial energy anisotropy of $E_x/E_z = 1.7$ and $E_y/E_z = 1.4$ are chosen for the ${}^6\text{Li}$ and ${}^{40}\text{K}$ cloud. The kinetic energy along E_z for both species is varied what leads to an energy imbalance between the clouds. The red curve corresponds to a guide to the eye and a linear fit to the data points, and the uncertainty arises from the average along the three spatial directions.

C.3 Energy dependence of scattering cross section

In this section, the influence of an energy-dependent scattering cross section is discussed. Especially for narrow Feshbach resonances, measurements on scattering properties can be affected by the finite value of the effective range r_{eff} (see also Sec. 2.3.5).

In the derivation of the rethermalization rate of cross-dimensional relaxation in Sec. 2.4.2.2, the scattering cross section is assumed to be energy independent. However, close to a Feshbach resonance the scattering amplitude, which is directly related to the scattering cross section, exhibits an energy dependence in the limit $|B - B_0| \ll \Delta B$ according to the expressions Eqs. (2.36) and (2.45). The effective range is negative $r_{\text{eff}} < 0$ close to resonance (Petrov, 2004b; Bruun *et al.*, 2005; Jensen *et al.*, 2006; Gurarie and Radzihovsky, 2007). The magnetic field positions of the two extrema of the energy dependent scattering cross section in the vicinity of a Feshbach resonance are given by

$$B_{\min} = B_0 + \Delta, \quad B_{\max} = B_0 + \frac{\Delta}{1 - 2/(a_{\text{bg}}k^2r_{\text{eff}})} \geq B_0. \quad (\text{C.15})$$

C. Initial parameters and constraints for cross-dimensional relaxation

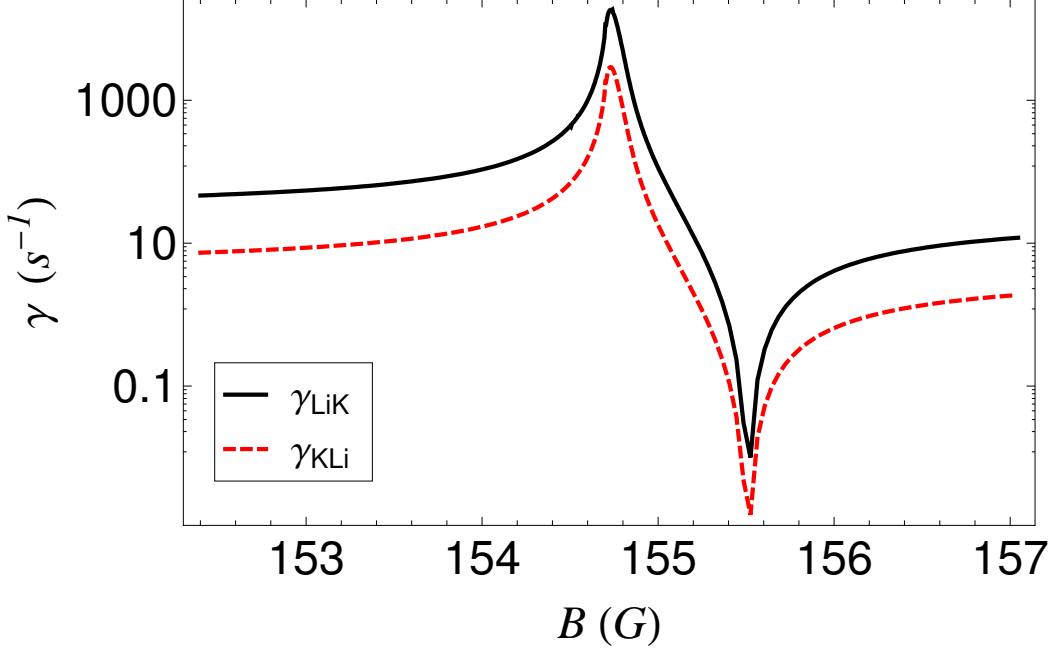


Figure C.7: Rethermalization rates γ_{LiK} and γ_{KLi} as a function of the magnetic field strength close to an interspecies Feshbach resonance. The rethermalization rates are determined by numerical integration over anisotropic classical Boltzmann distributions with the parameters $\nu_{x,\text{Li}} = \nu_{y,\text{Li}} = 963$ Hz, $\nu_{z,\text{Li}} = 479$ Hz, $\nu_{x,\text{K}} = \nu_{y,\text{K}} = 561$ Hz, $\nu_{z,\text{K}} = 279$ Hz, $E_{x,\text{K}} = E_{x,\text{Li}} = k_B 1.90 \mu\text{K}$, $E_{y,\text{K}} = E_{z,\text{Li}} = k_B 1.15 \mu\text{K}$, $E_{y,\text{K}} = E_{y,\text{Li}}$, $E_{y,\text{Li}} = E_{x,\text{Li}}$, $E_{y,\text{K}} = E_{x,\text{K}}$ (cylindrical symmetry), and resonance position at $B_0 = 154.7$ G. The step size is 5 mG.

Depending on the value of r_{eff} , the maximum of the observed scattering cross section is shifted with respect to the resonance position B_0 . Because of the negative sign of r_{eff} the maximum is moved to higher magnetic field values as compared to the resonance position. As a rough estimate the shift is found to be on the order of 40 mG with a typical Fermi wave number of $k \approx 10^7 \text{ m}^{-1}$ and the present Feshbach resonance parameters (cf. Tab. 2.2). A more accurate determination of the shift for the present experimental parameters can be obtained by calculating the thermal averages

$$\gamma_{12} \equiv -\frac{\langle \dot{\chi}_1 \rangle}{2\langle \chi_1 \rangle} = -n_{12} \frac{\langle \sigma_{12}(v_{\text{rel}}) v_{\text{rel}} \Delta \chi_1 \rangle}{2\langle \chi_1 \rangle} \quad (\text{C.16})$$

with an energy dependent scattering cross section $\sigma(v_{\text{rel}})$ and anisotropic momentum distributions in the center-of-mass frame (cf. Sec. C.1). The expression for $\langle \dot{\chi}_1 \rangle$ is given by Eq. (2.76) with the difference that the scattering cross section $\sigma(v_{\text{rel}})$ is part of the expression that is thermally averaged. Taking the ratio Γ_{12}/γ_{12} with Γ_{12} being the classical collision rate from Eq. (2.65), one obtains a measure for β_{12} , see definition in Eq. (2.83). Similar formulas can be derived for the rethermalization rate of species 2

C.3 Energy dependence of scattering cross section

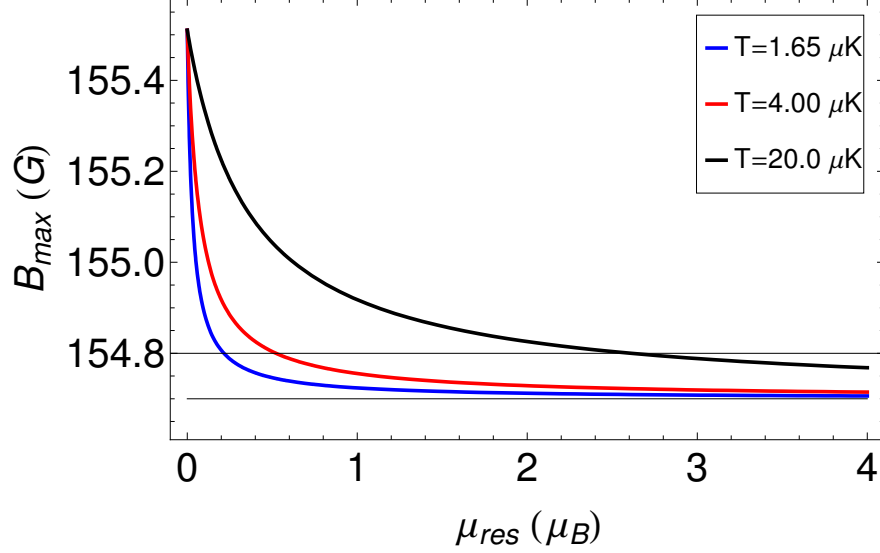


Figure C.8: Magnetic field position of the maximum rethermalization rate as a function of μ_{res} for different temperatures. The chosen parameters are $B_0 = 154.7$ G, $\Delta = 0.81$ G, $a_{\text{bg}} = 63.5 a_0$, and the respective masses for ${}^6\text{Li}$ and ${}^{40}\text{K}$.

equilibrating by collisions with species 1.

Using a constant effective range for the ${}^6\text{Li}$ - ${}^{40}\text{K}$ interspecies Feshbach resonance at 154.7 G as given in Tab. 2.2, the results for the Fano profiles of the rethermalization rates $\gamma_{\text{LiK}}(B)$ and $\gamma_{\text{KLi}}(B)$ are presented in Fig C.7. The magnetic field positions of the maximum rethermalization rates for ${}^6\text{Li}$ and ${}^{40}\text{K}$ are located at the same value, but are shifted by 30(5) mG towards higher magnetic field values with respect to the chosen resonance position at 154.7 G. This correction of 30 mG is within typical uncertainties occurring in the experiment (± 50 mG for the determination of the resonance position, see Sec. 6.4). The thermal averages in Eq. (C.16) are realized with anisotropic classical Boltzmann distributions by numerical integration. For the present experimental degeneracy parameter of $T/T_F \approx 0.5$, the use of Fermi-Dirac distributions as opposed to classical distributions does not alter the results considerably since the Fermi-Fermi mixture is not deeply degenerate. Due to simplicity, the magnetic field dependence of the effective range (Bruun *et al.*, 2005; Jensen *et al.*, 2006; Zinner and Thøgersen, 2009) is omitted here. The expression for $r_{\text{eff}}(B)$ from Eq. (2.54) would lead to similar positions of the two extrema as given in Eq. (C.15).

In Fig. C.8 the magnetic field position of the maximum rethermalization rate B_{max} is shown as a function of the difference of the magnetic moments of the unbound atoms and molecules μ_{res} . The effective range r_{eff} is inverse proportional to μ_{res} , see Eq. (2.45). If the magnetic moment μ_{res} is small, i.e. the effective range becomes large, the maximum of the rethermalization rate is shifted significantly, whereas for small values of r_{eff} the maximum approaches the resonance position.

Appendix D

Optical transition strength for high magnetic field

In this chapter, the optical transition strength for Zeeman states is derived for the case of low, high, and intermediate magnetic field strengths. For the latter neither the coupled nor the uncoupled basis describe the atomic system appropriately. This case applies to imaging of Zeeman states of ${}^6\text{Li}$ and ${}^{40}\text{K}$ for the interspecies Feshbach resonance at 155 G. The derivation is based on (Udem, 1994; Röhl, 1999; Gehm, 2003; LeBlanc, 2006).

D.1 Representation of the hyperfine structure and Zeeman operator

In the case of small external magnetic field strengths, the nuclear spin \mathbf{I} couples to the total electron spin \mathbf{J} what gives rise to the total spin operator \mathbf{F} with the corresponding quantum numbers F and m_F . The matrix elements of the hyperfine operator H_{hf} can be represented in the coupled basis

$$\begin{aligned} \langle I J F m_F | H_{\text{hf}} | I' J' F' m'_F \rangle = & (-1)^{I+J+F} h A_{\text{hf}} \frac{I J \delta_{m_F, m'_F} \delta_{F, F'} \left\{ \begin{matrix} J & I & F \\ I & J & 1 \end{matrix} \right\}}{\begin{pmatrix} J & 1 & J \\ -J & 0 & J \end{pmatrix} \begin{pmatrix} I & 1 & I \\ -I & 0 & I \end{pmatrix}} + \\ & (-1)^{I+J+F} h B_{\text{hf}} \frac{\delta_{m_F, m'_F} \delta_{F, F'} \left\{ \begin{matrix} J & I & F \\ I & J & 2 \end{matrix} \right\}}{\begin{pmatrix} J & 2 & J \\ -J & 0 & J \end{pmatrix} \begin{pmatrix} I & 2 & I \\ -I & 0 & I \end{pmatrix}}, \quad (\text{D.1}) \end{aligned}$$

where A_{hf} and B_{hf} are hyperfine structure constants and $\{\cdot\}$ are Wigner 6j symbols and (\cdot) are Wigner 3j symbols. On the other hand, if the magnetic field strength is large the coupling between \mathbf{I} and \mathbf{J} is negligible and the matrix elements of H_{hf} can be described within the uncoupled basis of the common eigenvectors of the operators \mathbf{I}^2 , I_z , \mathbf{J}^2 and

D.1 Representation of the hyperfine structure and Zeeman operator

J_z

$$\begin{aligned}
& \langle IJm_I m_J | H_{\text{hf}} | IJm'_I m'_J \rangle = \\
& = hA_{\text{hf}} (-1)^{m_J - m'_J} (-1)^{J+I-m_J-m_I} \sqrt{(2J+1)(J+1)J(2I+1)(I+1)I} \cdot \\
& \quad \cdot \begin{pmatrix} J & 1 & J \\ -m_J & m_J - m'_J & m'_J \end{pmatrix} \begin{pmatrix} I & 1 & I \\ -m_I & m'_J - m_J & m_I \end{pmatrix} + \\
& + hB_{\text{hf}} (-1)^{m_J - m'_J} (-1)^{J+I-m_J-m_I} \frac{\sqrt{(2J+3)(J+1)(2J+1)J(2J-1)(2I+3)(I+1)(2I+1)I(2I-1)}}{4IJ(2I-1)(2J-1)} \cdot \\
& \quad \cdot \begin{pmatrix} J & 2 & J \\ -m_J & m_J - m'_J & m'_J \end{pmatrix} \begin{pmatrix} I & 2 & I \\ -m_I & m'_J - m_J & m_I \end{pmatrix} \quad (\text{D.2})
\end{aligned}$$

An external magnetic field couples to the magnetic moment of the nucleus and of the electrons of the atom according to

$$H_Z = -\boldsymbol{\mu} \cdot \mathbf{B} = (g_J J_z + g_I I_z) \mu_B B_z, \quad (\text{D.3})$$

where z is the quantization axis. The uncoupled basis vectors $|IJm_I m_J\rangle$ are eigenvectors of the operators I_z and J_z , and consequently the matrix $\langle IJm_I m_J | H_Z | IJm'_I m'_J \rangle$ is diagonal

$$\langle IJm_I m_J | H_Z | IJm'_I m'_J \rangle = \delta_{m_I, m'_I} \delta_{m_J, m'_J} (g_J m_J + g_I m_I) \mu_B B_z. \quad (\text{D.4})$$

In the coupled basis the matrix elements of H_Z are given by

$$\begin{aligned}
& \langle IJFm_F | H_Z | IJF'm'_F \rangle = \\
& = \mu_B B_z (-1)^{F-m_F} \begin{pmatrix} F & 1 & F' \\ -m_F & 0 & m'_F \end{pmatrix} \sqrt{(2F+1)(2F'+1)} \cdot \\
& \quad \cdot \left[g_J (-1)^{I+J+1+F} \sqrt{(2J+1)(J+1)J} \begin{Bmatrix} J & F & I \\ F' & J & 1 \end{Bmatrix} + \right. \\
& \quad \left. + g_I (-1)^{I+J+1+F'} \sqrt{(2I+1)(I+1)I} \begin{Bmatrix} I & F & J \\ F' & I & 1 \end{Bmatrix} \right]. \quad (\text{D.5})
\end{aligned}$$

The eigenvalues of the hyperfine ground states for ${}^6\text{Li}$ and ${}^{40}\text{K}$ in the presence of a magnetic field $H_{\text{hf}} + H_Z$ are presented in Fig. D.1¹. For intermediate magnetic fields the atomic states can be represented by a linear combination of eigenvectors in the basis set $|Fm_F\rangle$ or equivalently by a linear combination of eigenvectors in the basis set $|IJm_I m_J\rangle$. For very strong magnetic fields the electronic and nuclear spins decouple and the problem is diagonalized by the set of eigenstates $|IJm_I m_J\rangle$.

¹For the magnetic field calibration as presented in Sec. 3.6.3 the Zeeman transition from $|9/2, -9/2\rangle$ to $|9/2, -7/2\rangle$ in ${}^{40}\text{K}$ is used with a magnetic field dependent transition frequency of $\nu[\text{MHz}] = 642.894 \text{ MHz} + 1.40135 \text{ MHz/G } B[\text{G}] - 1.40111 \text{ MHz} \sqrt{210541 + 713.763 \text{ 1/G } B[\text{G}] + 1/\text{G}^2 B[\text{G}]^2}$

D. Optical transition strength for high magnetic field

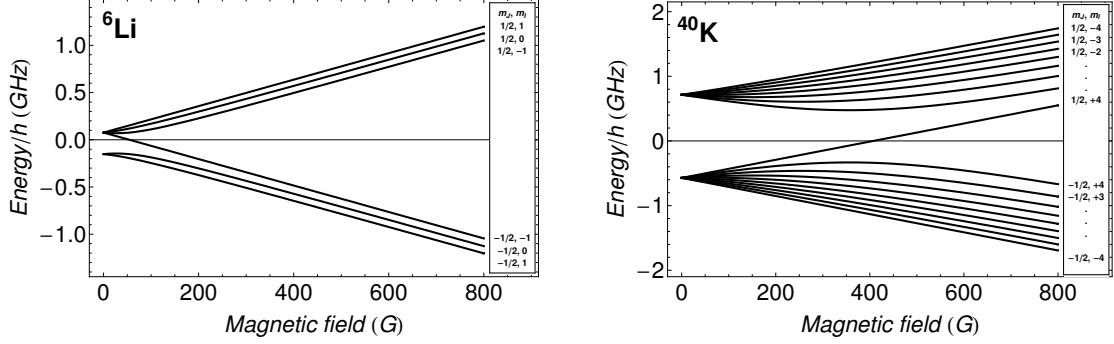


Figure D.1: Hyperfine splitting of the ground state of ${}^6\text{Li}$ and ${}^{40}\text{K}$.

D.2 Optical transition strength

For low magnetic fields, the quantum numbers F and m_F are good quantum numbers and in this case the low-field matrix elements of the electric dipole moment are given by the Wigner-Eckart theorem

$$\langle F m_F | d | F' m'_F \rangle = (-1)^{F'-1+m_F} \langle F || d || F' \rangle \begin{pmatrix} F & 1 & F' \\ -m_F & q & m'_F \end{pmatrix}, \quad (\text{D.6})$$

where $d = e \cdot z$ denotes the electric dipole operator. The selection rules in the low-field regime are $\Delta F = 0, \pm 1$, $\Delta L = \pm 1$, $\Delta m_F = 0, \pm 1$, and transitions with $F = 0 \not\leftrightarrow F' = 0$ are not allowed. From the symmetry of Wigner 3j symbols, q must obey $q = m_F - m'_F$. The case $q = 0$ denotes an optical transition with π -polarized light, whereas $q = \pm 1$ represents a σ^\mp -optical transition. The reduced matrix elements $\langle F || d || F' \rangle$ can be expressed by reduced matrix elements $\langle J || d || J' \rangle$ according to

$$\langle F || d || F' \rangle = (-1)^{J_{\max}+I+F_{\min}+1} \sqrt{(2F+1)(2F'+1)} \begin{Bmatrix} J' & J & 1 \\ F & F' & I \end{Bmatrix} \langle J || d || J' \rangle, \quad (\text{D.7})$$

where $\{\cdot\}$ denotes a Wigner 6j symbol, and the min, max subscripts correspond to the minimum or maximum values for F or J among the primed and unprimed variables. By inserting Eq. (D.7) in (D.6), one can obtain the optical transition strengths in units of the absolute square of the reduced matrix element $\langle J || d || J' \rangle$

$$S_{m_F, m'_F}^{\text{LF}} = \left| \frac{\langle F m_F | d | F' m'_F \rangle}{\langle J || d || J' \rangle} \right|^2. \quad (\text{D.8})$$

For high magnetic field strengths, the states are defined by the uncoupled basis vectors $|I J m_I m_J\rangle$. The selection rules are $\Delta J = 0, \pm 1$, $\Delta L = \pm 1$, $\Delta m_J = 0, \pm 1$ and $\Delta m_I = 0$. The normalized optical transition strength is dependent on the matrix element of the

D.2 Optical transition strength

electric dipole operator d between an initial state $|IJm_I m_J\rangle$ and a final state $|IJ'm'_I m'_J\rangle$

$$S_{(m_I m_J), (m'_I m'_J)}^{\text{HF}} = \left| \frac{\langle IJm_I m_J | d | IJ'm'_I m'_J \rangle}{\langle J || d || J' \rangle} \right|^2 = \frac{\left| (-1)^{J'-1+m_J} \begin{pmatrix} J & 1 & J' \\ -m_J & q & m'_J \end{pmatrix} \delta_{m_I, m'_I} \right|^2}{|\langle J || d || J' \rangle|^2}. \quad (\text{D.9})$$

Similar to the low-field case, $q = 0$ corresponds to an optical transition with π -polarized light and $q = \pm 1$ represents a σ^\mp -optical transition. It is sufficient to calculate relative probabilities within one manifold of J . This means that the reduced matrix element $\langle J || d || J' \rangle$ is a constant within one manifold.

At intermediate magnetic field strengths, neither the coupled basis $|Fm_F\rangle$ nor the uncoupled basis $|IJm_I m_J\rangle$ are good eigenstates. Therefore, by representing the states $|\psi\rangle$, which are involved in the optical transition, in the uncoupled basis

$$|\psi\rangle = \sum_{m_I, m_J} \langle IJm_I m_J | \psi \rangle \cdot |IJm_I m_J\rangle = \sum_{m_I, m_J} c_{m_I, m_J}^\psi \cdot |IJm_I m_J\rangle. \quad (\text{D.10})$$

and invoking Eq. (D.9), the optical transition strengths between different ground and excited states can be compared within one manifold

$$S_{\psi\psi'}^{\text{int}} = \left| \sum_{m_I, m_J, m'_I, m'_J} c_{m_I, m_J}^\psi c_{m'_I, m'_J}^{\psi'} \cdot \left(S_{(m_I m_J), (m'_I m'_J)}^{\text{HF}} \right)^{1/2} \right|^2. \quad (\text{D.11})$$

The projection coefficients c_{m_I, m_J}^ψ can be obtained by diagonalizing the matrices given in Eq. (D.2) and (D.4) $\langle IJm_I m_J | (H_{\text{hf}} + H_Z) | IJm_I m_J \rangle$.

In Tab. D.1 all possible optical transitions at high and low magnetic field are given for the relevant hyperfine states of ${}^6\text{Li}$ and ${}^{40}\text{K}$ for the interspecies Feshbach resonance at 155 G. Fig. D.2 presents the situation for various magnetic fields up to 200 G. One can see how the optical transition probability to low-field states vanish, and other states at higher fields become relevant as the magnetic field strength increases. Both the low- and high-field limit presented in Tab. D.1 is reproduced in Fig. D.2. At 155 G, the high-field limit of ${}^6\text{Li}$ and ${}^{40}\text{K}$ is not entirely satisfied. The optically excited state can still couple to Zeeman states other than the original state. For the chosen frequencies of the absorption imaging light pulses in the experiments, σ^- -transitions are driven.

D. Optical transition strength for high magnetic field

		${}^6\text{Li } F = \frac{1}{2}, m_F = \frac{1}{2}, m_J = -\frac{1}{2}, m_I = 1\rangle$		${}^{40}\text{K } F = \frac{9}{2}, m_F = -\frac{5}{2}, m_J = -\frac{1}{2}, m_I = -2\rangle$	
	B	S	Final state	S	Final state
σ^+	LF	5/36	$ F' = 3/2, m'_F = 3/2\rangle$	49/1620 56/891 3/110	$ F' = 7/2, m'_F = -3/2\rangle$ $ F' = 9/2, m'_F = -3/2\rangle$ $ F' = 11/2, m'_F = -3/2\rangle$
	HF	1/12	$ m'_J = 1/2, m'_I = 1\rangle$	1/12	$ m'_J = 1/2, m'_I = -2\rangle$
π	LF	5/54	$ F' = 3/2, m'_F = 1/2\rangle$	49/2430	$ F' = 7/2, m'_F = -5/2\rangle$
		2/27	$ F' = 1/2, m'_F = 1/2\rangle$	100/2673 6/55	$ F' = 9/2, m'_F = -5/2\rangle$ $ F' = 11/2, m'_F = -5/2\rangle$
	HF	1/6	$ m'_J = -1/2, m'_I = 1\rangle$	1/6	$ m'_J = -1/2, m'_I = -2\rangle$
σ^-	LF	5/108	$ F' = 3/2, m'_F = -1/2\rangle$	49/2430	$ F' = 7/2, m'_F = -7/2\rangle$
		4/27	$ F' = 1/2, m'_F = -1/2\rangle$	128/2673 9/55	$ F' = 9/2, m'_F = -7/2\rangle$ $ F' = 11/2, m'_F = -7/2\rangle$
	HF	1/4	$ m'_J = -3/2, m'_I = 1\rangle$	1/4	$ m'_J = -3/2, m'_I = -2\rangle$

Table D.1: Transition strengths S in units of $|\langle J || d || J' \rangle|^2$ for transitions coupling to the initial Zeeman states of ${}^6\text{Li } |F = 1/2, m_F = 1/2, m_J = -1/2, m_I = 1\rangle$ and ${}^{40}\text{K } |F = 9/2, m_F = -5/2, m_J = -1/2, m_I = -2\rangle$. All possible transitions are given for the low (LF) and high field (HF) limit.

D.2 Optical transition strength

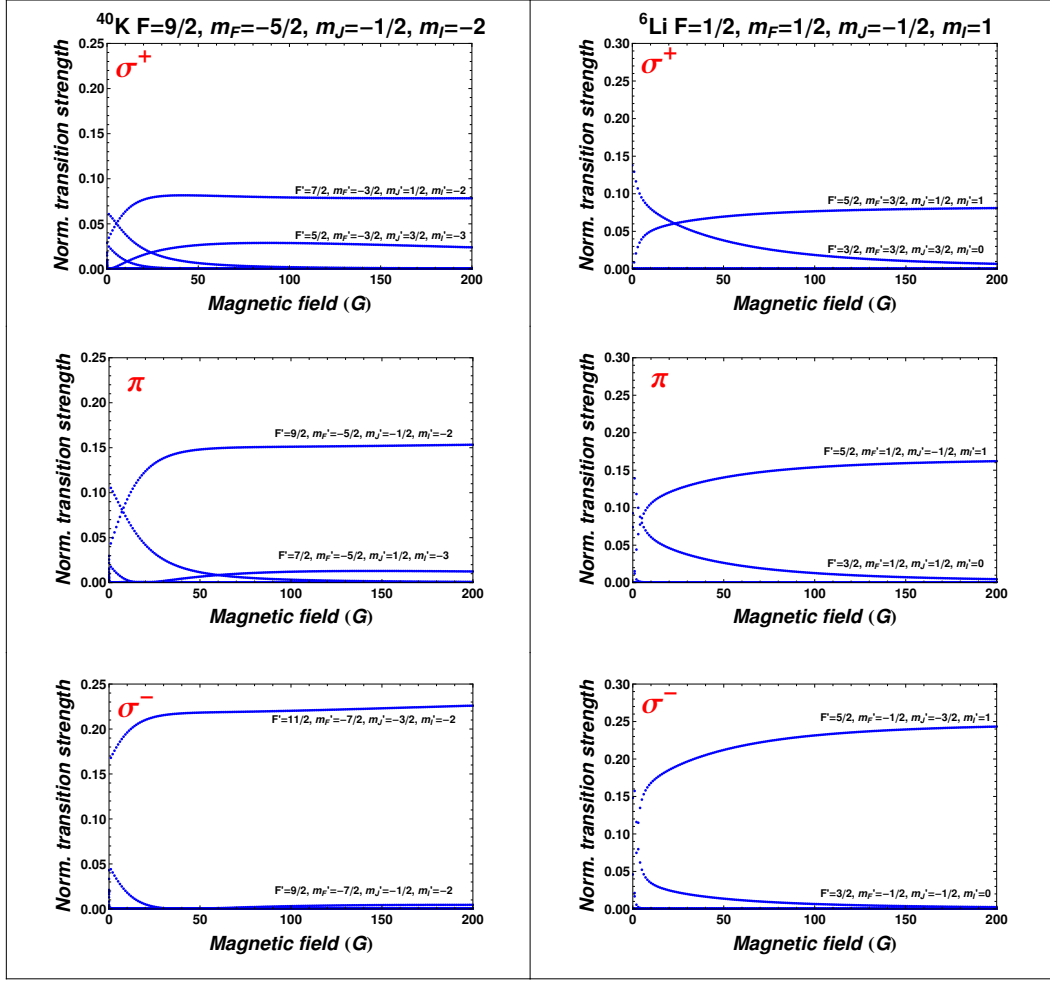


Figure D.2: Optical transition strengths for ^6Li and ^{40}K up to magnetic fields of 200 G. Only optical transitions of the Zeeman states are considered which are relevant for the investigated interspecies Feshbach resonance at 155 G, i.e. for ^6Li $|F = 1/2, m_F = 1/2, m_J = -1/2, m_I = 1\rangle$ and for ^{40}K $|F = 9/2, m_F = -5/2, m_J = -1/2, m_I = -2\rangle$. The transition strengths are given in units of the reduced matrix element $|\langle J = 1/2 || d || J' = 3/2 \rangle|^2$.

Bibliography

- S. Altshuler, L.M. Frantz, and R. Braunstein, *Reflection of Atoms from Standing Light Waves*, Phys. Rev. Lett. **17**, 231232 (1966).
- M.H. Anderson, J.R. Ensher, M.R. Matthews, C.E. Wieman, and E.A. Cornell, *Observation of Bose–Einstein Condensation in a Dilute Atomic Vapor*, Science **269**, 198 (1995).
- B.P. Anderson and M.A. Kasevich, *Macroscopic Quantum Interference from Atomic Tunnel Arrays*, Science **282**, 1686–1689 (1999).
- A.V. Andreev, V. Gurarie, and L. Radzihovsky, *Nonequilibrium Dynamics and Thermodynamics of a Degenerate Fermi Gas Across a Feshbach Resonance*, Phys. Rev. Lett. **93**, 130402 (2004).
- M.R. Andrews, C.G. Townsend, H.-J. Miesner, D.S. Durfee, D.M. Kurn, W. Ketterle, *Observation of Interference Between Two Bose Condensates*, Science **275**, 637–641 (1997).
- M. Arndt, O. Nairz, J. Vos-Andreae, C. Keller, G. van der Zouw, and A. Zeilinger, *Waveparticle duality of C₆₀ molecules*, Nature **401**, 680–682 (1999).
- V. Bagnato, D.E. Pritchard, and D. Kleppner, *Bose-Einstein condensation in an external potential*, Phys. Rev. A **35**, 43544358 (1987).
- M.A. Baranov, C. Lobo, and G.V. Shlyapnikov, *Superfluid pairing between fermions with unequal masses*, Phys. Rev. A **78**, 033620 (2008).
- M. Bartenstein, A. Altmeyer, S. Riedl, S. Jochim, C. Chin, J. Hecker Denschlag, and R. Grimm, *Crossover from a molecular Bose–Einstein condensate to a degenerate Fermi gas*, Phys. Rev. Lett. **92**, 120401 (2004).
- M. Bartenstein, A. Altmeyer, S. Riedl, R. Geursen, S. Jochim, C. Chin, J. Hecker Denschlag, and R. Grimm, *Precise Determination of ⁶Li Cold Collision Parameters by Radio–Frequency Spectroscopy on Weakly Bound Molecules*, Phys. Rev. Lett. **94**, 103201 (2005).
- D.M. Bauer, M. Lettner, C. Vo, G. Rempe, and S. Dürr, *Control of a magnetic Feshbach resonance with laser light*, Nature Physics **5**, 339–342 (2009).

BIBLIOGRAPHY

- P.F. Bedaque, H. Caldas, and G. Rupak, *Phase Separation in Asymmetrical Fermion Superfluids*, Phys. Rev. Lett. **91**, 247002 (2003).
- V. Bendkowsky, B. Butscher, J. Nipper, J.P. Shaffer, R. Löw, and T. Pfau, *Observation of ultralong-range Rydberg molecules*, Nature **458**, 1005–1008 (2009).
- K. Bergmann, H. Theuer, and B.W. Shore, *Coherent population transfer among quantum states of atoms and molecules*, Rev. Mod. Phys. **70**, 10031025 (1998).
- F. Bloch, *Über die Quantenmechanik der Elektronen in Kristallgittern*, Z. für Physik A **52**, 555–600 (1928).
- I. Bloch, T.W. Hänsch, and T. Esslinger, *Measurement of the spatial coherence of a trapped Bose gas at the phase transition*, Nature **403**, 166–170 (2000).
- I. Bloch, W. Zwerger, and J. Dalibard, *Many-body physics with ultracold gases*, Rev. Mod. Phys. **80**, 885–964 (2008).
- D. Blume and K.M. Daily, *Breakdown of Universality for Unequal-Mass Fermi Gases with Infinite Scattering Length*, Phys. Rev. Lett. **105**, 170403 (2010).
- S. Bose, *Plancks Gesetz und Lichtquantenhypothese*, Zeitschrift für Physik **26**, 178–181 (1924).
- T. Bourdel, J. Cubizolles, L. Khaykovich, K.M.F. Magalhães, S.J.J.M.F. Kokkelmans, G.V. Shlyapnikov, and C. Salomon, *Measurement of the Interaction Energy near a Feshbach Resonance in a ^6Li Fermi Gas*, Phys. Rev. Lett. **91**, 020402 (2003).
- T. Bourdel, L. Khaykovich, J. Cubizolles, J. Zhang, F. Chevy, M. Teichmann, L. Tarruell, S.J.J.M.F. Kokkelmans, and C. Salomon, *Experimental Study of the BEC–BCS Crossover Region in Lithium 6*, Phys. Rev. Lett. **93**, 050401 (2004).
- J.A. Bowers and K. Rajagopal, *Crystallography of color superconductivity*, Phys. Rev. D **66**, 065002 (2002).
- C.C. Bradley, C.A. Sackett, J.J. Tollett, and R.G. Hulet, *Evidence of Bose–Einstein Condensation in an Atomic Gas with Attractive Interactions*, Phys. Rev. Lett. **75**, 1687 (1995).
- G. Breit and I.I. Rabi, *Measurement of Nuclear Spin*, Phys. Rev. **38**, 2082–2083 (1931).
- G.M. Bruun, *Universality of a two-component Fermi gas with a resonant interaction*, Phys. Rev. A **70**, 053602 (2004).
- G.M. Bruun, A.D. Jackson, and E.E. Kolomeitsev, *Multichannel scattering and Feshbach resonances: Effective theory, phenomenology, and many-body effects*, Phys. Rev. A **71**, 052713 (2005).
- G.M. Bruun and G. Baym, *Bragg spectroscopy of cold atomic Fermi gases*, Phys. Rev. A **74**, 033623 (2006).

- H.P. Büchler, P. Zoller, and W. Zwerger, *Spectroscopy of Superfluid Pairing in Atomic Fermi Gases*, Phys. Rev. Lett. **93**, 080401 (2004).
- J.P. Burke, *Ph.D. thesis*, University of Colorado (1999).
- O. Carnal and J. Mlynek, *Young's double-slit experiment with atoms: A simple atom interferometer*, Phys. Rev. Lett. **66**, 2689–2692 (1991).
- L.D. Carr, D. DeMille, R.V. Krems and J. Ye, *Cold and ultracold molecules: science, technology and applications*, New J. Phys. **11**, 055049 (2009).
- R. Casalbuoni and G. Nardulli, *Inhomogeneous superconductivity in condensed matter and QCD*, Rev. of Mod. Phys., **76**, 263–320 (2004).
- J. Catani, G. Barontini, G. Lamporesi, F. Rabatti, G. Thalhammer, F. Minardi, S. Stringari, and M. Inguscio, *Entropy Exchange in a Mixture of Ultracold Atoms*, Phys. Rev. Lett. **103**, 140401 (2009).
- K.J. Challis, R.J. Ballagh, and C.W. Gardiner, *Bragg Scattering of Cooper Pairs in an Ultracold Fermi Gas*, Phys. Rev. Lett. **98**, 093002 (2007).
- M.S. Chapman, T.D. Hammond, A. Lenef, J. Schmiedmayer, R.A. Rubenstein, E. Smith, and D.E. Pritchard, *Photon Scattering from Atoms in an Atom Interferometer: Coherence Lost and Regained*, Phys. Rev. Lett. **75**, 3783–3787 (1995).
- C. Chin, M. Bartenstein, A. Altmeyer, S. Riedl, S. Jochim, J. Hecker Denschlag, and R. Grimm, *Observation of the Pairing Gap in a Strongly Interacting Fermi Gas*, Science **305** 1128–1130 (2004).
- J.K. Chin, D.E. Miller, Y. Liu, C. Stan, W. Setiawan, C. Sanner, K. Xu, and W. Ketterle, *Evidence for superfluidity of ultracold fermions in an optical lattice*, Nature **443** 961–964 (2006).
- C. Chin and V.V. Flambaum, *Enhanced Sensitivity to Fundamental Constants In Ultracold Atomic and Molecular Systems near Feshbach Resonances*, Phys. Rev. Lett. **96**, 230801 (2006).
- C. Chin, *A simple model of Feshbach molecules*, arXiv:cond-mat/0506313v2 (2008).
- C. Chin, R. Grimm, P.S. Julienne, and E. Tiesinga, *Feshbach resonances in ultracold gases*, Rev. Mod. Phys. **82**, 1225 (2010).
- J.F. Clauser and S. Li, *Talbot-vonLau atom interferometry with cold slow potassium*, Phys. Rev. A **49**, R2213–R2216 (1994).
- D. Clément, N. Fabbri, L. Fallani, C. Fort, and M. Inguscio, *Bragg Spectroscopy of Strongly Correlated Bosons in Optical Lattices*, J. Low Temp. Phys. **158**, 5-15 (2009).

BIBLIOGRAPHY

- C. Cohen–Tannoudji and S. Reynaud, *Dressed-atom description of resonance fluorescence and absorption spectra of a multi-level atom in an intense laser beam*, J. Phys. B **10**, 345 (1977).
- R. Combescot, S. Giorgini, and S. Stringari, *Molecular signatures in the structure factor of an interacting Fermi gas*, Europhys. Lett. **75**, 695-701 (2006).
- S.L. Cornish, N.R. Claussen, J.L. Roberts, E.A. Cornell, and C.E. Wieman, *Stable ^{85}Rb Bose-Einstein Condensates with Widely Tunable Interactions*, Phys. Rev. Lett. **85**, 1795–1798 (2000).
- L. Costa, J. Brachmann, A.–C. Voigt, C. Hahn, M. Taglieber, T.W. Hänsch, and K. Dieckmann, *s-Wave Interaction in a Two-Species Fermi–Fermi Mixture at a Narrow Feshbach Resonance*, Phys. Rev. Lett. **105**, 123201 (2010).
- L. Costa, J. Brachmann, A.–C. Voigt, C. Hahn, M. Taglieber, T.W. Hänsch, and K. Dieckmann, *Erratum: s-Wave Interaction in a Two-Species Fermi–Fermi Mixture at a Narrow Feshbach Resonance [Phys. Rev. Lett. 105, 123201 (2010)]*, Phys. Rev. Lett. **105**, 269903(E) (2010).
- P. Courteille, R.S. Freeland, D.J. Heinzen, F.A. van Abeelen, and B.J. Verhaar, *Observation of a Feshbach resonance in cold atom scattering*, Phys. Rev. Lett. **81**, 69–72 (1998).
- A.D. Cronin, J. Schmiedmayer, and D.E. Pritchard, *Optics and interferometry with atoms and molecules*, Rev. Mod. Phys. **81**, 1051 (2009).
- J. Cubizolles, T. Bourdel, S.J.J.M.F. Kokkelmans, G.V. Shlyapnikov, and C. Salomon, *Production of Long-Lived Ultracold Li_2 Molecules from a Fermi Gas*, Phys. Rev. Lett. **91**, 240401 (2003).
- J. Dalibard and C. Cohen–Tannoudji, *Dressed-atom approach to atomic motion in laser light: the dipole force revisited*, JOSA B **2**, 1707–1720 (1985).
- J.G. Danzl, E. Haller, M. Gustavsson, M.J. Mark, R. Hart, N. Bouloufa, O. Dulieu, H. Ritsch, and H.–C. Nägerl, *Quantum Gas of Deeply Bound Ground State Molecules*, Science **321**, 1062 (2008).
- K.B. Davis, M.–O. Mewes, M.R. Andrews, N.J. van Druten, D.S. Durfee, D.M. Kurn, and W. Ketterle, *Bose–Einstein Condensation in a Gas of Sodium Atoms*, Phys. Rev. Lett. **75**, 3969 (1995).
- B. Deh, *Ph.D. thesis*, Universität Tübingen (2008).
- B. Deh, C. Marzok, S. Slama, C. Zimmermann, and P.W. Courteille, *Bragg spectroscopy and Ramsey interferometry with an ultracold Fermi gas*, Appl. Phys. B **97**, 387–396 (2009).
- B. DeMarco, *Ph.D. thesis*, University of Colorado (2001).

- B. DeMarco and D.S. Jin, *Onset of Fermi Degeneracy in a Trapped Atomic Gas*, Science **285**, 1703–1706 (1999).
- B. DeMarco, S.B. Papp, and D.S. Jin, *Pauli Blocking of Collisions in a Quantum Degenerate Atomic Fermi Gas*, Phys. Rev. Lett. **86**, 5409–5412 (2001).
- D. DeMille, *Quantum Computation with Trapped Polar Molecules*, Phys. Rev. Lett. **88**, 067901 (2002).
- K. Dieckmann, *Ph.D. thesis*, University of Amsterdam (2001).
- K. Dieckmann, C.A. Stan, S. Gupta, Z. Hadzibabic, C.H. Schunck, and W. Ketterle, *Decay of an Ultracold Fermionic Lithium Gas near a Feshbach Resonance*, Phys. Rev. Lett. **89**, 203201 (2002).
- J.P. D’Incao and B.D. Esry, *Mass dependence of ultracold three-body collision rates*, Phys. Rev. A **73**, 030702R (2006).
- S. Dürr, T. Nonn, and G. Rempe, *Fringe Visibility and Which-Way Information in an Atom Interferometer*, Phys. Rev. Lett. **81**, 5705–5709 (1998a).
- S. Dürr, T. Nonn, and G. Rempe, *Origin of quantum-mechanical complementarity probed by a ‘which-way’ experiment in an atom interferometer*, Nature **395**, 33–37 (1998b).
- A. Einstein, *Quantentheorie des idealen einatomigen Gases*, Sitzungsber. Preuss. Akad. Wiss., 261–267 (1924).
- J.T. Eisinger, B. Bederson, and B.T. Feld, *The magnetic moment of ^{40}K and the hyperfine structure anomaly of the potassium isotopes*, Phys. Rev. **86**, 73 (1952).
- K. Enomoto, K. Kasa, M. Kitagawa, and Y. Takahashi, *Optical Feshbach Resonance Using the Intercombination Transition*, Phys. Rev. Lett. **101**, 203201 (2008).
- P.T. Ernst, S. Götze, J.S. Krauser, K. Pyka, D.-S. Lühmann, D. Pfannkuche, and K. Sengstock, *Probing superfluids in optical lattices by momentum-resolved Bragg spectroscopy*, Nature Physics **6**, 56–61 (2010).
- U. Fano, *Sullo spettro di assorbimento dei gas nobili presso il limite dello spettro d’arco*, Nuovo Cimento **12**, 154–161 (1935).
- U. Fano, *Effects of configuration interaction on intensities and phase shifts*, Phys. Rev. **124**, 1866 (1961).
- F.K. Fatemi, K.M. Jones, and P.D. Lett, *Observation of optically induced Feshbach resonances in collisions of cold atoms*, Phys. Rev. Lett. **85**, 4462–4465 (2000).
- P.O. Fedichev, Y. Kagan, G.V. Shlyapnikov, and J.T.M. Walraven, *Influence of nearly resonant light on the scattering length in low-temperature atomic gases*, Phys. Rev. Lett. **77**, 2913 (1996).

BIBLIOGRAPHY

- A.E. Feiguin and F. Heidrich–Meisner, *Pairing states of a polarized Fermi gas trapped in a one-dimensional optical lattice*, Phys. Rev. B **76**, 220508(R) (2007).
- H. Feshbach, *Unified theory of nuclear reactions*, Ann. Phys. **5**, 357–390 (1958).
- H. Feshbach, *Unified theory of nuclear reactions II*, Ann. Phys. **19**, 287–313 (1962).
- T. Fukuhara, Y. Takasu, S. Sugawa, and Y. Takahashi, *Quantum Degenerate Fermi Gases of Ytterbium Atoms*, J. Low Temp. Phys. **148**, 441–445 (2007).
- P. Fulde and R.A. Ferrell, *Superconductivity in a Strong Spin-Exchange Field*, Phys. Rev. **135**, A550A563 (1964).
- E. Gehm, *Ph.D. thesis*, Duke University (2003).
- M.E. Gehm, S.L. Hemmer, K.M. O’Hara, and J.E. Thomas, *Unitarity-limited elastic collision rate in a harmonically trapped Fermi gas*, Phys. Rev. A **68**, 011603(R) (2003).
- A. Gezerlis, S. Gandolfi, K.E. Schmidt, and J. Carlson, *Heavy-Light Fermion Mixtures at Unitarity*, Phys. Rev. Lett. **103**, 060403 (2009).
- D.M. Giltner, R.W. McGowan, and S.A. Lee, *Theoretical and experimental study of the Bragg scattering of atoms from a standing light wave*, Phys. Rev. A **52**, 3966-3972 (1995).
- S. Giorgini, L.P. Pitaevskii, and S. Stringari, *Theory of ultracold atomic Fermi gases*, Rev. Mod. Phys. **80**, 12151274 (2008).
- J. Goldwin, *Ph.D. thesis*, University of Colorado (2005).
- J. Goldwin, S. Inouye, M.L. Olsen, B. Newman, B.D. DePaola, and D.S. Jin, *Measurement of the interaction strength in a Bose–Fermi mixture with ^{87}Rb and ^{40}K* , Phys. Rev. A **70**, 021601(R) (2004).
- J. Goldwin, S. Inouye, M.L. Olsen, and D.S. Jin, *Cross-dimensional relaxation in Bose–Fermi mixtures*, Phys. Rev. A **71**, 043408 (2005).
- K. Góral, L. Santos, and M. Lewenstein, *Quantum Phases of Dipolar Bosons in Optical Lattices*, Phys. Rev. Lett. **88**, 170406 (2002).
- L.P. Gor’kov and T.K. Melik-Barkhudarov, *Contribution to the theory of superfluidity in an imperfect fermi gas*, Sov. Phys. JETP **13**, 1018-1022 (1962).
- P.L. Gould, G.A. Ruff, and D.E. Pritchard, *Diffraction of atoms by light: The near-resonant Kapitza-Dirac effect*, Phys. Rev. Lett. **56**, 827830 (1986).
- P.L. Gould, P.J. Martin, G.A. Ruff, R.E. Stoner, J.-L. Picqué, and D.E. Pritchard, *Momentum transfer to atoms by a standing light wave: Transition from diffraction to diffusion*, Phys. Rev. A **43**, 585–588 (1991).

-
- S.R. Granade, M.E. Gehm, K.M. O'Hara, and J.E. Thomas, *All-Optical Production of a Degenerate Fermi Gas*, Phys. Rev. Lett. **88**, 120405 (2002).
- M. Greiner, I. Bloch, T.W. Hänsch, and T. Esslinger, *Magnetic transport of trapped cold atoms over a large distance*, Phys. Rev. A **63**, 031401(R) (2001).
- M. Greiner, O. Mandel, T. Esslinger, T.W. Hänsch, and I. Bloch, *Quantum phase transition from a superfluid to a Mott insulator in a gas of ultracold atoms*, Nature **415**, 39–44 (2002).
- M. Greiner, C.A. Regal, and D.S. Jin, *Emergence of a molecular Bose–Einstein condensate from a Fermi gas*, Nature **426**, 537–540 (2003).
- M. Greiner, C.A. Regal, J.T. Stewart, and D.S. Jin, *Probing Pair-Correlated Fermionic Atoms through Correlations in Atom Shot Noise*, Phys. Rev. Lett. **94**, 110401 (2005).
- G.F. Gribakin and V.V. Flambaum, *Calculation of the scattering length in atomic collisions using the semiclassical approximation*, Phys. Rev. A **48**, 546–553 (1993).
- R. Grimm and F. Schreck, private communication.
- R. Grimm, M. Weidemüller, and Y.B. Ovchinnikov, *Optical dipole traps for neutral atoms*, Adv. At. Mol. Opt. Phys. **42**, 95–170 (2000).
- J. Grond, U. Hohenester, I. Mazets, and J. Schmiedmayer *Atom interferometry with trapped BoseEinstein condensates: impact of atomatom interactions*, New J. of Phys. **12**, 065036 (2010).
- K.B. Gubbels, J.E. Baarsma, and H.T.C. Stoof, *Lifshitz Point in the Phase Diagram of Resonantly Interacting ${}^6\text{Li}$ - ${}^{40}\text{K}$ Mixtures*, Phys. Rev. Lett. **103**, 195301 (2009).
- D. Guéry-Odelin, F. Zambelli, J. Dalibard, and S. Stringari, *Collective oscillations of a classical gas confined in harmonic traps*, Phys. Rev. A **60**, 4851 (1999).
- H. Guo, C.-C. Chien, and K. Levin, *Establishing the Presence of Coherence in Atomic Fermi Superfluids: Spin-Flip and Spin-Preserving Bragg Scattering at Finite Temperatures*, Phys. Rev. Lett. **105**, 120401 (2010).
- S. Gupta, *Ph.D. thesis*, Massachusetts Institute of Technology (2003).
- S. Gupta, A.E. Leanhardt, A.D. Cronin, and D.E. Pritchard, *Coherent manipulation of atoms with standing light waves*, C. R. Acad. Sci. Paris, Vol. **2**, Series IV, 479–495 (2001).
- S. Gupta, K. Dieckmann, Z. Hadzibabic, and D.E. Pritchard, *Contrast Interferometry using Bose–Einstein Condensates to Measure h/m and α* , Phys. Rev. Lett. **89**, 140401 (2002).

BIBLIOGRAPHY

- S. Gupta, Z. Hadzibabic, M.W. Zwierlein, C.A. Stan, K. Dieckmann, C.H. Schunck, E.G.M. van Kempen, B.J. Verhaar, and W. Ketterle, *Radio-Frequency Spectroscopy of Ultracold Fermions*, *Science* **300**, 1723 (2003).
- V. Gurarie and L. Radzihovsky, *Resonantly paired fermionic superfluids*, *Annals of Physics* **322**, 2–119 (2007).
- V. Gurarie, *Feshbach molecule production in fermionic atomic gases*, *Phys. Rev. A* **80**, 023626 (2009).
- Z. Hadzibabic, C.A. Stan, K. Dieckmann, S. Gupta, M.W. Zwierlein, A. Görlitz, and W. Ketterle, *Two-Species Mixture of Quantum Degenerate Bose and Fermi Gases*, *Phys. Rev. Lett.* **88**, 160401 (2002).
- C. Hahn, *Diploma thesis*, Ludwig-Maximilians-Universität München (2009).
- T.M. Hanna, E. Tiesinga, and P.S. Julienne, *Creation and manipulation of Feshbach resonances with radiofrequency radiation*, *New J. of Phys.* **12**, 083031 (2010).
- R. Haussmann, W. Rantner, S. Cerrito, and W. Zwerger, *Thermodynamics of the BCS-BEC crossover*, *Phys. Rev. A* **75**, 023610 (2007).
- F. Heidrich-Meisner, G. Orso, and A.E. Feiguin, *Phase separation of trapped spin-imbalanced Fermi gases in one-dimensional optical lattices*, *Phys. Rev. A* **81**, 053602 (2010).
- F. Henkel, *Diploma thesis*, Ludwig-Maximilians-Universität München (2005).
- H. Hu, P.D. Drummond, and X.J. Liu, *Universal thermodynamics of strongly interacting Fermi gases*, *Nature Physics* **3**, 469 (2007).
- E.R. Hudson, H.J. Lewandowski, B.C. Sawyer, and J. Ye, *Cold molecule spectroscopy for constraining the evolution of the fine structure constant*, *Phys. Rev. Lett.* **96**, 143004 (2006).
- Y. Inada, M. Horikoshi, S. Nakajima, M. Kuwata-Gonokami, M. Ueda, and T. Mukaiyama *Critical Temperature and Condensate Fraction of a Fermion Pair Condensate*, *Phys. Rev. Lett.* **101**, 180406 (2008).
- S. Inouye, M.R. Andrews, J. Stenger, H.-J. Miesner, D.M. Stamper-Kurn, and W. Ketterle, *Observation of Feshbach resonances in a Bose-Einstein condensate*, *Nature* **392**, 151–154 (1998).
- S. Inouye, J. Goldwin, M.L. Olsen, C. Ticknor, J.L. Bohn, and D.S. Jin, *Observation of heteronuclear Feshbach resonances in a mixture of bosons and fermions*, *Phys. Rev. Lett.* **93**, 183201 (2004).
- D. Jaksch, C. Bruder, J.I. Cirac, C.W. Gardiner, and P. Zoller, *Cold Bosonic Atoms in Optical Lattices*, *Phys. Rev. Lett.* **81**, 3108 (1998).

- D. Jaksch and P. Zoller, *The cold atom Hubbard toolbox*, *Annals of Physics* **315**, 52–79 (2005).
- L.M. Jensen, H.M. Nilsen, and G. Watanabe, *BCS–BEC crossover in atomic Fermi gases with a narrow resonance*, *Phys. Rev. A* **74**, 043608 (2006).
- S. Jochim, M. Bartenstein, G. Hendl, J. Hecker Denschlag, R. Grimm, A. Mosk, and W. Weidemüller, *Magnetic field control of elastic scattering in a cold gas of fermionic lithium atoms*, *Phys. Rev. Lett.* **89**, 273202 (2002).
- S. Jochim, M. Bartenstein, A. Altmeyer, G. Hendl, S. Riedl, C. Chin, J. Hecker Denschlag, and R. Grimm, *Bose–Einstein Condensation of Molecules*, *Science* **302**, 2101–2103 (2003a).
- S. Jochim, M. Bartenstein, A. Altmeyer, G. Hendl, C. Chin, J. Hecker Denschlag, and R. Grimm, *Pure Gas of Optically Trapped Molecules Created from Fermionic Atoms*, *Phys. Rev. Lett.* **91**, 240402 (2003b).
- A.M. Kaufman, R.P. Anderson, T.M. Hanna, E. Tiesinga, P.S. Julienne, and D.S. Hall, *Radio–frequency dressing of multiple Feshbach resonances*, *Phys. Rev. A* **80**, 050701(R) (2009).
- D.W. Keith, C.R. Ekstrom, Q.A. Turchette, and D.E. Pritchard, *An interferometer for atoms*, *Phys. Rev. Lett.* **66**, 26932696 (1991).
- W. Ketterle, D.S. Durfee, and D.M. Stamper–Kurn, *Making, probing and understanding Bose–Einstein condensates*, in *Proceedings of the International School of Physics – Enrico Fermi – Course CXL*, ed. by M. Inguscio, S. Stringari, and C.E. Wieman (IOS Press, Amsterdam), 67–176 (1999).
- W. Ketterle and M.W. Zwierlein, *Making, probing and understanding ultracold Fermi gases*, in *Proceedings of the International School of Physics – Enrico Fermi – Course CLXIV*, ed. by M. Inguscio, W. Ketterle, and C. Salomon (IOS Press, Amsterdam), 95–287 (2008).
- T. Kinoshita, T. Wenger, and D.S. Weiss, *Observation of a One-Dimensional Tonks–Girardeau Gas*, *Science* **305**, 1125–1128 (2004).
- C. Klempt, T. Henninger, O. Topic, M. Scherer, L. Kattner, E. Tiemann, W. Ertmer, and J.J. Arlt, *Radio–frequency association of heteronuclear Feshbach molecules*, *Phys. Rev. A* **78**, 061602(R) (2008).
- T. Köhler, K. Góral, and P.S. Julienne, *Production of cold molecules via magnetically tunable Feshbach resonances*, *Rev. Mod. Phys.* **78**, 1311–1361 (2006).
- M. Kozuma, L. Deng, E.W. Hagley, J. Wen, R. Lutwak, K. Helmerson, S.L. Rolston, and W.D. Phillips, *Coherent Splitting of Bose–Einstein Condensed Atoms with Optically Induced Bragg Diffraction*, *Phys. Rev. Lett.* **82**, 871–875 (1999).

BIBLIOGRAPHY

- R.V. Krems, *Cold controlled chemistry*, Phys. Chem. Chem. Phys. **10**, 4079–4092 (2008).
- E.D. Kuhnle, H. Hu, X.-J. Liu, P. Dyke, M. Mark, P.D. Drummond, P. Hannaford, and C.J. Vale, *Universal Behavior of Pair Correlations in a Strongly Interacting Fermi Gas*, Phys. Rev. Lett. **105**, 070402 (2010).
- T. Lahaye, T. Koch, B. Fröhlich, M. Fattori, J. Metz, A. Griesmaier, S. Giovanazzi, and T. Pfau, *Strong dipolar effects in a quantum ferrofluid*, Nature **448**, 672–675 (2007).
- T. Lahaye, C. Menotti, L. Santos, M. Lewenstein, and T. Pfau, *The physics of dipolar bosonic quantum gases*, Rep. Prog. Phys. **72** 126401 (2009).
- L.D. Landau and E.M. Lifshitz, *Vol. 3. Quantum Mechanics – Non-Relativistic Theory*, Pergamon Press Oxford (1991).
- F. Lang, K. Winkler, C. Strauss, R. Grimm, and J. Hecker Denschlag, *Ultracold Triplet Molecules in the Rovibrational Ground State*, Phys. Rev. Lett. **101**, 133005 (2008).
- A.I. Larkin and Y.N. Ovchinnikov, *Nonuniform state of superconductors*, Sov. Phys. JETP **20**, 762769 (1965).
- L.J. LeBlanc, *The hyperfine structure of potassium-40* (2006).
- L.J. LeBlanc and J.H. Thywissen, *Species-specific optical lattices*, Phys. Rev. A **75**, 053612 (2007).
- J. Levinsen, T.G. Tiecke, J.T.M. Walraven, and D.S. Petrov, *Atom-Dimer Scattering and Long-Lived Trimers in Fermionic Mixtures*, Phys. Rev. Lett. **103**, 153202 (2009).
- J. Levinsen and D.S. Petrov, *Atom-dimer and dimer-dimer scattering in fermionic mixtures near a narrow Feshbach resonance*, arXiv:1101.5979v1 (2011).
- M. Lewenstein, A. Sanpera, V. Ahufinger, B. Damski, A. Sen, and U. Sen, *Ultracold atomic gases in optical lattices: mimicking condensed matter physics and beyond*, Advances in Physics, **56**, 243–379 (2007).
- Z. Li, S. Singh, T.V. Tscherbul, and K.W. Madison, *Feshbach resonances in ultracold ^{85}Rb - ^{87}Rb and ^6Li - ^{87}Rb mixtures*, Phys. Rev. A **78**, 022710 (2008).
- Y.A. Liao, A.S.C. Rittner, T. Paprotta, W. Li, G.B. Partridge, R.G. Hulet, S.K. Baur, and E.J. Mueller, *Spin-imbalance in a one-dimensional Fermi gas*, Nature **467**, 567–569 (2010).
- W.V. Liu, and F. Wilczek, *Interior Gap Superfluidity*, Phys. Rev. Lett. **90**, 047002 (2003).
- T. Loftus, C.A. Regal, C. Ticknor, J.L. Bohn, and D.S. Jin, *Resonant Control of Elastic Collisions in an Optically Trapped Fermi Gas of Atoms*, Phys. Rev. Lett. **88**, 173201 (2002).

- O.J. Luiten, M.W. Reynolds, and J.T.M. Walraven, *Kinetic theory of the evaporative cooling of a trapped gas*, Phys. Rev. A **53**, 381 (1996).
- M. Mang, *Diploma thesis*, Ludwig–Maximilians–Universität München (2009).
- A. Marte, T. Volz, J. Schuster, S. Dürr, G. Rempe, E.G.M. van Kempen, and B.J. Verhaar, *Feshbach resonances in rubidium 87: Precision measurement and analysis*, Phys. Rev. Lett. **89**, 283202 (2002).
- P.J. Martin, B.G. Oldaker, A.H. Miklich, and D.E. Pritchard, *Bragg scattering of atoms from a standing light wave*, Phys. Rev. Lett. **60**, 515518 (1988).
- Y.N. Martinez de Escobar, P.G. Mickelson, M. Yan, B.J. DeSalvo, S.B. Nagel, and T.C. Killian, *Bose-Einstein Condensation of ^{84}Sr* , Phys. Rev. Lett. **103**, 200402 (2009).
- J.M. McNamara, T. Jelten, A.S. Tychkov, W. Hogervorst, and W. Vassen, *Degenerate Bose-Fermi Mixture of Metastable Atoms*, Phys. Rev. Lett. **97**, 080404 (2006).
- H.J. Metcalf and P. van der Straten, *Laser cooling and trapping*, Springer (1999).
- A. Micheli, G.K. Brennen, and P. Zoller, *A toolbox for lattice–spin models with polar molecules*, Nature Physics **2**, 341–347 (2006).
- P.W. Milonni and J.H. Eberly, *Lasers*, John Wiley & Sons (1988).
- A.J. Moerdijk, B.J. Verhaar, and A. Axelsson, *Resonances in ultracold collisions of ^6Li , ^7Li , and ^{23}Na* , Phys. Rev. A **51**, 48524861 (1995).
- C.R. Monroe, E.A. Cornell, C.A. Sackett, C.J. Myatt, and C.E. Wieman, *Measurement of Cs-Cs elastic scattering at $T = 30\ \mu\text{K}$* , Phys. Rev. Lett. **70**, 414–417 (1993).
- P.E. Moskowitz, P.L. Gould, S.R. Atlas, and D.E. Pritchard, *Diffraction of an Atomic Beam by Standing-Wave Radiation*, Phys. Rev. Lett. **51**, 370373 (1983).
- S.R. Muniz, D.S. Naik, and C. Raman, *Bragg spectroscopy of vortex lattices in Bose-Einstein condensates*, Phys. Rev. A **73**, 041605 (2006).
- D. Naik, A. Trenkwalder, C. Kohstall, F.M. Spiegelhalder, M. Zaccanti, G. Hendl, F. Schreck, R. Grimm, T.M. Hanna, and P.S. Julienne, *Feshbach resonances in the ^6Li – ^{40}K Fermi–Fermi mixture: Elastic versus inelastic interactions*, Eur. Phys. J. D (2011).
- S. Nascimbéne, N. Navon, K.J. Jiang, L. Tarruell, M. Teichmann, J. McKeever, F. Chevy, and C. Salomon, *Collective Oscillations of an Imbalanced Fermi Gas: Axial Compression Modes and Polaron Effective Mass*, Phys. Rev. Lett. **103**, 170402 (2009).
- S. Nascimbéne, N. Navon, K.J. Jiang, F. Chevy, and C. Salomon, *Exploring the thermodynamics of a universal Fermi gas*, Nature **463**, 1057 (2010).

BIBLIOGRAPHY

- K.-K. Ni, S. Ospelkaus, M.H.G. de Miranda, A. Pe'er, B. Neyenhuis, J.J. Zirbel, S. Kotochigova, P.S. Julienne, D.S. Jin, J. Ye, *A High Phase-Space-Density Gas of Polar Molecules*, *Science* **322**, 231 (2008).
- K.-K. Ni, S. Ospelkaus, D. Wang, G. Quémener, B. Neyenhuis, M.H.G. de Miranda, J.L. Bohn, J. Ye, and D.S. Jin, *Dipolar collisions of polar molecules in the quantum regime*, *Nature* **464**, 1324–1328 (2010).
- M.K. Oberthaler, R. Abfalterer, S. Bernet, J. Schmiedmayer, and A. Zeilinger, *Atom Waves in Crystals of Light*, *Phys. Rev. Lett.* **77**, 4980–4983 (1996).
- K.M. O'Hara, S.L. Hemmer, S.R. Granade, M.E. Gehm, J.E. Thomas, V. Venturi, E. Tiesinga, and C.J. Williams, *Measurement of the zero crossing in a Feshbach resonance of fermionic ^6Li* , *Phys. Rev. A* **66**, 041401 (2002a).
- K.M. O'Hara, S.L. Hemmer, M.E. Gehm, S.R. Granade, J.E. Thomas, *Observation of a Strongly Interacting Degenerate Fermi Gas of Atoms*, *Science* **298**, 2179–2182 (2002b).
- Y. Ohashi and A. Griffin, *BCS–BEC Crossover in a Gas of Fermi Atoms with a Feshbach Resonance*, *Phys. Rev. Lett.* **89**, 130402 (2002).
- Y. Ohashi and A. Griffin, *Single-particle excitations in a trapped gas of Fermi atoms in the BCS–BEC crossover region*, *Phys. Rev. A* **72**, 013601 (2005).
- M. Okano, H. Hara, M. Muramatsu, K. Doi, S. Uetake, Y. Takasu, and Y. Takahashi, *Simultaneous magneto-optical trapping of lithium and ytterbium atoms towards production of ultracold polar molecules*, *Appl. Phys. B* **98**, 691–696 (2010).
- R. Onofrio and C. Presilla, *Ultracold Atomic Fermi–Bose Mixtures in Bichromatic Optical Dipole Traps: A Novel Route to Study Fermion Superfluidity*, *J. Stat. Phys.* **115**, 57–89 (2004).
- C. Ospelkaus, S. Ospelkaus, L. Humbert, P. Ernst, K. Sengstock, and K. Bongs, *Ultracold Heteronuclear Molecules in a 3D Optical Lattice*, *Phys. Rev. Lett.* **97**, 120402 (2006).
- S. Ospelkaus, A. Pe'er, K.-K. Ni, J.J. Zirbel, B. Neyenhuis, S. Kotochigova, P.S. Julienne, J. Ye, and D.S. Jin, *Efficient state transfer in an ultracold dense gas of heteronuclear molecules*, *Nature Physics* **4**, 622–626 (2008).
- Y.B. Ovchinnikov, J.H. Müller, M.R. Doery, E.J.D. Vredenbregt, K. Helmerson, S.L. Rolston, and W.D. Phillips, *Diffraction of a Released Bose-Einstein Condensate by a Pulsed Standing Light Wave*, *Phys. Rev. Lett.* **83**, 284287 (1999).
- S.B. Papp, *Ph.D. thesis*, University of Colorado (2007).
- S.B. Papp and C.E. Wieman, *Observation of Heteronuclear Feshbach Molecules from a ^{85}Rb - ^{87}Rb Gas*, *Phys. Rev. Lett.* **97**, 180404 (2006).

- S.B. Papp, J.M. Pino, R.J. Wild, S. Ronen, C.E. Wieman, D.S. Jin, and E.A. Cornell, *Bragg Spectroscopy of a Strongly Interacting ^{85}Rb Bose–Einstein Condensate*, Phys. Rev. Lett. **101**, 135301 (2008).
- B. Paredes, A. Widera, V. Murg, O. Mandel, S. Fölling, I. Cirac, G.V. Shlyapnikov, T.W. Hänsch, and I. Bloch, *Tonks–Girardeau gas of ultracold atoms in an optical lattice*, Nature **429**, 277–281 (2004).
- G.B. Partridge, K.E. Strecker, R.I. Kamar, M.W. Jack, and R.G. Hulet, *Molecular Probe of Pairing in the BEC–BCS Crossover*, Phys. Rev. Lett. **95**, 020404 (2005).
- G.B. Partridge, W. Li, R.I. Kamar, Y. Liao, and R.G. Hulet, *Pairing and Phase Separation in a Polarized Fermi Gas*, Science **311**, 503 (2006).
- C.J. Pethick and H. Smith, *Bose–Einstein Condensation in Dilute Gases*, Cambridge University Press (2002).
- D.S. Petrov, C. Salomon, and G.V. Shlyapnikov, *Weakly Bound Dimers of Fermionic Atoms*, Phys. Rev. Lett. **93**, 090404 (2004a).
- D.S. Petrov, *Three–Boson Problem near a Narrow Feshbach Resonance*, Phys. Rev. Lett. **93**, 143201 (2004b).
- D.S. Petrov, C. Salomon, and G.V. Shlyapnikov, *Scattering properties of weakly bound dimers of fermionic atoms*, Phys. Rev. A **71**, 012708 (2005a).
- D.S. Petrov, C. Salomon, and G.V. Shlyapnikov, *Diatomic molecules in ultracold Fermi gases – novel composite bosons*, J. Phys. B **38**, S645 (2005b).
- D.S. Petrov, G.E. Astrakharchik, D.J. Papoular, C. Salomon, and G.V. Shlyapnikov, *Crystalline Phase of Strongly Interacting Fermi Mixtures*, Phys. Rev. Lett. **99**, 130407 (2007).
- Á. Rapp, G. Zaránd, C. Honerkamp, and W. Hofstetter, *Color Superfluidity and “Baryon” Formation in Ultracold Fermions*, Phys. Rev. Lett. **98**, 160405 (2007).
- C.A. Regal, *Ph.D. thesis*, University of Colorado (2005).
- C.A. Regal, C. Ticknor, J.L. Bohn, and D.S. Jin, *Creation of ultracold molecules from a Fermi gas of atoms*, Nature **424**, 47–50 (2003a).
- C.A. Regal, C. Ticknor, J.L. Bohn, and D.S. Jin, *Tuning p -wave interactions in an ultracold Fermi gas of atoms*, Phys. Rev. Lett. **90**, 053201 (2003b).
- C.A. Regal and D.S. Jin, *Measurement of positive and negative scattering lengths in a Fermi gas of atoms*, Phys. Rev. Lett. **90**, 230404 (2003c).
- C.A. Regal, M. Greiner, and D.S. Jin, *Observation of resonance condensation of fermionic atom pairs*, Phys. Rev. Lett. **92**, 040403 (2004a).

BIBLIOGRAPHY

- C.A. Regal, M. Greiner, and D.S. Jin, *Lifetime of Molecule–Atom Mixtures near a Feshbach Resonance in ^{40}K* , Phys. Rev. Lett. **92**, 083201 (2004b).
- F. Reif, *Statistische Physik und Theorie der Wärme*, de Gruyter, Berlin, New York (1987).
- O.K. Rice, *Predissociation and the crossing of molecular potential energy curves*, J. Chem. Phys. **1**, 375 (1933).
- M. Rizzi, M. Polini, M.A. Cazalilla, M.R. Bakhtiari, M.P. Tosi, and R. Fazio, *Fulde–Ferrell–Larkin–Ovchinnikov pairing in one-dimensional optical lattices*, Phys. Rev. B **77**, 245105 (2008).
- G. Roati, E. de Mirandes, F. Ferlaino, H. Ott, G. Modugno, and M. Inguscio, *Fermi–Bose Quantum Degenerate ^{40}K – ^{87}Rb Mixture with Attractive Interaction*, Phys. Rev. Lett. **89**, 150403 (2002).
- G. Roati, E. de Mirandes, F. Ferlaino, H. Ott, G. Modugno, and M. Inguscio, *Atom Interferometry with Trapped Fermi Gases*, Phys. Rev. Lett. **92**, 230402 (2004).
- J.L. Roberts, *Ph.D. thesis*, University of Colorado (2001).
- E. Röhl, *Diploma thesis*, Technical University Graz (1999).
- M.W.J. Romans and H.T.C. Stoof, *Bogoliubov theory of Feshbach molecules in the BEC–BCS crossover*, Phys. Rev. A **74**, 053618 (2006).
- M.S. Safronova, B. Arora, and C.W. Clark, *Frequency–dependent polarizabilities of alkali–metal atoms from ultraviolet through infrared spectral regions*, Phys. Rev. A **73**, 022505 (2006).
- L. Santos, G.V. Shlyapnikov, P. Zoller, and M. Lewenstein, *Bose–Einstein Condensation in Trapped Dipolar Gases*, Phys. Rev. Lett. **85**, 1791 (2000).
- L. Santos, G.V. Shlyapnikov, P. Zoller, and M. Lewenstein, *Erratum: Bose–Einstein Condensation in Trapped Dipolar Gases [Phys. Rev. Lett. 85, 1791 (2000)]*, Phys. Rev. Lett. **88**, 139904 (2002).
- F. Schreck, L. Khaykovich, K.L. Corwin, G. Ferrari, T. Bourdel, J. Cubizolles, and C. Salomon, *Quasipure Bose–Einstein Condensate Immersed in a Fermi Sea*, Phys. Rev. Lett. **87**, 080403 (2001).
- C.H. Schunck, Y. Shin, A. Schirotzek, M.W. Zwierlein, W. Ketterle, *Pairing Without Superfluidity: The Ground State of an Imbalanced Fermi Mixture*, Science **316**, 867–870 (2007).
- D.E. Sheehy and L. Radzihovsky, *BEC–BCS crossover, phase transitions and phase separation in polarized resonantly–paired superfluids*, Annals of Physics **322**, 1790–1924 (2006).

- Y. Shin, M.W. Zwierlein, C.H. Schunck, A. Schirotzek, and W. Ketterle, *Observation of Phase Separation in a Strongly Interacting Imbalanced Fermi Gas*, Phys. Rev. Lett. **97**, 030401 (2006).
- Y. Shin, C.H. Schunck, A. Schirotzek, and W. Ketterle, *Phase diagram of a two-component Fermi gas with resonant interactions*, Nature **451**, 689 (2008).
- J.H. Shirley, *Solution of the Schrödinger Equation with a Hamiltonian Periodic in Time*, Phys. Rev. **138**, B979–B987 (1965).
- C. Silber, S. Günther, C. Marzok, B. Deh, Ph.W. Courteille, and C. Zimmermann, *Quantum-Degenerate Mixture of Fermionic Lithium and Bosonic Rubidium Gases*, Phys. Rev. Lett. **95**, 170408 (2005).
- A. Simoni, F. Ferlaino, G. Roati, G. Modugno, and M. Inguscio, *Magnetic control of the interaction in ultracold K–Rb mixtures*, Phys. Rev. Lett. **90**, 163202 (2003).
- F.M. Spiegelhalder, A. Trenkwalder, D. Naik, G. Kerner, E. Wille, G. Hendl, F. Schreck, and R. Grimm, *All-optical production of a degenerate mixture of ^6Li and ^{40}K and creation of heteronuclear molecules*, Phys. Rev. A **81**, 043637 (2010).
- J. Stenger, S. Inouye, A.P. Chikkatur, D.M. Stamper-Kurn, D.E. Pritchard, and W. Ketterle, *Bragg Spectroscopy of a Bose–Einstein Condensate*, Phys. Rev. Lett. **82**, 4569 (1999).
- J. Stewart, J. Gaebler, C. Regal, and D. Jin, *Potential energy of a 40K Fermi gas in the BCS–BEC crossover*, Phys. Rev. Lett. **97**, 220406 (2006).
- K.E. Strecker, G.B. Partridge, and R.G. Hulet, *Conversion of an Atomic Fermi Gas to a Long-Lived Molecular Bose Gas*, Phys. Rev. Lett. **91**, 080406 (2003).
- M. Taglieber, *Ph.D. thesis*, Ludwig–Maximilians–Universität München (2008).
- M. Taglieber, A.–C. Voigt, F. Henkel, S. Fray, T.W. Hänsch, and K. Dieckmann, *Simultaneous magneto-optical trapping of three atomic species*, Phys. Rev. A **73**, 011402(R) (2006).
- M. Taglieber, A.–C. Voigt, T. Aoki, T.W. Hänsch, and K. Dieckmann, *Quantum Degenerate Two-Species Fermi–Fermi Mixture Coexisting with a Bose–Einstein Condensate*, Phys. Rev. Lett. **100**, 010401 (2008).
- M.K. Tey, S. Stellmer, R. Grimm, and F. Schreck, *Double-degenerate Bose-Fermi mixture of strontium*, Phys. Rev. A **82**, 011608(R) (2010).
- M. Tezuka and M. Ueda, *Density–Matrix Renormalization Group Study of Trapped Imbalanced Fermi Condensates*, Phys. Rev. Lett. **100**, 110403 (2008).
- M. Theis, G. Thalhammer, K. Winkler, M. Hellwig, G. Ruff, R. Grimm, and J. Hecker Denschlag, *Tuning the scattering length with an optically induced Feshbach resonance*, Phys. Rev. Lett. **93**, 123001 (2004).

BIBLIOGRAPHY

- T.G. Tiecke, *Ph.D. thesis*, University of Amsterdam (2009).
- T.G. Tiecke, M.R. Goosen, A. Ludewig, S.D. Gensemer, S. Kraft, S.J.J.M.F. Kokkelmans, and J.T.M. Walraven, *Broad Feshbach Resonance in the ${}^6\text{Li}$ - ${}^{40}\text{K}$ Mixture*, Phys. Rev. Lett. **104**, 053202 (2010a).
- T.G. Tiecke, M.R. Goosen, J.T.M. Walraven, and S.J.J.M.F. Kokkelmans, *Asymptotic Bound-state Model for Feshbach Resonances*, Phys. Rev. A **82**, 042712 (2010b).
- E. Tiemann, H. Knöckel, P. Kowalczyk, W. Jastrzebski, A. Pashov, H. Salami, and A.J. Ross, *Coupled system $a^3\Sigma^+$ and $X^1\Sigma^+$ of KLi : Feshbach resonances and corrections to the Born-Oppenheimer approximation*, Phys. Rev. A **79**, 042716 (2009).
- E. Timmermans, P. Tommasini, M. Hussein, A. Kerman, *Feshbach resonances in atomic Bose-Einstein condensates*, Physics Reports **315**, 199–230 (1999).
- A.G. Truscott, K.E. Strecker, W.I. McAlexander, G.B. Partridge, and R.G. Hulet, *Observation of Fermi Pressure in a Gas of Trapped Atoms*, Science **291**, 2570–2572 (2001).
- T. Udem, *Diploma thesis*, Justus-Liebig Universität Gießen (1994).
- G. Veeravalli, E. Kuhnle, P. Dyke, and C.J. Vale, *Bragg Spectroscopy of a Strongly Interacting Fermi Gas*, Phys. Rev. Lett. **101**, 250403 (2008).
- A.-C. Voigt, *Ph.D. thesis*, Ludwig-Maximilians-Universität München (2009).
- A.-C. Voigt, M. Taglieber, L. Costa, T. Aoki, W. Wieser, T.W. Hänsch, and K. Dieckmann, *Ultracold Heteronuclear Fermi-Fermi Molecules*, Phys. Rev. Lett. **102**, 020405 (2009).
- A.-C. Voigt, M. Taglieber, L. Costa, T. Aoki, W. Wieser, T.W. Hänsch, and K. Dieckmann, *Erratum: Ultracold Heteronuclear Fermi-Fermi Molecules [Phys. Rev. Lett. 102, 020405 (2009)]*, Phys. Rev. Lett. **105**, 269904(E) (2010).
- V. Vuletić, A.J. Kerman, C. Chin, and S. Chu, *Observation of low-field Feshbach resonances in collisions of cesium atoms*, Phys. Rev. Lett. **82**, 1406 (1999).
- J.T.M. Walraven, *Atomic hydrogen in magnetostatic traps*, in Quantum Dynamics of simple systems, ed. by G.-L. Oppo, S.M. Barnett, E. Riis, and M. Wilkinson (IOP:Bristol SUSSP Proceedings, Vol. 44) (1996).
- J.T.M. Walraven, *Elements of Quantum Gases: Thermodynamic and Collisional Properties of Trapped Atomic Gases*, Bachelor course at honours level, University of Amsterdam (2010).
- B. Wang, H.-D. Chen, and S. Das Sarma, *Quantum phase diagram of fermion mixtures with population imbalance in one-dimensional optical lattices*, Phys. Rev. A **79**, 051604(R) (2009).

BIBLIOGRAPHY

- C. Weber, G. Barontini, J. Catani, G. Thalhammer, M. Inguscio, and F. Minardi, *Association of ultracold double-species bosonic molecules*, Phys. Rev. A **78**, 061601(R) (2008).
- F. Werner, L. Tarruell, and Y. Castin, *Number of closed-channel molecules in the BEC–BCS crossover*, Eur. Phys. J. B **68**, 401–415 (2009).
- J. Werner, A. Griesmaier, S. Hensler, J. Stuhler, T. Pfau, A. Simoni, and E. Tiesinga, *Observation of Feshbach resonances in an ultracold gas of ^{52}Cr* , Phys. Rev. Lett. **94**, 183201 (2005).
- W. Wieser, *Diploma thesis*, Ludwig–Maximilians–Universität München (2006).
- E. Wille, F.M. Spiegelhalter, G. Kerner, D.Naik, A. Trenkwalder, G. Hendl, F. Schreck, R. Grimm, T.G. Tiecke, J.T.M. Walraven, S.J.J.M.F. Kokkelmans, E. Tiesinga, and P.S. Julienne, *Exploring an Ultracold Fermi–Fermi Mixture: Interspecies Feshbach Resonances and Scattering Properties of ^6Li and ^{40}K* , Phys. Rev. Lett. **100**, 053201 (2008).
- T. Zelevinsky, S. Kotochigova, and J. Ye, *Precision test of mass–ratio variations with lattice–confined ultracold molecules*, Phys. Rev. Lett. **100**, 043201 (2008).
- N.T. Zinner and M. Thøgersen, *Stability of a Bose–Einstein condensate with higher-order interactions near a Feshbach resonance*, Phys. Rev. A **80**, 023607 (2009).
- N.T. Zinner, *Effective Potential for Ultracold Atoms at the Zero-Crossing of a Feshbach Resonance*, arXiv:0909.1314v4 (2010).
- J.J. Zirbel, K.–K. Ni, S. Ospelkaus, T.L. Nicholson, M.L. Olsen, P.S. Julienne, C.E. Wieman, J. Ye, and D.S. Jin, *Heteronuclear molecules in an optical dipole trap*, Phys. Rev. A **78**, 013416 (2008).
- P. Zou, E.D. Kuhnle, C.J. Vale, and H. Hu, *Quantitative comparison between theoretical predictions and experimental results for Bragg spectroscopy of a strongly interacting Fermi superfluid*, Phys. Rev. A **82**, 061605(R) (2010).
- M.W. Zwierlein, C.A. Stan, C.H. Schunck, S.M.F. Raupach, S. Gupta, Z. Hadzibabic, and W. Ketterle, *Observation of Bose–Einstein Condensation of Molecules*, Phys. Rev. Lett. **91**, 250401 (2003).
- M.W. Zwierlein, C.A. Stan, C.H. Schunck, S.M.F. Raupach, A.J. Kerman, and W. Ketterle, *Condensation of Pairs of Fermionic Atoms near a Feshbach Resonance*, Phys. Rev. Lett. **92**, 120403 (2004).
- M.W. Zwierlein, J.R. Abo-Shaeer, A. Schirotzek, C.H. Schunck, and W. Ketterle, *Vortices and superfluidity in a strongly interacting Fermi gas*, Nature **435**, 1047–1051 (2005).
- M.W. Zwierlein, A. Schirotzek, C.H. Schunck, and W. Ketterle, *Fermionic Superfluidity with Imbalanced Spin Populations*, Science **311**, 492–496 (2006).

Danksagung

An erster Stelle möchte ich Herrn Prof. Dr. Theodor W. Hänsch danken, dass ich ein Teil seiner Arbeitsgruppe sein durfte. Es war mir eine sehr große Ehre und Freude in seinem inspirierenden Umfeld arbeiten zu dürfen. Die alljährlichen Seminare auf Schloss Ringberg zeigten mir stets wie fruchtbar, divers und lebhaft Diskussionen zu eigenen aber auch nah verwandten Gebieten in seiner Arbeitsgruppe sein können. Auf den Weihnachtsfeiern in der Innenstadt war immer für eine gute Stimmung gesorgt, die mir in Erinnerung bleiben wird.

Herrn Prof. Dr. Ulrich Schollwöck danke ich sehr für die freundliche Bereitschaft, die vorliegende Arbeit zu begutachten.

Herrn Prof. Dr. Kai Dieckmann, meinem Arbeitsgruppenleiter, bin ich in vielfältiger Hinsicht dankbar. Seine stets motivierte Art hatte mich vom ersten Tag meiner Bewerbung beeindruckt und mich vollends von dem Projekt überzeugt. Auch hatte er von Anfang an Vertrauen in mich gesetzt. Ich hatte gerade in meiner Anfangsphase enorm viel Neues gelernt was Technologien betrifft, aber auch, was aus meiner Sicht noch viel wichtiger ist, Neues in Bezug auf Arbeitsweise und -einstellung von ihm erfahren dürfen. In auftretenden Tiefphasen während meiner Zeit hatte er für mich auch menschlich gesehen immer die richtigen Worte gefunden, was ich ihm hochanrechne. Die Unterstützung gerade im letzten Teil meiner Promotionszeit über ferne Distanz nach Singapur funktionierte immer einwandfrei und effektiv, und die Diskussionen zur Interpretation von Messungen machten richtig viel Spaß. Ich wünsche ihm sowohl persönlich als auch beruflich das Beste für seine künftigen Aufgaben an dem neuen Ort.

Mit meinem Kollegen Arne-Christian Voigt verbindet mich eine tolle Zusammenarbeit. Als einer der "Gründungsväter" der Apparatur, hatte ich Vieles von ihm lernen können. Er führte mich in den gemeinsamen langen Messnächten in die Einzelheiten zur Bedienung der komplexen Apparatur ein. Wir hatten oftmals sehr interessante Gespräche im Labor geführt zur Interpretation von Messungen. Aber selbst in seiner eigenen zeitintensiven Schreibphase und als Postdoc fand er stets die Zeit mir ein kritischer und bereichernder Diskussionspartner zu sein, wofür ich ihm tiefen Dank schulde.

Die Arbeit mit Johannes Brachmann hatte ich durch seine besonnene und freundliche Art als sehr angenehm empfunden. Ich möchte mich für das Korrekturlesen meiner Arbeit bedanken. Ich wünsche ihm für seine weitere Zukunft alles Gute.

Mit Matthias Taglieber hatte ich leider nur wenig Überlapp im Labor, aber dafür hatte er immer ein offenes Ohr für Fragen und ich konnte sehr von seinem enormen Erfahrungsschatz am Experiment profitieren. Seine erfrischende Art war stets sehr belebend

bei uns im Labor.

Dr. Takatoshi Aoki aus Japan war ein sehr sympatischer Kollege, der in einer sehr zeitintensiven Phase am Experiment bei uns tätig war. Die schmackhaften Köstlichkeiten, die er regelmäßig aus seiner Heimat mitbrachte und an denen er uns teilnehmen ließ, entfachten unter anderem meine Leidenschaft für die japanische Küche.

Ich bedanke mich bei den Diplomanden¹ Carolin Hahn und Matthias Mang, die in besonderer Weise mit ihren unabhängigen Projekten zum Erfolg dieser Arbeit beigetragen haben. Ich wünsche beiden bei ihren momentanen Aufgaben alles Gute.

Die Unterstützung durch zahlreiche Werkstudenten, die viele wertvolle Arbeiten im Labor verrichteten, erbrachte ebenfalls einen unverzichtbaren Wert. Hier hatten auch die beiden bereits erwähnten Diplomanden, Benedikt Breitenfeld, Norbert Ortegel und Simon Müller den jeweiligen Doktoranden tatkräftig unterstützt. Wolfgang Wieser hat mit seinem enormen Wissen über das Design von elektronischen Schaltkreisen einen maßgeblichen Einfluss in unserer Gruppe genommen. Mit den beiden Austauschstudenten Gabriel Bismut und Zhenkai Lu war es toll zusammenzuarbeiten.

Für organisatorische, technische und elektronische Fragestellungen bin ich Fr. Gabriele Gschwendtner, Fr. Ingrid Hermann, Fr. Nicole Schmidt, Hr. Anton Scheich, Hr. Wolfgang Simon, Hr. Karl Linner und der Werkstatt der LMU sehr dankbar.

Bei den beiden Nachbargruppen an der LMU, die AG Weinfurter und AG Treutlein, möchte ich mich für die tolle Atmosphäre bedanken. Die Gruppen waren immer hilfsbereit und kameradschaftlich, wenn es um die Ausleihe von Komponenten und ähnlicher Hilfe ging. Die gemeinsamen Kuchenabenteuer und Mensaausflüge trugen sehr zu einer angenehmen Stimmung bei. Hier möchte ich stellvertretend insbesondere Florian Henkel, Daniel Schlenk, Michael Krug, Wenjamin Rosenfeld, Markus Weber, Jürgen Volz, Philipp Treutlein, David Hunger, Pascal Böhi, Max Riedel, Stephan Camerer, Maria Korppi, Andreas Jöckel und Jad Halimeh erwähnen auch für die sehr lustigen Abende abseits des Instituts.

Sehr lebhaft in Erinnerung wird mir der spektakuläre Umzug des Experiments bleiben. Hier verbrachte Tarun Johri als wissenschaftlicher Mitarbeiter einige Zeit bei uns im Labor, um einen Einstieg in das Experiment zu erhalten und den Umzug voranzutreiben. Zur Unterstützung waren auch Gan Eng Swee und Mohammad Imran aus Singapur angereist. Auch für organisatorische Belange möchte ich mich bei Fr. Chin Pei Pei vom CQT in Singapur bedanken.

Es hatten auch viele alte und neue Freunde indirekt zum Erfolg dieser Arbeit beigetragen. Sie hatten mich während der Dauer der Promotion immer sehr aufgemuntert und mir auch abseits der Physik tolle Diskussionsthemen eröffnet.

Am wichtigsten war mir die Unterstützung meiner Familie, die immer und zu allen Umständen mir tatkräftig den Rücken gestärkt hat. Zu jeder Zeit nahm meine Familie Anteil an meinem Weg, und ich weiß, dass ich ihr alles verdanke.

¹Werden Personenbezeichnungen aus Gründen der besseren Lesbarkeit lediglich in der männlichen oder weiblichen Form verwendet, so schließt dies das jeweils andere Geschlecht mit ein.